NANOENGINEERED IONIC-COVALENT ENTANGLEMENT (NICE) REINFORCED BIOINKS FOR 3D BIOPRINTING

A Dissertation

by

DAVID C. CHIMENE

Submitted to the Office of Graduate and Professional Studies of
Texas A&M University
in partial fulfillment of the requirements for the degree of

DOCTOR OF PHILOSOPHY

Chair of Committee,	Akhilesh K. Gaharwar
Committee Members,	Daniel Alge
	Kayla Bayless
	Roland Kaunas
Head of Department,	Michael J. McShane

October 2019

Major Subject: Biomedical Engineering

ABSTRACT

Three-dimensional (3D) bioprinting is emerging as a promising method for rapid fabrication of biomimetic cell-laden constructs for tissue engineering using cell-containing hydrogels, called bioinks, that can be cross-linked to form a hydrated matrix for encapsulated cells. Bioprinting currently enables precise deposition of viable cells in 2 dimensions, however, their printability in the Z-axis is severely limited because the inks are too weak to support additional layers or do not have the flow properties necessary to fabricate stable many-layered structures. Thus, extrusion-based 3D bioprinting has hit a bottleneck in progress over the lack of suitable bioinks. My research has focused on overcoming this limitation by developing a bioink able to bioprint in all 3 dimensions. Nanoengineered Ionic-Covalent Entanglement (NICE) bioink formulations combine nanocomposite and ionic-covalent entanglement (ICE) strengthening mechanisms to print customizable cell-laden constructs for tissue engineering with high structural fidelity and mechanical stiffness. Nanocomposite and ICE strengthening mechanisms complement each other through synergistic interactions, improving mechanical strength, elasticity, toughness, and flow properties beyond the sum of the effects of either reinforcement technique alone. NICE bioinks can be used to bioprint complex, large-scale, cell-laden constructs for tissue engineering with high structural fidelity and mechanical stiffness for applications in custom bioprinted scaffolds and tissue engineered implants. Next, we transform this platform technology into a specialized bioink for recreating missing bone tissue by testing bioink components to create a highly printable bioink with appropriate mechanical and degradation properties for osteogenic tissue formation. Then, bone marrow derived stem cells are encapsulated and bioprinted into custom structures using

patient scans, and are closely followed for stem cell differentiation, proliferation, histological changes, and blood vessel ingrowth. The overall effect of this research is the development of a new range of bioinks capable of replicating large 3D tissue structures, and the demonstration of their use for rapidly fabricating cell-containing custom scaffolds for bone tissue regeneration. I envision my research's continued development towards a realistic clinical process for bioprinting patient-specific bone tissue.

ACKNOWLEDGEMENTS

I would like to thank my dissertation advisor, Dr. Akhilesh Gaharwar, my committee members, Dr. Daniel Alge, Dr. Kayla Bayless, and Dr. Roland Kaunas for their help over the years. I would also like to thank my family and friends, and all of the teachers and mentors I've had along the way.

CONTRIBUTORS AND FUNDING SOURCES

Contributors

This work was supervised by a dissertation committee consisting of Professor Akhilesh K. Gaharwar and Professors Daniel Alge and Roland Kaunas of the Department of Biomedical Engineering and Professor Kayla Bayless of the Texas A&M Health Science Center Department of Molecular and Cellular Medicine.

Funding Sources

Graduate study was supported by the Bridge to the Doctorate Fellowship, the Graduate Enrichment Fellowship, and the Doctoral Diversity Fellowship from Texas A&M University.

I would like to acknowledge research support from the National Institute of Biomedical Imaging and Bioengineering (NIBIB) of the National Institutes of Health (NIH) Director's New Innovator Award (DP2 EB026265) and the National Science Foundation (NSF) Award (CBET 1705852).

NOMENCLATURE

hMSCs	Human Mesenchymal Stem Cells
nSi	Nanosilicates, Laponite XLG unless specified
GelMA	Gelatin Methacrylate
κCA	Kappa Carrageenan

TABLE OF CONTENTS

Page

LIST OF FIGURES

CHAPTER 1: INTRODUCTION

This dissertation contains the majority of my research during my time at A&M. It is divided into 6 major sections. In chapter 2, I review the state of existing bioink technology, focusing on how print performance is represented in literature and the limitations of existing bioink technology. Next, I discuss the state of emerging trends in the application of nanomaterials to solving engineering challenges in biomedical engineering. Finally, chapter 4 explores the material properties underlying the limited performance of hydrogel bioinks and how we can use emerging materials science research to work around those limitations to efficiently improve bioink mechanical properties and printability. In chapter 5, I apply this knowledge to take a popular biocompatible hydrogel(GelMa) and transform it into a bioink with superior printability and mechanical properties without sacrificing its biocompatibility. This NICE bioink is unique among existing bioinks because it combines superior printability, improved mechanical properties, and excellent bioactivity into a single bioink formulation. Chapter 6 focuses on demonstrating the practical use of the NICE bioink by showing how it can be optimized to work as a printable and customizable resorbable bone scaffold for regenerative bone tissue engineering. Chapter 7 contains the latest information on our ongoing *in vivo* studies on mice, which are intended as a precursor to further trials. Finally, the appendices briefly chronicle the development of heterogeneous bioinks based on the NICE formulation that are intended to create complex microenvironements for cells, as well as deliver bioactive factors and living cells. These bioinks can be used to create cell-specific microenvironments that are more precise than the current ~100 micron resolution of extrusion bioprinting.

CHAPTER 2: ADVANCED BIOINKS FOR 3D PRINTING: A MATERIALS SCIENCE PERSPECTIVE*

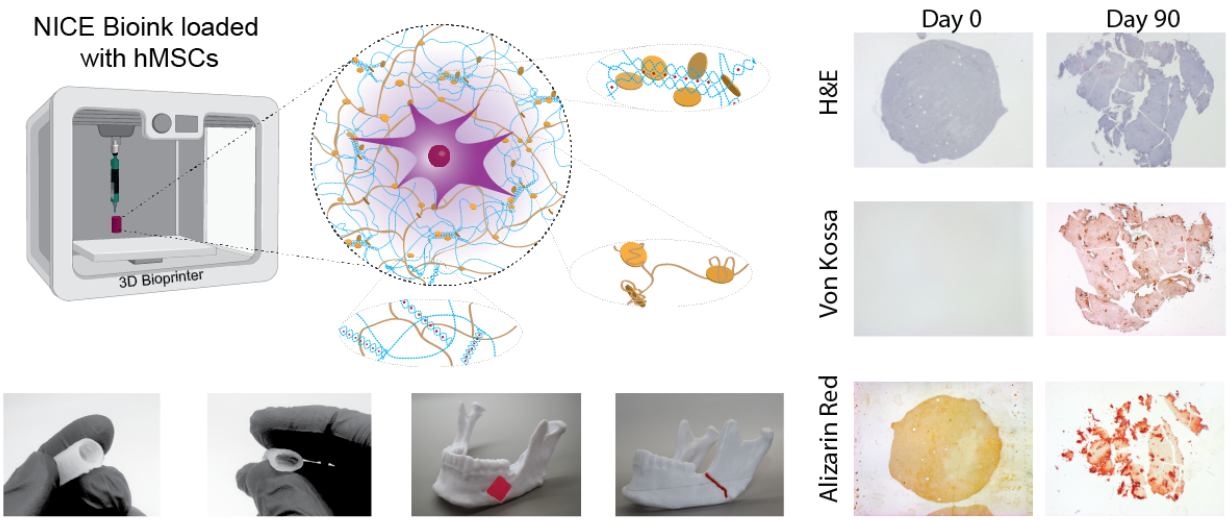

Figure 2-1. Overview of Nanoengineered Ionic Covalent Entanglement (NICE) bioinks. NICE bioinks combine nanoreinforcement and ionic-covalent entanglement of polymer networks to create patient-specific, osteoinductive implantable 3D scaffolds that can be bioprinted for repair of bone defects for regenerative medicine. This chapter contextualizes the development of NICE bioinks by providing an overview of advanced bioink design.

2.1 Overview

Advanced bioinks for 3D printing are rationally designed materials intended to improve the functionality of printed scaffolds outside the traditional paradigm of the "biofabrication window".

---

* Reprinted with permission from D. Chimene, K. K. Lennox, R. R. Kaunas, A. K. Gaharwar, Advanced bioinks for 3D printing: a materials science perspective. *Ann Biomed Eng* **44**, 2090-2102 (2016).

While the biofabrication window paradigm necessitates compromise between a bioink's suitability for fabrication and its ability to accommodate encapsulated cells, recent developments in advanced bioinks have resulted in improved bioink designs without these usual tradeoffs. Although research into these advanced bioink designs is relatively nascent, promising improvements demonstrate a new generation of bioinks for a range of biofabrication platforms. These advanced bioink designs have high print fidelity, shear-thinning characteristics, and result in scaffolds with high mechanical strength, high cytocompatibility, and the ability to modulate cellular functions. In this review, we describe some of the promising strategies being pursued to achieve these goals including multimaterial, interpenetrating networks, nanocomposites, and supramolecular bioinks. We also provide an overview of current and emerging trends in advanced bioink synthesis and biofabrication, and evaluate the potential applications of these novel biomaterials to translate into clinical use.

2.2 Introduction

The recent emergence of additive manufacturing(3D printing) technology is resulting in the development of bioprinted scaffolds loaded with cells for engineering complex tissue structures.(1-4) A vital yet limiting aspect of the design and implementation of a bioprinting system for tissue engineering is the selection of materials to be used as bioinks. Polymeric hydrogels, highly hydrated three-dimensional polymeric networks, are one of the most viable classes of bioink material candidates as they can mimic, augment or replace native tissue microenvironment and control cell fate.(5-9) In addition, hydrogel networks can also facilitate matrix remodeling, cell migration, and cell-cell adhesions necessary for normal development of a

functional tissue. The behavior of cells within these printed matrices is regulated by the physical and chemical properties of hydrogel networks. In the past decade, intelligent hydrogels that mimic the native microenvironment have been developed.(9-12)

Significant progress has been made in designing single-component hydrogels for bioprinting applications, but these hydrogels suffer from serious limitations.(4, 13, 14) These problems arise from the necessity of finding a compromise between hydrogel properties that are suitable for printing and properties that are ideal for cells. Cells generally thrive in porous networks and need cell binding domains to facilitate cell spreading and migration. The presence of biodegradable sites within hydrogel networks allows cells to remodel the surrounding microenvironment. However, single component hydrogels are typically optimized for bioprinting by increasing polymer concentration and crosslink density. These changes improve print fidelity but are detrimental to encapsulated cells because they prevent cell migration, limit nutrient diffusion, and reduce water content. (4, 15-19) Thus, there is a pressing need to develop advanced bioinks that combine improved printability, structure fidelity, functionality, and bioactivity.

In this review, we will focus on advanced hydrogel bioink designs that are currently being investigated for 3D bioprinting applications. Traditional hydrogels for bioprinting and bioprinting techniques have already been covered in recent, well-written reviews.(20, 21) Instead, we will highlight four advanced bioinks designs– multimaterial, IPNs, nanocomposite, and supramolecular networks that are currently being explored. These innovations in advanced hydrogel design work to provide high print fidelity, cytocompatibility, mechanical strength, and desirable cell-scaffold interactions. This review will focus on the materials science aspects of bioink development, provide a critical overview of these emerging bioink designs, and evaluate their potential for

engineering complex tissue structures. Finally, we will identify promising new research directions in the field of advanced hydrogels for bioprinting applications.

2.3 Design Parameters for Advanced Bioink Development

3D bioprinting is a process that uses computerized deposition of biologically relevant materials to create 3D tissue constructs. 3D bioprinting is gaining prominence in tissue engineering because it offers a straightforward method for fabricating 3D constructs containing complex geometric distributions of cell types, materials, and biochemical cues, which makes it a promising tool for the development of functional tissues.(19) Multiple bioprinting strategies including inkjet, extrusion, stereolithography, and laser induced forward transfer(LIFT) are being pursued with the goal of developing functional tissue constructs. Each of these modalities relies on a bioink that contains the cells, however, specific bioink requirements vary based on printing modality. For example, inkjet bioprinting requires low viscosities to avoid clogging and low thermal conductivity to prevent heat damage to the cells. In contrast, extrusion bioprinting can accommodate much higher viscosities but shear thinning materials are often necessary to prevent mechanical damage to the cells.(3, 4, 20) Despite these considerations, most developments in bioink design originate with extrusion 3D bioprinting, a modality that places very high demands on the mechanical and rheological properties of bioinks.(3, 4, 19)

In extrusion bioprinting, a bioink filament is continuously extruded through a deposition nozzle. A low viscosity is generally desirable during extrusion to avoid excessive fluid shear stress and potential for jamming. Upon deposition, a high viscosity or solidification rate is needed so that the filament retains its shape in order to maintain high print *fidelity*, i.e. the precision of the printed

structures. For example, thermoresponsive gelation of gelatin can be employed in bioprinting since it aids in retaining shape of printed constructs. However, gelatin has not often been used alone for bioprinting because its reversible sol-gel transition poses difficulties in optimizing printing temperature and viscosity. Similarly, PEG hydrogels are too soft to maintain their shape after printing. Bioinks have the additional constraint that the cells must remain viable during extrusion and solidification phases. Many extrudable hydrogels such as agarose maintain their structural integrity through high polymer concentrations. These conditions are too harsh (viscosity) for cell survival and thus agarose hydrogels are mostly used in 3D printing as sacrificial structures. (4, 19, 22-24)

The *biofabrication window* **(Figure 2-2)** is a concept that describes the compromises that have traditionally been made to create bioinks that have suboptimal, yet passable, print fidelity while maintaining cell viability. Low-viscosity bioinks that are cytocompatible can be used if printed with another sacrificial bioink. The rate of gelation, which can rely on conformation changes or crosslinking of polymer network, also affects print fidelity by determining how quickly the bioink can be crosslinked after printing.(4)

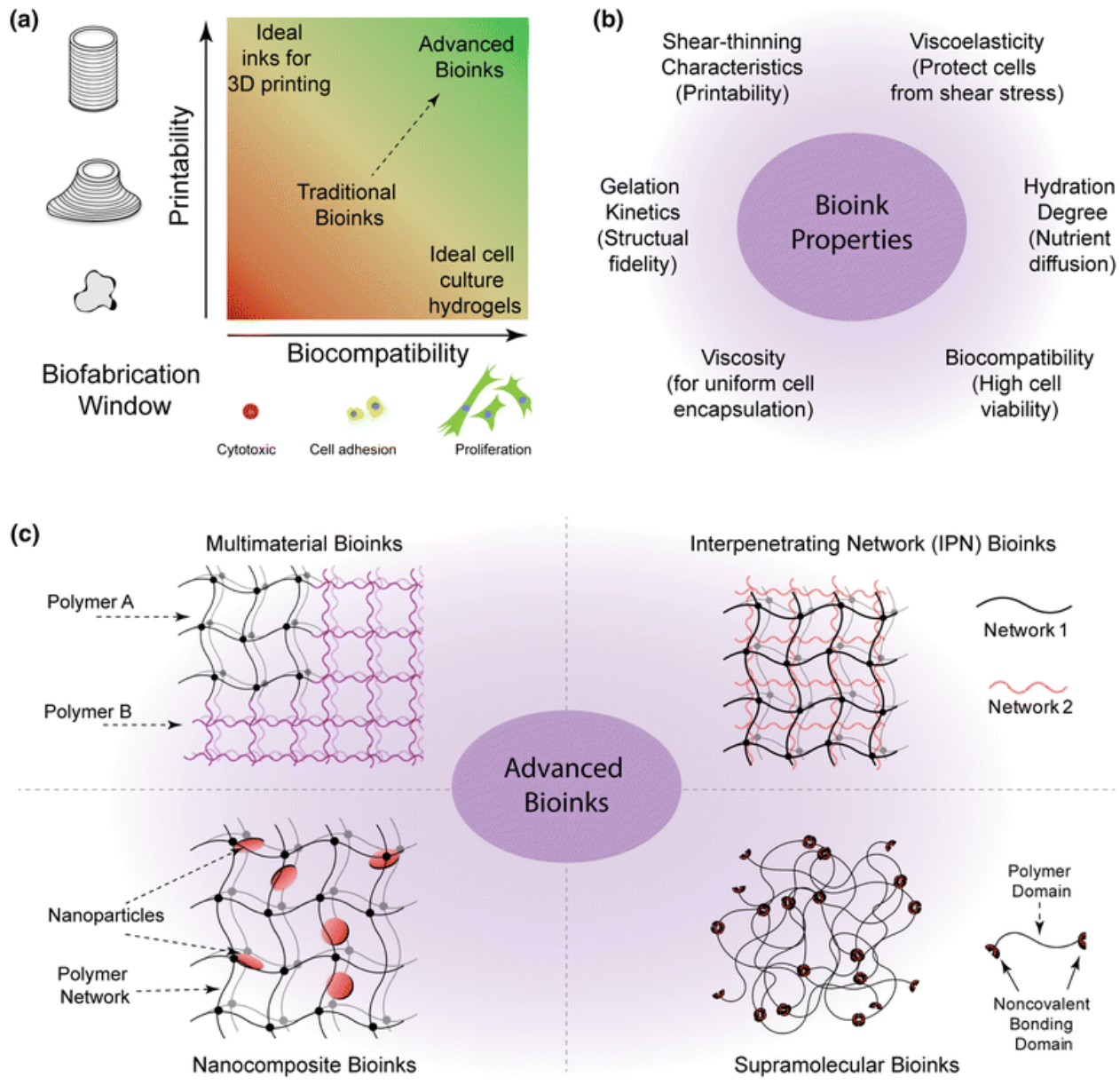

Figure 2-2. Advanced bioinks for 3D printing. (a) Biofabrication window for rational design of bioinks requires compromise between printability and biocompatibility. (b) Ideal bioink characteristics require interplay between different materials properties. (c) Advanced bioinks can be classified into four major categories.

In addition to the print fidelity and cytocompatibility requirements described by the biofabrication window, a bioink plays a significant role in determining cell behavior beyond simple cytocompatibility. Cell interactions with the ECM *in vivo* have important consequences on cell behavior and health that are still being explored. Similarly, a bioink's cell interactions can determine its bioactivity: it can determine whether a cell proliferates, differentiates, and creates new ECM or remains passively trapped within the bioink. Bioactivity is defined as the beneficial effects a substance has on a living system. Bioactivity in bioinks depends on the biochemical and biomechanical interactions between cells and the bioink.

Soluble factors like drugs and growth hormones(e.g. bone morphogenetic proteins, fibroblast growth factors) that can be diffused in vitro into a tissue scaffold can strongly influence cell behavior even in otherwise bioinert environments. For in vivo applications however, soluble factors typically diffuse out of hydrogels quickly. Nanomaterials offer new ways of modifying release kinetics, including stimuli responsive release, which could increase the effectiveness of soluble factors. Bioactivity is also dependent on the bioink material itself. Some natural hydrogels like gelatin and fibrin are intrinsically bioactive and contain cell attachment molecules(CAMs). Synthetic hydrogels have also been functionalized with CAMs to attempt to replicate this bioactivity. (6, 19, 25-27)

Beyond biochemistry, mechanical cues from the bioink can also influence cell fate. ECM stiffness has been shown to direct cell differentiation, with stiffer ECMs directing MSCs toward osteogenic or chondrogenic lineages. Bioink stiffness can be modulated without increasing polymer crosslinking or concentration by employing interpenetrating networks or nanocomposite designs, as discussed later. Nanomaterials can also influence cell behavior in other ways, for example, graphene's electrical conductivity can influence neural activity. Material alignments can

induce cells to organize relative to ECM alignment. This alignment technique has been used in tissue scaffolds for muscle and fibrous tissue. Mechanical stimulation can also be used to influence cell behavior. Bioreactors can direct cell behavior by reproducing physiological conditions. For example, pulsatile flow bioreactors can increase collagen production in blood vessel scaffolds, while cyclic stretching and flexure increased collagen and DNA production in engineered heart valves. Cyclic tensile forces have also been used to improve skeletal muscle cell alignment and contractility.(19, 24, 25, 28, 29)

Another important consideration for bioink development is the ability of the hydrogel network to respond to cell-mediated matrix remodeling. Biodegradation of bioinks can occur via enzymatic (mostly natural polymers such as collagen or gelatin), hydrolytic (synthetic polymers such as polyesters) and ion exchange (such as carrageenans and alginate).(19, 30, 31) The degradation kinetics of bioinks can modulate ECM production and remodeling.(19, 31) Interplay between these parameters is needed to design and develop advanced bioink compositions.

Advanced bioinks use multiple strategies to improve bioink print fidelity and maintain cytocompatibility. For example, bioinks designed with shear thinning properties have lower viscosities at the high shear rates generated during extrusion. After extrusion, viscosity increases result in high print fidelity and cell viability. Interpenetrating network, nanocomposite, multimaterial, and supramolecular hydrogels can all exhibit shear thinning characteristics. Functional groups can also be added to accelerate solidification upon exposure to UV irradiation. Further, functional groups and nanoparticles can provide bioactive properties to the bioink to direct cell function.

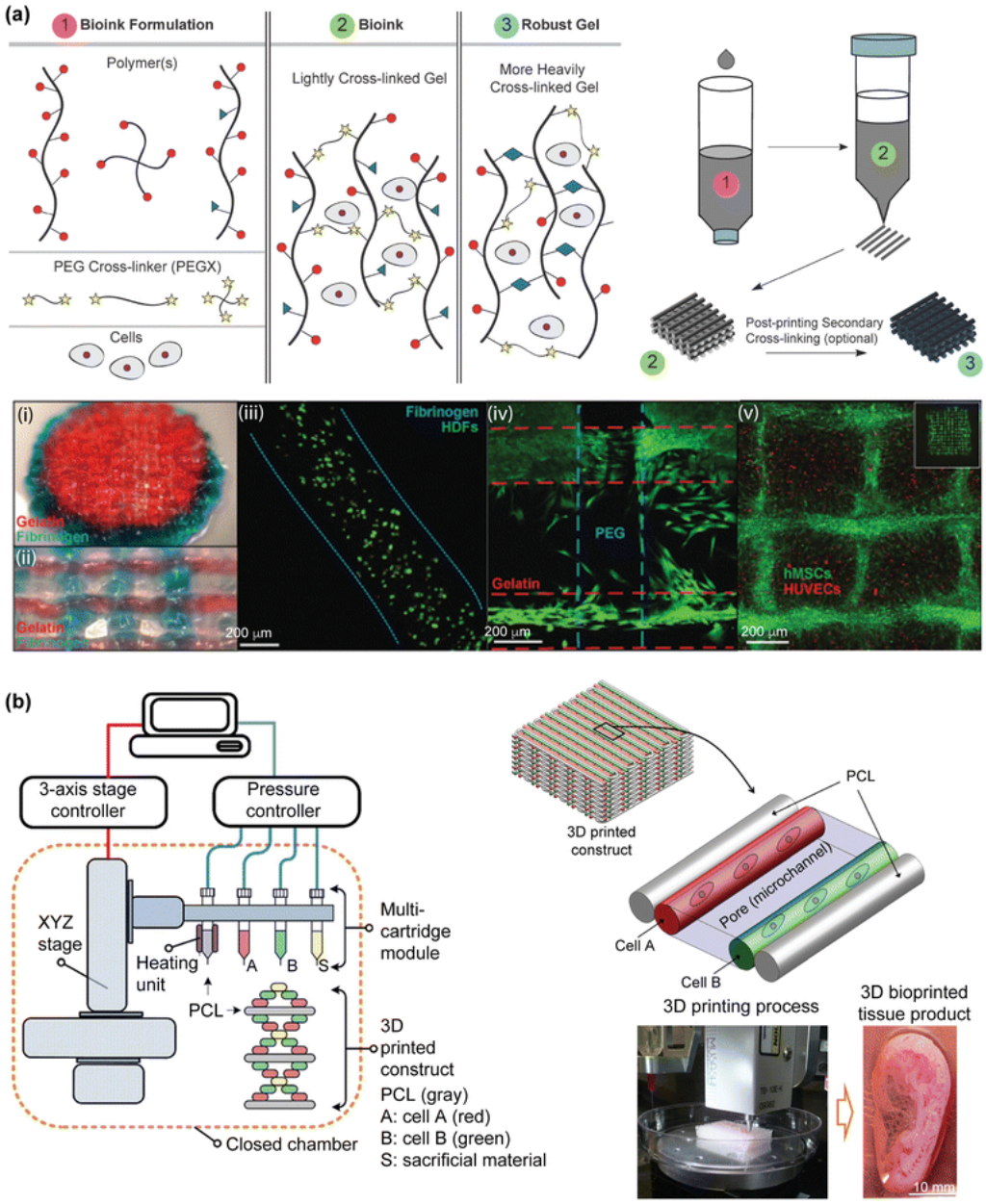

Figure 2-3. Multimaterial bioinks for 3D bioprinting. (a) Bioinks consist of GelMA and PEG crosslinker. The length of PEG crosslinker can be modulated to control the mechanical properties of printed structures. Cells can be incorporated within the bioink prior to printing. 3D printed structures show high cell viability and support cell proliferation. (b) Multi-head printer used to print a complex interwoven scaffold consisting of hydrogel

bioinks, polycaprolactone(PCL) and Pluronic F-127. Adapted and reproduced by permission from Wiley 2015 and Nature American Inc. 2016.

2.4 Multimaterial Bioinks for 3D Printing

Multimaterial hydrogel bioinks are the most widely investigated bioinks to overcome the limitations of single component hydrogels. For example, alginate has been used as a single component hydrogel in tissue engineering because it is biocompatible and can be ionically crosslinked using calcium ions to obtain mechanically robust hydrogels. In this review, we define biocompatibility as the ability of a material to be implanted *in vivo* without causing deleterious local or systemic reactions. In contrast, cytocompatibility is defined as the ability of a material to interact with cells without causing harm. Unfortunately, alginate also has low print fidelity and is largely bioinert, meaning that it does not meaningfully interact with cells. For example, it cannot be remodeled or strongly adhered to by encapsulated cells and does not influence cell differentiation. Alginate's lack of cell adhesion moieties(CAMs) reduces its cytocompatibility, since lack of adhesion can induce cell apoptosis through anoikis. To overcome these limitations, Chung *et al.* incorporated gelatin to increase the viscosity and cytocompatibility of alginate bioink.[32] Gelatin is denatured collagen which is capable of reversible thermal gelation and has cell adhesive arginyl-glycyl-aspartic acid (RGD) domains. Addition of gelatin increased the viscosity of the alginate and significantly increased the storage modulus when the composite was cooled below the gelation temperature of gelatin, resulting in improved print fidelity. The compression modulus of alginate and alginate-gelatin hydrogels were similar after ionic

crosslinking of the alginate. They showed that the addition of gelatin to alginate can be used to fabricate bioinks with higher viscosity and print fidelity for 3D extrusion-based bioprinting. However, due to ionic crosslinking, the bioprinted structure lost its mechanical integrity after 3-4 days. Thus, while the composite improved printing performance, the long-term mechanical properties remained sub-optimal.(32)

Covalent crosslinking is an effective method for improving the physiological stability of printed structures. Kesti *et al.* developed a dual crosslinked bioink consisting of methacrylated hyaluronan (HA-MA) and thermoresponsive polymer poly(N-isopropylacrylamide) (pNIPAAM) grafted hyaluronan (HA-pNIPAAM) for enhanced mechanical integrity.[33] HA-MA is a promising bioactive hydrogel for tissue engineering and can be covalently crosslinked after UV exposure, but is not suitable alone for printing because of its low viscosity. They first conjugated pNIPAAM to HA-MA to obtain a quickly gelling thermoresponsive component as a temporary support, making it suitable for 3D bioprinting. The thermoresponsive nature of the HA-pNIPAAM component provides rapid gelation and post-printing structural fidelity. This bioink was able to print strands down to 620 μm wide and 200 μm in height from a 300 μm needle. After the HA-MA had been crosslinked, the HA-pNIPAAM was rinsed away, leaving only an intact HA-MA scaffold. The presence of only HA-MA significantly increased the viability of encapsulated cells. This strategy may have the potential to be generalized to other hydrogels to improve pre-crosslinking storage modulus.(33)

In a similar experiment, Duan *et al*. developed bioink from HA-MA and gelatin methacrylate (GelMA) to print 3D trileaflet heart valves.(34) GelMA was incorporated to improve cell adhesion characteristics of the composite network. HA-MA increased bioink viscosity and resulting hydrogel stiffness, while GelMA was shown to also enhance viscosity and maintenance

of a fibroblastic phenotype of encapsulated human aortic valve interstitial cells (HAVIC). Seven days after printing, the encapsulated HAVIC showed enhanced production of collagen and glycosaminoglycan, indicating extracellular matrix (ECM) remodeling. This development is particularly important because previous synthetic scaffolds with much higher stiffness than natural heart valves showed limited remodeling. Though the bioprinted construct is not as strong as native heart valve leaflets, recently developed bioreactors have shown that subjecting encapsulated VIC cells to cyclic flexure and stretch conditions can significantly increase collagen production(stretch +423% / flexure +63%) and DNA content relative to static culture. Incorporation of both of these techniques in the future may lead to higher ECM production within heart valve tissue scaffolds, which could improve scaffold robustness prior to implantation.(28, 34)

To improve the hydrogel tunability, Rutz *et al.* designed a bioink from GelMA and multifunctional PEG crosslinkers (PEGX) **(Figure 2-3)**.(23) They used long PEGX crosslinkers to loosely connect the gelatin backbone to provide necessary viscosity for bioprinting applications with low gelatin concentrations. The increased viscosity of the bioink resulted in high structural fidelity without directly crosslinking gelatin polymers to each other. PEGX crosslinking allowed properties like viscosity and biodegradability to be tuned without compromising cytocompatibility. Taken together, these multimaterial hydrogels are a facile and effective approach for obtaining desirable bioink characteristics without compromising cell viability.

Recently, printing strategies have begun to use multiple bioinks to fabricate large and complex constructs. Kang *et al.* used a multi-head printer to print a complex interwoven scaffold consisting of hydrogel bioinks and polycaprolactone(PCL) and Pluronic F-127.(22) PCL was selected for its biocompatibility and relatively low melting temperature (~60°C), while Pluronic F-127 was selected as a sacrificial material due to its thermosensitive characteristics. The bioinks were

synthesized using gelatin, fibrinogen, hyaluronic acid (HA), and glycerol. Fibrinogen was used to provide cell adhesion properties, while gelatin was used to improve print fidelity. HA and glycerol acted as plasticizers. This multimaterial bioink was printed to obtain an interwoven support structure for mechanically weak bioinks. After the printing process, the fibrinogen was crosslinked using thrombin and the sacrificial components (Pluronic F-127, gelatin, HA, and glycerol) were rinsed out. Interweaving these materials resulted in a support structure for the mechanically weak bioink component. After printing, the fibrinogen was crosslinked using thrombin and the sacrificial components (Pluronic F-127, gelatin, HA, and glycerol) were rinsed away. The strategy of interweaving PCL to create microchannels enabled cells to survive within the thick tissue structure. This strategy resulted in high cell viability (>90%) and proliferation. This kind of multimaterial printing has the potential to bypass diffusion limits and fabricate thick scaffolds.

Finally, some recent strategies seek to alter bioink printability by extruding into hydrogel support baths. Hinton et al. developed a bioink containing collagen, Matrigel, fibrinogen, and hyaluronic acid.29 They used this multimaterial bioinks to build complex structures by embedding the printed structure within a secondary ‘‘sacrificial’’ hydrogels (gelatin slurry). After printing the structure, the gelatin support bath was removed by heating the bath to physiological temperature. Models of complex structures such as a human right coronary arterial tree and explanted an embryonic chick heart can be printed with high structural fidelity **(Figure 2-4)**. In another approach, Bhattacharjee et al. used a similar method to print thin rings of fluorescently labeled endothelial cells into a Carbopol granular gel medium.(35) This printing process relies on the Bingham plastic and thixotropic flow of the support materials. Although cell-containing bioinks were only printed into simple flat structures, the studies demonstrated that this technique can also be used to achieve very

high fidelity with biocompatible materials like alginate. This technique represents a promising new approach to improving the printability of bioinks without sacrificing biocompatibility.

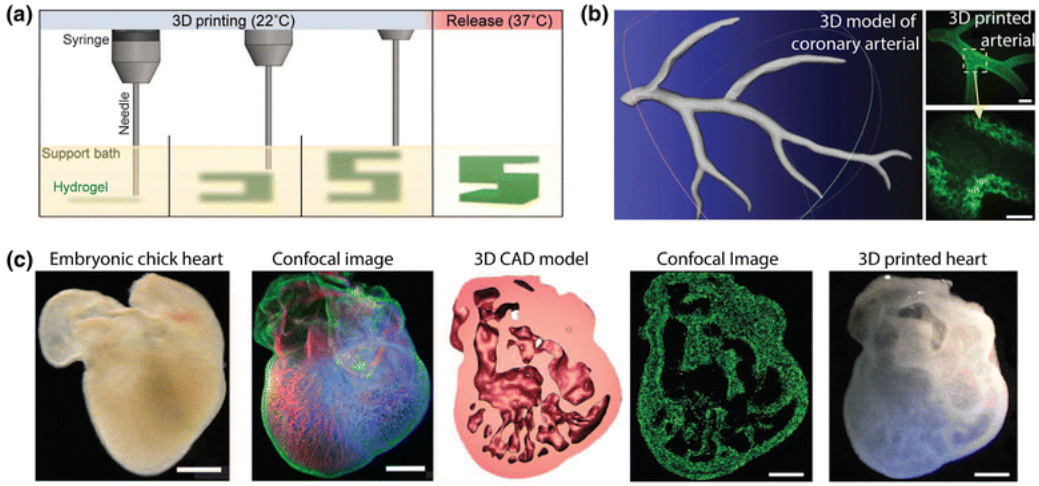

Figure 2-4. Multimaterial bioinks for 3D bioprinting using a sacrificial support bath. (a) 3D printing of a multimaterial bioink within a thermoreversible support bath. A range of complex tissue structures such as (b) a human right coronary arterial tree and (c) an explanted embryonic chick heart can be printed using computer models (Scale bar 5 1 mm). Adapted and reproduced by permission from American Association for the Advancement of Science 2015.

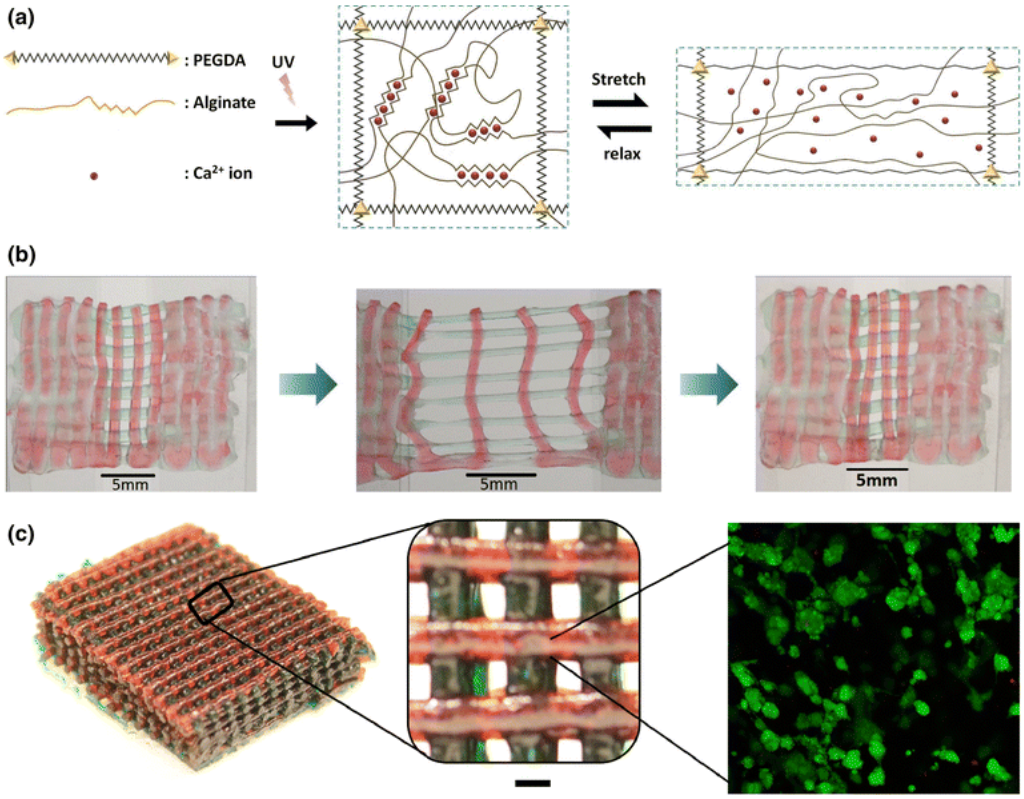

Figure 2-5. Interpenetrating network (IPN) bioinks for 3D printing. (a) IPNs were synthesized by covalently crosslinking PEG and ionically crosslinking alginate. (b) A mesh printed with the tough and biocompatible hydrogel can be subjected cyclic mechanical deformation. (c) Encapsulated cells show high cell viability. Adapted and reproduced by permission from Wiley 2015.

2.5 Interpenetrating Networks Bioinks for 3D Printing

Interpenetrating Networks (IPNs) are composite hydrogels in which each polymer network has limited interactions with the other.(36-40) Unlike multimaterial hydrogels, where different constituent polymers may be crosslinked together, IPNs are composed of separate polymer networks that are physically entangled within each other. The IPNs are often crosslinked using

different chemistries to encourage each polymer network to only crosslink with itself.(39) Limited unintentional inter-network crosslinking may occur depending on the type of polymers and crosslinking reactions used, which is believed to be significant in semi-IPNs where only one of the polymer networks has been crosslinked.(36-40) IPNs have been shown to have enhanced toughness and fracture strength compared to the single component networks of either of its constituent polymers. Generally, the primary network is composed of a flexible & elastic polymer, while the secondary network consists of a high-stiffness, brittle polymer at much lower concentration.

Double network (DN) hydrogels are a subset of IPNs that have been synthesized through a two-step polymerization. In the first step of traditional DN network preparation, polymer chains are covalent crosslinking to obtain the primary hydrogel network. The secondary polymer monomers then disperse throughout the primary network to later be crosslinked to obtain the DN hydrogels. Although this method has been widely used for DN hydrogel formation, it is too slow to be suitable for 3D bioprinting. More recently, ionic-covalent entanglement (ICE) gels are being developed that are both physically and chemically crosslinked. ICE gels form sufficiently fast to facilitate their use in 3D printing.(39, 41)

Recently, Bakarich *et al.* demonstrated the use of ICE hydrogels containing acrylamide and alginate for 3D bioprinting.(38) The acrylamide solution loaded with alginate maintained the printed shape and allowed formation of a covalently crosslinked acrylamide network. After covalent crosslinking, the alginate component was physically crosslinked with calcium chloride solution. The physical crosslinking of the gel was shown to restrict hydrogel swelling in water and increased both stiffness and failure stress by roughly an order of magnitude: from 23 to 260 kPa, and from 11 to 130 kPa, respectively. Additionally, soaking in calcium chloride increased strain

at failure for the gels from ~23% to 90%. This experiment demonstrated the utility of ICE bioinks as well as the improved mechanical properties that can be achieved with the addition of a biocompatible secondary network to create IPNs.(38)

In another study, Hong *et al.* fabricated elastomeric ICE hydrogels from poly(ethylene glycol) diacrylate (PEGDA) and alginate **(Figure 2-5)**.(42) The addition of calcium ions to ICE hydrogels increased fracture strength from ~200 J/m^2 to over 1500 J/m^2, comparable to native cartilage. Moreover, the hydrogel networks were able to sustain mechanical stress without significant plastic deformation. This behavior was mainly attributed to reversible crosslinking of the alginate that can reconfigure during deformation and the elastomeric characteristics of the PEGDA network. The encapsulated cells within these ICE hydrogels showed high cell viability (75.5 ± 11.6%) over a period of 7 days. IPNs could also be further modified with nanomaterials to obtain high print fidelity. Overall, this study showed that ICE hydrogels can be used to fabricate mechanically tough 3D-printed structures for regenerative engineering.

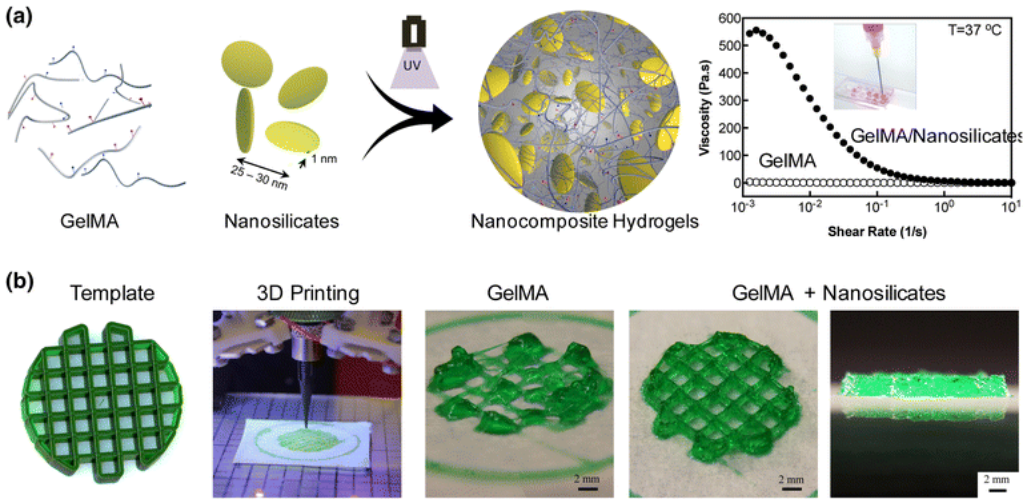

Figure 2-6. Nanoengineered bioinks for 3D printing. (a) Shear-thinning hydrogels were prepared by combining synthetic nanosilicates with gelatin methacrylate (GelMA). (b) The addition of nanosilicates to GelMA results in high print fidelity and structural stability. After

UV crosslinking, printed hydrogels showed high physiological stability. Adapted and reproduced by permission from American Chemical Society 2015.

2.6 Nanocomposite Bioinks for 3D Printing

Nanoengineered hydrogels have been investigated for a range of biomedical and biotechnological applications.(6, 10) Small amounts of nanoparticles added to polymeric hydrogels can result in significant improvements in various physical and chemical characteristics including high stiffness, shear-thinning characteristics, and resistance to degradation under physiological conditions.(43-45) Depending on the type of nanoparticles used to reinforce the hydrogel network, unique properties such as bioactivity, controlled drug release, electrical conductivity, photoresponsiveness, and magnetism can be incorporated.(6) Although several nanocomposite hydrogels have been developed for tissue engineering applications, very few studies have investigated their potential for 3D bioprinting.

In a recent study, Gao *et al.* explored the bioactive potential of hydroxyapatite nanoparticles (nHAp) by designing nanoengineered bioinks for bone tissue engineering.(46) They fabricated bioinks by combining poly(ethylene glycol) dimethacrylate (PEGDMA) with nHAp (~200 nm) and/or bioactive glass (BG) (~20 μm) for 3D printing. Although the addition of nHAp to PEGDMA increases mechanical strength, the effects of the nanoparticles on shear-thinning characteristics and print fidelity were not measured. Human mesenchymal stem cells (hMSCs) were printed with bioinks consisting of nHAp and BG using layer-by-layer assembly, resulting in uniform cell distribution within the hydrogel and high cell viability (>80%). The addition of nHAp resulted in significant increases in ECM deposition and upregulation of bone-related gene expression

(collagen I, osteocalcin, collagen X, and MMP13) compared to PEGDMA scaffold alone. Taken together, this study demonstrates that addition of nHAp to PEG bioinks increases compressive modulus and promotes osteogenic differentiation of hMSCs.

Other types of nanoparticles such as synthetic silicate clays are extensively used for bioprinting applications. These clays are 2D coin-shaped nanomaterials characterized by a high surface-to-volume ratio and an unusual charge distribution (negatively charged flat surfaces and positively charged edges).(25) These characteristics result in strong, reversible non-covalent interactions with natural and synthetic polymers and overall shear-thinning mechanical properties. These shear-thinning characteristics are important for bioprinting applications as high fidelity structures can be obtained by controlling the shear viscosity of bioinks. Xavier *et al.* synthesized bioactive bioinks using these synthetic nanosilicates and GelMA **(Figure. 1-6)**.(27) While GelMA hydrogels provide cell adhesion sites, their poor mechanical strength limits their utility as a bioink. The addition of nanosilicates to GelMA increased viscosity at low shear rates, and at high shear rates had similar viscosity to pure GelMA. The nanocomposite pre-polymer solutions exhibited shear thinning characteristics, which allowed the successful printing of complex shapes with high shape fidelity. Hong *et al*. showed similar behavior upon incorporation of silicate nanoparticles to ICE hydrogels (PEGDA/alginate).(42) Xavier *et al.* also showed that addition of nanosilicates to GelMA promotes osteoblast differentiation and induces production of mineralized ECM.(27) Taken together, this research exemplifies the potential of new nanocomposite bioinks for bioprinting applications.

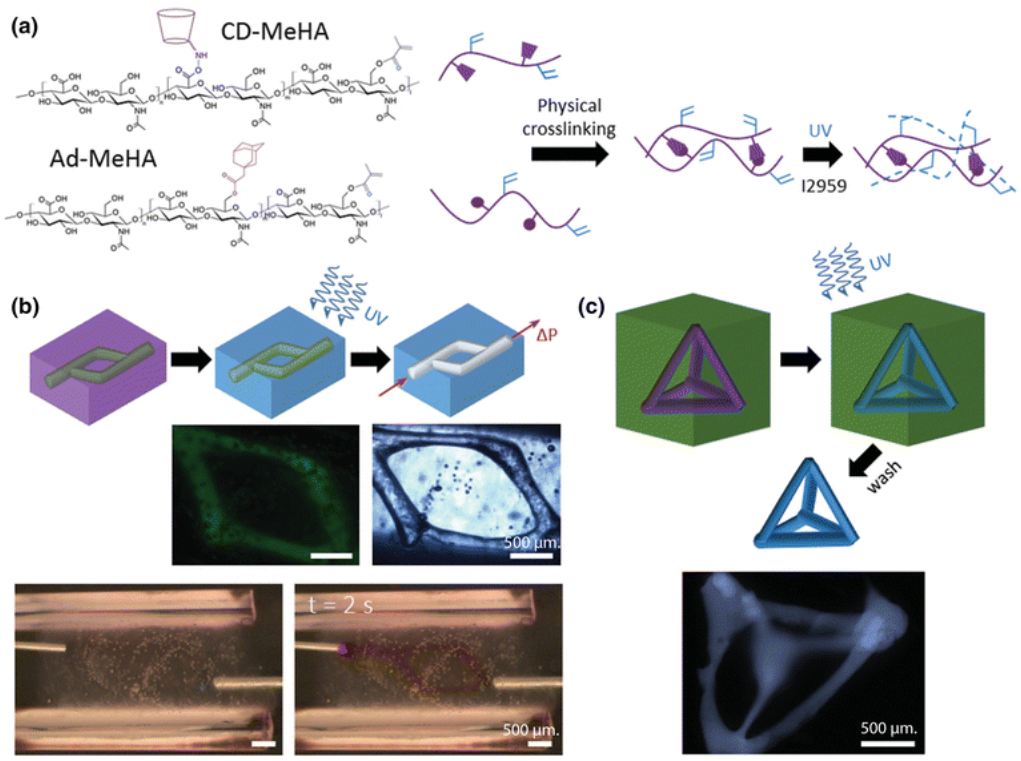

Figure 2-7. Supramolecular bioinks for extrusion-based 3D bioprinting applications. (a) Hydrogels were fabricated by combining CD-MeHA with Ad-MeHA to obtain physically crosslinked bioinks. (b) After exposing the printed structure to UV light, covalently crosslinked supramolecular hydrogels were obtained. (c) The printed structure shows high mechanical integrity and can be used to print complex structures. Adapted and reproduced by permission from Wiley 2015.

2.7 Supramolecular Bioinks for 3D Printing

Hydrogels for tissue engineering applications should be mechanically tough and capable of surviving repeated mechanical deformation. When subjected to repeated stress, bonds in conventional hydrogels can break, resulting in progressive loss of mechanical integrity. To

overcome this drawback, current research has been directed towards supramolecular bioinks for bioprinting applications.(47, 48) Supramolecular polymers are composed of short repeating units with functional groups that can interact non-covalently with other functional units, forming large, polymer-like entanglements. Under high stress, these non-covalent bonds are reversibly broken to dissipate energy. The reversibility of these bonds also leads to shear-thinning properties that facilitate their use in bioprinting.

In a recent study, Highley *et al.* described a straightforward method for fabricating shear-thinning and mechanically resilient hydrogels for 3D bioprinting applications using a cytocompatible hyaluronic acid (HA)-based supramolecular hydrogel **(Figure 2-7)**.(49) HA was modified with either adamantane or β-cyclodextrin functional groups that can interact with each other through guest-host interactions and can rapidly form a supramolecular polymer. The reversible nature of the non-covalent bonds in the hydrogel caused the gel to exhibit low viscosity under mechanical deformation (or at high strain) and recovery of mechanical integrity after cessation of stress. The rapid increase in viscosity after strain cessation prevents the bioink from continuing to flow after printing, resulting in high structural fidelity and integrity. The bioink was shown to be highly cytocompatible (>80% cell viability). HA macromers were also ~25% methacrylated in order to allow for UV crosslinking after 3D printing, as the supramolecular bonds themselves lacked the mechanical strength for long-term stability.

DNA hybridization represents another approach to fabricating supramolecular hydrogels. Li *et al.* developed supramolecular polypeptide–DNA hydrogel for rapid *in situ* 3D bioprinting by designing two bioinks – one containing a polypeptide–DNA conjugate and the other containing the complementary DNA linker **(Figure 2-8)**.(50) DNA hybridization between the complementary DNA molecules leads to rapid crosslinking and gelation within one second. The rigidity of DNA

polymers allows for the printing of structures on the millimeter scale with high structural integrity. These scaffolds were shown to have high cytocompatibility and could be biodegraded by proteases and nucleases.

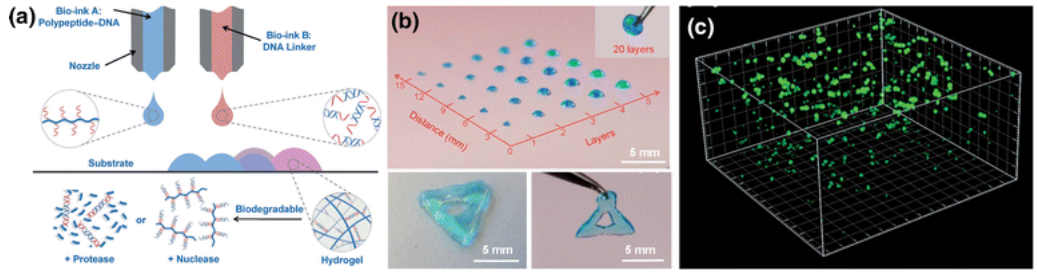

Figure 2-8. 3D bioprinting of supramolecular bioinks. (a) Polypeptide–DNA hydrogels were synthesized by using two bioinks [Bioink A (blue): polypeptide–DNA, and Bioink B (red): DNA linker]. Hybridization of these two bioinks result in crosslinking, leading to hydrogel formation. (b) Hydrogels with different sizes and complex structures can be obtained. (c) Encapsulated cells showed high viability. Adapted and reproduced by permission from Wiley 2015.

2.8 Emerging trends and Future Outlook

The current bottleneck in designing complex tissue structures using 3D printing is the limited availability of versatile bioinks. Despite multimaterial bioinks being the most explored solution, many promising combinations of innovative polymers have yet to be evaluated. For example, PEG hydrogels functionalized with RGD or other binding moieties can provide cell adhesion to otherwise bioinert hydrogels.(51) Combinations of different strategies described in this review can lead to development of the next generation of bioinks. For example, mechanical improvement of

multicomponent polymeric bioinks can be obtained by incorporation of shear-thinning nanoparticles. Incorporation of bioactive components such as growth factor-loaded nanoparticles or microparticles within polymeric network will provide additional tools to control cell fate.

Advanced bioinks should be able to print complex tissue structures such as vascularized tissues and biomimetic architectures. In addition, they should be able to modulate cell phenotype within the printed structure. We can expect to see an increased number of strategies to better meet these requirements. Breakthroughs in related fields such as nanomaterials, stem cell technology, 3D printing equipment, and polymer chemistry will certainly facilitate the development of hydrogel bioink technologies in perhaps unexpected ways. For example, current research into nanomaterials is primarily in the fundamental research stage, with relatively few studies applying this technology to biomedical engineering.(25) While current bioink research has so far been confined primarily to silicate nanoparticles and graphene, promising categories of nanoparticles including stimuli-responsive nanomaterials and two-dimensional nanomaterials have the promise to add additional functionalities to bioinks.(25)

The combination of new strategies to control stem cell differentiation is expected to play a prominent role in designing advanced bioinks. Bioinks with sustained release of growth factors will not only provide favorable conditions for directed stem cell differentiation, but will also reduce the amount of growth factor required. The use of controlled and stimuli-responsive release of immunomodulators and growth factors has the potential to add another level of control of the bioactivity of bioinks.(25, 52) In addition, stem cell fate can also be directed towards different lineages using mechanical cues. Cells respond to cyclic strain on GelMA nanocomposites by aligning to an extent dependent on stiffness of the hydrogel.[34] While the role of mechanical cues in tissue engineering fields are relatively well established(27, 53), they have not been applied to

3D printed constructs. In the near future, we can expect to see incorporation of these modalities within 3D printing.

Bioprinters with multiple printing heads are also needed to rapidly produce complex tissue structures. 3D bioprinters with multiple heads have the ability to deposit multiple formulations simultaneously to fabricate complex and biomimetic tissue structures including vascularized tissue. Multi-head 3D printers with the ability to control multiple physical and biological characteristics simultaneously need to be developed.(54) With these types of bioprinters, it would be possible to print structures with multiple cell types and multiple ECM matrixes with different stiffnesses. This system would also provide control over the spatial distribution of biochemical cues. Recently, studies have explored the use of multiple polymeric bioinks for printing complex tissue structures.(55, 56) In the future we expect to see a significant development in advanced bioink compositions for printing complex structures that are currently not feasible due to technological limitations.

2.9 Conclusion

3D bioprinting is a promising solution to some of the most daunting obstacles facing the field of tissue engineering, including vascularization of tissue constructs, creation of complex architectures, and directing stem cell differentiation. However, the lack of suitable bioinks has emerged as one of the most significant obstacles to the advancement of 3D bioprinting research. Traditional single component hydrogels have lacked one or more of the characteristics desired in a bioink, including low structural fidelity and printability, weak mechanical strength, and limited bioactivity and biodegradability. Attempts to rectify mechanical and rheological shortcomings of

bioinks through increased polymer and crosslink density tend to reduce the cytocompatibility of single component bioinks. Recent developments in advanced bioinks avoid these tradeoffs without sacrificing cell viability.

Multimaterial hydrogels are gaining popularity as a facile and effective method for obtaining desirable bioink characteristics. Due to high viscosity and shear-thinning characteristics, multimaterial bioinks have desirable printability and high structural fidelity. Meanwhile, IPN bioinks have been shown to combine the physical and chemical characteristics of multiple polymeric hydrogels into a single hydrogel. This is especially evident in terms of IPN mechanical properties, which combine the stiffness of the ionically crosslinked networks with the elasticity and strain recovery characteristics of covalently crosslinked networks. A range of IPNs have been formulated that have high stiffness at lower polymer concentrations than single component hydrogels, resulting in a useful blend of stiffness and cytocompatibility that is likely to continue to be explored for bioinks development. Nanocomposites hydrogels provide a facile method to combine multiple functionalities within 3D printed structures by incorporating inorganic nanoparticles with unique characteristics. These nanoparticles physically interact with polymer chains and result in shear-thinning hydrogels, which are highly desirable for bioprinting applications. Finally, supramolecular hydrogels have favorable shear-thinning characteristics, which are beneficial for cell encapsulation and 3D bioprinting. In addition, their printed structures offer high shape fidelity for millimeter sized structures. However, these bioinks are still limited in terms of mechanical strength, an area that will need to be improved in order to allow for their further application in 3D bioprinting. Despite these drawbacks, supramolecular hydrogels are promising candidates for bioink applications due to their ability to create non-covalent bonds to reversibly link polymers together. Overall, advances in bioink design promise to bring 3D

bioprinting and tissue engineering closer to clinical applications in treating a wide range of tissue ailments, from closer goals like improved arthritis and burn treatments towards eventual complex organ replacement.

CHAPTER 3: TWO-DIMENSIONAL NANOMATERIALS FOR BIOMEDICAL APPLICATIONS: EMERGING TRENDS AND FUTURE PROSPECTS[†]

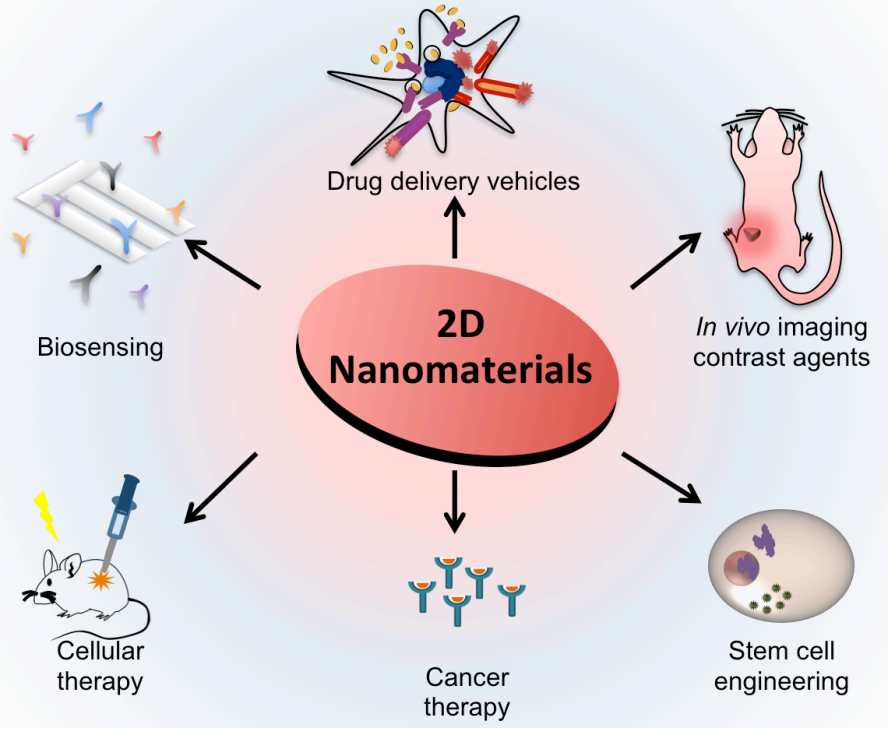

Figure 3-1. An Overview of the Myriad Biomedical Uses for 2D Nanomaterials

3.1 Overview

Two-dimensional (2D) nanomaterials are ultrathin nanomaterials with a high degree of anisotropy and chemical functionality. Research on 2D nanomaterials is still in its infancy, with the majority of research focusing on elucidating the unique material characteristics and very few

[†] Reprinted with permission from D. Chimene, D. L. Alge, A. K. Gaharwar, Two-dimensional nanomaterials for biomedical applications: emerging trends and future prospects. *Advanced Materials* **27**, 7261-7284 (2015).

reports focusing on biomedical applications of 2D nanomaterials. Nevertheless, recent rapid advances in 2D nanomaterials have raised important yet exciting questions about their interactions with biological moieties. 2D nanoparticles such as carbon-based 2D materials, silicate clays, transition metal dichalcogenides (TMDs), and transition metal oxides (TMOs) provide enhanced physical, chemical, and biological functionality owing to their uniform shapes, high surface-to-volume ratios, and surface charge. In this review, we focus on state-of-the-art biomedical applications of 2D nanomaterials as well as recent developments that are shaping this emerging field. Specifically, we describe the unique characteristics that make 2D nanoparticles so valuable, as well as the biocompatibility framework that has been investigated so far. Finally, to both capture the growing trend of 2D nanomaterials for biomedical applications and identify promising new research directions, we provide a critical evaluation of potential applications of recently developed 2D nanomaterials.

3.2 Introduction

Although graphene was assumed for decades to be thermodynamically unstable and impossible to isolate, the advent of isolated graphene layers sparked an explosion of interest in two-dimensional (2D) nanomaterials.(57-59) Graphene was quickly shown to have exceptional mechanical strength, high thermal conductivity, and unusual electrical properties, including high conductivity and charge carrier mobility, all stemming from its 2D structure. One feature that stood out to researchers was that graphene's properties were drastically different from the 0D, 1D, and 3D forms of carbon. Just a few years after graphene was first isolated, dimensionality is recognized as one of the most important and influential material parameters of nanomaterials.(60-62)

Graphene's unprecedented properties sparked a search for additional 2D nanomaterials with their own unique properties. This search has led to dozens of 2D nanomaterials being reported in the past few years including graphene, synthetic silicate clays, layered double hydroxides (LDHs), transition metal dichalcogenides (TMDs), transition metal oxides (TMOs), and other types of 2D nanomaterials (**Figure 3-2**). 2D nanomaterials are defined as particles that have one dimension that is confined to the nanometer length scale (<100nm). Due to their unique shape, they have very high surface-to-volume ratios as well as anisotropic physical and chemical properties compared to 3D nanomaterials.

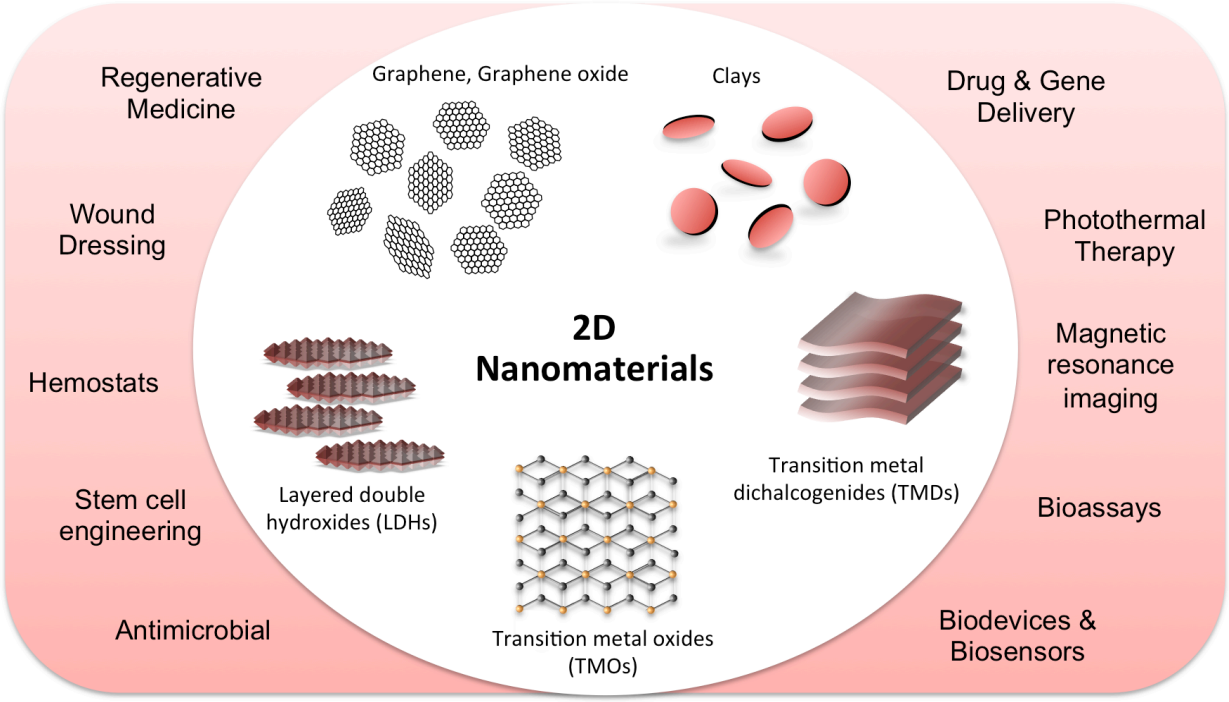

Figure 3-2. Two-dimensional (2D) nanomaterials investigated for biological applications include carbon-based nanomaterials (graphene, graphene oxide (GO) and rGO), silicate clays, layered double hydroxides (LDHs), transition metal dichalcogenides (TMDs) and transition metal oxides (TMOs).

2D nanomaterials are highly diverse in terms of their mechanical, chemical, and optical properties, as well as in size, shape, biocompatibility, and degradability. These diverse properties make 2D nanomaterials suitable for a wide range of applications, including drug delivery, imaging, tissue engineering, and biosensors, among others.(63-72) However, their low-dimension nanostructure gives them some common characteristics. For example, 2D nanomaterials are the thinnest materials known, which means that they also possess the highest specific surface areas of all known materials. This characteristic makes these materials invaluable for applications requiring high levels of surface interactions on a small scale. As a result, 2D nanomaterials are being explored for use in drug delivery systems, where they can adsorb large numbers of drug molecules and enable superior control over release kinetics. Additionally, their exceptional surface area to volume ratios and typically high modulus values make them useful for improving the mechanical properties of biomedical nanocomposites, even at very low concentrations. Their extreme thinness has been instrumental for breakthroughs in biosensing and gene sequencing. Moreover, the thinness of these molecules allows them to respond rapidly to external signals such as light, which has led to utility in optical therapies of all kinds, including imaging applications, photothermal therapy, and photodynamic therapy.

Despite the rapid pace of development in the field of 2D nanomaterials, these materials must be carefully evaluated for biocompatibility in order to be relevant for biomedical applications. The newness of this class of materials means that even the relatively well-established 2D materials like graphene are poorly understood in terms of their physiological interactions with living tissues. Additionally, the complexities of variable particle size and shape, impurities from manufacturing,

and protein and immune interactions have resulted in a patchwork of knowledge on the biocompatibility of these materials.

Unfortunately, the cyto- and bio- compatibility of 2D nanoparticles cannot be inferred from the corresponding bulk material, as size and shape significantly affect the body's interactions with the material. Additionally, it should be noted that among various articles reporting the benefits of nanomaterials for biomedical use, there is a notable scarcity of toxic reactions reported. The primary mechanism of harm that nanomaterials have been suggested to cause is through oxidative damage from free radicals. Oxidative damage may be the result of immune responses elicited by the material, the presence of oxidizing contaminants, or from intrinsic properties of the molecules themselves or their degradation products. Additionally, the slow clearance of some nanoparticles by the body may result in particle accumulation in the liver, kidneys, spleen, or lungs. Damage has also been suggested to occur via apoptosis, hemolysis, or thrombosis. Some 2D nanomaterials also contain metals not usually found above trace levels in humans. Again, however, none of these mechanisms can be generalized, as toxicity has been shown to depend on nanomaterial size, surface area, and composition. Size and shape might affect toxicity by making phagocytosis by macrophages impossible, or by allowing nanoparticle aggregates to form. Surface area increases the material's ability to interact with the body, which could increase immunogenicity. The composition of nanomaterials can obviously affect biocompatibility. However, it can also affect protein adsorption on the surface of the nanomaterial. It is well established in the biomaterials community that protein adsorption is rapid *in vivo* and that this process drives the biological response to implanted materials.(73, 74) However, protein adsorption onto nanomaterial surfaces, which will depend on both chemical composition and location of the nanomaterial, remains uncharacterized.

In comparison to other types of nanomaterials, 2D nanomaterial safety information for materials besides graphene is practically nonexistent. No systematic evaluation of the biocompatibility of any 2D nanomaterial has been completed. With that in mind, preliminary reports have indicated that some of the 2D nanomaterials are highly biocompatible *in vitro* and *in vivo*. These materials have been shown to not cause significant harm in individual, small-scale studies. As a result, each of these materials is being regarded with cautious optimism in terms of its potential in biomedicine. A recent literature search (according to ISI web of science, April 2015) indicated immense interest in evaluating the biological properties of different types of 2D nanomaterials for biomedical applications including tissue engineering, cancer therapy and drug delivery, biosensors, and bioimaging (**Figure 3-3**). This high level of interest clearly indicates that 2D nanomaterials are an emerging material technology that has transformative potential for biomedical and biotechnological innovation.

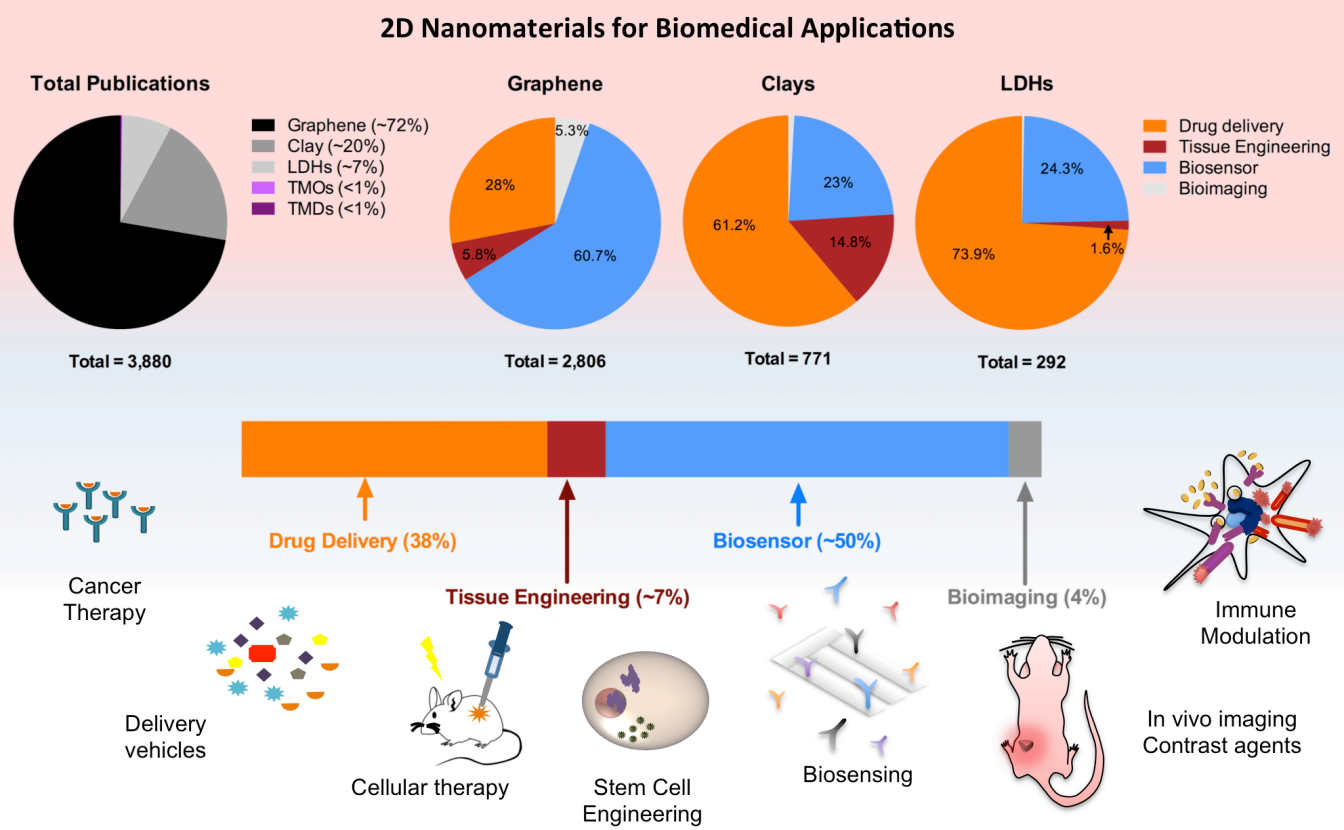

Figure 3-3. Current research trends in 2D nanomaterials and some of their promising biomedical applications. A recent surge in 2D nanomaterials research is evident from the number of publications in last few years. The publication data was obtained from ISI web of science in April 2015. Carbon-based 2D nanomaterials are being extensively investigated for biomedical applications, followed by clay-based nanomaterials and LDHs. Only a few reports focus on the biomedical applications of TMOs and TMDs. Most of the biomedical applications of 2D nanomaterials are in the areas of biosensors and drug delivery, followed by tissue engineering and bioimaging.

2D nanomaterials research is still in its infancy, with the bulk of research focusing on elucidating the unique material properties of 2D nanomaterials. Accordingly, high profile reviews of 2D

nanomaterials, including Butler et al. and Xu et al., have been centered largely on synthesis techniques, fundamental research, and electronic applications stemming from the unique structures of 2D nanomaterials.(75, 76) However, the recent explosion of research into the biomedical applications of 2D nanomaterials has created a new area of translational research. Reviews articles in this area including Dawson et al. and Kuthati et al. provide close looks at particular subsets of 2D nanomaterials and applications.(77, 78) To date, however, there has not yet been a review that encompasses all biomedical 2D nanomaterials research, providing an systematic overview of the field, its recent developments and direction, and comparing the emerging biomedical applications of each family of 2D nanomaterials.

In this review, we focus on state-of-the-art biomedical applications of 2D nanomaterials, highlight recent developments that are shaping this emerging field, and evaluate the potential applications of recently developed 2D nanomaterials. The discussion is limited to the most promising nanoparticles from each family of 2D nanoparticles (carbon-based, clays, LDHs, TMDs, TMOs, and other types of 2D nanomaterials) that are relevant for biomedical and biotechnological applications. The scope of this paper is to capture the current state of 2D nanomaterial research for biomedical applications and to identify promising new research directions in the field. Additionally, we will review the unique characteristics that make 2D nanoparticles such exciting and useful materials.

3.3 Structures of 2D Nanomaterials

The physical, chemical and biological properties of nanomaterials strongly depend on their atomic arrangements. 2D nanomaterials are very unique compared to other types of nanomaterials

because one of their dimensions is only a few atomic layers thick (**Figure 3-4**).(79) Graphene is the archetypal 2D nanomaterial and exhibits many of the structural motifs that define this category of nanomaterials. The structure of graphene is a single monolayer of carbon atoms that are bonded together via covalent sp^2 bonds in a flat and regular hexagonal pattern. In contrast, GO is based on the same regular hexagonal pattern of carbon atoms, but instead of being entirely composed of sp^2 bonded carbon atoms, it has frequent sp^3 carbons bound to functional groups above or below the plane of the nanomaterial. This makes GO less flat than graphene and results in significant local polarity of the structure. rGO is a structural intermediate between graphene and GO. It can be synthesized by the reduction of GO *via* various methods, which remove most of the functional groups and partially restore the sp^2 hybridization. The result is a sparsely functionalized graphene monolayer with a higher concentration of structural defects than graphene.(80)

Other 2D nanomaterials with structures similar to graphene include silicene, germanene, hexagonal boron nitride (hBN), and graphitic carbon nitride (C3N4). Silicene and germanene are 2D allotropes of silicon and germanium, respectively, with buckled, rather than flat, monolayers. C3N4 on the other hand, is an alternating monolayer of carbon and nitrogen atoms. Similarly, hexagonal boron nitride (hBN) is composed of covalently bound alternating nitrogen and boron atoms.

In contrast to 2D nanomaterials of a monoatomic thickness, some materials like 2D clays, LDHs, TMOs, and TMDs are composed of stable, single crystal units. Laponite, for example, is a 2D nanoclay with 3 layers comprising 2 tetrahedral silica sheets sandwiching an interior octahedral layer of magnesium and lithium cations. Substitutions and edge valences give these nanoparticles permanent negative face charges and positive edge charges, both of which can be stabilized by ionic interactions. Individual laponite nanoparticles are typically disc shaped, with a diameter of

roughly 30 nm and a thickness of less than 1 nm.(76, 77) LDHs are also called anionic clays; they have positively charged faces, which is a rare quality relative to negatively charged faces.(81) LDHs are structurally similar to brucite, the mineral form of magnesium hydroxide, and consist of magnesium cations surrounded octahedrally by hydroxide ions, but with partial Al^{3+} substitution for Mg^{2+}, resulting in a positive surface charge.(81, 82)

2D TMOs can have different structures depending on their individual components. MgO_2 and TiO_2, which are the most commonly used, generally have octahedral conformations. Similar to clays and LDHs, they often exist as stacks with interlayer ions holding these stacks together. 2D TMO nanoparticles are less than 1 nm thick but have been synthesized up to widths of 100 microns.(83) 2D TMDs have a three layer atomic structure where the outside layers are chalcogens covalently bonded to a metal atom inner layer. Each of these layers is in a triangular lattice structure. This crystal structure forms a 2D hexagonal lattice alternating between chalcogenide and metal atoms. TMD monolayers are roughly 0.6 nm thick.(76, 84)

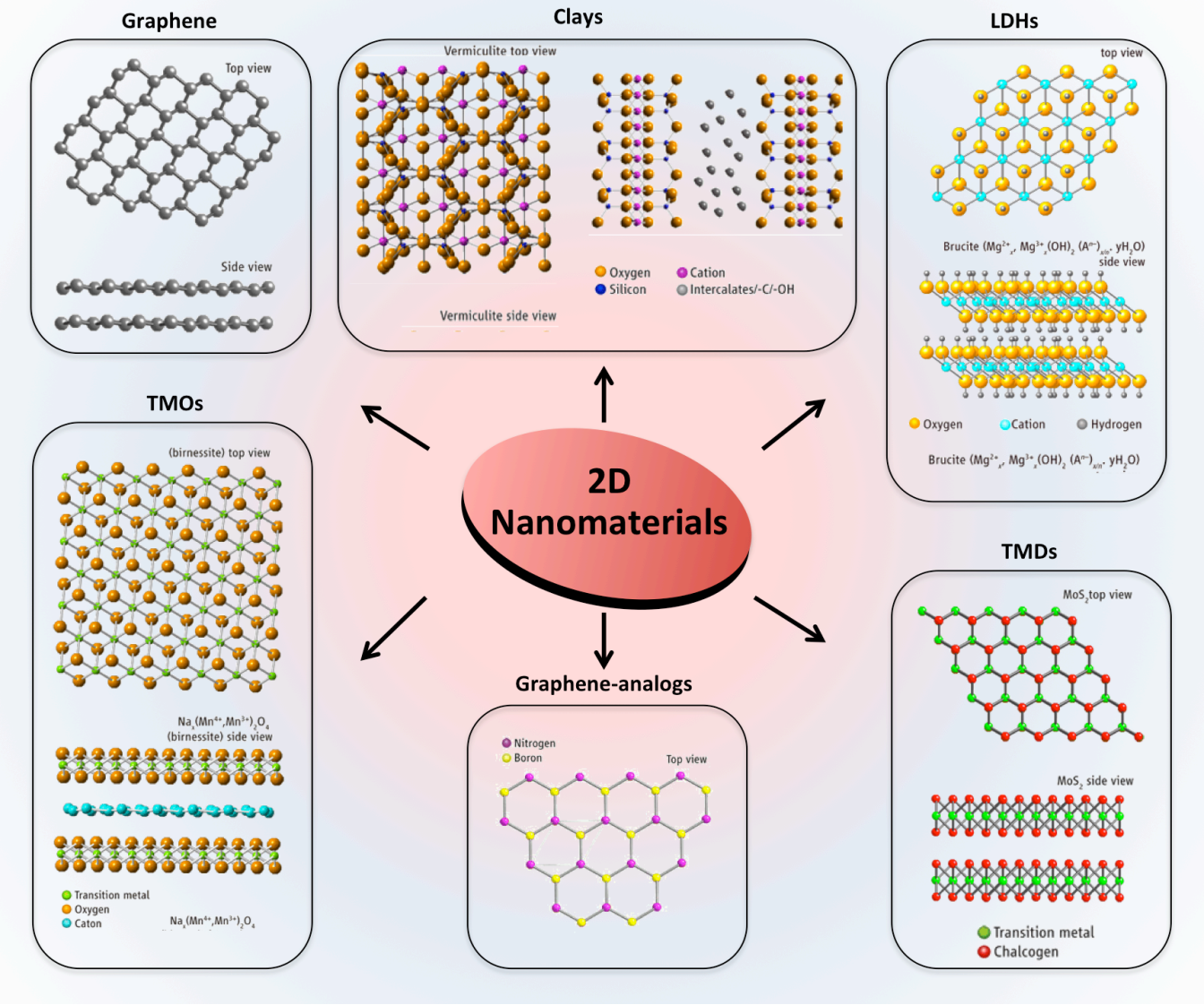

Figure 3-4. Structures of 2D nanomaterials highlighting a nanosheet network in which one of the dimensions are only a few atomic layers thick. Structures for graphene, clays, LDHs, TMOs, TMDs, and graphene-analogs (hBN) are illustrated here. Reproduced with permission(79). Copyright 2013, American Association for the Advancement of Science.

3.4 Carbon-based 2D nanomaterials for Biomedical Applications

Graphenes are the best-researched as well as the oldest 2D nanomaterials, first being isolated in 2004.(57-59) The application of graphene in tissue engineering expanded swiftly due to its unprecedented mechanical strength, electrical conductivity, biocompatibility, and thermal conductivity.(85) Additionally, graphene has a higher specific surface area, lower production and purification costs, and greater ease of functionalization compared to its 1D counterpart, carbon nanotubes. Graphene is often partially oxidized into graphene oxide (GO) in order to increase its hydrophilicity and enable facile functionalization, but this modification comes at the expense of electrical conductivity.(86) Reduced graphene oxide (rGO), which can be easily produced in large quantities from GO, is often used as a substitute for pure graphene due to its lower cost, but it has inferior properties due to structural defects.(87-92) The graphene family is therefore composed of 3 materials: graphene, GO, and rGO. As numerous reviews are available on graphene-based materials for biomedical applications (85, 87), we will highlight only some representative recent examples in the areas of tissue engineering, drug delivery and biosensing.

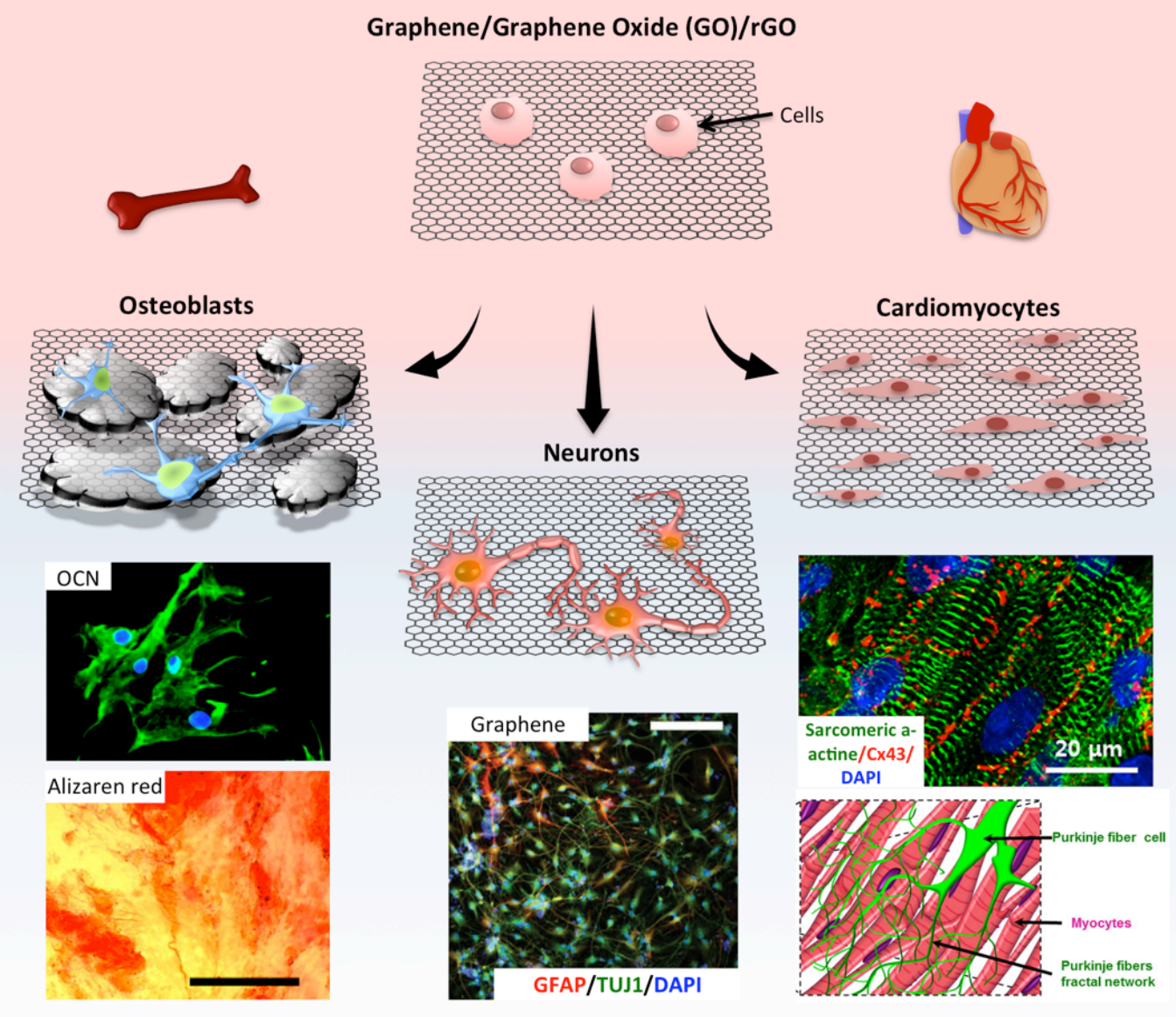

Figure 3-5. Application of carbon-based 2D nanomaterials for tissue engineering. Graphene/GO/rGO have been used to control and direct cellular fate towards osteoblasts(93), neurons(94) and cardiomyocytes(95). Reproduced with permission(93-95) 2011 and 2013, American Chemical Society and 2013 Elsevier Inc.

3.4.1 Graphene

One promising future avenue for graphene-based biomaterials is in the area of tissue engineering. Recently, Qui *et al.* synthesized a nanocomposite aerogel with a highly interconnected architecture from poly(N-isopropylacrylamide) (PNIPAM) and graphene.(96) The graphene aerogel exhibited one order of magnitude higher modulus compared to graphene-free PNIPAM hydrogels. The addition of graphene also significantly improved the electrical conductivity and thermo-responsive properties of the nanocomposite hydrogels compared to PNIPAM hydrogels. This effect was mostly attributed to the prefabrication of a graphene aerogel, which ensured high connectivity between graphene sheets. Moreover, building the nanocomposite from an aerogel also obviated the need to functionalize the graphene into GO for dispersal into solution. Using this approach, graphene could be used in place of less conductive GO for a wide range of applications, potentially leading to a new generation of graphene nanocomposites with superior electrical and mechanical properties.

Graphene is able to increase the mechanical strength and stiffness of hydrogel scaffolds without compromising cytocompatibility, and it has been shown to accelerate the adhesion, proliferation, and differentiation of human mesenchymal stem cells (hMSCs) toward an osteogenic cell fate.(93) Nayak *et al.* showed that in the presence of osteogenic medium, graphene coating enhances differentiation of hMSCs **(Figure 3-5)**.(93) The ability of graphene to promote the differentiation of hMSCs is attributed to its ability to adsorb proteins and bioactive molecules such as dexamethasone and β-glycerophosphate.(97) In another study, graphene was used to engineer 3D porous scaffolds for osteogenic differentiation of hMSCs for bone regeneration.(98) A 3D graphene foam structure was fabricated using a temporary scaffold that was fully removed via

$FeCl_3$ etching. These graphene foams were capable of inducing osteogenic differentiation of hMSCs without any osteoinductive growth factors. The ability of graphene foams to induce osteogenic differentiation was attributed to the high mechanical stiffness of foam, as hMSCs are known to respond to high stiffness environments by differentiating into osteoblasts.(98)

Due to the high electrical conductivity of graphene-based nanocomposites, these materials are being explored for tissue engineering and biosensing applications that require electrical stimulation for functioning. For example, in a recent study Tang *et al*. engineered an electrically conductive graphene substrate to direct cell fate by increasing electrical interactions between neural stem cells (NSCs).(94) They observed a nearly two-fold increase in the neuron density and excitability (as measured by spontaneous spikes in calcium ions) on a graphene substrate compared to tissue culture polystyrene (control). This improvement in NSC differentiation was credited to the high electrical conductivity of graphene, making it a promising substrate for both culturing neurons and for creating biocompatible neural interfaces **(Fig 3-5)**.(94)

In another study, a graphene-based biosensor was developed to detect bacterial binding on tooth enamel.(99) Mannoor *et al.*, printed a graphene biosensor on a bioresorbable silk substrate and transferred it to a tooth surface.(99) Self-assembly and disassembly of antimicrobial peptides on the graphene surface was used to detect the presence of pathogen. They showed that by coupling this peptide-graphene nanosensor with a resonant coil, it was possible to transmit the signal for wireless detection (**Figure 3-6**). Overall, these studies highlight the application of graphene-based biomaterials for tissue engineering and biosensing applications.

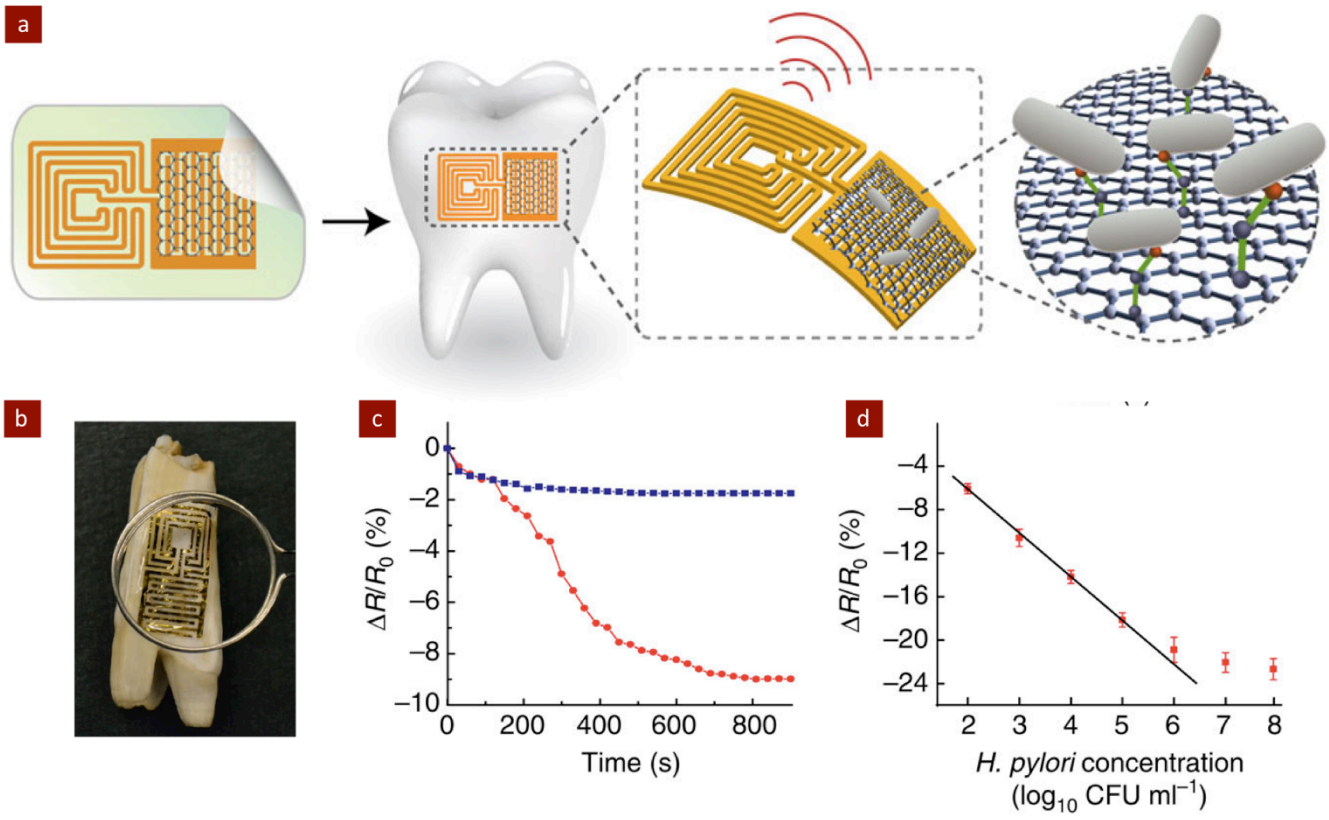

Figure 3-6. Graphene-based biosensors have been designed for the detection of pathogens. (a) & (b) Graphene-based wireless biosensors printed onto bioresorbable silk can be transferred onto the surface of a tooth to detect binding of bacteria. (c) The changes in graphene resistance over time following exposure to H. pylori cells in human saliva (red line) are compared to 'blank' saliva (blue line). (d) The changes in graphene resistance versus concentration of pathogen illustrate efficacy of the graphene-based biosensor. Reproduced with permission(99). Copyright 2012, Macmillan Publishers Limited.

3.4.2 Graphene Oxide (GO)

The oxidation of graphene to GO *via* oxidative exfoliation (Hummer's method) reduces the electrical conductivity and mechanical strength of the material but also makes it more suitable for biomedical applications by effectively rendering the material hydrophilic. This process facilitates material interactions with biomacromolecules such as proteins and extracellular matrix (ECM) components as well as certain drugs. Moreover, GO functionalization, which can enhance cyto- and bio-compatibility, is facile due to the presence of hydroxyl groups.(100) One useful characteristic of GO nanosheets is that they repel each other with variable force depending on pH. This electrostatic property can be exploited to create pH-responsive nanocomposites. Bai *et al*. synthesized a GO-poly(vinyl alcohol) nanocomposite for controlled drug release.(101) Under acidic conditions, the nanocomposite remained solid and was able to retain vitamin B12, the model drug. However, under alkaline conditions, the nanocomposites dissolved rapidly, resulting in rapid release of the entrapped drug. This triggered release was due to the ionization of the carboxyl groups present on GO. The high specific surface area of GO also significantly reduced drug diffusion from the intact nanocomposite. These self-assembling networks could potentially be useful for pH-triggered drug delivery, particularly for oral delivery of acid sensitive drugs.(101, 102)

Due to its sheet-like structure and the presence of hydroxyl groups on its surface, GO interacts with a range of synthetic and natural polymers and provides physical reinforcement.(85) Moreover, due to its high electrical conductivity, GO can be used to engineer electrically conductive patches for tissue engineering applications **(Figure 3-6)**.(95, 103) In a recent study, the addition of GO to methacrylated gelatin was used to enhance the electrical conductivity of nanocomposite hydrogels.(103) The enhanced electrical conductivity resulted in higher proliferation of cardiomyocytes seeded on the hydrogel surface, suggesting that this material could

be used as a cardiac patch.(95, 103) In a separate study, to increase the hydrogel stiffness, the surface of GO was modified with methacrylate groups to covalently crosslink the surface of the GO to the methacrylated gelatin during polymerization.(104) A two- to three-fold increase in mechanical stiffness was observed upon addition of a small amount (3mg/mL) of GO to the gelatin hydrogels. Importantly, these nanocomposite scaffolds supported increased cell viability, proliferation, and spreading in a 3D environment.

The large surface area, aromatic structure, and functional groups make GO well suited as a nanocarrier for stimuli-responsive nanocomposites for drug delivery.(105) Conducting polymers such as polypyrrole (PPy) are used as electrically-responsive drug delivery systems but have limited loading capacity. In a recent study, Weaver *et al.* developed electrically responsive GO-PPy nanocomposites for controlled drug delivery.(106) The GO-PPy nanocomposites could entrap and release two-fold more dexamethasone, an anti-inflammatory molecule, relative to pure PPy. Additionally, incorporation of GO resulted in enhanced sensitivity of the nanocomposites to electrical stimulation and allowed for linear release kinetics over 400 stimulation cycles without any measurable drug release in the absence of stimulation. Drug loading and release rates were also shown to be tunable by changing the sonication time of GO. The significant increase in drug loading and the improved release kinetics were attributed to the high surface area of GO. The significant control over the release kinetics, drug loading capacity, and ability to respond to external stimulation to release entrapped drug could be used for a range of biomedical applications including cancer treatment, immunotherapies, and tissue engineering.

GO-loaded hydrogels can also be used for gene delivery for the treatment of myocardial infarction. Paul *et al.* decorated the surface of GO with polyethylenimine (PEI) to enhance the loading and delivery of a VEGF DNA plasmid (**Figure 3-7**).(107) They engineered an injectable

hydrogel loaded with functionalized GO for minimally invasive therapy. The results indicated that use of functionalized GO for gene delivery reduced *in vivo* scar formation compared to VEGF plasmid and hydrogel groups, highlighting the potential of GO as a gene delivery agent.

Although GO is less conductive than graphene, its bioactivity and electrical conductance make it a promising new dopant for electrically-responsive nanocomposites for neural interfaces.(108) Poly(3,4-ethylene dioxythiophene) (PEDOT) has been extensively studied for use in neural interfacing due to its biocompatibility and electrical conductance, but success has been limited due to a lack of functional groups on the PEDOT backbone for anchoring biomolecules. To address this limitation, Luo *et al.* developed GO-PEDOT nanocomposites with improved bio-interfacing.(109) The electrical conductivity and ability of GO to promote neural outgrowth make it an obvious choice for doping PEDOT while preserving its electrical conductivity. The GO-PEDOT nanocomposite retained its conductivity and allowed for covalent conjugation of peptides on its surface. The addition of GO significantly improved neuron outgrowth and attachment on GO-PEDOT surface relative to the current standard, PEDOT-PSS. The surface of GO has a high density of carboxyl groups, allowing it to conjugate multiple biomolecules and thus providing a suitable surface for enhanced interactions with neurons. Overall, graphene-based nanocomposites are emerging as promising materials for neural applications, and several exciting approaches are currently being explored.(85, 93, 109-112)

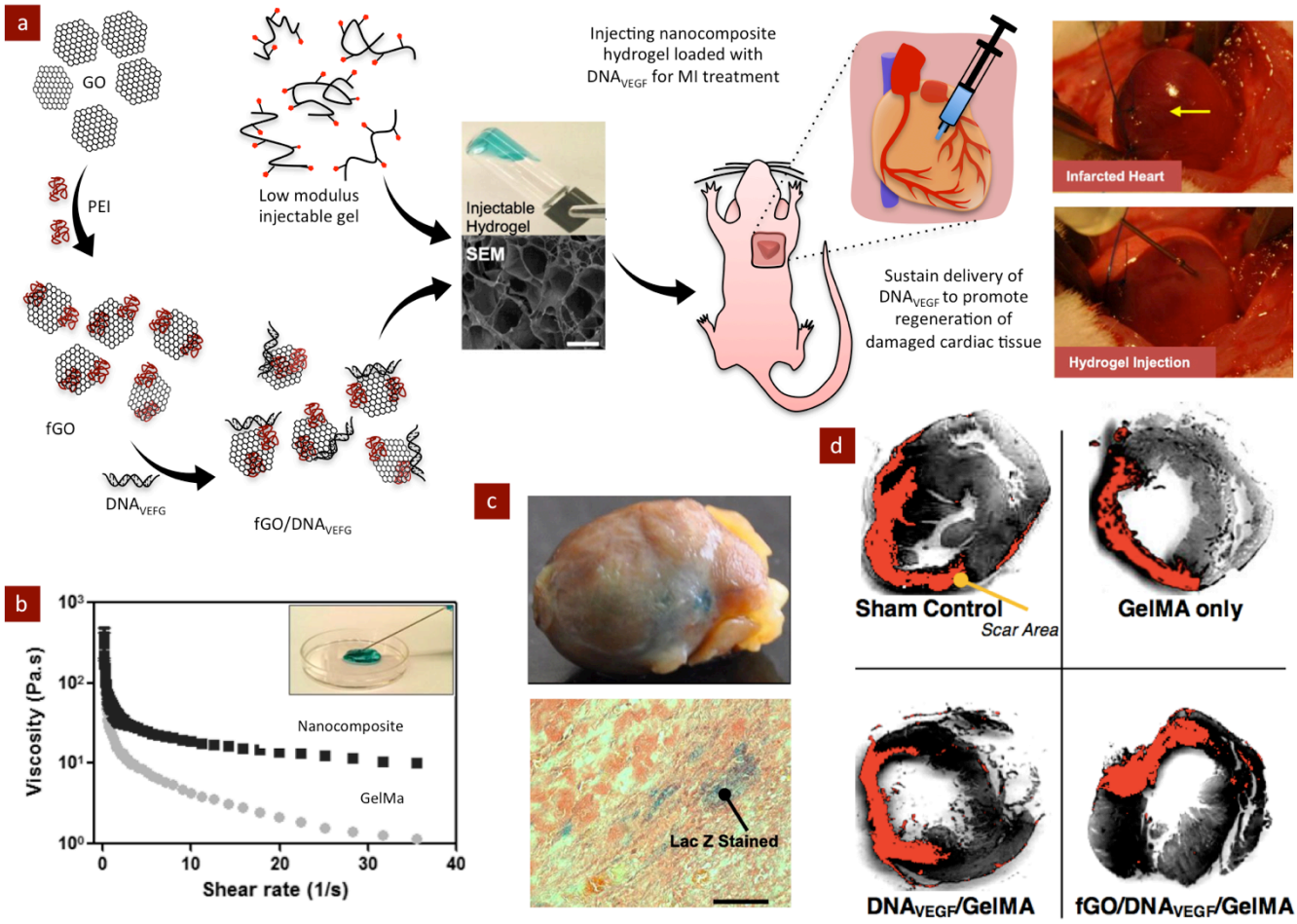

Figure 3-7. Nanocomposite hydrogel loaded with functionalized GO (fGO) for gene delivery. (a) GO is functionalized with cationic polyethylenimine (PEI) to hold anionic DNA_{VEGF} plasmids. fGO/DNA_{VEGF} with the plasmid physically adsorbed on the fGO surface was incorporated within a prepolymer solution of GelMA and then lightly crosslinked to obtain low modulus injectable hydrogels. Photocrosslinked hydrogels loaded with fGO/DNA_{VEGF} were injected into infarcted heart tissue. (b) Shear viscosity of fGO/GelMA and GelMA hydrogels indicates that the addition of GO resulted in increased mechanical stiffness. (c) Localization of injected gel in the infarcted area is shown by Laz Z staining. (d)

Reduction of *in vivo* scar formation (red area) with fGO/VEGF plasmid/GelMa treatment. Reproduced with permission(107) 2014, American Chemical Society.

3.4.3 Reduced Graphene Oxide (rGO)

Reduced graphene oxide is commonly produced from GO, which takes advantage of the ease of fabrication of GO, and exhibits many of the properties of pure graphene sheets. The reduction of GO sheets removes most of the functional groups from the nanosheets, leaving only the carbon sheet behind, along with some structural defects. rGO has been used extensively in biosensing applications, photodynamic therapy (PDT) and photothermal therapy (PTT) due to its enhanced availability and better electrical conductivity compared to GO. Compared to traditional materials like CNTs and silicon nanowires, rGO has higher specific surface area and higher carrier mobility, and has been shown to immobilize high densities of receptor biomolecules on its surface.(113-116) These features make rGO an attractive choice for high-sensitivity, high-resolution biosensors. For example, rGO has been used to fabricate an ultrasensitive label-free field effect transistor (FET) biosensor that could be used to detect prostate specific antigen at concentrations from 100 fg/mL up to 10ng/mL at high specificity without the need for labeling. Several studies have created other FET biosensors using rGO for detecting various biomolecules, including DNA and E. coli antigens. Importantly, because of their ease of fabrication, low cost, and potential for high sensitivity and specificity, the biosensing technologies being created using rGO could lead to improved diagnostic techniques and, ultimately, better patient outcomes.(113-116)

rGO-based materials are also being actively researched as PTT agents due to their effectiveness, low cost, and cytocompatibility.(117, 118) GO has previously been used to create similar PTT agents, but high doses and power were required due to GO's poor NIR absorption. rGO absorbs approximately, 20% of NIR light, nearly seven-fold more than GO, due to a larger number of π- π bonds.(117, 118) This superior absorptivity allows rGO to be effective at a significantly lower dose compared to GO, CNTs and gold nanoparticles. Functionalization of rGO with ligands for selective cancer cell targeting and doxorubicin delivery has also been demonstrated, suggesting that this nanomaterial may be a candidate for PTT/PDT combined therapy. Notably, rGO is a promising material for PTT because it is comparable in efficacy to gold nanoparticles, is cheaper and easier to mass produce, and can be loaded with chemotherapeutic drugs.(117, 118)

3.4.4 Multi-component Carbon-based Hybrid Nanomaterials

Some researchers have begun experimenting with designing hybrid nanocomposites. (119) Experimental evidence indicates synergistic effects of having multiple types of nanomaterials present within a polymeric structure.(120-123) Various combinations involving multiple dimensionalities of nanomaterials including CNTs, graphenes, fullerenes, and nanodiamonds have each resulted in unique synergistic effects. For example, CNT-GO-polypropylene nanocomposites have been shown to possess enhanced mechanical strength, thermal stability, and electrical conductivity compared two component nanocomposites, and fullerene-CNT-propylene nanocomposites have also demonstrated improved mechanical and thermal properties.(120, 121, 123) Research indicates that the mechanism of this synergy is multifaceted: one factor that has

been identified is that using multiple carbon allotropes enhances the dispersion of nanocomposites throughout the hydrated polymeric network (hydrogel). The allotropes of carbon used for nanocomposites exhibit similar chemical properties, but have very different physical structures, allowing for different hydrogel-nanoparticle bonding patterns within the same structure. Further research is required to fully characterize the mechanism behind the synergistic effects. Hybrid nanocomposites have mainly been researched in the domain of material science, but have clear applications in tissue engineering, and they are likely to expand into tissue engineering applications in the near future. Another example of the use of hybrid nanocomposites is electrospun microfibrous polycaprolactone (PCL) scaffolds loaded with both graphene and single walled CNTs.(124) In Holmes *et al.* PCL-graphene-single wall CNTs nanocomposites were shown to have higher stiffness, enhanced hMSC proliferation, and enhanced chondrogenic differentiation and collagen II synthesis compared to a pure PCL scaffold.(124) Although this study did not compare the results to single nanomaterial controls, it nevertheless demonstrates the suitability of these hybrid nanocomposites for tissue engineering.

Overall, graphene, GO, and rGO, represent the largest group of 2D nanomaterials for biomedical applications. Due to their outstanding physical, chemical, electrical, and biological characteristics, they have been investigated for a wide range of biomedical applications including tissue engineering, drug delivery, bioimaging, and biosensing.(100, 125, 126) Whether these materials will continue to be preponderant in these areas remains to be seen, as a new range of 2D nanomaterials with unique property combinations of their own are emerging. Due to the large volume of carbon-based biomedical research, this section has only provided a brief overview of some of the recent and relevant biomedical applications. The main challenge that these materials face include their *in vivo* safety and biocompatibility. The lack of control over the dimensions of

carbon-based 2D nanomaterials makes it difficult to employ a standardized approach to evaluate the cyto- and bio- compatibility of these materials and make comparisons with other nanomaterials. Additionally, improved control over nanosheet size, size distribution, and functionalization needs to be achieved in order to better understand how these materials interact with biological entities such as proteins, DNA and cells. In biosensing and bioimaging, weak fluorescence and broad emissions are some of the limitations that also need to be addressed before we can utilize this new array of nanomaterials for clinical applications.

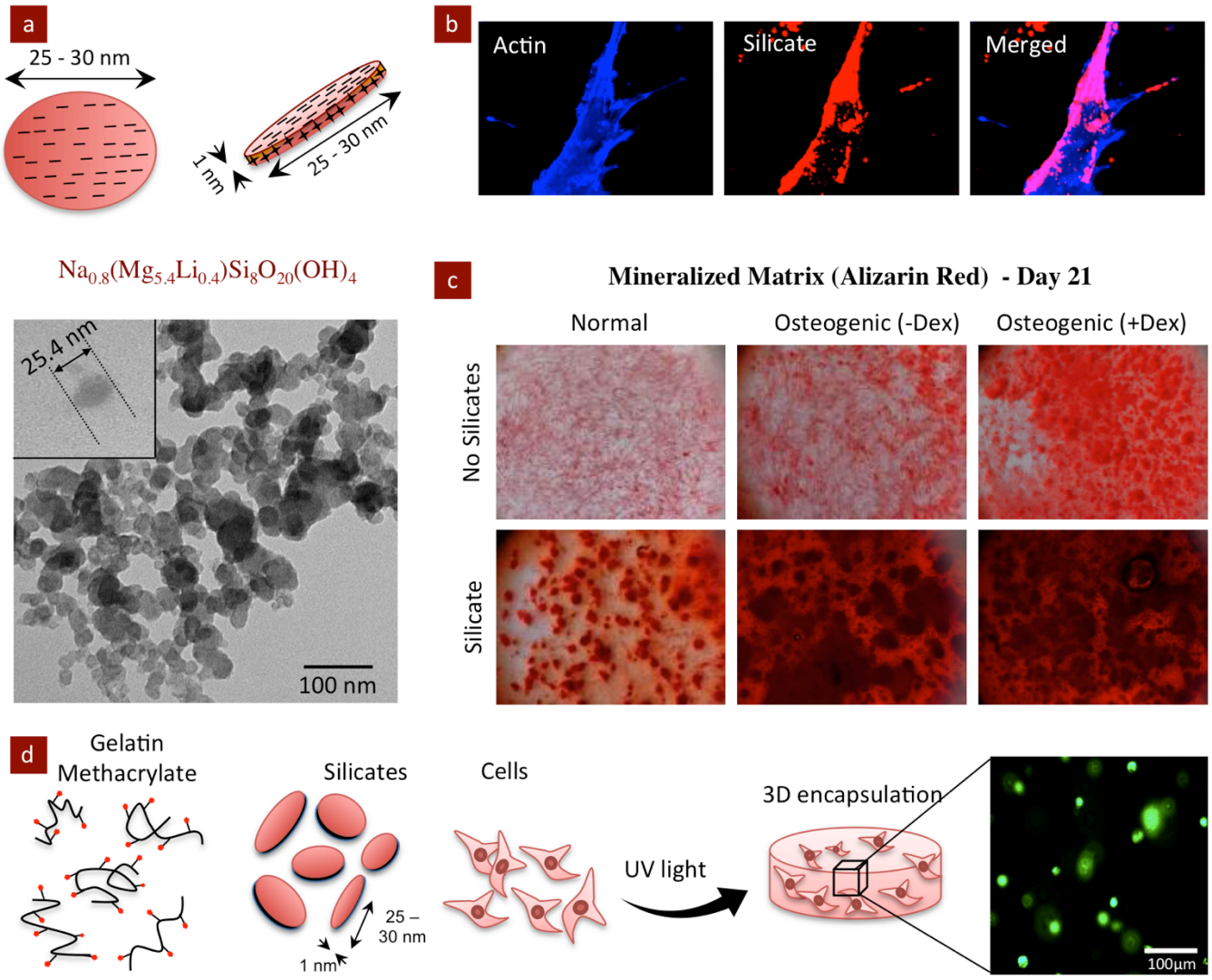

Figure 3-8. Bioactive silicate nanoclays induce osteogenic differentiation of stem cells and can be used for bone regeneration. (a) Schematic and TEM images of Laponite nanoparticles showing shape and size. (b) Fluorescence imaging demonstrating internalization of silicate nanoparticles within stem cells. (c) The effect of silicate nanoparticles on the production of mineralized ECM indicates the osteoinductive properties of silicates. (d) Nanocomposite hydrogels for bone regeneration were fabricated by combining photocrosslinkable polymer

(GelMA), silicate nanoparticles and stem cells. Reproduced with permission(26, 127) 2013, John Wiley & Sons, Inc. and 2014, American Chemical Society.

3.5 Silicate Clays as Bioactive Nanomaterials for Biomedical Applications

Silicate clays have been widely used in modern medicine for several decades as antacids and topical creams, but their application as biomaterials remained relatively uninvestigated until recently.(10, 77) 2D clay nanoparticles used in biomedical engineering are typically layered silicates that are 10-100 nm in diameter and ~1nm in thickness. The most useful clay nanoparticles for biomedical applications also have a distinct layered structure that generates a permanent negative surface charge on each face of the particle and a positive charge along the edges, which gives these nanoparticles high drug loading capacity, aqueous stability, shear thinning characteristics, and enhanced cell-nanomaterial interactions.(6, 10) The silicates with this structure are kaolinite, palygorskite, sepiolite, and the smectites (laponite, montmorillonite, saponite, and hectorite).(77) Among these, the smectites are the most extensively investigated for biomedicine applications. In the smectite group of 2D clay nanoparticles, nanoplatelets are composed of a metal cation layer sandwiched between two tetrahedral silica sheets, a 2:1 layer conformation. Each smectite's faces have a weak net negative charge caused by cationic substitution, and unbalanced charges create a net positive charge on the edges of each nanoparticle. The relative weakness of their surface charges compared to similar clays makes smectites the most attractive clay for biomedical purposes. Their smaller surface charges make delamination into individual nanoplatelets a facile process that greatly increases smectite's surface area and increases nanoscale interactions with other molecules.

The biocompatibility of clay nanoparticles has not been systematically investigated, but is much better understood than that of most other 2D nanomaterials. *In vitro* and *in vivo* testing of a smectite clay (Laponite®), for example, has demonstrated favorable cyto- and bio- compatibility, and in vivo degradation of smectite nanoparticles has been observed.(127, 128) Biodegradation of clay nanoparticles is also nearly unique among 2D nanomaterials, as most of the clays are composed of minerals that are already present in body and have been shown to degrade into these nontoxic components under physiological conditions. Thus, their degradation pathway is better understood than other nanomaterials.

Interaction with silicate nanoparticles can stimulate the differentiation of certain stem cells into osteoblasts. The ability of silicate nanoplatelets to promote differentiation of hMSCs and human adipose stem cells (hASCs) over a period of 28 days was previously investigated (**Figure 3-8**).(129-131) At a lower concentration of silicate nanoparticles (100 □g/mL), no significant effects on cellular morphology, proliferation, viability, or the production of reactive oxygen species (ROS), reactive nitrogen species (RNS) and lactose dehydrogenase (LDH) were observed, indicating high cyto-compatibility.(129) However, at higher concentrations of silicate nanoparticles, a significant reduction in metabolic activity was observed, with the half-maximum inhibitory concentration (IC_{50}) being ~4 mg/mL.(129) When compared to similarly sized carbon-based nanoparticles, silicate nanoparticles were only cytotoxic at a ten-fold higher concentration, indicating comparatively high cytocompatibility.(129) Moreover, these silicate nanoparticles are readily internalized by cells via clathrin-mediated endocytosis due to their ability to interact with proteins and cell surfaces.(130)

Silicate nanoparticles are not only short-term cytocompatible with human cells, they have also been shown to increase both cell adhesion and survival on hydrogel surfaces. In Liu *et al.*, silicate

nanoparticles were shown to improve cell adhesion on a PNIPAm-PEG-silicate nanocomposite.(77, 132) Other studies have shown that silicate nanoparticles promote initial cell adhesion, spreading and proliferation when added to non-fouling surfaces.(133-135) Silicate nanoparticles have also been shown to improve the mechanical stiffness of collagen-based hydrogels by four-fold.(127) These behaviors are all attributed to non-covalent interactions between the charged nanoparticle surfaces and polymer chains. Because these noncovalent interactions can break and re-form, they also impart hydrogel nanocomposites with shear thinning viscoelastic properties that make them well-suited for minimally invasive therapies.(6, 26, 133) Additionally, the inclusion of silicate nanoparticles has been shown to increase alkaline phosphatase activity and *in vitro* matrix mineralization. The ability of silicate nanoparticles to increase bioactivity in other polymers has recently been demonstrated as well. For example, in one recent study laponite nanoparticles were shown to enhance osteogenic differentiation on electrospun polycaprolactone scaffolds.(6, 26, 127)

Recently, silicate nanoparticles have begun to be investigated for musculoskeletal tissue engineering applications.(6, 77) Silicate nanoparticles can stimulate the differentiation of stem cells into osteoblasts and promote production of type I collagen, even in the absence of exogenous growth factors such as bone morphogenic protein 2 (BMP2).(6, 77) These particles trigger upregulation of osteogenic genes including alkaline phosphatase, Runt-related transcription factor-2, osteocalcin and osteopontin. Moreover, with the addition of a small amount of nanoparticles, stem cells produce a significantly higher amount of mineralized matrix compared to stem cells seeded on tissue culture polystyrene. The osteoinductive characteristics of clay nanoparticles are attributed to their dissolution products—Na^{+}, Mg^{2+}, $Si(OH)^{4}$, and Li^{+}—which might promote osteogenic pathways. In particular, orthosilicic acid ($Si(OH)_4$) upregulates bone-related gene

expressions and promotes collagen I synthesis(136), while Li^+ activates canonical Wnt signaling by inhibiting glycogen synthase kinase-3 beta, which leads to the upregulation of osteogenesis-associated genes like Runx-2 transcription factor.(137) The ability to stimulate stem cell differentiation without exogenous growth factors represents a potentially important pathway in tissue engineering because the use of growth factors to direct differentiation generally requires supraphysiological doses that may cause serious consequences in vivo.(138) Using growth factor-free approaches like nanosilicates may provide an alternative with fewer side effects.

The well characterized biodegradability and high loading efficiency of silicate nanoparticles have made them a good choice for drug delivery. Silicate nanoparticles can noncovalently adsorb a wide range of biomolecules, including therapeutics.(139) Silicate nanoparticles can also passively target tumors due to the enhanced permeability and retention (EPR) effect, and can be functionalized with biological molecules in order to actively target tumors.(140, 141) *In vitro* and *in vivo* experiments with doxorubicin have shown better efficacy than free doxorubicin due to higher cell uptake, and *in vivo* experiments have confirmed that doxorubicin-loaded silicate nanoparticles target tumor cells *via* the EPR effect, increase drug uptake by tumor cells, and exhibit pH sensitive drug release. Additionally, mice treated with doxorubicin-loaded silicate nanoparticles had normal blood and serum biochemistry parameters, while free doxorubicin-treated mice showed decreased parameters. This data together show that 2D silicate nanoparticles can be used for drug delivery and can enhance efficacy, reduce systemic toxicity, and increase survival.

Another strategy for improving drug delivery using silicate nanoparticles involves the incorporation of nanosilicates in injectable hydrogels.(139) Embedding silicate nanoparticles in a hydrogel matrix delays the release of drug molecules, creating a desirable sustained release profile.

Additionally, silicate-hydrogel nanocomposites exhibit shear-thinning properties that make them particularly well suited for injection applications. In Goncalves *et al.*, alginate-silicate-doxorubicin injectable hydrogels were synthesized for cancer therapeutics. The strong interaction of silicate nanoparticles with both the drug and polymer resulted in the formation of a cohesive hydrogel with reduced burst release, increased drug-loading, and a sustained drug release profile over a period of 11 days at tumor pH ~6.5. In contrast, alginate-doxorubicin hydrogels immediately released most of the loaded drug within 1-3 days. These results indicate that the injectability of silicate nanocomposites can be exploited for drug delivery purposes by engineering desired release profiles, which is a significant obstacle for contemporary drug delivery vehicles.(139)

One biomedical application to which silicate clays are uniquely suited is hemostasis. Kaolinite has been used to evaluate blood-clotting disorders since the 1950s, and a zeolite product (QuikClot) is approved for controlling hemorrhages.(128, 142) Recently, silicate clay nanomaterials have been investigated for improving hemostatics.(128) Most hemostatic agents, including zeolite, are powders, which are only effective on external wounds. 2D silicate clay nanoparticles were incorporated in collagen-based hydrogels to engineer shear-thinning hemostatic gels (**Figure 3-9**).(128) The shear-thinning nanocomposite gels were shown to be self-healing and could regain their mechanical integrity quickly (<10s) after injection. These nanocomposite gels demonstrated a clot time comparable to injected thrombin (the gold standard), a clot strength similar to natural clots, and excellent biocompatibility. The nanocomposite gel achieved 100% survival in test rats with otherwise lethal liver bleeding, and they fully degraded within 28 days, allowing unimpeded healing. This gel can be injected to treat wounds that are unreachable by powders and has a much lower risk of being washed to other sites in the body

compared to other injectable hemostatics, making it a promising leap forward in hemostatic technology with the potential to save many lives.

Overall, 2D silicate clay nanoparticles are being extensively investigated for biomedical applications including controlled cell adhesion, stem cell differentiation, drug/gene delivery, and hemostatic agents. This broad utility is mainly attributed to the shape and surface charge characteristics of these silicate clays, which result in enhanced interactions with biological moieties such as polymers, biomolecules and cells. In the future, we expect to see translational research based on these silicate clays in the fields of tissue engineering, immune modulation, and cancer research.

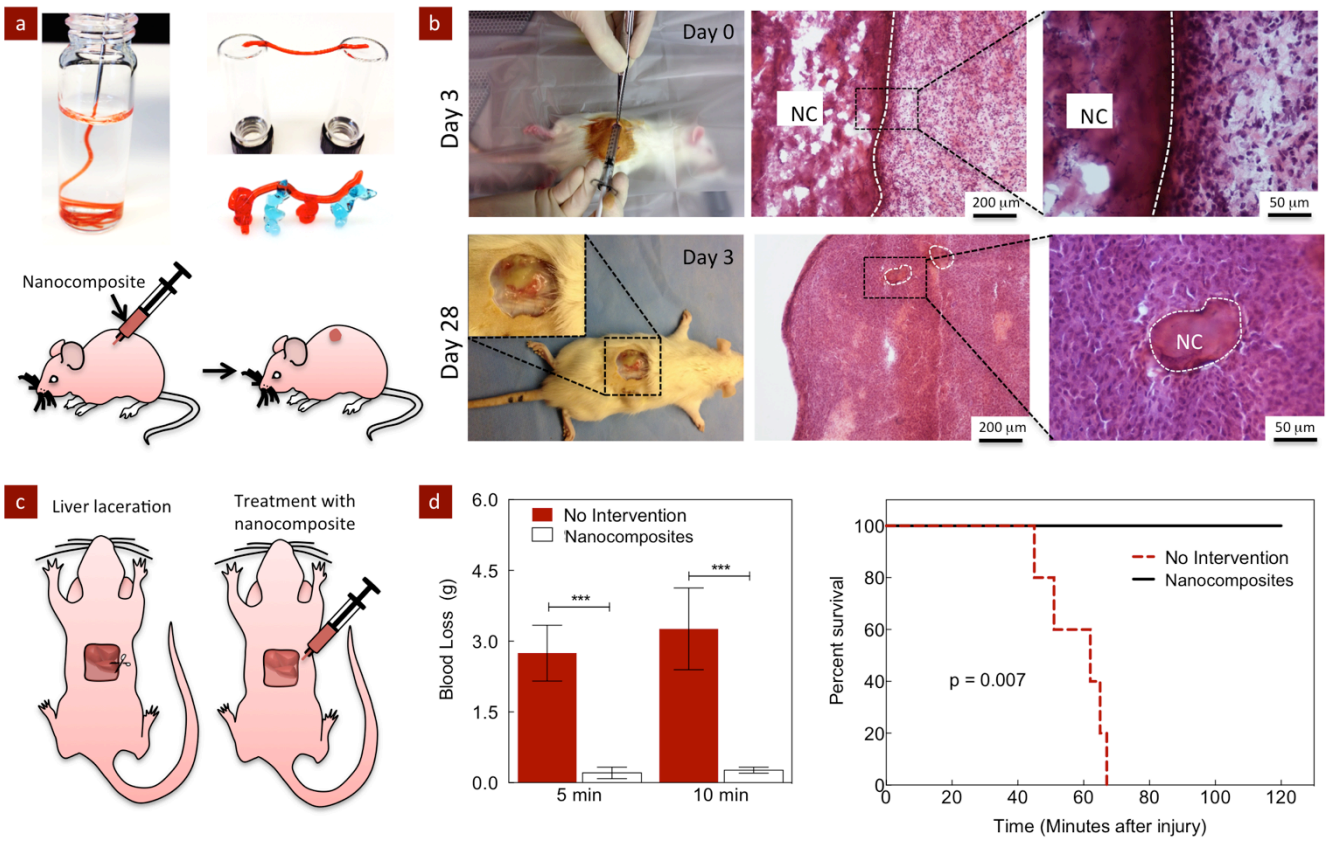

Figure 3-9. Silicate nanoclays as a hemostatic agents. (a) The addition of silicate nanoparticles within gelatin results in the formation of injectable and self-healing

nanocomposite hydrogels. (b) Histological staining (hematoxylin and eosin) demonstrating the favorable degradation rate and mild inflammatory response to nanocomposite hydrogels. (c) Surgical used to test the *in vivo* efficacy of the nanocomposite hydrogels as a hemostatic agent. (d) Results showing that the application of the nanocomposite hydrogel to liver lacerations significantly reduced mortality due to their ability to clot blood. Reproduced with permission(128) 2014, American Chemical Society.

3.6 Layered Double Hydroxides (LDHs)

LDHs are relatively under-researched compared to the other families of 2D nanomaterials, despite having very promising applications in biomedical engineering.(143) LDHs consist of an inner layer of cationic metal atoms sandwiched between hydroxide layers. These sheets are found naturally in stacks held together by intercalated anion layers. In contrast to silicate clays, LDH nanoparticles have a higher layer charge density, requiring more chemical modifications or interlayer composition changes to exfoliate individual nanosheets. Until recently, a lack of effective exfoliation techniques hindered the development of LDH nanoplatelet applications compared to clays. Higher charge densities also cause LDH nanoparticles to bind more strongly to anionic moieties. LDH nanoparticles are attracting research interest for drug delivery applications due to their low toxicity and ability to noncovalently bind anionic drug molecules and genetic material.(144-146) In addition, LDH nanocomposites have been shown to exhibit good mechanical and thermal properties. Rare earth hydroxides have been investigated for use in bioimaging.

LDHs are highly cytocompatible, have high charge density and anion exchange abilities, and exhibit pH-sensitive drug release.(147) Additionally LDH nanoparticles have been shown to

be taken up by cells *via* clathrin-mediated endocytosis and to be resistant to endosomal effects due to their buffering properties. These properties rank LDH nanoparticles among the most promising candidates for controlled drug delivery. A recent study by Saifullah *et al.* reported the development of a biocompatible nanodelivery system using LDHs. The tuberculosis drug isoniazid was bound to Mg/Al LDHs and its release kinetics were measured in a simulated buffer solution. The LDHs demonstrated improved cytocompatibility, and drug delivery was more effective compared to free isoniazid when evaluated using normal human lung and murine fibroblast cells. Moreover, the use of LDHs resulted in sustained release kinetics of the entrapped drug.(147)

Another advantage of LDH nanosheets in drug delivery is their ability to be targeted to specific cell types (e.g. cancerous tissue) and their retention in cells.(148) LDHs are notable among drug delivery nanomaterials in their ability to protect drugs from premature release. This can be particularly important for highly toxic drugs like chemotherapeutics. In a recent paper by Ma *et al.*, LDH nanosheets were loaded with cisplatin, and inhibitory concentrations of cisplatin and cisplatin-loaded LDH nanosheets were determined using an array of cancerous and non-cancerous cell lines. This study revealed that the LDH nanosheet delivery system enhanced cisplatin effectiveness by 11-fold and significantly decreased cytotoxicity to non-cancerous cells. The increase in anti-cancer effectiveness was attributed to increased cellular uptake of the drug-loaded nanoparticles due to endocytosis. Cellular uptake in cancerous cells exposed to the LDHs was increased 15-fold. In contrast, normal cells were unable to uptake LDH and no significant apoptosis was observed. The exact mechanism behind this selectivity is not clear, but this research promises to improve the efficacy of existing chemotherapy drugs.

LDHs have also been used as a combined delivery agent for therapeutics and nucleic acids. In one study focused on evaluating use of LDHs for dual delivery of drugs and RNA, Li *et al.* used

LDH nanosheets to simultaneously deliver both 5-fluorouracil (5-FU), an anticancer drug, and Allstars Cell Death siRNA (CD-siRNA), a blend of silencing RNAs targeting cell survival genes (**Figure 3-10**).(149) This approach exploited the anionic exchange capacity of LDH nanosheets to exchange anionic drug molecules and oligonucleotides into interlayer spaces, thereby protecting these molecules during delivery. The results from this study confirmed that the combination therapy results in synergistic cytotoxicity for cancer cells.

Although LDHs are insulators, their biocompatibility, high catalytic activity, high charge density, and strong adsorption have made LDHs an attractive building block for biosensors, where electrical conductance can be handled by another material. For example, Sun *et al.* fabricated a Mg_2Al/graphene nanocomposite biosensor by combining the excellent adsorption, protective effects, and biocompatibility of LDHs with the high electrical conductivity of graphene.(150, 151) The nanocomposite showed enhanced electrochemical properties and was proven to be a stable and sensitive biosensor. This result was attributed to the ability of LDHs and graphene to facilitate a direct electron transfer process.

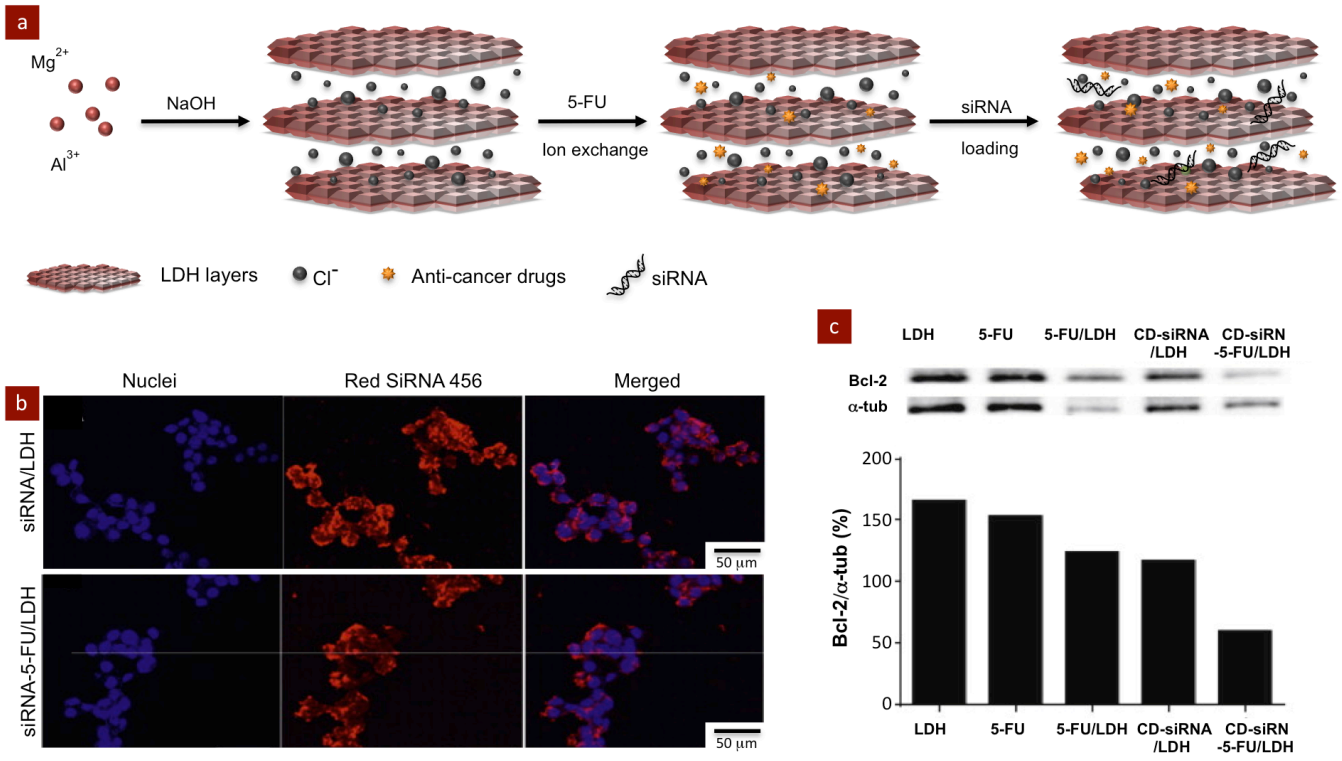

Figure 3-10. Application of LDHs in drug delivery. (a) LDHs bind to negatively charged molecules, including nucleic acids and anionic drugs, due to their high anion exchange capacity. (b) Cellular uptake of siRNA/LDH and siRNA/-5-FI/LDHs nanohybrids. (c) Suppression of Bcl-2 protein expression in MCF-7 cells after single or combined treatment with 5-FU and CD-siRNA delivered by LDHs. Reproduced with permission(149) 2014, Elsevier.

Recently, LDHs have also been evaluated as a nanomaterial for creating mechanically stiff nanocomposites for tissue engineering applications. The addition of LDHs to poly(vinyl alcohol) (PVA) resulted in a four-fold increase in tensile strength over pure PVA and an elastic modulus comparable to lamellar bone.(152) The increase in mechanical strength was attributed to a high PVA-LDH interfacial strength owing to the hydrogen bonding interactions between LDH platelets

and PVA, which facilitated load transfer between the matrix and nanoparticles. In another study, LDH-based PLGA nanocomposites were designed as guided tissue regeneration membranes for regenerating lost periodontal bone.(153) For periodontal abscesses, guided tissue regeneration (GTR) films have recently been created for surgical implantation between the tooth root and gingiva. In general, GTR films are intended to allow undisturbed repopulation of the tooth root with osteoblasts and periodontal ligament cells. However, most films have only demonstrated limited efficacy due to their lack of bioactivity. Chakraborti *et al.* designed bioactive PLGA-LDH nanocomposites loaded with alendronate and tetracycline to facilitate periodontal regeneration, and *in vitro* characterization showed significant increases in both alkaline phosphatase activity and mineralized matrix formation.(153)

Overall, LDHs are a relatively new type of 2D nanomaterial for biomedical applications, but these nanomaterials have excellent biocompatibility, anion exchange capacity, and potential for drug delivery applications. Similar to silicate clay, LDHs can be used for various tissue engineering applications, as most of the components of LDHs are minerals that can be easily absorbed by the body without any significant side effects. Nevertheless, additional studies are required to more thoroughly evaluate the use of LDHs for these applications. We can expect to see the use of LDHs for biomedical applications continue to increase in the coming years.

3.7 2.7. Transition Metal Dichalcogenides (TMDs) for Biomedical Applications

TMDs are 2D nanoparticles that consist of a monolayer of transition metal atoms sandwiched between two layers of chalcogen atoms (any group 16 element, usually sulfur, selenium, or telluride) in a hexagonal lattice.(76) There are roughly 60 known TMDs. However, only two-thirds

of these have layered structures, and among these, only three materials have received significant attention: molybdenum disulfide (MoS_2), tungsten disulfide (WS_2), and titanium disulfide (TiS_2). TMD nanoparticles stand out as biomaterials because of their catalytic properties, photoluminescence, optical absorption, direct band gap, and high wear resistance. (79, 154, 155) TMDs are also inherently thin, flexible, and strong. Notably, 2D TMDs are distinguished by a much higher structural rigidity when compared to commonly used 2D nanomaterials like graphene and hexagonal boron nitride (hBN). MoS_2 and WS_2 have flexural rigidities of 27 and 30 eV $Å^{\cdot 2}$/atom, respectively, while graphene and hBN are around 3.5 eV $Å^{\cdot 2}$/atom. Together, these properties make TMDs useful in biosensors, nanocomposites, bioimaging, and PTT/PDT.

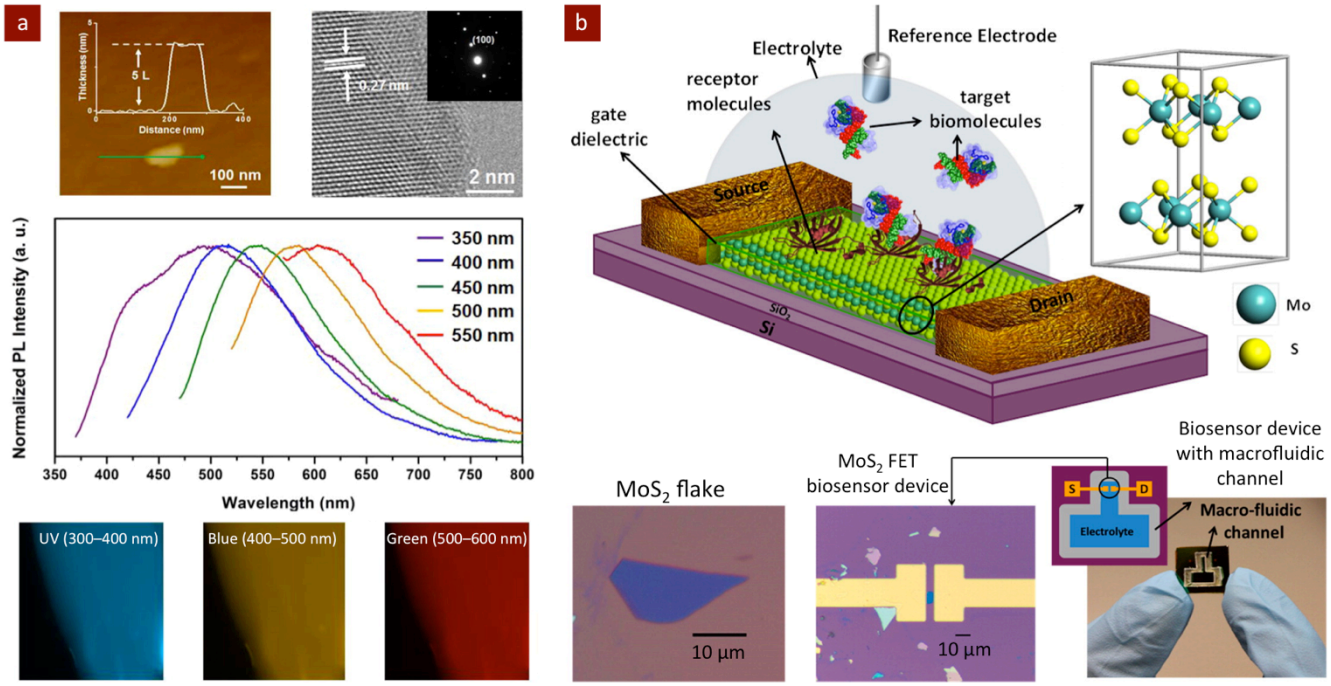

Figure 3-11. TMDs are used as biosensors due to their photoluminescence (PL) characteristics. (a) AFM and HRTEM image of a typical quasi-2D MoS_2 flake are shown. The plot shows the PL spectra of quasi-2D MoS_2 nanoflakes at different excitation wavelengths. The fluorescent images are of MoS_2 thin films at different excitation

wavelengths. (b) Schematic of a MoS_2-based FET biosensor device. Reproduced with permission(156, 157) 2014, American Chemical Society.

3.7.1 Molybdenum disulfide (MoS_2)

As TMD monolayers are fairly new, most research has been on the fundamental characteristics of the materials rather than translational applications. TMDs can be metallic, semi-metallic, or semiconducting, can be magnetic or nonmagnetic, have anisotropic thermal conductance, and have exhibited superconducting properties. These characteristics led initial research on TMD applications towards electronics, and indeed 2D TMDs are considered among the most promising building materials for nanoelectronics. One biomedical application of TMDs is in engineering atomically thin nanopores for higher sensitivity DNA translocation.(158-160) Among DNA sequencing technologies, nanopore sequencing is a promising approach to the challenge of sequencing a single DNA molecule. Nanopore sequencing utilizes a nano-size pore that is obstructed to different degrees by each of the four nucleotides as they pass through the pore. Changes in the amount of current that passes through the pore are characteristic of each nucleotide. Until recently, the only way to make nanopores sensitive enough to recognize individual nucleotides was by using membrane protein complexes. Efforts to replace these bio-pores with solid state nanopores have been stymied by the inability to create nanopores out of SiN_x thin enough to differentiate individual nucleotides. To address this problem Liu *et al.* used a monolayer or few layers of MoS_2, which can have sub-nanometer thickness.(158) A transmission electron microscope was used to drill through the MoS_2 nanosheets as they were suspended on a 20 nm thick SiN_x membrane. This technique increased the resolution of the solid-state nanopore

sequencing from 20 nm to less than 1 nm, breaking down a significant barrier to single nucleotide resolution. The use of the TMDs for this biomedical engineering application is important because, unlike 2D graphene and boron nitride, it has an intrinsic band gap, which opens up the possibility of sequence-specific transistors. Moreover, MoS_2 does not require surface treatments in order to avoid strong interactions with the DNA, unlike graphene, and has a wider window of applied voltages. In this way, MoS_2 is being used in the next step towards single molecule sequencing, one of the ultimate goals of the field of DNA sequencing.(158-160)

Other recent biosensing applications have taken advantage of the highly photoluminescent qualities of TMDs. 2D and Quasi-2D MoS_2 nanosheets are photoluminescent nanomaterials, and their photoluminescence (PL) can be controlled via the intercalation of positive ions between the sheets.(155) The PL effect of these materials is the result of the p, s, and d orbitals of the molybdenum atoms in MoS_2. The fewer the number of layers, the better the PL efficiency of the nanoflakes. This property is useful in biomedical applications because it has been shown that the photoluminescence of MoS_2 can be controlled by altering electrical gating, light polarization, mechanical stress, and cation intercalation, which causes structural lattice expansion.(155) PL characteristics of MoS2 are highlighted in **Figure 3-11a**.(156) The change in PL potential caused by ionic changes can be used as a detector of cation concentrations in biological systems. Cations including H^+, Li^+, Na^+, and K^+ play vital roles in a wide variety of bioprocesses and have been shown to alter the photoluminescence of MoS_2.

In another biosensing study, MoS_2 nanoflakes were used to design a glucose sensor in conjunction with the enzyme glucose oxidase (GOx).(156) The combined MoS_2-GOx system was subjected to different glucose concentrations *in vitro* under a small voltage (1 V). This experiment showed that the PL of the system increased with increasing glucose concentration up to 50 mM,

with a time delay of roughly 60s. This result demonstrated the potential of TMDs for designing nano-sized biosensors. In this experiment the biosensor was saturated at glucose concentrations over 50 mM, which is lower than the expected range of glucose concentrations *in vivo*. Nevertheless, the use of TMDs for optical biosensing applications is promising and this work could provide insight for the next generation of nano-biosensors.

Finally, MoS_2's potential as a FET has also been utilized in a new approach to FET biosensing (**Figure 3-11b)**.(157) FETs use an electric field to alter the conductivity of channels in a semiconductor and have attracted considerable attention in biomedical research due to their potential for sensing a wide variety of biological phenomena spanning from protein sensing to pH detection in a fast and inexpensive manner. However, their utility has been impaired due to the limited sensitivity of currently used 3D FETs. Recently, 1D FETs have shown promise for overcoming some of the challenges in 3D FETs system, but their use has been limited by fabrication challenges. Graphene FETs have been attempted but are less sensitive due to their lack of an intrinsic band gap. Recently, Sarkar *et al.* developed 2D FETs using MoS_2 nanoparticles.(157) These FET sensors displayed high sensitivity compared to 1D and 3D FETS, as well as facile and low cost fabrication. These FETs were tested as pH and biotin sensors. In the case of the pH sensor, detection was based on the protonation and deprotonation of -OH groups on the dielectric surface. This protonation/deprotonation changes the surface charge of the dielectric surface, which alters the current that can pass through the transistor at a certain voltage. This system was shown to be sensitive across a range from pH 3-9. The biomolecule detection FET utilized a biotin-functionalized surface. A significant decrease in current through the transistor was recorded when the streptavidin was introduced into the system due to the negative charge of streptavidin being bound on the FET's dielectric surface. The use of 2D TMDs for this

biomedical application is important because their intrinsic properties make them very amenable for fabricating cheap, robust, and sensitive FETs. This technology can be expected to lead to significant advances in nanosensor-based diagnostics.(157)

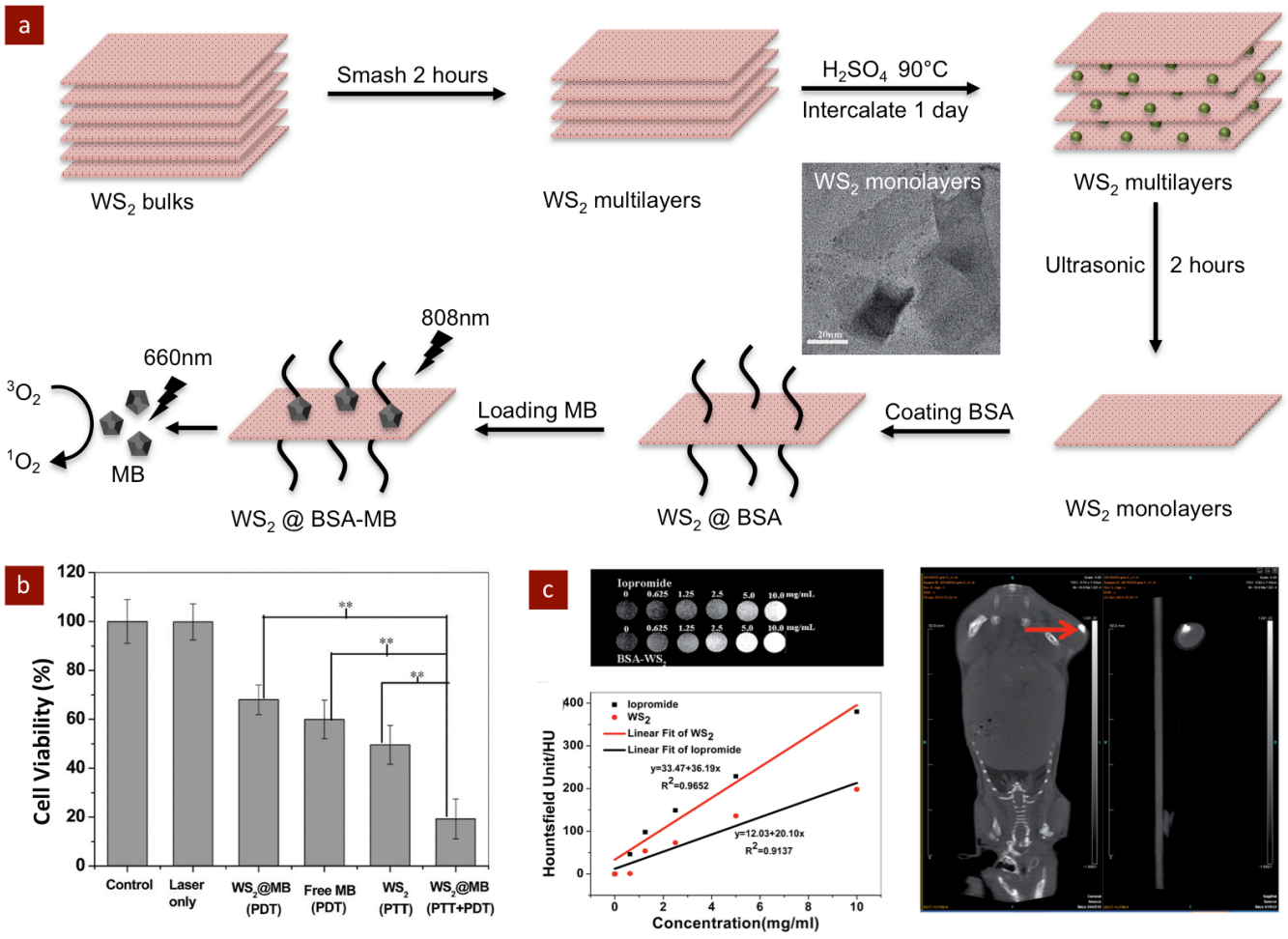

Figure 3-12. TMDs for drug delivery and phototherapies. (a) Schematic showing the synthetic procedure for producing WS_2 nanosheets and their application as a multifunctional photosensitizer delivery system for combined photothermal and photodynamic therapy (i.e., PTT and PDT) of cancer. TEM image of the as synthesized WS_2 nanosheets. (b) Effect of different therapeutic approaches (PDT, PTT, and PTT + PDT) on *in vitro* cytotoxicity. The use of WS_2 nanosheets significantly reduced cancer cell viability, highlighting its efficacy for

PTT and PTT+PDT treatments. (c) *In vitro* and *in vivo* CT images showing BSA–WS_2 nanosheets. The graph compares the radiodensity of WS_2 nanosheets to iopromide, a commonly used CT contrast agent. Reproduced with permission(161) 2014, The Royal Society of Chemistry.

3.7.2 Tungsten disulfide (WS_2)

Another 2D TMD nanomaterial being evaluated for biosensing applications is WS_2 nanosheets. WS_2 nanosheets have been shown to have intrinsic peroxidase-like activity that can catalyze the donation of hydrogen from tetramethylbenzidine (TMB) to hydrogen peroxide, a reaction that changes the color of TMB.(162) This feature led to the development of a testing kit for determining glucose levels in blood, in which WS_2 nanosheets were combined with TMB and glucose oxidase to create a sensor that changes color depending on blood glucose concentrations between 5 and 300 μM. Overall, WS_2 nanosheets could lead to the development of highly efficient biosensors by mimicking enzymatic catalysis process.(162)

In addition to their uses in biosensing, the optical properties of TMDs can be harnessed for creating smart drug delivery vehicles. For example, Yong *et al.* engineered WS_2 sheets as a drug delivery platform for smart photodynamic therapy (PDT) and as a photothermal therapy (PTT) agent (**Figure 3-12**).(161) PDT uses photosensitizing drugs that can convert O_2 into reactive oxygen species for cancer treatment, whereas PTT uses optically absorptive molecules to efficiently heat cancer cells under near infrared irradiation. TMD nanosheets have attracted research attention for drug delivery applications due to their high surface area, which gives them a protein adsorption capacity comparable to GO. More critically, WS_2 has been shown to be well

suited for combining PTT and PDT due to its low toxicity, good water solubility, and high NIR absorption capability. Similar to rGO, TMD nanosheets have a higher extinction coefficient than gold nanorods. They are also easy to purify and are directly dispersible in water. Wang et al. loaded the photosensitizer methylene blue onto bovine serum albumin (BSA)-coated WS_2 for use as a PTT/PDT combined therapy *in vitro*. (163) The WS_2 were shown to create only a small number of singlet oxygen until activated by 808 nM NIR light, which increased singlet oxygen generation (SOG) by 5 times. The authors proposed that the WS_2 sheets quench singlet oxygen generation when methylene blue is adsorbed, and during NIR activation the methylene blue is released from the nanosheets, effecting the increase in SOG. This mechanism would increase the targetability of PDT therapies, reducing side effects compared to other therapies. Notably, *in vivo* treatment of induced tumors with the combined PTT & PDT resulted in 20% cell viability, while PTT treatment with WS_2 left 50% of cells viable and PDT only treatment with WS_2 resulted in cell viability exceeding 60%. These results indicate that the combined therapy is more effective than PDT or PTT therapy alone for WS_2, and that combined PTT & PDT therapies may increase the clinical efficacy PDT and PTT cancer therapies.(163-165)

The broad photoresponsive uses of WS_2 are not restrained to cancer treatments; they can be exploited for imaging applications as well. Computed tomography (CT) imaging relies on contrast agents to absorb x-rays, which increases image contrast in the targeted area, and high atomic number elements like tungsten are frequently used as contrast agents due to their high opacity to absorb x-rays. Photoacoustic tomography (PAT), is a newer imaging modality that utilizes non-ionizing radiation and requires NIR absorbance contrast agents. PAT imaging does not penetrate as deeply as CT but offers improved spatial resolution. In a recent paper by Cheng *et al.*, WS_2 nanosheets were successfully adapted as a theranostic device, combining both imaging

modalities and PTT functionality. PEG functionalized WS_2 nanosheets were shown to be biocompatible and passively accumulate in tumor tissue, and they were highly effective for PTT and as CT and PAT bimodal contrast enhancement agents (**Figure 3-13**). This research shows that WS_2 nanosheets are a promising material for theranostic treatments, whose combined treatments are expected to improve clinical outcomes and reduce the costs of medical procedures.(165)

3.7.3 Titanium disulfide (TiS_2)

Recently, a new type of 2D TMD based on titanium (TiS_2) has been explored for PTT and bioimaging applications.(166) Qian *et al*. used a bottom-up solution-phase approach to synthesize TiS_2 nanosheets that were subsequently modified with PEG to obtain aqueous stable TiS_2-PEG. Preliminary *in vitro* studies indicated that TiS_2 nanosheets were highly cytocompatible over the short course of these studies. Due to high NIR absorbance by TiS_2-PEG, this material has been used as a theranostic for PTT and as a photoacoustic contrast agent simultaneously. While the results were promising, additional pharmacokinetics data and studies on the long-term dose-dependent toxicology of TiS_2 nanosheets are needed.

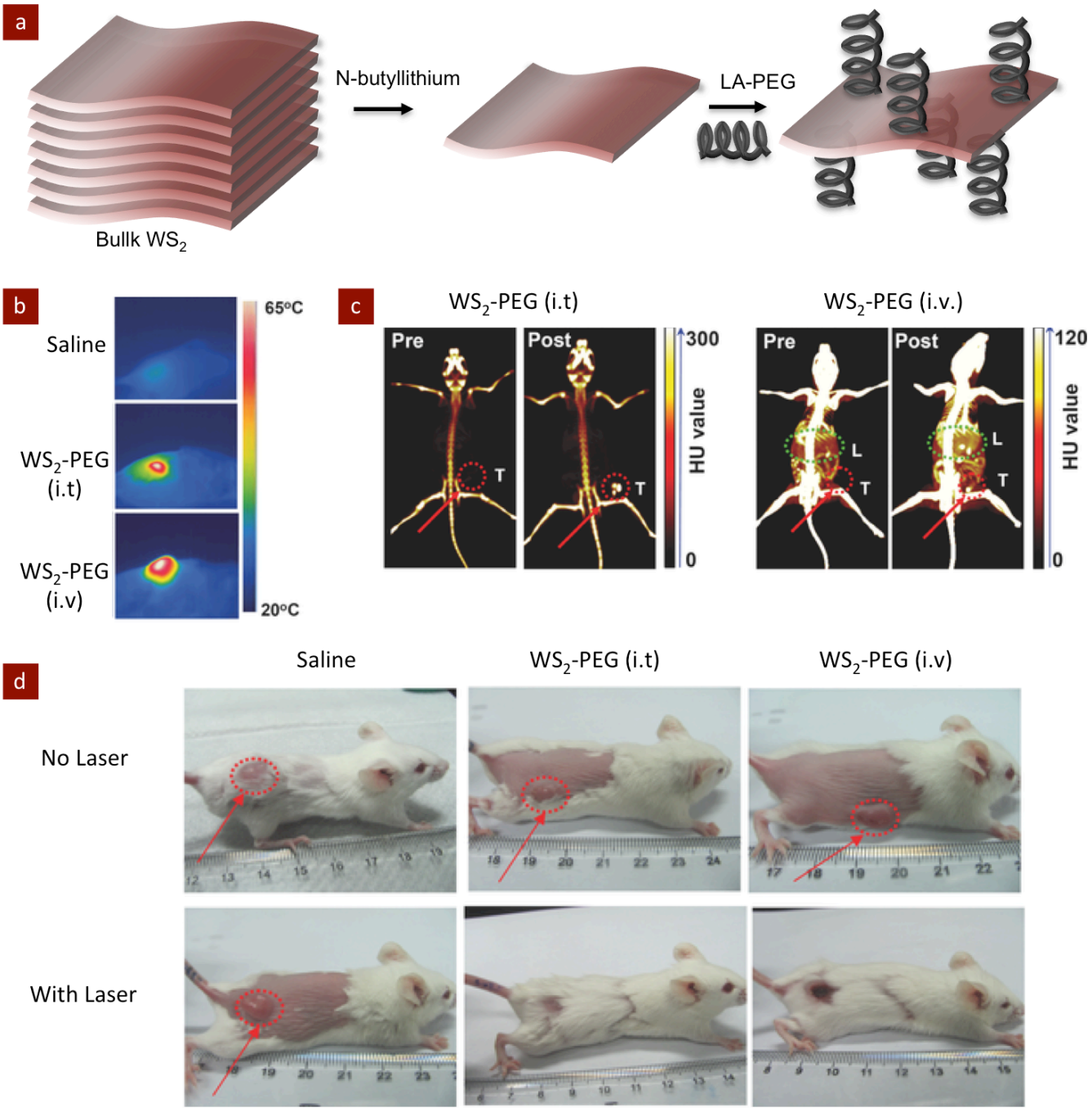

Figure 3-13. The optical properties of TMDs are being investigated for imaging as well as PTT treatment. (a) WS_2 can be exfoliated and functionalized with PEG to enhance stability in salt solutions. (b) IR imaging shows the *in vivo* heating of WS_2-PEG nanoparticles via infrared laser irradiation. (c) CT imaging of tumor-bearing mice after intratumoral (IT) or

intravenous (IV) WS_2-PEG administration demonstrating enhanced contrast, particularly in tumors and the liver. (d) *In vivo* tumor reduction with WS_2-PEG PTT. Reproduced with permission(161, 165) 2014, John Wiley & Sons, Inc.

3.7.4 Summary of TMDs

Overall, 2D TMDs are nanomaterials with interesting electronic and optical properties that have been primarily used for nanoelectronics but are seeing increased use in biomedical applications. TMD nanosheets are highly photoluminescent, highly NIR absorbent, have a direct band gap, and display good mechanical properties, including high rigidity and excellent wear resistance. These properties have made TMD nanosheets an attractive nanomaterial for biosensors, bioimaging, drug delivery, and PTT/PDT treatments. Although TMD research is expanding, the fundamental properties of these materials are not nearly as well understood as some other 2DNMs like graphenes or silicates. Additionally, large-scale fabrication of these materials has proven difficult, and control over a number of specifications like sheet dimensions and quality are still lacking. Nevertheless, TMD nanosheets are promising materials for applications in biomedical engineering and their use should continue to expand as these limitations are addressed in the coming years.

3.8 Transition Metal Oxides (TMOs) for Biomedical Applications

TMOs are notable among the families of 2D nanomaterials because of their wide diversity of material properties. Nanomaterials in this family typically have wide bandgaps, giving them unique photochemical and electric properties. Other nanomaterials in this family have been shown to exhibit ferromagnetic, redox properties, and high thermal resistance. TMO nanoparticles have a relatively long history of study into their material properties, but this research has focused almost exclusively on 0D, 1D, and 3D nanostructures due to the relative difficulty of fabricating 2D TMOs.(79, 143, 167) In the past few years, delamination and bottom up synthesis of TMOs has made their study more practical. The members of this family that have been successfully delaminated into nanosheets include titanium dioxide (TiO_2), manganese dioxide (MnO_2), zinc oxide (ZnO), cobalt (II, III) oxide (Co_3O_4), tungsten trioxide (WO_3), and iron (II, III) oxide (Fe_3O), among others. Materials in this family commonly feature divalent cation interlayers, which keep the sheets in stacks. These interlayers can be broken up through cation exchange to substitute bulkier cations into this interlayer, pushing the sheets farther apart and weakening electrostatic interactions.(167, 168) Due to the novelty of the 2D forms of these materials, relatively little biomedical research has been completed on them compared to TMDs and particularly graphene. Most of the research that has been published has focused on two of the better studied materials: MnO_2 and TiO_2.(143, 169) In this section, we will highlight some of the promising research areas on TMOs for biomedical applications.

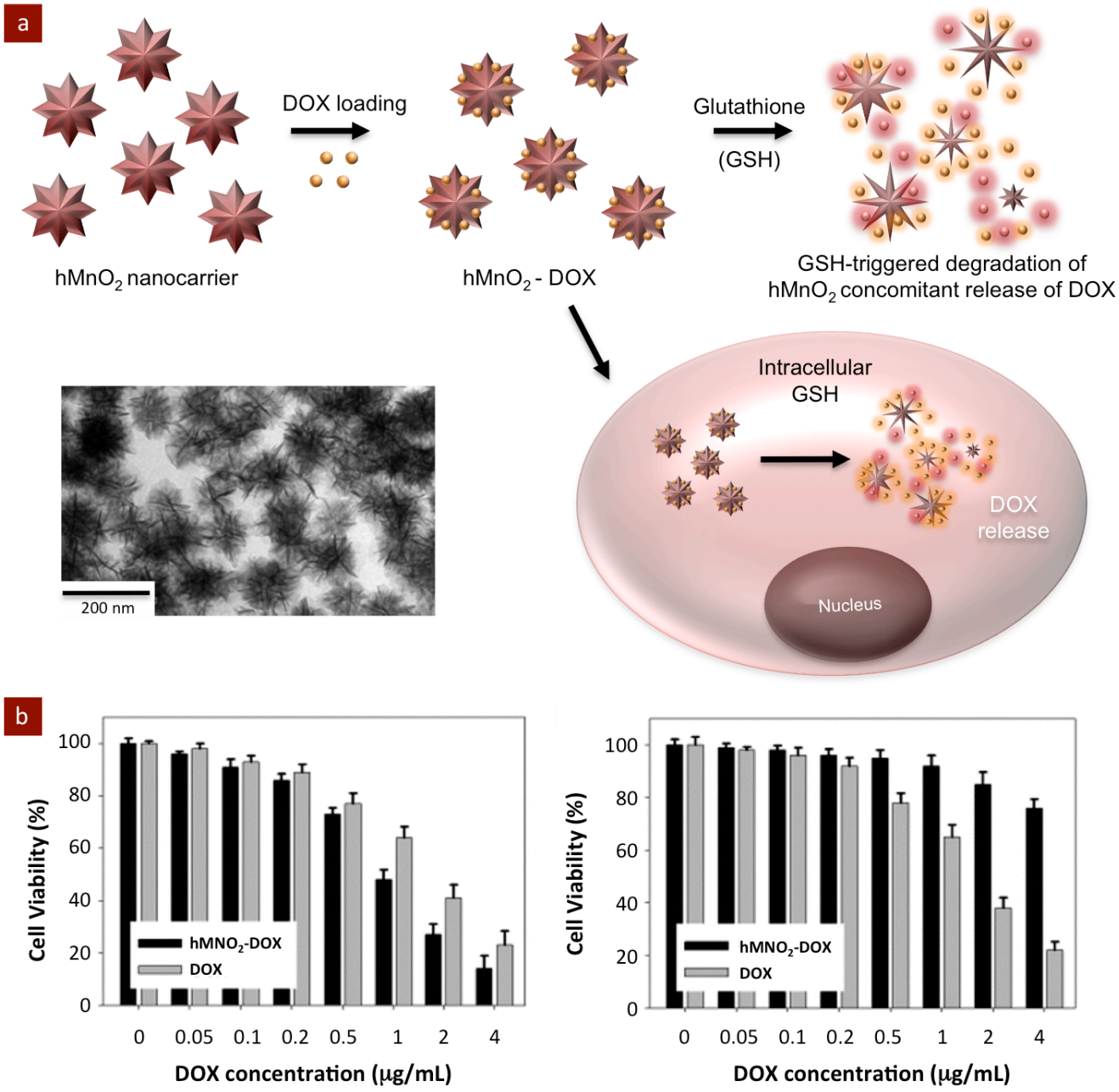

Figure 3-14. Application of TMOs for drug delivery. (a) TMO nanocarriers, such as MnO_2 nanoplatelets, can efficiently transport drugs to tumor cells. TEM images of MnO_2 nanocarriers are shown. MnO_2 particles are internalized inside the cell body and quickly dissolve in the presence of intracellular glutathione to release DOX. (b) Delivery of DOX

using MnO_2 nanocarriers was effective compared to free DOX. Moreover, MnO_2 nanocarriers are specific to tumor cells (left) over normal cells (right). Reproduced with permission(170) 2014, John Wiley & Sons, Inc.

3.9 Manganese dioxide (MnO_2)

Manganese dioxide (MnO_2) nanosheets are composed of metal oxide octahedral unit monolayers, alternating with interlayer cations. MnO_2 exhibits cation exchange properties, is semimetallic, and electrochromic. MnO_2 is particularly noteworthy for its facile redox activity relative to other TMOs. MnO_2 nanosheets have been used for biosensing, imaging, and drug delivery applications. For example, a recent paper by Chen *et al.* used MnO_2 nanosheets for a theranostic treatment in which the material acted as a contrast agent for MRIs but could also steadily break apart under the mildly acidic conditions found inside tumors to deliver therapeutics (**Figure 3-14**).(170) MnO_2 nanosheets were modified with poly(ethylene glycol) (PEG) to improve its stability under physiological conditions and loaded with doxorubicin (Dox) for targeted drug release. Under *in vivo* conditions, these nanosheets were shown to increase MRI signal intensity within tumors. This result was due to the release of Mn(II) particles within the tumor upon breakup of the nanosheet. Additionally the MnO_2-Dox-PEG system resulted in 59.6% cell death in 48 hours, compared to 26.5% cell death from free Dox. This combined dual-functionality system represents an important tool in the development of cancer therapies by combining intelligent design of drug delivery and tumor imaging systems using 2D nanomaterials.(171)

MnO_2 nanosheets have also recently been developed for biosensing applications, including as fluorescence resonance energy transfer (FRET) biosensors.(172, 173) FRET biosensing is a

staple technique in biosensing research and is used to detect ion concentrations, pH, proteins, metabolites, cancer cells, and DNA sequences. MnO_2 nanosheets have received significant attention for these applications due to their utility in energy storage technologies, including supercapacitors and lithium batteries. MnO_2 nanosheets are known to be effective energy absorbers, and due to their high surface area and light absorption they have been explored for use as FRET biosensors. Yuan *et al.* used MnO_2 nanosheets to develop a label-free platform for homogenous FRET biosensing. MnO_2 nanosheets were combined with aptamers conjugated to fluorophores to create FRET biosensors for ochratoxin A and cathepsin D. Because of the water solubility of MnO2 as well as its broad, intense light absorption due to its lattice structure, MnO_2 is adaptable to a wide range of fluorophores that emit light at different frequencies, these probes were tested under a range of physiological conditions in order to ensure their specificity. These tests indicated that MnO_2 nanosheets are a favorable nanoplatform for homogenous biosensing and are easy to make, amenable to a wide range of conditions, highly specific, and robust.(173)

In another biosensing application study, Deng et al. combined MnO_2 nanosheets with lanthanide-doped upconverting nanoparticles for rapid, selective detection of glutathione in aqueous solutions and living cells.(174) In this approach, they synthesized MnO_2 nanosheets on nanoparticle surfaces, and the MnO_2 nanosheets acted as a quencher for upconverted luminescence. The addition of glutathione reduces MnO_2 into Mn^{2+}. Thus by monitoring the glutathione concentration intracellularly, a platform for targeted drug and gene delivery can be designed.

3.9.1 Titanium dioxide (TiO_2)

Another TMO that has been used for biomedical applications is TiO_2 nanosheets. Although TiO_2 has a similar structure to MnO_2, it has significantly different properties. TiO_2 is semiconductive with a wide band gap, giving it good optical absorbance at UV wavelengths, and has a high-k dielectric constant. These features have led to TiO_2 being evaluated for PDT, cell imaging, biosensing, and drug delivery applications. TiO_2 is used as shorthand for titanium oxide in this section because it approximates the formula of titanium oxides. However it is not necessarily the precise composition of titanium oxide.(83, 168, 175, 176) It is well known that TiO_2 nanoparticles produce oxidative radicals upon exposure to UV light (<385 nm). These radicals have been shown to be capable of killing a wide variety of cells and have demonstrated *in vivo* efficacy. Nitrogen-doped TiO_2 nanosheets showed improved visible light absorbance, resulting in higher radical production.(177) This shift from UV to visible light makes PDT with TiO_2 nanoparticles more practical for clinical application as a noninvasive cancer treatment. Additionally, Elvira *et al.* incorporated specificity into TiO_2 by immobilizing monoclonal antibodies for neural stem cells onto the nanoparticles.(178) The antibody-associated nanoparticles were shown to accumulate on the target cells, resulting in highly selective PDT. This approach has the potential to lead to the development of highly specific cancer therapies and expand the therapeutic options available to patients. In another application, TiO_2 nanosheets were combined with acrylamide to fabricate nanocomposite hydrogels that mimic some of the physical and chemical properties of articular cartilage.(179) This technique relied on the use of a strong magnetic field to coaxially align the TiO_2 nanosheets before polymerization. This new nanocomposite design has many potential applications in biomedical engineering as a new paradigm in nanocomposites.

3.9.2 Summary of TMOs

Overall, TMOs are being investigated for bioimaging, biosensing, PDT, and drug delivery applications. These applications of 2D TMOs stem from the redox activity, cation exchange capabilities, and varied electrical and optical characteristics. TiO_2 nanosheets are frequently used for their photocatalytic and dielectric properties, while MnO_2 nanosheets are more often used for their semi-metallic and redox properties. TMO nanosheets, like many other 2D nanomaterials, remain insufficiently evaluated for biocompatibility. In the future, new biomedical research in this area should further leverage the optical and electronic properties of these materials.

3.10 Other types of 2D nanomaterials

Some 2D nanomaterials do not fit neatly into any of the categories described above. These materials form single layer nanosheets like graphene but do not consist of simple repeating patterns of carbon atoms. Graphitic carbon nitride, for example, alternates carbon and nitrogen heteroatoms, forming a strong, regular structure with semiconducting and catalytic properties. Similarly, hexagonal boron nitride forms a hexagonal monolayer of alternating boron and nitrogen atoms. Other materials include silicene and germanene, which are group IV elements that share many atomic properties with carbon. These elements have long been speculated to be able to form their own 2 dimensional allotropes, but these allotropes were not synthesized until this decade. In this final section, these unique materials are examined individually in the context of biomedical engineering.

3.10.1 Graphitic Carbon Nitride (C3N4)

2D, or graphitic, carbon nitride (C_3N_4) is a relatively new material, having only been synthesized in the last couple of years.(180, 181) Ultrathin graphitic C_3N_4 (g- C_3N_4) nanosheets were produced for the first time in 2012, and have been found to exhibit high intrinsic photoabsorption and photoresponsiveness, semiconductive properties, high stability under physiological conditions, and good *in vitro* biocompatibility.(160, 180-183) These properties lend the material to applications as an imaging agent, drug delivery vehicle, and in biosensing. C_3N_4 nanosheets may improve the current state of the art in bioimaging by providing a nontoxic alternative-imaging agent. C_3N_4 sheets have been demonstrated to be able to bind to cell nuclei, enabling facile intracellular fluorescence imaging due to their high PL quantum yields.(182) Studies have also indicated that these nanosheets may be especially useful for phototherapies after they have been endocytosed into the cell. For example, in Lin *et al.*, C_3N_4 nanosheets were demonstrated to enhance confocal fluorescence imaging without damaging living HeLa cells (**Figure 3-15**).(183, 184) C_3N_4 nanosheets have also been shown to have a high capacity for drug loading, being able to bind up to 18,200 mg/G of doxorubicin.(183) These nanocarrier sheets had significant in vitro anti-cancer activity, though not as much as free doxorubicin. Doxorubicin release was via a pH-responsive mechanism: increased hydrophilicity of doxorubicin at lower pHs caused it to dissociate from the nanocarrier. In another recent trial, ultrathin C_3N_4-Fe_3O_4 nanocomposites were shown to have a high photocatalytic efficiency.(180) Carbon nitride nanosheets have also been shown to be an effective biosensor due to their semiconductive properties, fluorescence, and high stability under a wide variety of conditions. Ma *et al.* showed that protonated C_3N_4 nanosheets can be used to directly monitor heparin concentration.(185) A

broad linear heparin concentration range from 0.05-5 ug/mL, which is clinically relevant, can be quantified with excellent sensitivity and specificity. C_3N_4 has also been demonstrated as an effective biosensor for glucose and in combination with GO as a simultaneous biosensor for ascorbic acid, dopamine, and uric acid.(116) Although C_3N_4 nanosheets are relatively new 2D nanomaterials, they are clearly useful for biomedical applications and could also be used to engineer efficient medical devices.

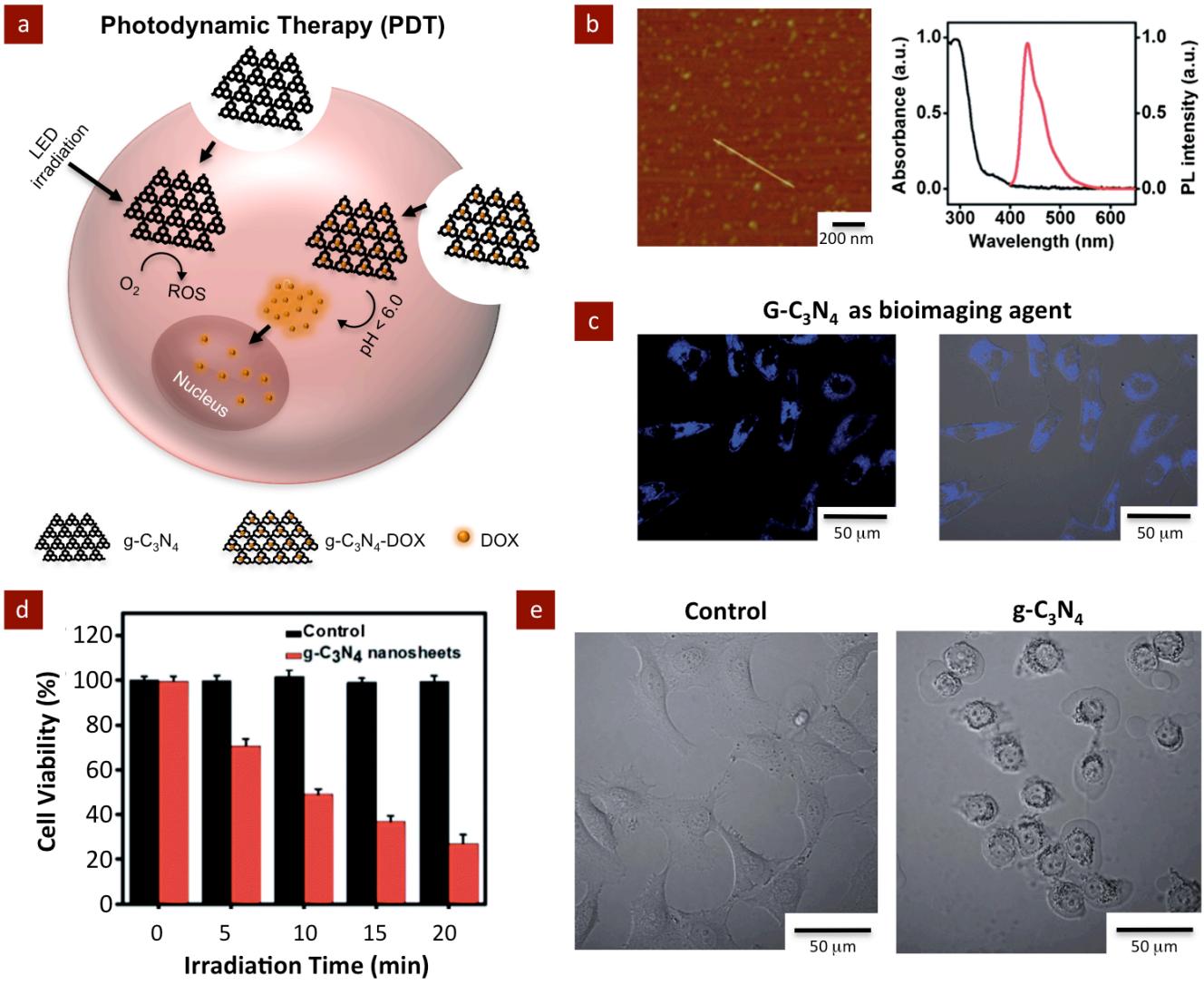

Figure 3-15. Application of g-C_3N_4 for intracellular imaging, PTT and PDT. (a) g-C_3N_4 nanosheet can be used to deliver therapeutic cargo and for PDT due to its ability to absorb visible light. (b) AFM images and absorption spectra of g-C_3N_4 nanosheets. (c) g-C_3N_4 nanosheets can be used as bioimaging agents. (d) Cell viability results demonstrating the ability of g-C_3N_4 nanosheets to be used for PDT therapy. (e) Cell morphology before and after PDT with g-C_3N_4. Reproduced with permission(183) 2014, The Royal Society of Chemistry.

3.10.2 Hexagonal Boron Nitride (hBN)

Similar to graphitic carbon nitride, hexagonal boron nitride (hBN) nanosheets are also monolayers with alternating nitrogen moieties.(75, 186-189) However, hBN alternates nitrogen with boron atoms, which are less electronegative than carbon. The stronger polarity of the nitrogen-boron bond affects many of its properties, including its UV luminescence and wide band gap semiconductivity. Because of these characteristics as well as its chemical and thermal stability and wide availability, hBN has garnered significant attention for use in electronics applications.(186) Importantly, hBN monolayers make the synthesis of hybrid nanostructures of graphene and hBN with tunable band gaps possible, which is a widely sought after goal in electronics research.(190) However, the unique properties of hBN also make it a promising material for a wide variety of biomedical applications that have just begun to be explored. hBN has a number of favorable biological properties, including cytocompatibility and a demonstrated propensity for being endocytosed into cells. Like all 2D nanomaterials, the biocompatibility of hBN has yet to be definitively established, but preliminary studies have shown hBN may have

better biocompatibility than graphene. This research has led to exploration of hBN as a more biocompatible alternative to graphene in drug delivery, imaging, and biosensing applications.(75, 187-189)

Like graphene, pure hBN is not suitable for drug delivery due to its poor solubility in physiological solutions.(142) However, also like graphene, hBN can be functionalized through hydroxylation to increase its water solubility. Recently, a new synthesis method involving thermal substitution of boric acid with C_3N_4 has been demonstrated to produce highly hydroxylated hBNs that have high water solubility (2.0 mg/mL) and low cytotoxicity *in vitro* (**Figure 3-16**).(142) The behavior of hydroxylated hBN nanosheets has been compared to that of graphene oxide. Weng *et al.* showed that these hydroxylated hBNs were capable of adsorbing up to 300% of their weight in doxorubicin.(142) These drug-loaded hydroxylated hBNs exhibited pH dependent release kinetics, with acidic pHs freeing doxorubicin in higher amounts and at higher rates. While drug-free hydroxylated hBN was highly cytocompatible, the doxorubicin-loaded nanosheets reduced cancer cell viability to 18-21%. The authors suggested that this increase in toxicity over free DOX was the result of the nanosheets being endocytosed and releasing their payload in the acidic lysosomes. The combination of high biocompatibility and drug loading, and improved antitumor effectiveness makes hydroxylated hBN a possible clinical drug delivery vehicle that could improve the effectiveness of chemotherapeutics while also reducing side effects.

The endocytosis and biocompatibility of hBN nanosheets mentioned above also make them an attractive material for live cell imaging. Peng *et al*. functionalized hBNs with graphene quantum dots (GQDs), taking advantage of their stability and endocytosis to create a new intracellular fluorescent marker.(191) Green fluorescent GQDs were incorporated onto hBN nanosheets and exposed to HeLa cell cultures. This results demonstrated strong fluorescence, stability, good

solubility, and low cytotoxicity, as well as the ability to efficiently penetrate cells. This technology has the potential to expand the capabilities of live cell imaging technologies by increasing the stability of intracellular fluorescent markers.

One area of biomedical engineering where hBN nanosheets are noticeably absent is tissue engineering. Given their shape, strength, and biocompatibility, hBN nanosheets have excellent potential for use in tissue engineering applications. The use of hBN nanosheets specifically in hydrogel nanocomposites has yet to be explored, though hBN nanotubes have recently demonstrated osteoinductive effects on MSCs.(192) However, a range of nanocomposites have been fabricated from hBN by combining it with different polymers.(193) For example, a nanocomposite of hBN with gelatin has been fabricated (189) and, due to the similarity of gelatin with the native ECM of tissues, these nanocomposite can be explored for tissue engineering and stem cell applications. It is expected that this new type of 2D nanomaterial can be used as a reinforcing or bioactive agent within a hydrogel matrix to modulate the differentiation of stem cells.

Overall, hBN has shown compelling mechanical and chemical properties that suggest many potential uses in biomedicine. Thus far, however, the exploration of hBN's applications has been hampered by synthetic difficulties. The chemistry of boron and nitrogen is not nearly as well explored as that of carbon, which limits researcher's ability to manipulate and functionalize hBN. Additionally, synthesis and dispersion difficulties continue to slow research progress. Once these problems are overcome, hBN's role in biomedical engineering can be expected to expand significantly.

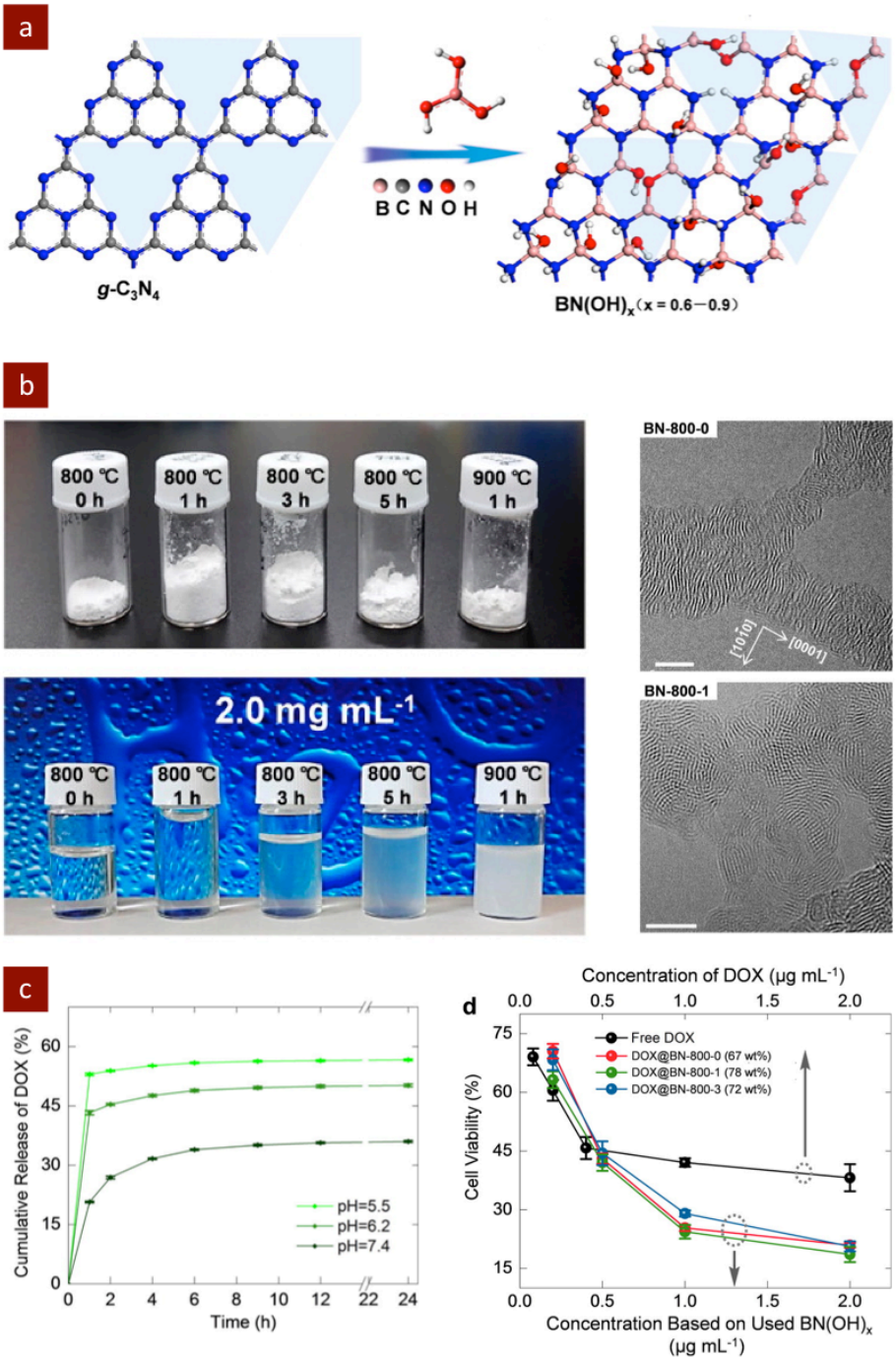

Figure 3-16. hBN nanosheets for drug delivery application. (a) The surface modification of *g*-C_3N_4 was performed with boric acid treatment to obtain (b) water-soluble hBN. HRTEM images of hBN show the sheet network. (c) The release of DOX from DOX@BN networks

was affected by pH conditions. The cell viability results show the effect of DOX release from the BN network on human prostate cancer cells. Reproduced with permission.(142) 2014, American Chemical Society.

3.10.3 Silicene and Germanene

Recently, new 2D allotropes known as silicene and germanene have been reported.(194, 195) The basic physical properties of silicene, synthesized in 2012, and germanene, synthesized in 2014, are only just beginning to be explored. Silicene and germanene have similar electrical conductance to graphene. However, these 2D nanosheets also have unique and useful properties, such as high flexibility and compressibility, as well as strain dependent increases in thermal and electrical conductivity. Recently, it was reported that both 2D silicene and germanene have high structural stability, high phonon scattering ability, and high energy electrical transport properties.(196) These interesting properties coupled with their ability to integrate with electronic devices can provide multiple opportunities in the area of bioelectronics. Until facile synthetic techniques are developed for these materials, however, these materials will remain unfortunately rare and scarcely explored. More information on the calculated properties of silicene and germanene can be found in these reviews.(75, 76, 197)

3.11 Emerging trends and future outlook

The biomedical applications of 2D nanomaterials are rapidly expanding and promising improvements in areas such as bioimaging, drug delivery, biosensors, tissue engineering,

photothermal therapy, photodynamic therapy, and hemostatic wound dressings have been demonstrated. The complex relationships between material properties, structure, shape and defects have emerged as a field that is ripe for development across the scientific community. With our recently acquired knowledge of the rules of nature that govern the atomic-, nano-, micro-, and macro- scales, we are well positioned to unravel and control the complexity that determines functionality of these newly developed 2D materials.

In the future, the field of 2D nanomaterials will likely include a wider selection of nanomaterials that includes novel materials as well as a better understanding of the physical, chemical and biological characteristics of different types of 2D nanomaterials that govern their utility in biomedical and biotechnological applications. New 2D nanomaterials that have only just been synthesized, like silicene and germanene, have yet to be fully characterized, and are a long way from translational applications. However, these and other undiscovered materials may have unprecedented properties that could hold the keys to new biomedical research breakthroughs.

One particularly important emerging trend in nanomaterials is the development of a new generation of intelligent structures that are multifunctional, adaptive, programmable, and biocompatible. By combining rational design of 2D nanomaterials with computational modeling and detailed physical, chemical and structural characterizations, it is possible to engineer designer materials. Specifically, there is immense interest in engineering nanocomposites loaded with nanomaterials with tunable mechanical, structural, chemical, and biological properties through precise control of size, shape, and composition of the 2D nanoscale building blocks. With proper orientation and assembly, 2D nanomaterials could potentially lead to 3D mesostructures with unrivaled properties for a host of technologies. While the importance of mesostructured materials is well appreciated in the broader materials science community, the implications for biomaterials

can perhaps best be appreciated by considering that, while nature uses a variety of nanoscale building blocks, the key properties of cells, tissues, and organisms rely on the proper assembly of these building blocks into larger mesoscale structures.(198, 199) Mesoscale particles comprising drug-loaded nanoparticles have shown promising results for multi-stage controlled delivery of therapeutic agents. However, thinking more broadly, a more complete understanding of how nanomaterials can be assembled into mesostructured materials and devices could lead to exciting advances throughout biomedical engineering. Thus, it is our expectation that the introduction of 2D nanomaterials to the biomedical community represents a paradigm-shift in applying fundamental materials science knowledge to biomedical engineering that will enable engineering of the next generation of medical devices.

As we move from basic science towards translational research, an increase in novel combinations of nanomaterials as well as innovative processing strategies and applications will emerge. Nanocomposites containing multiple dimensions of nanomaterials such as 0D, 1D, 2D, and 3D nanostructures have recently been reported to exhibit synergistic properties combinations. Some of these nanocomposites are highlighted in carbon-based 2D nanomaterials. Combinations of carbon nanotubes and 2DNMs like graphene, clays, LDHs, or TMDs are beginning to attract attention as a way to obtain synergistic property combinations. For example, a nanocomposite comprising polypropylene (PP) loaded with GO and CNTs exhibited increased tensile strength, elastic modulus, and electrical conductivity, among other properties.(200, 201) In the future we anticipate that many material combinations will be explored for biomedical applications.

As new types of 2D nanomaterials are discovered and characterized, their interactions with biological entities need to be investigated in detail. Specifically, it is important to understand the effects of 2D nanomaterial size, shape, chemical composition and surface characteristics on protein

adsorption, cellular internalization, and binding to sub-cellular components. Recent literature indicates that 2D nanomaterials can be exploited to control stem cell fate. For example, graphene(93), silicate clay(26), hBN(192) have all been shown to induce the osteogenic differentiation of stem cells in the absence of any other osteogenic agents. At the atomic-level there is nothing common between these materials except the 2D shape. Thus, from our observations, there is a strong indication that nanoparticle shape may play a major role in directing cellular processes including differentiation, proliferation, adhesion and migration. As the field advances, it will be critical to understand the interactions of 2D nanomaterials with cellular components such as structural proteins, genetic materials, and metabolites, to understand how these nanomaterials control or affect various signaling pathways. This knowledge will broaden our understanding of how nanomaterial shape can be used to control specific biological process.

One of the primary challenges facing the biomedical application of 2D nanomaterials is biocompatibility. Because 2D nanomaterials is a nascent field, only a few types of 2D nanomaterials have been evaluated for biocompatibility. Moreover, the cyto- and bio-compatibility of 2D nanomaterials are poorly understood due to several confounding factors such as size and shape, which are difficult to control with current synthesis methods. This lack of control over the structure of 2D nanomaterials makes the systematic evaluation of their biological interactions challenging. Thus, there is an immediate need to address this problem so that efforts can be focused towards identifying a library of 2D nanomaterials that are appropriate for various biomedical applications. Additionally, most biocompatibility evaluations to date have been superficial, and the long-term effects and the fate of 2D nanomaterials inside the body are not known. Long-term *in vivo* evaluations are necessary before the promising benefits demonstrated by many 2D nanomaterials can be translated into clinical use.

3.12 Conclusion

Unprecedented challenge and opportunity exist in developing 2D nanomaterials for next-generation technologies for basic cell biology, medical diagnostics, regenerative medicine, drug and gene delivery, stem cell engineering, cancer therapy, biosensing, and bioelectronics. Although, graphene, GO, and rGO remain the focal points of research in this field, novel 2D nanomaterials such as clay, LDH, TMDs, and TMOs are being evaluated for new applications. The biocompatibility, bioactivity, uniform particle size, and permanent surface charges of LDHs and clays are being exploited primarily or drug delivery, tissue engineering, and biosensing. Meanwhile, the relatively underutilized TMOs and TMDs are finding utility in bioimaging, biosensing, drug delivery, and novel cancer treatments. Recently investigated materials like hBN and C_3N_4 nanosheets have shown promise for a variety of applications due to their similarity to graphene, and these materials are likely to be evaluated extensively once their synthetic difficulties are overcome.

Importantly, the potential biomedical applications of 2D nanomaterials are vast. Once the biocompatibility of these materials is confirmed, their exceptional properties have the potential to be translated from bench to bedside, which could lead to transformative advances in biomedical science and clinical outcomes. Here, we attempted to review the most promising technologies in 2D nanomaterials, which only represents a fraction of this exciting and rapidly expanding field.

3.13 References

1 Geim, A. K. & Novoselov, K. S. The rise of graphene. *Nature materials* **6**, 183-191 (2007).

2 Novoselov, K. *et al.* Two-dimensional gas of massless Dirac fermions in graphene. *Nature* **438**, 197-200 (2005).

3 Geim, A. K. Graphene: status and prospects. *science* **324**, 1530-1534 (2009).

4 Novoselov, K. S. *et al.* Electric Field Effect in Atomically Thin Carbon Films. *Science* **306**, 666-669, doi:10.1126/science.1102896 (2004).

5 Young, R. J., Kinloch, I. A., Gong, L. & Novoselov, K. S. The mechanics of graphene nanocomposites: A review. *Composites Science and Technology* **72**, 1459-1476, doi:http://dx.doi.org/10.1016/j.compscitech.2012.05.005 (2012).

6 Novoselov, K. S. Nobel Lecture: Graphene: Materials in the Flatland*. *Reviews of Modern Physics* **83**, 837-849 (2011).

7 Gnach, A., Lipinski, T., Bednarkiewicz, A., Rybka, J. & Capobianco, J. A. Upconverting nanoparticles: assessing the toxicity. *Chemical Society Reviews*, doi:10.1039/C4CS00177J (2015).

8 Palombo, M. *et al.* Pharmaceutical and Toxicological Properties of Engineered Nanomaterials for Drug Delivery. *Annual review of pharmacology and toxicology* **54**, 581-598, doi:10.1146/annurev-pharmtox-010611-134615 (2014).

9 Aillon, K. L., Xie, Y., El-Gendy, N., Berkland, C. J. & Forrest, M. L. Effects of nanomaterial physicochemical properties on in vivo toxicity. *Advanced Drug Delivery Reviews* **61**, 457-466 (2009).

10 Grainger, D. W. Nanotoxicity assessment: all small talk? *Advanced Drug Delivery Reviews* **61**, 419-421, doi:http://dx.doi.org/10.1016/j.addr.2009.04.003 (2009).

11 Aggarwal, P., Hall, J. B., McLeland, C. B., Dobrovolskaia, M. A. & McNeil, S. E. Nanoparticle interaction with plasma proteins as it relates to particle biodistribution, biocompatibility and therapeutic efficacy. *Advanced Drug Delivery Reviews* **61**, 428-437, doi:http://dx.doi.org/10.1016/j.addr.2009.03.009 (2009).

12 Jones, C. F. & Grainger, D. W. In vitro assessments of nanomaterial toxicity. *Advanced Drug Delivery Reviews* **61**, 438-456, doi:http://dx.doi.org/10.1016/j.addr.2009.03.005 (2009).

13 Smith, M. J., Brown, J. M., Zamboni, W. C. & Walker, N. J. From Immunotoxicity to Nanotherapy: The Effects of Nanomaterials on the Immune System. *Toxicological Sciences* **138**, 249-255, doi:10.1093/toxsci/kfu005 (2014).

14 Chen, Y., Tan, C., Zhang, H. & Wang, L. Two-dimensional graphene analogues for biomedical applications. *Chemical Society Reviews*, doi:10.1039/C4CS00300D (2015).

15 Shvedova, A. A., Kagan, V. E. & Fadeel, B. Close Encounters of the Small Kind: Adverse Effects of Man-Made Materials Interfacing with the Nano-Cosmos of Biological Systems. *Annual Review of Pharmacology and Toxicology* **50**, 63-88, doi:doi:10.1146/annurev.pharmtox.010909.105819 (2010).

16 Zhuang, X., Mai, Y., Wu, D., Zhang, F. & Feng, X. Two-Dimensional Soft Nanomaterials: A Fascinating World of Materials. *Advanced Materials* **27**, 403-427, doi:10.1002/adma.201401857 (2015).

17 Anderson, J. M., Rodriguez, A. & Chang, D. T. in *Seminars in immunology.* 86-100 (Elsevier).

18 Ratner, B. D. & Bryant, S. J. Biomaterials: where we have been and where we are going. *Annu. Rev. Biomed. Eng.* **6**, 41-75 (2004).

19 Butler, S. Z. *et al.* Progress, Challenges, and Opportunities in Two-Dimensional Materials Beyond Graphene. *ACS Nano* **7**, 2898-2926, doi:10.1021/nn400280c (2013).

20 Xu, M., Liang, T., Shi, M. & Chen, H. Graphene-Like Two-Dimensional Materials. *Chemical Reviews* **113**, 3766-3798, doi:10.1021/cr300263a (2013).

21 Dawson, J. I. & Oreffo, R. O. C. Clay: New Opportunities for Tissue Regeneration and Biomaterial Design. *Advanced Materials* **25**, 4069-4086, doi:10.1002/adma.201301034 (2013).

22 Kuthati, Y., Kankala, R. K. & Lee, C.-H. Layered double hydroxide nanoparticles for biomedical applications: Current status and recent prospects. *Applied Clay Science* **112–113**, 100-116, doi:http://dx.doi.org/10.1016/j.clay.2015.04.018 (2015).

23 Nicolosi, V., Chhowalla, M., Kanatzidis, M. G., Strano, M. S. & Coleman, J. N. Liquid exfoliation of layered materials. *Science* **340** (2013).

24 Pei, S. & Cheng, H.-M. The reduction of graphene oxide. *Carbon* **50**, 3210-3228, doi:http://dx.doi.org/10.1016/j.carbon.2011.11.010 (2012).

25 Rives, V. Layered double hydroxides: present and future. (Nova Publishers, 2001).

26 Evans, D. & Slade, R. T. in *Layered Double Hydroxides* Vol. 119 *Structure and Bonding* (eds X. Duan & DavidG Evans) Ch. 5, 1-87 (Springer Berlin Heidelberg, 2006).

27 Osada, M. & Sasaki, T. Exfoliated oxide nanosheets: new solution to nanoelectronics. *Journal of Materials Chemistry* **19**, 2503-2511, doi:10.1039/B820160A (2009).

28 Liu, G.-B., Xiao, D., Yao, Y., Xu, X. & Yao, W. Electronic structures and theoretical modelling of two-dimensional group-VIB transition metal dichalcogenides. *Chemical Society Reviews*, doi:10.1039/C4CS00301B (2015).

29 Goenka, S., Sant, V. & Sant, S. Graphene-based nanomaterials for drug delivery and tissue engineering. *Journal of Controlled Release* **173**, 75-88 (2014).

30 Zhu, Y. *et al.* Graphene and graphene oxide: synthesis, properties, and applications. *Advanced materials* **22**, 3906-3924 (2010).

31 Shen, H., Zhang, L., Liu, M. & Zhang, Z. Biomedical applications of graphene. *Theranostics* **2**, 283-294 (2012).

32 Fan, H. *et al.* Fabrication, mechanical properties, and biocompatibility of graphene-reinforced chitosan composites. *Biomacromolecules* **11**, 2345-2351, doi:10.1021/bm100470q (2010).

33 Moon, I. K., Lee, J., Ruoff, R. S. & Lee, H. Reduced graphene oxide by chemical graphitization. *Nature Communication* **1**, 73 (2010).

34 Compton, O. C. & Nguyen, S. T. Graphene Oxide, Highly Reduced Graphene Oxide, and Graphene: Versatile Building Blocks for Carbon-Based Materials. *Small* **6**, 711-723, doi:10.1002/smll.200901934 (2010).

35 Bianco, A. Graphene: Safe or Toxic? The Two Faces of the Medal. *Angewandte Chemie International Edition* **52**, 4986-4997, doi:10.1002/anie.201209099 (2013).

36 Sharifi, S. *et al.* Toxicity of nanomaterials. *Chemical Society Reviews* **41**, 2323-2343, doi:10.1039/C1CS15188F (2012).

37 Qiu, L. *et al.* Mechanically Robust, Electrically Conductive and Stimuli-Responsive Binary Network Hydrogels Enabled by Superelastic Graphene Aerogels. *Advanced Materials* **26**, 3333-3337, doi:10.1002/adma.201305359 (2014).

38 Nayak, T. R. *et al.* Graphene for Controlled and Accelerated Osteogenic Differentiation of Human Mesenchymal Stem Cells. *ACS Nano* **5**, 4670-4678, doi:10.1021/nn200500h (2011).

39 Lee, W. C. *et al.* Origin of Enhanced Stem Cell Growth and Differentiation on Graphene and Graphene Oxide. *ACS Nano* **5**, 7334–7341 (2011).

40 Crowder, S. W. *et al.* Three-dimensional graphene foams promote osteogenic differentiation of human mesenchymal stem cells. *Nanoscale* **5**, 4171-4176, doi:10.1039/C3NR00803G (2013).

41 Tang, M. *et al.* Enhancement of electrical signaling in neural networks on graphene films. *Biomaterials* **34**, 6402-6411, doi:http://dx.doi.org/10.1016/j.biomaterials.2013.05.024 (2013).

42 Mannoor, M. S. *et al.* Graphene-based wireless bacteria detection on tooth enamel. *Nature communications* **3**, 763 (2012).

43 Reshma, S. & Mohanan, P. Graphene: A Multifaceted Nanomaterial for Cutting Edge Biomedical Application. *Int J Med Nano Res* **1** (2014).

44 Bai, H., Li, C., Wang, X. & Shi, G. A pH-sensitive graphene oxide composite hydrogel. *Chemical Communications* **46**, 2376-2378, doi:10.1039/C000051E (2010).

45 Li, D., Müller, M. B., Gilje, S., Kaner, R. B. & Wallace, G. G. Processable aqueous dispersions of graphene nanosheets. *Nature Nanotechnology* **3**, 101-105, doi:10.1038/nnano.2007.451 (2008).

46 Shin, S. R. *et al.* Cell-laden Microengineered and Mechanically Tunable Hybrid Hydrogels of Gelatin and Graphene Oxide. *Advanced Materials* **25**, 6385-6391, doi:10.1002/adma.201301082 (2013).

47 Shin, S. R. *et al.* Carbon-nanotube-embedded hydrogel sheets for engineering cardiac constructs and bioactuators. *ACS nano* **7**, 2369-2380 (2013).

48 Cha, C. *et al.* Controlling Mechanical Properties of Cell-Laden Hydrogels by Covalent Incorporation of Graphene Oxide. *Small* **10**, 514-523 (2014).

49 Liu, J., Cui, L. & Losic, D. Graphene and graphene oxide as new nanocarriers for drug delivery applications. *Acta Biomaterialia* **9**, 9243-9257 (2013).

50 Weaver, C. L., LaRosa, J. M., Luo, X. & Cui, X. T. Electrically Controlled Drug Delivery from Graphene Oxide Nanocomposite Films. *ACS Nano* **8**, 1834-1843, doi:10.1021/nn406223e (2014).

51 Paul, A. *et al.* Injectable graphene oxide/hydrogel-based angiogenic gene delivery system for vasculogenesis and cardiac repair. *ACS nano* **8**, 8050-8062 (2014).

52 Green, R. A., Lovell, N. H., Wallace, G. G. & Poole-Warren, L. A. Conducting polymers for neural interfaces: Challenges in developing an effective long-term implant. *Biomaterials* **29**, 3393-3399 (2008).

53 Luo, X., Weaver, C. L., Tan, S. & Cui, X. T. Pure graphene oxide doped conducting polymer nanocomposite for bio-interfacing. *Journal of Materials Chemistry B* **1**, 1340-1348, doi:10.1039/C3TB00006K (2013).

54 Park, S. Y. *et al.* Enhanced Differentiation of Human Neural Stem Cells into Neurons on Graphene. *Advanced Materials* **23**, H263-H267, doi:10.1002/adma.201101503 (2011).

55 Serrano, M. C. *et al.* 3D free-standing porous scaffolds made of graphene oxide as substrates for neural cell growth. *Journal of Materials Chemistry B* **2**, 5698-5706 (2014).

56 Akhavan, O., Ghaderi, E., Abouei, E., Hatamie, S. & Ghasemi, E. Accelerated differentiation of neural stem cells into neurons on ginseng-reduced graphene oxide sheets. *Carbon* **66**, 395-406 (2014).

57 Cai, B. *et al.* Ultrasensitive Label-Free Detection of PNA–DNA Hybridization by Reduced Graphene Oxide Field-Effect Transistor Biosensor. *ACS Nano* **8**, 2632-2638, doi:10.1021/nn4063424 (2014).

58 Kim, D.-J. *et al.* Reduced graphene oxide field-effect transistor for label-free femtomolar protein detection. *Biosensors and Bioelectronics* **41**, 621-626, doi:http://dx.doi.org/10.1016/j.bios.2012.09.040 (2013).

59 Chang, J. *et al.* Ultrasonic-assisted self-assembly of monolayer graphene oxide for rapid detection of Escherichia coli bacteria. *Nanoscale* **5**, 3620-3626, doi:10.1039/C3NR00141E (2013).

60 Zhang, H. *et al.* Graphitic carbon nitride nanosheets doped graphene oxide for electrochemical simultaneous determination of ascorbic acid, dopamine and uric acid. *Electrochimica Acta* **142**, 125-131, doi:http://dx.doi.org/10.1016/j.electacta.2014.07.094 (2014).

61 Robinson, J. T. *et al.* Ultrasmall Reduced Graphene Oxide with High Near-Infrared Absorbance for Photothermal Therapy. *Journal of the American Chemical Society* **133**, 6825-6831, doi:10.1021/ja2010175 (2011).

62 Akhavan, O., Ghaderi, E., Aghayee, S., Fereydooni, Y. & Talebi, A. The use of a glucose-reduced graphene oxide suspension for photothermal cancer therapy. *Journal of Materials Chemistry* **22**, 13773-13781, doi:10.1039/C2JM31396K (2012).

63 Lau, H. K. & Kiick, K. L. Opportunities for Multicomponent Hybrid Hydrogels in Biomedical Applications. *Biomacromolecules* (2015).

64 Song, P. *et al.* Striking multiple synergies created by combining reduced graphene oxides and carbon nanotubes for polymer nanocomposites. *Nanotechnology* **24**, 125704 (2013).

65 Song, P., Zhao, L., Cao, Z. & Fang, Z. Polypropylene nanocomposites based on C60-decorated carbon nanotubes: thermal properties, flammability, and mechanical properties. *Journal of Materials Chemistry* **21**, 7782-7788, doi:10.1039/C1JM10395D (2011).

66 Shin, M. K. *et al.* Synergistic toughening of composite fibres by self-alignment of reduced graphene oxide and carbon nanotubes. *Nat Commun* **3**, 650 (2012).

67 Song, P. a., Liu, L., Huang, G., Yu, Y. & Guo, Q. Largely enhanced thermal and mechanical properties of polymer nanocomposites via incorporating C 60 @graphene nanocarbon hybrid. *Nanotechnology* **24**, 505706 (2013).

68 Holmes, B., Fang, X., Zarate, A., Keidar, M. & Zhang, L. G. Enhanced human bone marrow mesenchymal stem cell chondrogenic differentiation in electrospun constructs with carbon nanomaterials. *Carbon* **97**, 1-13, doi:http://dx.doi.org/10.1016/j.carbon.2014.12.035 (2016).

69 Byun, J. Emerging Frontiers of Graphene in Biomedicine. *Journal of microbiology and biotechnology* **25**, 145-151 (2015).

70 Shen, H., Zhang, L., Liu, M. & Zhang, Z. Biomedical Applications of Graphene. *Theranostics* **2**, 283-294, doi:10.7150/thno.3642 (2012).

71 Carrow, J. K. & Gaharwar, A. K. Bioinspired Polymeric Nanocomposites for Regenerative Medicine. *Macromolecular Chemistry and Physics* **216**, 248-264, doi:10.1002/macp.201400427 (2015).

72 Gaharwar, A. K., Peppas, N. A. & Khademhosseini, A. Nanocomposite hydrogels for biomedical applications. *Biotechnology and Bioengineering* **111**, 441-453, doi:10.1002/bit.25160 (2014).

73 Xavier, J. R. *et al.* Bioactive Nanoengineered Hydrogels for Bone Tissue Engineering: A Growth-Factor-Free Approach. *ACS Nano*, doi:10.1021/nn507488s (2015).

74 Gaharwar, A. K. *et al.* Shear-Thinning Nanocomposite Hydrogels for the Treatment of Hemorrhage. *ACS Nano* **8**, 9833-9842, doi:10.1021/nn503719n (2014).

75 Gaharwar, A. K. *et al.* Bioactive Silicate Nanoplatelets for Osteogenic Differentiation of Human Mesenchymal Stem Cells. *Adv. Mater.* **25**, 3329-2226, doi:DOI: 10.1002/adma.201300584 (2013).

76 Mihaila, S. M. *et al.* The osteogenic differentiation of SSEA-4 sub-population of human adipose derived stem cells using silicate nanoplatelets. *Biomaterials* **35**, 9087-9099 (2014).

77 Xavier, J. R. *et al.* Bioactive Nanoengineered Hydrogels for Bone Tissue Engineering: A Growth-Factor-Free Approach. *ACS Nano* **DOI 10.1021/nn507488s** (2015).

78 Dan, L., Tao, W., Xinxing, L. & Zhen, T. Accelerated cell sheet detachment by copolymerizing hydrophilic PEG side chains into PNIPAm nanocomposite hydrogels. *Biomedical Materials* **7**, 055008 (2012).

79 Gaharwar, A. K., Schexnailder, P. J., Kline, B. P. & Schmidt, G. Assessment of using Laponite® cross-linked poly(ethylene oxide) for controlled cell adhesion and mineralization. *Acta Biomaterialia* **7**, 568-577, doi:http://dx.doi.org/10.1016/j.actbio.2010.09.015 (2011).

80 Schexnailder, P. J. *et al.* Tuning Cell Adhesion by Incorporation of Charged Silicate Nanoparticles as Cross-Linkers to Polyethylene Oxide. *Macromolecular bioscience* **10**, 1416-1423 (2010).

81 Gaharwar, A. K. *et al.* Physically Crosslinked Nanocomposites from Silicate-Crosslinked PEO: Mechanical Properties and Osteogenic Differentiation of Human Mesenchymal Stem Cells. *Macromolecular bioscience* **12**, 779-793 (2012).

82 Gaharwar, A. K. *et al.* Bioactive Silicate Nanoplatelets for Osteogenic Differentiation of Human Mesenchymal Stem Cells. *Advanced Materials* **25**, 3329-3336, doi:10.1002/adma.201300584 (2013).

83 Reffitt, D. *et al.* Orthosilicic acid stimulates collagen type 1 synthesis and osteoblastic differentiation in human osteoblast-like cells in vitro. *Bone* **32**, 127-135 (2003).

84 Gregory, C. A., Singh, H., Perry, A. S. & Prockop, D. J. The Wnt signaling inhibitor dickkopf-1 is required for reentry into the cell cycle of human adult stem cells from bone marrow. *Journal of Biological Chemistry* **278**, 28067-28078 (2003).

85 Luginbuehl, V., Meinel, L., Merkle, H. P. & Gander, B. Localized delivery of growth factors for bone repair. *European Journal of Pharmaceutics and Biopharmaceutics* **58**, 197-208, doi:http://dx.doi.org/10.1016/j.ejpb.2004.03.004 (2004).

86 Gonçalves, M. *et al.* Antitumor Efficacy of Doxorubicin-Loaded Laponite/Alginate Hybrid Hydrogels. *Macromolecular Bioscience* **14**, 110-120, doi:10.1002/mabi.201300241 (2014).

87 Li, K. *et al.* Enhanced In Vivo Antitumor Efficacy of Doxorubicin Encapsulated within Laponite Nanodisks. *ACS Applied Materials & Interfaces* **6**, 12328-12334, doi:10.1021/am502094a (2014).

88 Wu, Y. L. *et al.* Folic acid-modified laponite nanodisks for targeted anticancer drug delivery. *Journal of Materials Chemistry B* **2**, 7410-7418, doi:10.1039/c4tb01162g (2014).

89 Weng, Q. *et al.* Highly Water-Soluble, Porous, and Biocompatible Boron Nitrides for Anticancer Drug Delivery. *ACS Nano* **8**, 6123-6130, doi:10.1021/nn5014808 (2014).

90 Ma, R. & Sasaki, T. Nanosheets of Oxides and Hydroxides: Ultimate 2D Charge-Bearing Functional Crystallites. *Advanced Materials* **22**, 5082-5104, doi:10.1002/adma.201001722 (2010).

91 Khan, S. *et al.* Nanohybrid Based on Antibiotic Encapsulated Layered Double Hydroxide as a Drug Delivery System. *Appl Biochem Biotechnol*, 1-17, doi:10.1007/s12010-014-1211-9 (2014).

92 Bi, X., Fan, T. & Zhang, H. Novel Morphology-Controlled Hierarchical Core@Shell Structural Organo-Layered Double Hydroxides Magnetic Nanovehicles for Drug Release. *ACS Applied Materials & Interfaces* **6**, 20498-20509, doi:10.1021/am506113s (2014).

93 Rives, V., del Arco, M. & Martín, C. Intercalation of drugs in layered double hydroxides and their controlled release: A review. *Applied Clay Science* **88–89**, 239-269, doi:http://dx.doi.org/10.1016/j.clay.2013.12.002 (2014).

94 Saifullah, B. *et al.* Development of a biocompatible nanodelivery system for tuberculosis drugs based on isoniazid-Mg/Al layered double hydroxide. *International Journal of Nanomedicine* **9**, 4749-4762, doi:10.2147/IJN.S63608 (2014).

95 Ma, R., Wang, Z., Yan, L., Chen, X. & Zhu, G. Novel Pt-loaded layered double hydroxide nanoparticles for efficient and cancer-cell specific delivery of a cisplatin prodrug. *Journal of Materials Chemistry B* **2**, 4868-4875, doi:10.1039/C4TB00645C (2014).

96 Li, L., Gu, W., Chen, J., Chen, W. & Xu, Z. P. Co-delivery of siRNAs and anti-cancer drugs using layered double hydroxide nanoparticles. *Biomaterials* **35**, 3331-3339, doi:http://dx.doi.org/10.1016/j.biomaterials.2013.12.095 (2014).

97 Sun, W. *et al.* Electrochemical biosensor based on graphene, Mg2Al layered double hydroxide and hemoglobin composite. *Electrochimica Acta* **91**, 130-136, doi:http://dx.doi.org/10.1016/j.electacta.2012.12.088 (2013).

98 Liu, L.-M. *et al.* Hemoglobin/DNA/layered double hydroxide composites for biosensing applications. *Analytical Methods* **5**, 3565-3571, doi:10.1039/C3AY00038A (2013).

99 Shu, Y., Yin, P., Liang, B., Wang, H. & Guo, L. Bioinspired Design and Assembly of Layered Double Hydroxide/Poly(vinyl alcohol) Film with High Mechanical Performance. *ACS Applied Materials & Interfaces* **6**, 15154-15161, doi:10.1021/am503273a (2014).

100 Chakraborti, M., Jackson, J. K., Plackett, D., Brunette, D. M. & Burt, H. M. Drug intercalation in layered double hydroxide clay: Application in the development of a nanocomposite

film for guided tissue regeneration. *International Journal of Pharmaceutics* **416**, 305-313, doi:http://dx.doi.org/10.1016/j.ijpharm.2011.06.016 (2011).

101 Sorkin, V., Pan, H., Shi, H., Quek, S. Y. & Zhang, Y. W. Nanoscale Transition Metal Dichalcogenides: Structures, Properties, and Applications. *Critical Reviews in Solid State and Materials Sciences* **39**, 319-367, doi:10.1080/10408436.2013.863176 (2014).

102 Pumera, M. & Loo, A. H. Layered transition-metal dichalcogenides (MoS2 and WS2) for sensing and biosensing. *TrAC Trends in Analytical Chemistry* **61**, 49-53, doi:http://dx.doi.org/10.1016/j.trac.2014.05.009 (2014).

103 Liu, K., Feng, J., Kis, A. & Radenovic, A. Atomically Thin Molybdenum Disulfide Nanopores with High Sensitivity for DNA Translocation. *ACS Nano* **8**, 2504-2511, doi:10.1021/nn406102h (2014).

104 Branton, D. *et al.* The potential and challenges of nanopore sequencing. *Nat Biotech* **26**, 1146-1153 (2008).

105 Rong, M. *et al.* Fluorescence sensing of chromium (VI) and ascorbic acid using graphitic carbon nitride nanosheets as a fluorescent "switch". *Biosensors & bioelectronics* **68**, 210-217, doi:10.1016/j.bios.2014.12.024 (2015).

106 Ou, J. Z. *et al.* Ion-Driven Photoluminescence Modulation of Quasi-Two-Dimensional MoS2 Nanoflakes for Applications in Biological Systems. *Nano Letters* **14**, 857-863, doi:10.1021/nl4042356 (2014).

107 Sarkar, D. *et al.* MoS2 Field-Effect Transistor for Next-Generation Label-Free Biosensors. *ACS Nano* **8**, 3992-4003, doi:10.1021/nn5009148 (2014).

108 Lin, T. *et al.* Visual detection of blood glucose based on peroxidase-like activity of WS2 nanosheets. *Biosensors and Bioelectronics* **62**, 302-307, doi:http://dx.doi.org/10.1016/j.bios.2014.07.001 (2014).

109 Yong, Y. *et al.* WS2 nanosheet as a new photosensitizer carrier for combined photodynamic and photothermal therapy of cancer cells. *Nanoscale* **6**, 10394-10403, doi:10.1039/C4NR02453B (2014).

110 Wang, S. *et al.* Biocompatible PEGylated MoS2 nanosheets: Controllable bottom-up synthesis and highly efficient photothermal regression of tumor. *Biomaterials* **39**, 206-217, doi:http://dx.doi.org/10.1016/j.biomaterials.2014.11.009 (2015).

111 Chou, S. S. *et al.* Chemically Exfoliated MoS2 as Near-Infrared Photothermal Agents. *Angewandte Chemie* **125**, 4254-4258, doi:10.1002/ange.201209229 (2013).

112 Cheng, L. *et al.* PEGylated WS2 Nanosheets as a Multifunctional Theranostic Agent for in vivo Dual-Modal CT/Photoacoustic Imaging Guided Photothermal Therapy. *Advanced Materials* **26**, 1886-1893, doi:10.1002/adma.201304497 (2014).

113 Qian, X., Shen, S., Liu, T., Cheng, L. & Liu, Z. Two-dimensional TiS2 nanosheets for in vivo photoacoustic imaging and photothermal cancer therapy. *Nanoscale*, doi:10.1039/C5NR00893J (2015).

114 Sun, Z. *et al.* Generalized self-assembly of scalable two-dimensional transition metal oxide nanosheets. *Nat Commun* **5**, doi:10.1038/ncomms4813 (2014).

115 Wang, L. & Sasaki, T. Titanium Oxide Nanosheets: Graphene Analogues with Versatile Functionalities. *Chemical Reviews* **114**, 9455-9486, doi:10.1021/cr400627u (2014).

116 Osada, M. & Sasaki, T. Two-Dimensional Dielectric Nanosheets: Novel Nanoelectronics From Nanocrystal Building Blocks. *Advanced Materials* **24**, 210-228, doi:10.1002/adma.201103241 (2012).

117 Chen, Y. *et al.* Break-up of Two-Dimensional MnO2 Nanosheets Promotes Ultrasensitive pH-Triggered Theranostics of Cancer. *Advanced Materials* **26**, 7019-7026, doi:10.1002/adma.201402572 (2014).

118 Omomo, Y., Sasaki, T., Wang & Watanabe, M. Redoxable Nanosheet Crystallites of MnO2 Derived via Delamination of a Layered Manganese Oxide. *Journal of the American Chemical Society* **125**, 3568-3575, doi:10.1021/ja021364p (2003).

119 Ping, J. *et al.* Recent advances in aptasensors based on graphene and graphene-like nanomaterials. *Biosensors and Bioelectronics* **64**, 373-385 (2015).

120 Yuan, Y., Wu, S., Shu, F. & Liu, Z. An MnO2 nanosheet as a label-free nanoplatform for homogeneous biosensing. *Chemical Communications* **50**, 1095-1097, doi:10.1039/C3CC47755J (2014).

121 Deng, R., Xie, X., Vendrell, M., Chang, Y.-T. & Liu, X. Intracellular glutathione detection using MnO2-nanosheet-modified upconversion nanoparticles. *Journal of the American Chemical Society* **133**, 20168-20171 (2011).

122 Fei Yin, Z., Wu, L., Gui Yang, H. & Hua Su, Y. Recent progress in biomedical applications of titanium dioxide. *Physical Chemistry Chemical Physics* **15**, 4844-4858, doi:10.1039/C3CP43938K (2013).

123 Rajh, T., Dimitrijevic, N. M., Bissonnette, M., Koritarov, T. & Konda, V. Titanium Dioxide in the Service of the Biomedical Revolution. *Chemical Reviews* **114**, 10177-10216, doi:10.1021/cr500029g (2014).

124 Xiang, Q., Yu, J. & Jaroniec, M. Nitrogen and sulfur co-doped TiO 2 nanosheets with exposed {001} facets: synthesis, characterization and visible-light photocatalytic activity. *Physical Chemistry Chemical Physics* **13**, 4853-4861 (2011).

125 Elvira, G. *et al.* Targeting Neural Stem Cells with Titanium Dioxide Nanoparticles Coupled to Specific Monoclonal Antibodies. *Journal of Biomaterials Applications* **26**, 1069-1089, doi:10.1177/0885328210393294 (2012).

126 Liu, M. *et al.* An anisotropic hydrogel with electrostatic repulsion between cofacially aligned nanosheets. *Nature* **517**, 68-72, doi:10.1038/nature14060 http://www.nature.com/nature/journal/v517/n7532/abs/nature14060.html - supplementary-information (2015).

127 Liu, C. G., Wu, X. T., Li, X. F. & Zhang, X. G. Synthesis of graphene-like g-C3N4/Fe3O4 nanocomposites with high photocatalytic activity and applications in drug delivery. *RSC Advances* **4**, 62492-62498, doi:10.1039/C4RA10616D (2014).

128 Zhang, X. *et al.* Enhanced Photoresponsive Ultrathin Graphitic-Phase C3N4 Nanosheets for Bioimaging. *Journal of the American Chemical Society* **135**, 18-21, doi:10.1021/ja308249k (2012).

129 Zhang, X. *et al.* Single-Layered Graphitic-C3N4 Quantum Dots for Two-Photon Fluorescence Imaging of Cellular Nucleus. *Advanced Materials* **26**, 4438-4443, doi:10.1002/adma.201400111 (2014).

130 Lin, L.-S. *et al.* Graphitic-phase C3N4 nanosheets as efficient photosensitizers and pH-responsive drug nanocarriers for cancer imaging and therapy. *Journal of Materials Chemistry B* **2**, 1031-1037, doi:10.1039/C3TB21479F (2014).

131 Lin, T. *et al.* Graphite-like carbon nitrides as peroxidase mimetics and their applications to glucose detection. *Biosensors and Bioelectronics* **59**, 89-93, doi:http://dx.doi.org/10.1016/j.bios.2014.03.023 (2014).

132 Ma, T. Y., Tang, Y., Dai, S. & Qiao, S. Z. Proton-Functionalized Two-Dimensional Graphitic Carbon Nitride Nanosheet: An Excellent Metal-/Label-Free Biosensing Platform. *Small* **10**, 2382-2389, doi:10.1002/smll.201303827 (2014).

133 Lin, Y. & Connell, J. W. Advances in 2D boron nitride nanostructures: nanosheets, nanoribbons, nanomeshes, and hybrids with graphene. *Nanoscale* **4**, 6908-6939, doi:10.1039/c2nr32201c (2012).

134 Wang, J., Zhao, R., Liu, Z. & Liu, Z. Widely tunable carrier mobility of boron nitride-embedded graphene. *Small* **9**, 1373-1378, doi:10.1002/smll.201202978 (2013).

135 Peng, Q., Ji, W. & De, S. Mechanical properties of the hexagonal boron nitride monolayer: Ab initio study. *Computational Materials Science* **56**, 11-17, doi:http://dx.doi.org/10.1016/j.commatsci.2011.12.029 (2012).

136 Biscarat, J., Bechelany, M., Pochat-Bohatier, C. & Miele, P. Graphene-like BN/gelatin nanobiocomposites for gas barrier applications. *Nanoscale* **7**, 613-618, doi:10.1039/C4NR05268D (2015).

137 Lei, W., Liu, D., Qin, S., Portehault, D. & Chen, Y. I. Boron (Carbon) nitride nanomaterials. *Nanotubes and Nanosheets: Functionalization and Applications of Boron Nitride and Other Nanomaterials*, 59 (2015).

138 Peng, J. *et al.* Fabrication of graphene quantum dots and hexagonal boron nitride nanocomposites for fluorescent cell imaging. *Journal of biomedical nanotechnology* **9**, 1679-1685 (2013).

139 Li, X. *et al.* Boron nitride nanotube-enhanced osteogenic differentiation of mesenchymal stem cells. *Journal of Biomedical Materials Research Part B: Applied Biomaterials*, n/a-n/a, doi:10.1002/jbm.b.33391 (2015).

140 Meng, W., Huang, Y., Fu, Y., Wang, Z. & Zhi, C. Polymer composites of boron nitride nanotubes and nanosheets. *Journal of Materials Chemistry C* **2**, 10049-10061 (2014).

141 Balendhran, S., Walia, S., Nili, H., Sriram, S. & Bhaskaran, M. Elemental Analogues of Graphene: Silicene, Germanene, Stanene, and Phosphorene. *Small* **11**, 640-652, doi:10.1002/smll.201402041 (2015).

142 Dávila, M. E., Xian, L., Cahangirov, S., Rubio, A. & Lay, G. L. Germanene: a novel two-dimensional germanium allotrope akin to graphene and silicene. *New Journal of Physics* **16**, 095002 (2014).

143 Roome, N. J. & Carey, J. D. Beyond Graphene: Stable Elemental Monolayers of Silicene and Germanene. *ACS applied materials & interfaces* **6**, 7743-7750 (2014).

144 Jose, D. & Datta, A. Structures and chemical properties of silicene: unlike graphene. *Accounts of chemical research* **47**, 593-602 (2013).

145 Tasciotti, E. *et al.* Mesoporous silicon particles as a multistage delivery system for imaging and therapeutic applications. *Nat Nano* **3**, 151-157 (2008).

146 Serda, R. E., Godin, B., Blanco, E., Chiappini, C. & Ferrari, M. Multi-stage delivery nano-particle systems for therapeutic applications. *Biochimica et Biophysica Acta (BBA) - General Subjects* **1810**, 317-329 (2011).

147 Song, P. a. *et al.* Striking multiple synergies created by combining reduced graphene oxides and carbon nanotubes for polymer nanocomposites. *Nanotechnology* **24**, 125704 (2013).

148 Zhao, M.-Q., Zhang, Q., Huang, J.-Q. & Wei, F. Hierarchical Nanocomposites Derived from Nanocarbons and Layered Double Hydroxides - Properties, Synthesis, and Applications. *Advanced Functional Materials* **22**, 675-694, doi:10.1002/adfm.201102222 (2012).

CHAPTER 4: HYDROGEL BIOINK REINFORCEMENT FOR ADDITIVE MANUFACTURING: A FOCUSED REVIEW OF EMERGING STRATEGIES[‡]

4.1 Overview

Bioprinting is an emerging approach for fabricating cell-laden 3D scaffolds. Bioprinting enables robotic deposition of cells and materials into custom shapes and patterns to replicate complex tissue architectures. Bioprinting uses hydrogel solutions called bioinks as both cell carriers and structural components, requiring bioinks to be highly printable while providing a robust and cell-friendly scaffold. Unfortunately, conventional hydrogel bioinks have not been able to meet these requirements. While conventional hydrogels bioinks are relatively weak due to their heterogeneously crosslinked networks and lack of energy dissipation mechanisms, their mechanical properties can be significantly improved by designing energy dissipation mechanisms into their structures. Advanced bioink designs using various methods of dissipating mechanical energy are aimed at developing next-generation cellularized 3D scaffolds to mimic anatomical size, tissue architecture, and tissue specific functions. These next-generation bioinks need to have high print fidelity and provide and a biocompatible microenvironment along with improved mechanical properties. To design these advanced bioink formulations, it is important to understand the structure-property-function relationships of the hydrogel network. By specifically leveraging biophysical and biochemical characteristics of hydrogel networks, high performance bioinks can

[‡] Reprinted with permission from D. Chimene, R. Kaunas, A. K. Gaharwar, Hydrogel Bioink Reinforcement for Additive Manufacturing: A Focused Review of Emerging Strategies. *Advanced Materials* **0**, 1902026 (2019).

be designed to control and direct cell functions. In this review article, we will critically evaluate current and emerging approaches in hydrogel design and bioink reinforcement techniques used to design the next generation of inks. This bottom-up perspective provides a materials-centric approach to bioink design for 3D bioprinting.

4.2 Introduction

4.2.1 The Rise of 3D Bioprinting

3D printing was first made a reality in the 1980's when Charles Hull developed stereolithography, a technique for converting 3D computer design files into physical objects by projecting a series of light patterns into a pool of photopolymers.(202) This development was quickly followed by the emergence of other 3D fabrication strategies, including fused deposition modeling (FDM) in 1989, which builds objects by precisely depositing successive layers of molten thermoplastic using a mobile heated nozzle.(203) FDM has evolved to become the most popular 3D printing technique due to its low cost and accessibility, and has experienced a rapid explosion in popularity since its patent expiration in 2009. Since then, open source designs like RepRap printers ("Replicating Rapid-Prototyper"), which can 3D print many of their own components, have dramatically driven down printer costs from the tens of thousands of dollars to fewer than 200 dollars. This has brought the technology into the hands of millions of hobbyists and academics alike.(204, 205) The widespread adoption of 3D printing technology has led to its application to new fields, including regenerative medicine. 3D printers are being commercialized to rapidly create custom prosthetics for patients and to precisely replicate patient anatomy to allow surgeons to simulate procedures with 3D printed body parts. Most recently, 3D printing has been adopted for tissue engineering with the goal of developing highly customized cell-laden scaffolds to enable

healthy human tissue to be re-grown from a patient's own stem cells. This technique of 3D printing living cells is called 3D bioprinting.(205, 206)

3D bioprinting can localize different cell types and materials to mimic the anatomical complexity of tissues and organs.(207, 208) However, 3D bioprinting living cells requires a very specific set of conditions that are best met with a different class of materials: hydrogels. For example, cells require an aqueous environment to live, and need sufficient oxygen and nutrient diffusion, as well as appropriate pH and osmolarity along with key vitamins and minerals for cellular functions. Certain cell types require specific cell attachment sites and substrate properties in order to proliferate. Finally, cells must have room to create new extracellular matrix (ECM). This means that printed materials should degrade into nontoxic components over time to promote neo tissue formation.(204, 206, 209)

4.2.2 Conventional Hydrogel Bioinks and Their Limitations

Hydrogels are able to meet these stringent requirements and are the basis of almost all bioink formulations. Hydrogels are loosely crosslinked networks of highly hydrophilic polymers that can absorb many times their dry weight in water, generally ranging from 70% to over 99% water content. This high water content makes hydrogels highly porous and permeable, allowing rapid diffusion of oxygen and nutrients throughout the scaffold.(206, 209) Many hydrogels are also porous enough to allow cell migration, and some are also degradable, providing initial support for cells, then degrading away as cell populations grow and remodel their surroundings. Hydrogels can also be created from proteins and extracellular matrix components, including collagen and

hyaluronic acid, providing environmental cues to help direct stem cell growth. Finally, many hydrogels can be crosslinked into solid viscoelastic structures using cell-friendly methods, which are not damaging to living cells and minimize physiological stress on printed cells encapsulated within the scaffold. These characteristics allow hydrogels to closely mimic the native microenvironment of cells, making them the nearly-universal choice for 3D bioprinting.(7, 9, 24, 209)

Conventional hydrogels are the randomly crosslinked, single network hydrogels with no internal mechanism for mechanical energy dissipation which make up the majority of hydrogels used in biomedical research. While conventional hydrogels are inherently suited for cell growth, they lack mechanical properties needed for optimal 3D printing. Adapting them to 3D printing has therefore proven to be a consistent challenge to the field. Prior to crosslinking, hydrogels are typically liquid polymer solutions, making it impossible to support subsequent layers. Many conventional hydrogels crosslink too slowly or remain too weak to be practical for structures taller than a few millimeters. Hydrogel networks are conventionally strengthened by increasing their polymer content and crosslink density, however, increased polymer content and dense crosslinks interfere with cell culture by reducing the permeability and porosity that cells require. Crosslinks also form randomly in conventional hydrogels, causing variations in crosslink density that concentrate stress on the least extensible chains under deformation.(24, 206, 209) These factors make conventional hydrogel reinforcement undesirable in bioinks.

This required compromise between biocompatibility and printability properties to make acceptable bioinks is often thought of as a biofabrication window. However, new approaches are

being developed to improve the biofabrication window by efficiently strengthening hydrogels while retaining favorable biological properties **(Figure 4-1a)**. The most popular techniques include polymer functionalization, interpenetrating networks, nanocomposites, supramolecular bioinks, and thermoplastic reinforcement. While multiple reviews of bioinks currently exist, they lack a mechanistic approach to structure-property-function relationships in bioinks.(24, 206, 209)

The bioink reinforcement techniques discussed in this review exhibit enhanced performance brought about by distinct network structures, but they also share some fundamental traits. A general principle for tough hydrogels is that they can relax stress concentrations and dissipate mechanical energy, increasing the energy required before cracks form and propagate. This is important for bioink reinforcement because it means fracture energy depends not just on the energy needed to break the polymer chains in a propagating crack's path, but also on the amount of mechanical energy that the surrounding region can dissipate. Bioink literature does not always report fracture energy, so we discuss available mechanical measures when necessary.

Bioinks assume multiple functions key to bioprinting success, many of which are interrelated through properties affecting the hydrogel structure. However, existing literature hasn't adequately explored these relationships. In this review, we bridge this literary gap by examining the relationships between a bioink's hydrogel structure, properties, and function. We critically examine how the fundamental concepts of hydrogel network structures relate to the mechanical, rheological, and biological properties that are critical to bioprinting success. Then we discuss specific emerging bioink reinforcement mechanisms and their effects on key bioink properties. Finally, we evaluate promising approaches to next-generation bioink designs. Understanding the

fundamental mechanisms of hydrogel reinforcement and how they can be applied to design advanced bioinks will provide an in-depth understanding of trends emerging in the development of high performance bioinks.

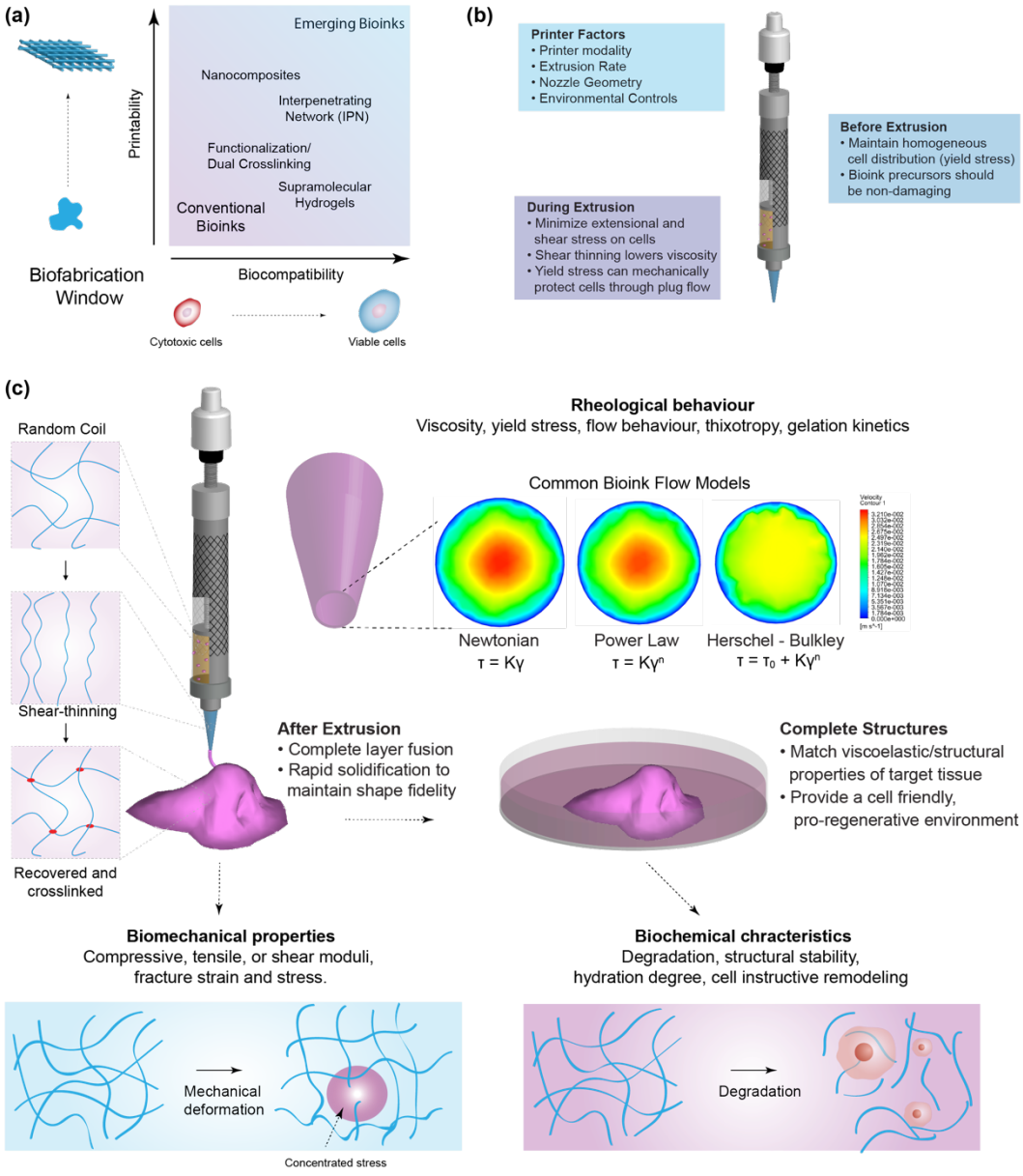

Figure 4-1. Hydrogel bioink design considerations for reinforcement approaches. (a) The biofabrication window depicts the compromise between printability and biocompatibility

needed to make acceptable bioinks. Emerging bioink reinforcement techniques improve fabrication while maintaining biocompatibility. (b) Bioink considerations at different fabrication stages. A range of printing factors can determine success or failure of a bioprint. (c) The rheological, biomechanical, and biochemical characteristics of bioinks play major roles in extrusion bioprinting. The structural and mechanical properties of a bioink are key metrics of its performance at both the macro and micro scale, influencing everything from structural integrity to biomechanical and biochemical cellular interactions. Mechanical reinforcement also significantly affects a bioink's 3D printability by altering its flow properties. The most common bioink flow models include Newtonian, Power Law, and Herschel-Bulkley fluids. Bioink flow properties significantly alter flow velocity profiles during printing and determine the amount of stress that encapsulated cells experience during the printing process, and also impact 3D printability through viscoelastic behavior after extrusion.

4.3 Bioink characteristics

The cell-friendly nature of hydrogels has made them the material of choice for printing 3D cell constructs.(9, 210, 211) Hydrogels consist of highly hydrophilic polymer networks that can absorb many times their own weight in water. They are used in a wide range of commercial products, ranging from baking and food additives to medical devices. Hydrogel networks can be held together in their solid state by physical and/or covalent interactions called crosslinks. The mechanical properties of these crosslinked networks are determined by complex interactions

between the polymer network structure and aqueous components. Before hydrogels form crosslinks, they exist as polymer solutions that can have fluid-like properties (also known as sols) that depend on their composition. This is typically the state of a bioink during extrusion (**Figure 4-1b**). Controlling both the non-crosslinked solution (bioink) fluid properties and the crosslinked hydrogel (structure or, when bioprinted, scaffold) mechanical properties is a major focus of bioprinting research.

In this section we will review key rheological, structural, biomechanical, and biochemical properties of bioinks, and discuss how they are related to bioink performance. It is important to recognize that these properties are interrelated in complex ways that must be considered when optimizing bioink performance. As research on bioinks has progressed, certain factors in each of these areas have been widely identified as critical to bioink performance (e.g. shear thinning, elastic modulus); others are still being evaluated (e.g. shear recovery, stress relaxation). While many of these factors are not consistently reported in bioprinting literature, they are nevertheless beneficial to consider when evaluating bioink designs.

4.3.1 Hydrogel Bioink Network and Design Parameters

We begin by describing the fundamental mechanics of hydrogel networks to better contextualize discussions of reinforcement strategies in later sections.(212-216) Polymer networks have been widely used in engineering since the 1840s, when Charles Goodyear developed the first elastomers through rubber vulcanization. The vulcanization process crosslinks the network to prevent polymer

chains from flowing, effectively solidifying the rubber across a wide range of temperatures. Elastomers remain the most widely used polymer networks today, with applications ranging from tires to disposable surgical gloves.(4) In contrast, the history of hydrogel polymer networks is much shorter and intimately tied to biomedical engineering. Synthetic hydrogels were first engineered in the 1950s when hydroxyethyl methacrylate was developed as a contact lens material, and their potential for mimicking the body's natural environment was quickly investigated.(8) The range of biomedical applications involving hydrogels quickly expanded to include burn treatments, drug delivery, cosmetics, and implants.(9-11) Hydrogel research has grown exponentially over the past few years due to their application to regenerative medicine and bioprinting.(9, 10) Like elastomers, hydrogels are essentially an aqueous polymer chains whose flow is prevented by crosslinks that provide elastic strength.(4)

4.3.2 Soft Network Basics

Classical polymer networks are mainly formed in two ways: by simultaneous polymerization and crosslinking of a monomer solution, and by crosslinking existing polymer chains together. Both methods generally create randomly-crosslinked, heterogeneous networks containing both densely and sparsely crosslinked regions.(212) Upon loading, this heterogeneity leads to localized stress concentrations that form weaker failure zones in the polymer network. Thus, the distribution of crosslinks is a key determinant to polymer network mechanical properties. Individual polymer chains behave like entropic springs whose elasticity is dependent on their configurational degrees of freedom. While crosslinking increases the number of polymer chains in a network, the individual chains become shorter, thus lowering configurational entropy and creating a stiffer and more brittle network.(212) The energy required to break a polymer chain is proportional to its

length. Shorter polymer chains also constrain the extensibility of the network. The overall impacts of these competing effects of crosslinking are increases tensile strength at the price of reduced threshold fracture energy.(217) In other words, extensive crosslinking makes conventional hydrogels stiff and brittle while loosely crosslinked hydrogels are softer but relatively tough.(213, 215) Thus, while crosslinks are vital to polymer network structure, increased crosslinking leads to a random, heterogeneous network structure and rapidly decreases extensibility, causing brittleness and adversely affecting mechanical reinforcement.(212, 216, 217)

4.3.3 Fracture Energy and Energy Dissipation

Current bioink literature often characterizes gels with just a few mechanical parameters, such as fracture strain and stress, and compressive, tensile, or shear moduli. These parameters are important, but only partially describe the mechanical properties of a hydrogel. A parameter that is particularly useful for comparing overall mechanical properties in polymer networks is fracture energy, alternatively referred to as tearing energy or critical strain energy release rate.(216) Fracture energy describes the amount of energy required to perpetuate a fracture through the network. It is defined as the energy required to create a unit area of crack growth ($J\ m^{-2}$).(213, 214, 217) Fracture energy is an attractive metric because it is an intrinsic material property that is independent of geometry and is thus generally consistent across different test methods.

In polymer networks, fracture energy ($\Gamma(v)$) can be divided into two components according to its governing equation (Equation 1):(212)

$\Gamma(v) = \Gamma_0(1 + \varphi(a_T v))$, alternatively written as $\Gamma = \Gamma_0 + \Gamma_D$

Equation. 1

Where, $\Gamma_0 = N_x U_b \Sigma$ and $\Gamma_D = \Gamma_0 \varphi(a_T v)$

The first component, the threshold (or intrinsic) fracture energy (Γ_0), is defined as the amount of energy required to break the polymer chains per unit area of the crack plane as it propagates. The required energy depends on the density of polymer chains crossing the crack plane (Σ), the number of bonds in those polymer chains (N_x), and the energy to break each bond (U_b).(212, 213) This energy is local to the area of crack plane path and does not depend on surrounding bulk material. The density of polymer chains in hydrogels is proportional to their volume fraction, giving them a much lower intrinsic fracture energy (~10 J m^{-2}) relative to dry networks (~50-100 J m^{-2}).(213, 216)

The second component can be thought of as viscoelastic mechanical energy (Γ_D) dissipated into the surrounding network. Γ_D scales linearly with Γ_0, where $\varphi(a_T v)$ is a mechanical dissipation factor that is velocity-and-temperature-dependent and is characteristic of the material.(218) The scaling factor $\varphi(a_T v)$ shows a Power Law dependence on crack velocity, so rapid crack propagation requires significantly more energy than gradual crack expansion.(212) Furthermore, Γ_D depends on the bulk properties of the material in the region surrounding the crack. In tough polymer networks, Γ_D can contribute dramatically more to the total fracture energy than Γ_0.(219) For elastomers, the most important mechanism of mechanical energy dissipation is through molecular

friction between polymer chains as they translate and rearrange in response to applied stress. Conventional hydrogel networks lack this internal friction mechanism due to the large amount of water between polymer chains, thus leading to rapid crack propagation.(212, 213, 217)

In summary, hydrogels share many structural similarities with other soft polymer networks, but their hydrated structure causes their mechanical properties to differ in key ways. In all soft polymer networks, intrinsic fracture energy (Γ_0) depends on the length, number, and bond strength of polymer chains in the crack plane. Crosslinking increases elastic modulus and tensile strength, but reduces fracture energy and extensibility.(217) The low chain density in hydrogels reduces the intrinsic fracture energy (Γ_0) in proportion to polymer volume fraction, and functionally eliminates mechanical energy dissipation (Γ_D) through molecular friction. Together, these severely constrain the mechanical properties of conventional hydrogels.(212)

Fortunately, understanding these structural limitations also provides us with a clear pathway for improving the mechanical properties of hydrogel bioinks by designing novel mechanical energy dissipation mechanisms into the bioink network structure. Incorporating new mechanisms for dissipation can dramatically improve hydrogel stiffness, failure stress, and fracture energy by as many as three orders of magnitude while maintaining a highly extensible network.(214) It is important to recognize that much of the emerging bioink reinforcement technology maintains this common theme: incorporating mechanical energy dissipation (Γ_D) into the hydrogel structure, while maintaining high printability and a cell-friendly environment. Interpenetrating networks, nanocomposites, supramolecular bioinks, and composite bioinks all share this theme. Intrinsic

fracture energy (Γ_0) is also improved by increasing crosslink stability (functionalization) and/or improving network homogeneity (click reactions and sliding crosslinks).(212, 213)

4.3.4 Rheological Characteristics of Bioinks and Flow Modeling

While the effects of mechanical reinforcement on flow properties are often underappreciated, bioink reinforcement cannot be completely understood without also considering these effects. (220-222) During extrusion, bioinks are typically non-crosslinked polymer solutions or even pre-polymer solutions. In this section, we discuss the flow characteristics of bioink solutions that determine printability, including viscosity, shear thinning, thixotropy, thermal gelation, and yield stress. We also outline the impact that bioink reinforcement can have on these properties, as well as discuss flow models that help characterize these effects **(Figure 4-1)**.

The viscosity of a bioink is a key characteristic in determining its flow behavior and is among the most commonly measured values during the bioink optimization process. Viscosity can have mixed effects on bioink performance. High viscosity allows extruded bioink to better hold its shape and improves mechanical stability, which is especially beneficial in printing taller structures. However, higher viscosity increases shear stress during printing, which can damage cells by directly disrupting cell membranes and can reduce proliferation in surviving cells. This effect is dependent on cell type and density, as well as the level and duration of shear stresses to which cells are exposed.(7) Further, the relatively high resistance to flow can cause the extruder to clog, which contributes to inconsistent ink deposition. Conversely, low viscosity can reduce bioink printability and cause inhomogeneous cell distribution and rapid cell sedimentation.(12, 13)

Changes in bioink concentration, polymer molecular weight, ion content, temperature, and encapsulated cell density will directly influence bioink viscosity. Thus, all reinforcement techniques are likely to impact viscosity.

4.3.5 The Newtonian Model

Bioinks that maintain a consistent viscosity over the range of expected print conditions are often modeled using a Newtonian fluid model **(Figure 4-1c)**, where shear rate (γ) is equal to shear stress (τ) divided by viscosity (K). However, this behavior is mostly seen in bioinks with low polymer concentrations, where viscosity is dominated by small, isotropic molecules, or at very low shear rates where Brownian motion can prevent polymer alignment.(209, 223) In practice, most bioinks used in extrusion 3D printing are non-Newtonian, meaning that their apparent viscosity depends on shear rate or deformation history. Non-Newtonian effects are generally caused by reorientation of large polymer chains and disruption of electrostatic interactions, which are common features of reinforced bioinks.(224)

4.3.6 The Power Law Model

In shear-thinning bioinks, increasing shear rates force polymer chains to align along the flow direction, which reduces apparent viscosity. The disruption of electrostatic interactions at higher shear rates also decreases apparent viscosity. Shear-thinning properties are beneficial in bioprinting because they combine the high print fidelity of viscous bioinks with high cell viability due to low shear stresses experienced during the bioprinting process. Shear-thinning is more

apparent in high molecular weight polymers and at higher polymer concentrations.(209) The simplest method for modeling shear thinning behavior is with the Power Law relationship **(Figure 4-1c)**, where shear stress (τ) is related to shear rate (γ) by the flow behavior index (n) and consistency index (K), which is the viscosity at 1 s^{-1} shear rate. In this model, n=1 for Newtonian fluids, while n values <1 would be progressively more shear thinning. The Power Law model is useful and simple to use for many bioinks under printing conditions.(222)

4.3.7 The Herschel Bulkley Model

In addition, many non-Newtonian bioinks demonstrate viscoelastic properties like yield stress, which can significantly affect flow behavior. Yield stress is the minimum stress needed to initiate flow. Until shear stress exceeds the yield stress, the bioink behaves like a solid.(209, 225) Print fidelity and mechanical integrity are improved by yield stress because the bioink remains solid-like indefinitely after extrusion, even without crosslinking. Additionally, it can shield encapsulated cells from shear forces during extrusion by creating plug flow in the center of the flow profile, thus shearing is confined to a narrow region along the extruder walls. (211, 222, 225) Very high yield stress can make bioinks difficult to work with. For example, high yield stress interferes with standard pipetting and cell dispersion techniques, requiring alternatives like syringes and manual mixing to be used instead.(211, 220) Yield stress behavior in hydrogels is caused by non-covalent and electrostatic interactions, which are frequently a feature of bioink reinforcement. Changes in yield stress have been noted in a range of bioinks, and have been credited with improving bioink printability and cell survival.(211, 220) To account for yield stress, a Herschel-Bulkley model is often employed **(Figure 4-1c)**, which is similar to a Power Law model with an additional term (τ_0)

for the yield stress, below which the bioink is assumed to behave as a solid. The Herschel-Bulkley fluid model can accurately map the behavior of non-Newtonian fluids exhibiting shear thinning and yield stress, and has been adopted for bioink modeling in several recent reports.(211, 221, 226)

4.3.8 Carreau equation

More complex models can be used for characterizing bioink behavior as well, including the Carreau equation, which is particularly useful for describing different flow behaviors of bioinks at very low and high shear rates. Fluids are treated as Newtonian fluids with constant viscosity when shear rates are too low to overcome the random motion orientation of polymer chains, and as Power Law fluids at intermediate shear rates. At higher shear rates, the fluids become Newtonian again as they reach their infinite shear rate viscosity. This model was recently used to characterize the flow behavior of a polylactide (PLA) microfiber-reinforced alginate bioink.(223, 227)

4.3.9 Limitations of Existing Flow Models

While existing flow models can help predict bioink behavior during printing, shear recovery becomes important after extrusion but is not accounted for in these models.(222) When shear thinning bioinks are deposited after extrusion, their viscosity does not recover instantaneously.(228) Recent papers have demonstrated that rapid shear recovery improves print fidelity by quickly locking extruded bioink in place.(211, 222, 229-231) Thermoresponsive materials can assist shear recovery by solidifying bioinks in response to a temperature change, which can be exploited to quickly recover viscosity and storage modulus well above their initial

values.(211, 220) This effect is particularly evident when bioprinting taller structures where lower layers soon bear the weight of overlying filaments.(211, 231-233) This property can be characterized by designing peak-hold experiments to mimic the shear-deformation and recovery of bioink during the printing process.(232)

Overall, current flow models are very useful for screening potential bioinks in conjunction with practical experiments. While optimal flow properties vary with experimental goals and print conditions, emerging research indicates that shear thinning, yield stress, and rapid shear recovery are key determinants of bioink printability.(211, 220, 222, 231) These properties are important for successfully bioprinting large-scale, freestanding scaffolds with challenging geometries, including structures with high aspect ratios and overhangs.(211, 231-233) Mechanical reinforcement is key to creating next generation bioinks, but there is still little data on its effects on print performance interactions. Future bioink reinforcement papers can help address this knowledge gap by publishing these rheological properties along with their other experimental results. Current bioink flow models are sufficiently accurate for describing bioink behavior under expected conditions, but do not account for more complex non-Newtonian behaviors like time-dependent effects, thermosensitivity, and wall-slip effects.(222, 225, 226, 234) As bioinks become increasingly complex, more elaborate models should be adopted to more faithfully describe bioink behavior. Rheology and flow modeling are powerful tools to provide scientists a better understanding of the behavior of newly developed bioinks.

4.3.10 Biomechanical properties of bioinks

Due to their high water content, hydrogels used in tissue engineering are softer than many biomaterials, ranging from an elastic modulus <1 kPa for soft collagen gels to >1 mPa for reinforced double network hydrogels. A desired stiffness is typically achieved by tailoring polymer selection and increasing polymer mass fraction, crosslink density, and molecular weight.(235, 236) However, increasing these features generally interferes with the microarchitecture and cytocompatibility of the hydrogels. For example, densely crosslinked hydrogels form stiff structures, but cells become trapped in the network, preventing them from thriving by limiting nutrient diffusion and restricting space for migration and proliferation. Dense crosslinks also limit flexibility and extensibility of the printed scaffold.(206, 209)

4.3.11 Macroscopic Requirements

The mechanical properties of a bioink are crucial to its performance on both the macro and micro scale **(Figure 4-1c)**. Macroscopically, the eventual goal of bioprinted tissue constructs is implantation into the body, which requires a minimum level of mechanical properties difficult for many bioinks to attain. The ideal mechanical properties of an implant should match those of the target tissue, including stiffness, viscoelasticity, and yield stress/strain. For example, soft tissue implants need to sustain similar levels of compression to the surrounding tissue without failing or separating from surrounding tissue. Especially in bioprinting, hydrogels must also be able to mechanically support themselves after extrusion without significant sagging or deformation,

which can interfere with layer-on-layer deposition. A bioink's ability to self-support depends on both its mechanical and rheological properties, as well as crosslinking kinetics.

4.3.12 Cell-scale Biomechanics

Beyond these macroscopic considerations, the mechanical properties of hydrogels also play an important role in the success or failure of tissue regeneration. For example, elastic modulus (or stiffness) profoundly influences the behavior of encapsulated cells, such as the matrix stiffness-dependent differentiation of mesenchymal stem cells (MSC).(237, 238) Matrix stiffness also plays a key role in tissue repair processes by helping guide fibroblasts and MSCs towards injured tissue and modulating cell proliferation rates.(236) While matrix stiffness has been the primary focus among studies evaluating the effects of mechanical properties on cell-laden scaffolds, emerging research suggests that more complex viscoelastic properties also significantly direct cell behavior. The viscoelasticity of native extracellular matrix plays an important role in regulating cell behavior, and viscoelasticity in hydrogel scaffolds is being likewise recognized for its influence on cell spreading, proliferation, and differentiation. For example, viscoelastic hydrogels demonstrating stress relaxation have been shown to encourage myoblast proliferation even on softer hydrogels when compared to purely elastic hydrogels.(239) Similarly, rapid stress relaxation increases proliferation, spreading, and osteogenic differentiation of MSCs.(240, 241)

4.3.13 Extrinsic Mechanical Cues

Extrinsic mechanical signals can also act as biomechanical cues in hydrogels through a process called mechanotransduction.(53, 242) Dynamic cyclic 10% compression of MSCs has been shown to promote chondrogenesis, and dynamic deformation has also been shown to induce cell alignment.(243) To complicate matters, cell-material interactions and the intrinsic mechanical properties discussed above can modulate the way cells experience external cues. Timing and duration of mechanical signals can also determine differentiation.(242) The direction and extent of MSC alignment in response to static and cyclic strain is highly dependent on matrix stiffness.(244) Mechanobiology is a quickly growing body of research, but not all research in the area can be applied to bioprinting: 3D cell encapsulation provides a much more complex environment than 2D seeding, and can evoke radically different responses.(241, 245) Currently, research on cells encapsulated in hydrogel bioinks focuses primarily on matrix stiffness and viscoelasticity, although this may change as more is learned on this topic.(53, 241-243, 245, 246)

The structural and biomechanical properties of hydrogel scaffolds are closely related, and structural properties likewise play an important role in determining cell behavior. Pore size and interconnectivity, isotropy, and degradability are all important determinants of cell behavior.(236) Small pore sizes prevent cell migration and reduce nutrient diffusion, while larger pores generally encourage cell migration and proliferation, but decrease mechanical properties. Isotropic features like aligned fibers or pores can also direct cell migration within scaffolds.(247) Finally, biodegradability is also an important consideration, since cells require more space to grow as they progressively generate new tissue, as we discuss below.(246)

4.3.14 Stability and biochemical interactions of bioinks

The biochemical environment of a hydrogel is related to biomechanical properties: the biomechanical environment provides cues for cell behavior, and biochemistry can affect the way encapsulated cells respond to these cues **(Figure 4-1c)**. For example, cells can sense matrix stiffness through integrin proteins, so hydrogels without integrin binding sites diminish cell responses to matrix stiffness.(238, 248) Additionally, hydrogel biodegradation is an important factor in hydrogel design. Degradability is desirable in many applications where the hydrogel is meant to be replaced with functional tissue over time. In these instances, the degradation rate should be coupled to the rate of tissue generation to optimize tissue regrowth. Some materials, like peptides, can be enzymatically degraded by cell enzymes that break down extracellular matrix. Other materials, including some polysaccharide networks, degrade through ion exchange that disrupts ionic crosslinks in the hydrogel. Even typically non-degradable polymers, like poly(ethylene glycol) (PEG), can be made to degrade through introduction of hydrolytically sensitive moieties.(249) Overall, the mechanical, structural, and biochemical characteristics of a hydrogel bioink are an important consideration in tissue engineering, and it is important to note that the reinforcement techniques we discuss in this review affect mechanical properties beyond elastic modulus, and research in this area is rapidly developing.(236, 240, 242, 248, 250)

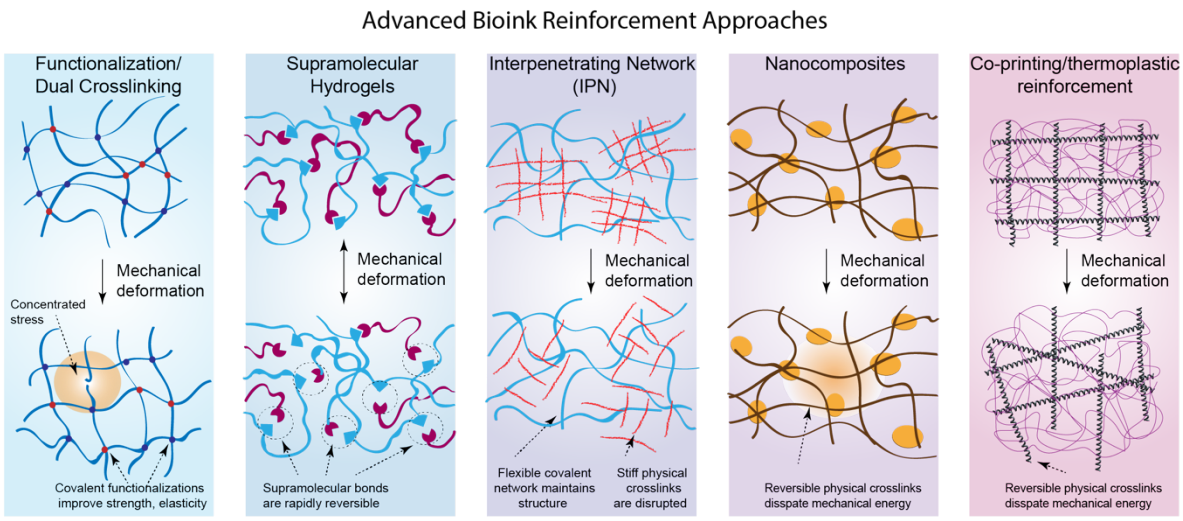

Figure 4-2. Overview of mechanical reinforcement techniques. Conventional bioinks are typically randomly crosslinked single networks. Established techniques for mechanically reinforcing bioinks include polymer functionalization, supramolecular networks, ionic-covalent entanglement (ICE), nanocomposite based bioink, and co-printing/thermoplastic reinforcement.

4.4 Bioink reinforcement techniques for additive manufacturing

The complex and sometimes opposing needs of bioinks has led to a concerted push to invent new ways of incorporating the best possible qualities into bioinks. Early 3D printed hydrogels simply compromised between mechanical properties and cytocompatibility to produce bioinks that were mediocre in both regards. As bioprinting has expanded, there has been a considerable upsurge in development of new techniques to reinforce bioinks through novel technologies. This section will cover emerging trends in bioink reinforcement and how these changes to hydrogel networks affect the key characteristics discussed in the previous section. Specifically, we will discuss bioink

reinforcement approaches such as polymer functionalization, supramolecularly reinforced hydrogels, interpenetrating networks (IPNs), nanocomposites, and thermoplastic reinforcement **(Figure 4-2)**. In randomly crosslinked single networks, stress is concentrated in areas with the shortest distances between crosslinks, while slack remains in zones with longer distances between crosslinks**.** Polymer functionalization can introduce new, stronger crosslinking mechanisms. Sometimes multiple crosslinking mechanisms can be combined to make a dual-crosslinked network. Supramolecular hydrogels incorporate rapidly reversible crosslinks that act as weak points, preventing permanent damage to the network. When ionic-covalent entanglement (ICE) networks are stretched, the physical interactions of the stiffer ionic network are reversibly disrupted to dissipate mechanical energy, resulting in a tougher network. Meanwhile the covalent network maintains hydrogel elasticity**.** Embedded nanoparticles can act as reversible electrostatic crosslinkers, diffusing stress and dissipating mechanical energy when nanoparticle-polymer bonds are disrupted. Co-printing typically shields and supports weak bioinks, but emerging methods incorporate thermoplastics efficiently at the micro-scale.

These emerging bioink reinforcement methods improve hydrogel mechanical properties from multiple different approaches, including strengthening crosslinks, homogenizing stress distribution, and dissipating mechanical energy through sacrificial bonds. For example, sliding crosslinks can move in response to applied stress, preventing stress from concentrating in any one area, thus avoiding premature fracturing of the network. Newer research is also combining multiple bioink reinforcement strategies, for example by employing both ICE and nanocomposite reinforcement to synergistically improve mechanical properties and printability. Other strategy combinations under development include supramolecular interpenetrating networks(IPNs) and

nanoreinforced dual-crosslinked bioinks. In the following section, we will briefly discuss the theory behind each reinforcement approach and the recent breakthroughs for their use in bioprinting, as well as outline existing limitations and directions for future development.(212, 213)

4.4.1 Polymer functionalization and dual-crosslinked networks

One of the most important design shifts during the bioprinting revolution has been the increased use of polymers modified with new chemical moieties. This polymer functionalization can introduce new crosslinking methods and incorporate new biological activity into bioinks. Hydrogels fabricated from synthetic polymers are usually covalently crosslinked networks, while hydrogels from natural polymers are physically crosslinked through conformation changes and physical interactions. Physical crosslinks are weaker than covalent crosslinks but are reversible, and are typically sensitive to environmental factors like temperature, pH, and ion concentrations. Functionalizing natural polymers with covalent crosslinks can improve mechanical properties and reduce sensitivity to environmental conditions. The permanence and increased bond energy of covalent crosslinks over physical interactions has driven research into incorporating covalent functionalization into natural hydrogels to increase their strength and durability after 3D printing.(251) Many natural bioinks including alginate, gelatin, hyaluronic acid, and collagen have been reinforced through functionalization to improve mechanical strength and stability in *in vivo* conditions.(206, 252) Polymer functionalization can also be used to modulate properties of bioinks by including sites for degradation and cell attachment. In this section, we will discuss current and emerging approaches to bioink functionalization.

4.4.2 Methacrylate Functionalization

One of the most popular polymer functionalization methods is to incorporate covalent crosslinking by modifying the polymer backbone using methacrylate groups.(253) In this method, a polymer is exposed to methacrylic anhydride to form methacrylate functional groups that can be photocrosslinked in the presence of a photoinitiator. This technique is an attractive modification for adding covalent crosslinking to natural polymers such as gelatin, which is otherwise physically crosslinked through non-covalent bonds below body temperature. Functionalized gelatin methacryloyl (GelMA) maintains many essential bioactive properties of gelatin, including cell attachment and enzymatic degradation.(254) GelMA prints poorly at physiological temperature. However, by leveraging the sol-gel transition of GelMA, cell-laden bioink can be printed into multilayer structures by cooling the bioink to 4 ^{o}C for several minutes before printing.(255) In contrast to gelatin, photocrosslinked GelMA is stable at body temperature, has higher fracture energy, is more resistant to degradation, and is able to be photopatterned through selective light exposure.(255, 256) The mechanical properties of 3D printed structures using GelMA bioinks can be readily modified by changing polymer concentration, which can be used to direct cell function.(257) 3D vascularized structures can be obtained using sacrificial materials within GelMA hydrogels or microbead-laden hollow GelMA hydrogel fibers.(257)

Methacrylation has been applied to polysaccharides as well, including alginate, hyaluronic acid (HA) and kappa carrageenan (κCA). As most of the acrylated and methacrylated polymers have low viscosity, cure-on-site techniques using UV light have been developed to print these types of polymer bioinks by crosslinking and extruding the bioinks simultaneously. A range of cell-laden,

low viscosity bioinks can be bioprinted this way, including methacrylated hyaluronic acid (MeHA), GelMA, PEG diacrylate (PEGDA),and norbornene-functionalized hyaluronic acid (NorHA). Interestingly, the NorHA bioink was repeated using a visible light photoinitiator instead of the UV-sensitive photoinitiator, but there was no significant difference in cell viability.(258) Polysaccharide hydrogels are generally stiff, but brittle, showing significant plastic deformation and poor recovery upon compressive loading. Covalent functionalization can also decrease stiffness but improve elastic recovery in these bioinks, as demonstrated using a methacrylated κCA (MκCA) bioink.(256, 259-261) Covalent functionalization often interferes with the formation of physical crosslinks, which rely on conformation changes that are sensitive to alterations in polymer structure. However, some polymers retain the ability to physically crosslink after functionalization, allowing both crosslinking methods to be combined into a dual-crosslinked network.(255, 260, 262)

4.4.3 Click Chemistry and other Functionalization Methods

Another alternative bioink functionalization method utilizes click reactions, rather than free radical chain polymerization, to covalently crosslink gelatin polymers.(263, 264) Click reactions are a set of synthesis reactions that are highly selective, thermodynamically favorable, and proceed under mild conditions. Thiol-ene click reactions in particular have gained interest for functionalizing biomaterials due to their ease of use and the availability of cysteine residues in peptide polymers.(265) Thiol-ene click reactions are based on reactions between thiols and alkene groups, which can be designed to favor chain transfer over propagation, resulting in a step growth polymerization that recycles radical species.(265) These reactions are not inhibited by oxygen and

proceed efficiently at much lower radical concentrations compared to free radical polymerization, which translates to roughly 30x faster crosslinking times in a more cell compatible environment. This rapid crosslinking can improve printability by solidifying extruded bioink within a few seconds of extrusion, reducing structural sagging. The rapid crosslinking kinetics of thiol-ene click reaction has been used to bioprint structures up to 20 layers tall using allylated gelatin (GelAGE).(263) Click crosslinking utilizes a step growth process that creates hydrogels with similar elastic moduli to methacryloyl hydrogels, but produces more homogenous networks, which reduces stress concentrations and has been shown to improve extensibility and fracture toughness.(251, 263-268) Finally, there are also non-photocrosslinking agents useful for bioinks. For example, tyrosinase has been used as an alternative to photoinitiator for catalyzing the crosslinking of collagen and gelatins for bioink reinforcement.(269, 270)

To summarize, functionalization reinforces bioinks by introducing covalent crosslinking mechanisms, which are stronger and more stable than physical crosslinks. These reactions are increasingly popular due to the rapid and permanent nature of the crosslinks. Functionalization techniques can improve the fracture energy (Γ) of hydrogel networks, and some reactions, like thiol-ene click reactions, also improve network homogeneity, which increases extensibility. Polymer functionalization improves the network's intrinsic fracture energy (Γ_0) by increasing crosslink bond energy. However, total fracture energy remains relatively low unless it is combined with an energy dissipative mechanism to increase Γ_D, like interpenetrating networks, nanocomposites, or supramolecular bonds. This makes functionalization a common step in fabricating high performance bioinks, as we discuss below.

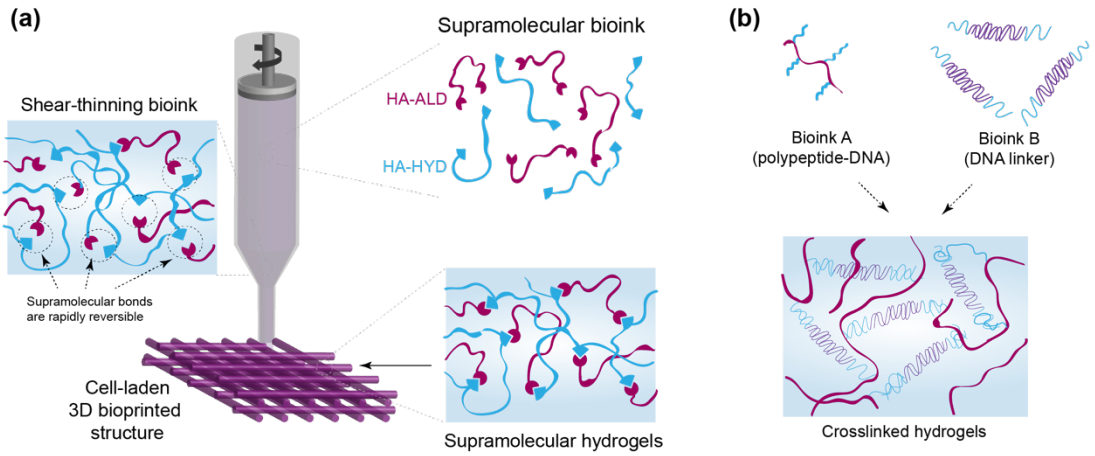

Figure 4-3. Supramolecular mechanisms for bioink reinforcement. (a) Supramolecular bonds act as reversible crosslinks. They are disrupted when a crack propagates through the hydrogel, but quickly re-form, regaining their strength. (b) Complementary bio-inks of polypeptide and DNA can be deposited alternatingly to obtain supramolecular 3D printed structure. These self-healing structures can encapsulate cells.

4.4.4 Supramolecular Bioinks

Sacrificial bonds improve bioink mechanical properties by dissipating stress to increase fracture energy. When these sacrificial bonds show reversible characteristics, the network can potentially resist many cycles of deformation. This is a driving force for development of another interesting class of self-healing inks known as supramolecular bioinks (**Figure 4-3**). Supramolecular

hydrogels are composed of short polymer strands that self-assemble into a network through non-covalent interactions between functional end-groups. When these interactions are mechanically disrupted, they can re-form rapidly without permanent losses in performance.(271) These characteristics impact viscoelastic properties in interesting ways. For example, supramolecular networks demonstrate elastic properties below their yield point, but behave like a viscous liquid after yielding. After shear stress is removed, supramolecular hydrogels re-form into an elastic solid. Developing models to correlate these flow properties with supramolecular structure is still an active area of research.(216, 272, 273) These properties have been used to develop a supramolecular bioink by modifying HA with adamantane (Ad) and β-cyclodextrin (β-CD) (Ad–HA and CD–HA). 3D printed structures that use these HA-based supramolecular bioinks are able to sustain complex shapes.(271) However, it was difficult to obtain multilayered structures using HA-based supramolecular bioinks due to their limited mechanical properties.

Supramolecular bonds attract interest among bioink researchers because they combine the reversibility of physical bonds with the versatility and customization of covalent crosslinking techniques.(274) Supramolecular bonds differ from covalent bonds because they do not have permanent crosslinks. Instead, bonds between molecules exist in a dynamic equilibrium between the bound and unbound states, meaning that bonds are constantly breaking apart and re-forming. Two important factors help determine how this affects hydrogel behavior: bond lifetime and the equilibrium constant (K_{eq}). The equilibrium constant reflects the free energy difference between the bound and unbound states. Higher equilibrium constants favor extensive complexation within the network, which generally creates more connected, stronger hydrogels. Bond lifetime is a kinetic factor determined by the size of activation energy barriers and contributes to

supramolecular hydrogels' time dependent mechanical properties. Supramolecular bonds do not contribute to fracture energy when their lifetime is much smaller than the timescale of deformation, but they behave much like permanent bonds during more rapid deformation. These thermodynamic and kinetic factors help explain some of the unusual behaviors of supramolecular bioinks.(272) Supramolecular bioinks are sensitive to their environment, which can be exploited for creating bioinks. For example, a supramolecular bioink was developed to undergo reversible thermal gelation over room temperature using a living cationic ring-opening polymerization mechanism.(275) This network notably demonstrated good mechanical properties for a thermally gelling bioink, having a storage modulus of 4 kPa.(275)

4.4.5 Guest-Host Interactions

Despite their interesting properties, the application of many supramolecular hydrogels for bioprinting has been limited due to their weakened strength in the presence of water, which competitively binds with monomer functional groups.(272, 276) In the past few years, stronger water-compatible bonds have been developed, and more mechanically stable supramolecular hydrogels are being investigated for bioprinting. Supramolecular moieties can be vulnerable to creep and erosion, so they are often combined with covalent crosslinks and other mechanical reinforcement strategies in bioinks. For example, supramolecular bioinks were recently combined with methacrylation functionalization as a method to reinforce a weak supramolecular bioink.(277) In this study, hyaluronic acid polymers were methacrylated for covalent crosslinking and also functionalized with either guest (adamantane) or host (b-cyclodextrin) moieties to enable supramolecular crosslinking. This dually crosslinkable network resulted in a self-healing bioink

that could be stabilized for at least 30 days after printing using covalent crosslinking. In contrast, guest-host (GH)-only gels relaxed too quickly to be printed effectively.(277, 278)

Recently, the same GH bioinks were reinforced further by creating a supramolecular reinforced dual-network bioink by adding a covalently crosslinked second network.(279) Compared to the methacrylated GH network (MethGH), a tethered interpenetrating network (MethGH-DN) reinforcement significantly improved mechanical properties, including compressive modulus (3 vs. 11 kPa) and tensile toughness (2 vs. 13 kJ/m^3). Reinforcement was maintained through successive compression cycles, and qualitative tests showed rapid healing within ~1s. Interestingly, the MethGH-DN was also superior to an interpenetrating network with a non-methacrylated GH first network, particularly at low strain rates and cyclic compressions, which demonstrates that tethering the first network to the second is necessary to preventing Mullins-type softening with this supramolecular bioink.(279)

4.4.6 Other Supramolecular Interactions

Beyond these hybrid bioinks, supramolecular hydrogel research continues to advance. This may lead to an increase in pure supramolecular bioinks as well. One recent folate-based supramolecular bioink combines hydrogen bonding and π–π bond stacking with zinc coordination bonds to create a scaffold with a storage modulus as high as 100 kPa. Scaffolds were biocompatible and self-supporting, although their long-term shape stability remains to be investigated.(280) Another interesting recent approach combines dynamic and covalent crosslinking into a single moiety. Gallol antioxidants, which cause fruit browning, form dynamic hydrogen bonds with protein

backbones that initially provide rapid self-healing and shear recovery properties to the bioink.(281) Over the course of a day, the gallol functional groups are gradually oxidized to form permanent covalent bonds. This allows a single functional group to operate as a dynamic and covalent crosslinker depending on scaffold age.

Another class of supramolecular bioink are fabricated using polypeptide–DNA hydrogels. This study showed that by alternatingly depositing two complementary bio-inks, a stable bioprinted structure loaded with cells can be obtained.(282) Interestingly, these relatively large 3D printed structures are able to retain their shapes up to several millimeters in height without collapse. Due to the presence of DNA building blocks, these gels have self-healing properties. However, stability of these hydrogels for long-term cell culture needs to be examined for future applications.

The ability to heal is common in living tissues, hence bioinks capable of healing damage are attractive choices for implantable materials. Like many biological materials, supramolecular hydrogels are often made with non-covalent bonds between small, self-assembling blocks, which makes them an attractive option for biomedical applications, including drug delivery and injectable materials. However, the complex and often toxic preparation of these materials, as well as the lower strength of supramolecular interactions, have limited their application as bioinks. Recent advancements in the design of supramolecular hydrogels, as well as their combination with other reinforcement techniques, are making them an increasingly attractive choice for 3D bioprinting.

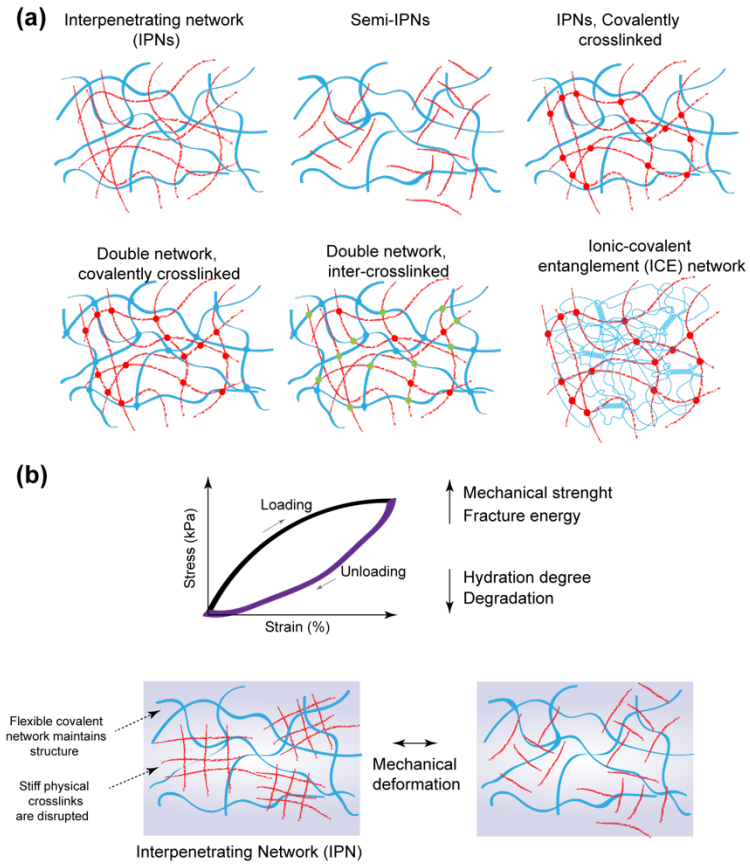

Figure 4-4. Bioink based in interpenetrating networks. (a) Schematic demonstrating various type of interpenetrating networks. Interpenetrating networks are composed of 2 separate-but-entangled networks: one brittle network of sacrificial crosslinks, and one flexible, loosely crosslinked network. In Semi-IPNs, one network is not fully crosslinked. Some IPNs also contain some inter-crosslinks that tether between networks. IPNs are called double networks (DNs) when both networks are covalently crosslinked, and Ionic-Covalent-Entanglement networks (ICEs) when the sacrificial network is ionically crosslinked. ICE hydrogels represent most of the IPNs in bioprinting literature. (b) The reversible sacrificial bonds present in ICEs provide high mechanical strength and fracture toughness compared

to single network bioinks. In addition, ICE networks are able to regains physical crosslinks over time, recovering stiffness.

4.4.7 Interpenetrating networks

Interpenetrating networks (IPNs) increase fracture energy (Γ), toughness, and stiffness through a highly heterogeneous hydrogel architecture.

IPNs consist of two interwoven but independent networks: one that is loosely crosslinked and ductile, and another that is densely crosslinked and brittle **(Figure 4-4)**. The contrasting properties of these separate-but-entangled polymer networks work together to increase fracture energy by efficiently dispersing mechanical energy during cracking. The brittle network's sacrificial bonds fracture around the crack tip to dissipate mechanical energy, while the ductile network deforms to disperse stress across a large damage zone around the crack. This increases mechanical dissipation and spreads fracture energy across a wider zone, greatly increasing fracture energy.(1, 2) Mechanical energy dissipation through sacrificial bond rupture is calculated using the equation ΓD = 2(Uf)(Nf)(h), where Uf is the energy required to fracture a sacrificial chain, Nf is the volume density of fracturing sacrificial chains in the process zone, and h is the thickness of the process zone. This equation is of the same form as that describing intrinsic fracture energy (Γ0), but while Γ0 calculates chain fracture along the crack path, the sacrificial bonds in IPNs rupture in a much larger area around the crack called the process zone. This is due to the sacrificial network being much more stiff and brittle than the elastic network, meaning that deformation sufficient to break the elastic network must deform a large zone of sacrificial bonds. Since mechanical energy

dissipation (ΓD) is dependent on effective fracturing, the sacrificial network is most effective with a high number of short chains.(4, 5)

There are two main kinds of IPN hydrogels: (a) double networks (DN), where both networks are held together with covalent crosslinks, and (b) ionic-covalent entanglement (ICE) networks, where the sacrificial network is crosslinked with physical bonds. DN and ICE hydrogel networks are structurally similar and the initial energy dissipation of both is described with essentially the same equation ($\Gamma_D = 2(U_{dc})(N_{dc})(h)$), although the energy required to de-crosslink the physical network (U_{dc}), is generally < U_f.(213) Comparing DN and ICE networks, we see several key mechanical differences. Thanks to their purely covalent structure, DNs have high bond energy, can remain elastic under 40-50% deformation, are nearly independent of strain rate, and are less sensitive to environmental effects like temperature, ions, and pH. On the downside, their bond breaking is not reversible, so once sacrificial bonds are ruptured, the hydrogel's mechanical properties are determined only by the intact extensible network. This makes DNs susceptible to fatigue over repeated stress cycles. In contrast, ICE networks are more sensitive to environmental effects, display hysteresis at lower strains, and are more strain rate dependent. However, physical crosslinks in ICE networks can re-form over time, allowing the hydrogel to regain sacrificial bonds.(214, 283)

4.4.8 Ionic Covalent Entanglement Bioinks

In bioinks, the most promising IPNs are formed through ICE. This is because conventional DN networks form over too long a timescale for bioprinting applications.(206) ICE hydrogels are formed with an ionically crosslinked rigid polymer and a covalently crosslinked elastic polymer.

Using two distinct crosslinking mechanisms greatly reduces the time required to form the IPN.(206) Combining two different types of crosslinks into single hydrogel replaces mechanical energy dissipation through disrupting permanent sacrificial bonds (seen in DNs) with a reversible dissociation of ionic network crosslinks. This can be modeled as a continuous pulling apart of aggregated ionically crosslinked polymers, which can cause velocity dependent fracture behaviors.(284)

The potential for these ICE physical crosslinks to re-form over time as a mechanism for creating bioinks with increased toughness has led to increased interest within the bioink development field. For example, an ICE interpenetrating network composed of 2.5wt% alginate and 20wt% PEG was printed into a crosshatch pattern structure capable of expanding to 300% of its initial length. These hydrogels were able to partially recover their fracture energy after deformation when stored in a humid chamber for 24 hours, but bioprinting was not attempted.(42) In a more recent study, an ICE network was used for bioprinting in combination with nanosilicates.(211) A 1% κCA physical network was combined with a 10% GelMA covalent network, causing a nearly 3x increase in modulus (κCA: 12 kPa, κCA -GelMA: 35 kPa). ICE networks significantly decreased the brittleness of the κCA network, increasing maximum stress at 70% compression from 16 to 141 kPa, and improved recovery from 25% to 84% during a 5-cycle compression test. Nanosilicate reinforcement of the ICE network improved mechanical properties even further. ICE networks have good potential for creating highly deformable, cytocompatible bioinks with increased toughness.(42, 211)

Another example of an ICE network bioink was recently reported using 1.5% gellan gum and 10% PEGDA.(285) Gellan gum is an anionic polysaccharide popular in bioprinting for its shear thinning properties and viscosity, but its application is limited by its brittleness and poor mechanical properties as a physically crosslinked single network. Gellan gum was incorporated into an ICE by adding a 10% PEGDA polymer network. Crosslinking the PEGDA network alone gave the bioink a 60 kPa compressive modulus and 34 kPa compressive strength, while allowing ions in the culture media to crosslink the gellan gum component increased these values to 184 kPa and 55 kPa, respectively.(285) These studies demonstrate that ionically crosslinkable, high molecular weight polysaccharides like gellan gum and carrageenan are well suited for use in ICE bioinks. Their molecular weight makes them effective viscosity modifiers useful for simultaneously improving both bioink flow and mechanical properties even at small polymer concentrations.(211, 285)

4.4.9 Double Network Bioinks

In a recent study, a covalent-dynamic-covalent double network bioink was developed using two separate hyaluronic acid networks.(286) These dynamic-covalent interpenetrating networks are a promising method for combining the greater bond strength of covalent bonds with the self-healing properties of ICEs. Hyaluronic acid was modified using two distinct methods to provide two independent networks via thiol-ene click crosslinking and hydrazone dynamic covalent bonds. This double network increased failure stress from 10 to 30 kPa over hydrazone crosslinking alone, and increased Young's modulus from 1 to 3 kPa. Additionally, bioprinted structures could be cut apart and recombined with other structures. After 10 minutes, the interfaces healed well enough

that they could not be pulled apart manually. Near complete recovery of failure stress was attained after 30 min in 1.5 wt% hydrogels; however, recovery dropped to 50% upon increasing the composition to 3% hydrogel. This result suggests that denser hydrogels may require longer healing times or may not be completely recoverable. The authors hypothesize that restricted polymer mobility at higher concentrations may cause this effect. While the impact of double networking on the efficiency of the self-healing hydrazone bonds was not addressed, the use of dynamic covalent double networks represents an interesting new avenue of IPN research.(286)

In summary, IPNs improve mechanical properties by distributing mechanical energy over a broad damage zone using a brittle sacrificial network combined with an extensible second network. ICEs are being adopted for bioprinting because of their fast, cell-friendly formation and recoverable mechanical properties. The physically crosslinked polymer is also frequently a viscosity modifier, improving printability properties simultaneously.

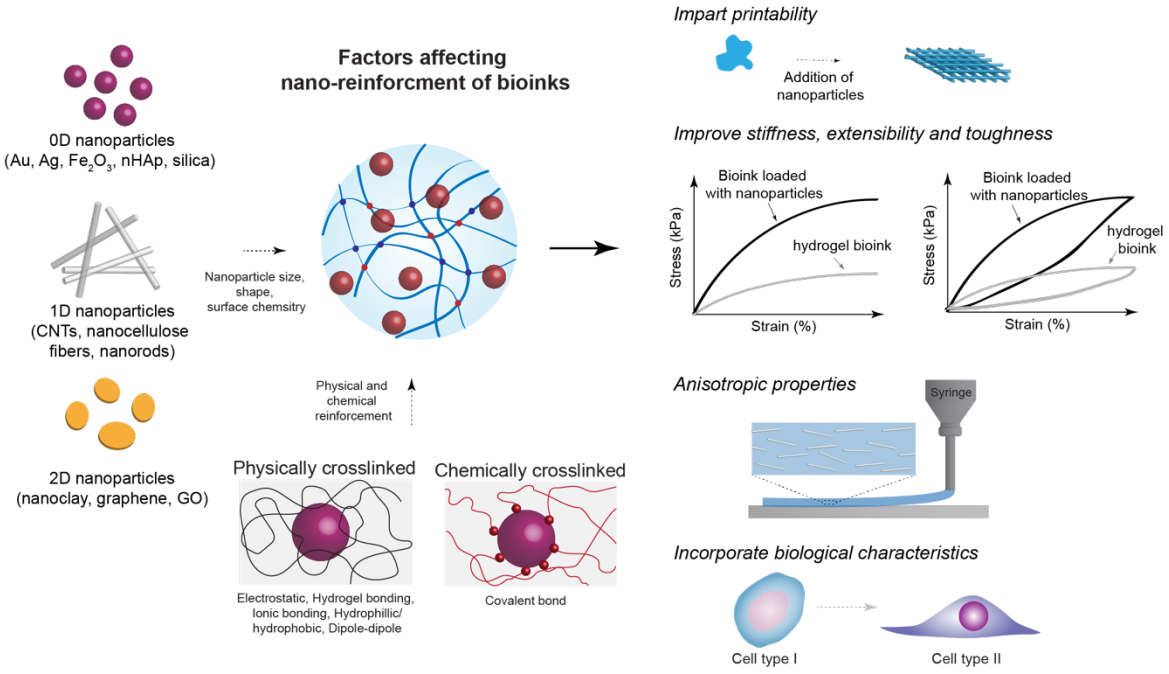

Figure 4-5. Bioink based on nanocomposite reinforcement. Nanoparticles with a range of sizes, shapes, and surface chemistries can mechanically reinforce bioinks through physical and covalent interactions. Nanoparticles reinforcement of hydrogel bioinks has been shown to improve printability, rheological properties, and mechanical properties. The use of anisotropic nanoparticles such as 1D or 2D nanomaterials in bioinks can imbue printed structures with anisotropic properties. Bioactive nanoparticles are able to direct cell function in 3D bioprinted structures. These bioactive effects occur through drug loading, direct interactions, or indirectly by affecting hydrogel viscoelastic properties.

4.4.10 Nanocomposite reinforcement

Nanomaterials have rapidly gained interest within the biomedical engineering community over the past few years.(25) Due to their high specific surface area, even small concentrations of nanoparticles can significantly impact the properties of a hydrogel network.(25, 287) The unique properties of nanomaterials have been exploited for many biomedical applications, including imaging, drug delivery, cancer therapies, and biosensor development. Incorporation of nanomaterials has been used to add new functionalities to bioinks, like electrical conductivity, stimuli responsiveness, control over cell behavior, printability improvements, and mechanical reinforcement.(25, 206, 287)

4.4.11 Nanosilicates

Nanocomposite reinforcement of bioinks can improve bioink printability and bioactivity and can often be easily incorporated into existing bioinks. Silicate nanoclays, for example, are the most widely used nanoparticle for bioink mechanical reinforcement and have been incorporated into a wide range of popular bioinks, including alginate, PEG, GelMA, hyaluronic acid, and kappa carrageenan. Due to the ease of incorporating some nanomaterials into aqueous solutions, nano-reinforcement can be combined with other types of mechanical reinforcement techniques like supramolecular and ICE reinforced bioinks.(206, 210, 288) For example, the compressive modulus for 2.5% kCa was increased from 85 to 208 kPa with the inclusion of 6% nanoclay, without apparent harm to encapsulated cells over 7 days.(232) In another recent study, 7% nanoclay was

incorporated into a 20% PEGDA bioinks co-printed with a 20% hyaluronic acid for osteoblast-laden scaffolds for bone regeneration.(289) The inclusion of nanoclay increased compression modulus from 332 kPa to 976 kPa. In both of these studies, the use of nanocomposite reinforcement also improved the printability of the bioinks through both physical nanoclay-polymer interactions and nanoclay-nanoclay interactions.(232, 289)

The mechanism of hydrogel nanomaterial reinforcement has also been a very active field of study.(290) The reinforcement mechanisms can vary depending on nanoparticle size, shape, and surface chemistry (**Figure 4-5**). Reinforcement of hydrogels is generally thought to occur through nanoparticles acting as reversible crosslinkers spanning multiple polymer chains. This allows stress to be efficiently dispersed across the network and dissipated through the breaking of nanoparticle-polymer crosslinks. This mechanism has been shown to improve stiffness, extensibility and toughness of the nanoparticle-crosslinked hydrogels. Improved extensibility is thought to be due to shorter polymer chains unbinding from the nanoparticle to dissipate stress, thus avoiding large-scale crack propagation.(212, 213, 290, 291)

4.4.12 Carbon Based Nanocomposites

Electrically conductive nanoparticles have also been investigated as bioink reinforcement. For example, carboxyl-functionalized multiwalled carbon nanotubes (CNTs) were covalently bonded to alginate to improve mechanical properties and electrical conductance of a methacrylated collagen scaffold for myocardial tissue engineering.(292) CNT nanocomposite scaffolds

maintained physiological stability (43-54 kPa elastic modulus) over a 20 day culture period, while significantly reducing impedance at 5 Hz.(292) These CNT-reinforced bioprinted scaffolds improved cell proliferation and differentiation, suggesting that electrically conductive nano-reinforcement may be particularly suitable for myocardial tissue regeneration.(292) Graphene and its derivatives, graphene oxide (GO) and reduced graphene oxide (rGO), are noted for their use in reinforcing hydrogels and enhancing electrical conductivity, and are being widely adapted for biomedical applications including tissue engineering, drug delivery, and biosensing.(25) GO in particular is popular for its ease of functionalization and water solubility, and has been used to increase the compressive modulus of gelatin, chitosan, and alginate scaffolds. GO was recently used to reinforce a GelMA-PEGDA hydrogel (105 vs. 135 kPa compressive modulus at 1 mg/mL) and induce chondrogenic differentiation of seeded hMSCs. rGO has also been used to reinforce GelMA from 2 to 23 kPa at 3 mg/mL in a scaffold for cardiac tissue engineering, while also improving cardiac beating and contractility among seeded cardiomyocytes.(25, 293-295) GO has also been shown to improve printability of alginate by reducing layer sagging in printed structures.(229)

Other nanomaterials like cellulose nanofibers are also being investigated for bioink reinforcement. Cellulose nanofibers have high specific surface area and can form sacrificial hydrogen bonds that can be disrupted to dissipate stress.(206, 296, 297) Cellulose nanofiber reinforcement has been shown to increase the compressive modulus of a 5% GelMA bioink from <1kPa to 8 kPa by adding 2% cellulose nanofibers.(298) Their inclusion also improved bioink printability by increasing shear-thinning and zero shear viscosity. Similar success has also been reported using cellulose nanofibers to improve printability and mechanical properties in an alginate

bioink.(299) More recently, promising results have also been reported using methylcellulose to nanoreinforce alginate and hyaluronic acid bioinks and improve printability.(300, 301) Interestingly, a recent paper on nanocellulose fiber-PEGDM (polyethylene glycol dimethacrylate) nanocomposites reports that cyclic preloading can cause nanocellulose fibers to rearrange and relax residual stresses, increasing fracture strength and crack initiation energy by over 20%, while decreasing modulus and fracture energy.(302)

4.4.13 Other Nanoreinforced Bioinks

Hydroxyapatite nanoparticles are an attractive additive for tissue engineering because of their bone-like mineral content and osteogenic potential, which has led to increased popularity in nanocomposite bioinks. In a recent study, incorporating 20 mg/mL nanohydroxyapatite increased elastic modulus in both 3%(w/v) alginate (3.5 to 18.8 kPa) and 2%(w/v) chitosan (4.6 to 15.0 kPa) nanocomposite bioinks.(303) Additionally, HA nanoparticles increased low shear viscosity with the addition of hydroxyapatite nanoparticles, but increased shear thinning behavior. HA nanoparticles also recover sufficient viscosity after extrusion to maintain printed shape fidelity, which was quantified using shear recovery tests. Overall, HA nanoparticles are most popular in bone tissue engineering for their osteogenic effects, but they also demonstrate significant mechanical and printability effects as well.(223, 304)

There has also been developing interest in synthesizing custom nanoparticles in order to better control the properties of bioinks. Silica nanoparticles were recently modified with aminopropyl groups to create cationic silica nanoparticles (AmNPs), creating strong electrostatic interactions

between anionic polymers and the AmNPs.(305) This enhanced the zero-shear viscosity, shear-thinning properties, and yield stress of an alginate-gellan gum (3% and 3.5% w/v) bioink while maintaining rapid shear recovery. The 6% AmNP nanoreinforcement increased compressive modulus (~50 to 85 kPa) and storage modulus (252 to 2390 kPa) over unreinforced bioink. This is a promising development because unmodified silica nanoparticles have very limited effect on mechanical properties, but cationic functionalization significantly improved interactions with the anionic bioink, demonstrating that the nanoreinforcement mechanism was due to electrostatic interactions. Interestingly, nanoreinforcement was improved by decreasing nanoparticle size and polymer chain length. This is likely because shorter polymer chains aggregate less and thus form more polymer-nanoparticle interactions, while smaller nanoparticle diameters have higher specific surface area so polymer chains are more likely to form inter-particle, rather than intra-particle bonds.(305, 306)

4.4.14 Biocompatibility

While improved printability and mechanical strength make nanocomposites popular for bioinks, the complexities of nanoparticle interactions pose difficult questions about how to evaluate their long-term biocompatibility. One major difficulty is that at the nano-scale, material properties can change fundamentally with particle size, morphology, and functionalization as well as chemical composition. Differences in these properties can drastically affect nanomaterial interactions with biological systems at the subcellular level by altering cell uptake, degradability, and immunogenicity. This means that biocompatibility cannot be inferred from studies on bulk materials nor studies on nanoparticles of the same composition but different morphology.

Consequently, there are contradictory studies on the biocompatibility of many nanomaterials, and a systematic understanding of their biological effects remains elusive. When evaluating nanomaterials for biocompatibility, it is important to match their morphology, functionalization, and composition, and to evaluate whether nanoparticles are behaving as expected during toxicity tests. Because nanoparticles can aggregate, form sediments, or remain disaggregated depending on environmental conditions, it is important to evaluate toxicity under conditions that match expected use. Finally, the novelty of nanomedicine has resulted in significant regulatory uncertainty as regulators have not yet established clear rules on evaluating nanomaterial safety, although this gap has been acknowledged and is being addressed by regulators. Overall, significant progress has been made in understanding *in vitro* and *in vivo* responses to various nanoparticles, but our understanding of nanomaterial biological interactions remains incomplete. Further research addressing this is necessary for translating this research into clinical applications.(25, 307)

4.4.15 Thermoplastic Co-Printing

Thermoplastic 3D printed structures have been adopted for tissue engineering, typically as a macroporous structural support for cells. However, their inability to directly print cells has led to co-printing thermoplastics along with hydrogels. For example, thermoplastic can be printed first as the structural component to provide a mechanically stable scaffold, followed by printing cell-containing bioink.(308) Polycaprolactone (PCL) is the most common thermoplastic for co-printing because of its biocompatibility and relatively low melting temperature (60°C), which allows co-extrusion with less risk of thermal injury to cells. In one recent work, a strong thermoplastic

scaffold of PCL and tricalcium phosphate (compression modulus ~40 kPa) was used for bone and cartilage regeneration, although it contained relatively small amounts of bioink.(308, 309)

4.4.16 Hydrogel Co-Printing

One key limitation of thermoplastic co-printing is the inability to extrude fine thermoplastic filaments that interface effectively with hydrogels.(297) An interesting non-thermoplastic approach used for co-printing includes the use of a high-strength methacrylated poloxamer hydrogel alongside a 5% GelMA bioink (2.7 kPa).(221) This composite structure reached an overall stiffness of ~200 kPa using 50vol% of reinforcing gel.(221) This approach mitigates some of the disadvantages of thermoplastic reinforcement, including reduced diffusion and bioink-reinforcement interface issues, and potentially enables co-printing to be used for soft tissue implants as well.(221)

In a more recent study, a hydrogel support materials was nano-reinforced to make a stiff scaffold for bone tissue regeneration. The bioink and support hydrogels were 20% hyaluronic acid solution and 20wt%PEGDA + 7wt% nanoclay (Laponite) with a water content of only 74%, resulting in a water-stable and printable ink. Adding nanoclay increased the compressive modulus from 22 to 90 kPa, and increased compressive strength at 90% compression from 332 to 976 kPa. Hydrogel reinforcements like these provide advantages of thermoplastic co-printing while allowing better control over nutrient diffusion and degradation.(289)

4.4.17 Thermoplastic Micro-Reinforcement

Micron-scale thermoplastics have also recently been explored as a bioink reinforcement. In this study, microfluidic fabrication was used to create sub-micron diameter PLA fibers which were suspended in an alginate bioink. This system was used to increase the Young's modulus of an alginate bioink by 3-4 fold.(223) Microfiber reinforced bioinks also altered flow properties by increasing zero-shear viscosity. Interestingly, alginate present in the bioink dominates viscosity at higher shear rates.(223) Micron-scale thermoplastic fibers are finely integrated throughout the bioink, directly combining the load-bearing properties of thermoplastic reinforcement directly into the bioink, as opposed to an external support. This approach allows thermoplastic reinforcement to be applied to soft tissues as well as bone, and improves bioink flow properties as well, although more research is needed to evaluate the generalizability of this promising technique.

The use of co-printed reinforcement remains an option for allowing the use of otherwise unprintable bioinks by extruding them onto a plastic support structure. While this technique can be applied to any bioink and can resemble the mechanical properties of hard tissues, challenges remain, particularly reduced nutrient diffusion, stress shielding, and separate degradation kinetics that may influence tissue regrowth. Alternatives are being developed to circumvent these problems. The development of smaller scale, more efficient reinforcement techniques can make co-printing more attractive for bioinks.

4.5 Emerging trends & future approaches

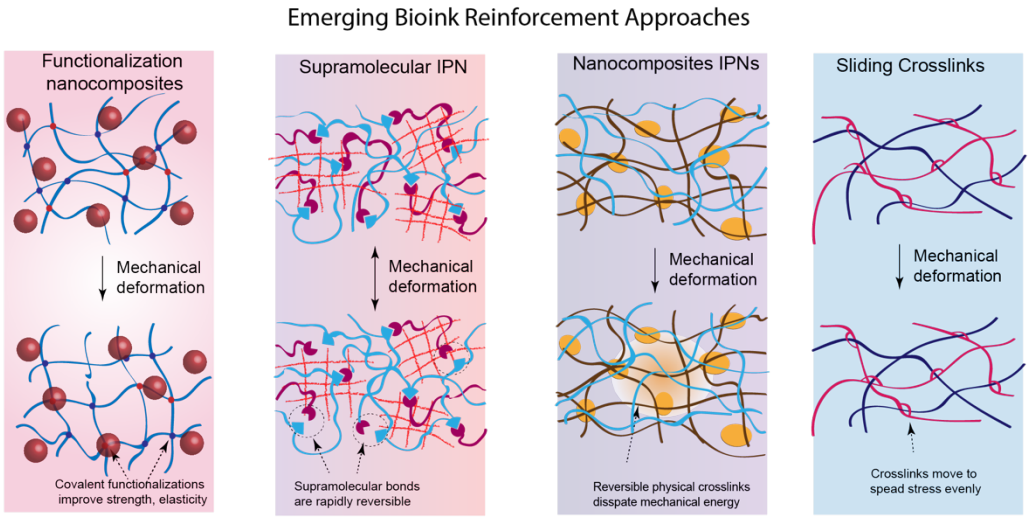

Figure 4-6. Emerging approaches for mechanical reinforcement. Combining reinforcement mechanisms together can provide bioinks with superior properties. Functionalized nanocomposites enable covalent nanoparticle interactions, which can improve strength and elasticity. Supramolecular IPNs can combine rapid supramolecular healing with the stability and strength of IPN networks. Nanoreinforcement of IPN networks results in very efficient bioink reinforcement with mechanical properties superior to either technique alone. Sliding crosslinks improve hydrogel extensibility by preventing stress concentrations, and could eventually be incorporated into bioinks.

4.5.1 Trending towards combinatorial approaches

One of the most promising future trends in mechanical bioink reinforcement is the combination of individual reinforcement techniques to make composite bioinks with interesting new properties. While individual reinforcement techniques laid out in this paper use very different strategies to

improve the underlying mechanical properties of bioinks, many of the mechanisms behind these reinforcement strategies are not mutually exclusive and can be combined with other techniques, effectively creating new strategies that can compensate for weaknesses and integrate the strengths of different reinforcement mechanisms (**Figure 4-6)**. Most combinatorial approaches are still in the beginning stages of development, but some interesting developments are already being published.

For example, supramolecularly functionalized hyaluronic acid (HA) was mixed with a covalently crosslinked methacrylated HA (Me-HA) to form an interpenetrating network.(279) While supramolecular networks are typically vulnerable to permanent deformation, the supramolecular polymers in this case were lightly tethered to the Me-HA network with covalent bonds. The cell-containing Me-HA single network's compressive modulus (2 kPa) was increased to 6 kPa as a supramolecular IPN network, and further increased to 11 kPa when the supramolecular network was covalently tethered to the covalent network. This design notably combines the mechanical properties of IPN reinforcement alongside the rapid self-healing of supramolecular polymers.(279)

Advancements in hydrogel reinforcement are also leading to interest in incorporating weaker materials efficiently into hydrogels. For example, a weak silk sericin hydrogel was recently incorporated into an interpenetrating network with GelMA for wound dressing applications.(310)

Nanocomposite reinforcement in particular is being combined with a number of other bioink reinforcement technologies because some materials like nanosilicates can be easily incorporated

into aqueous solutions and affect both mechanical and flow properties of the bioink.(211) In this work, ionic-covalent-entanglement (10% GelMA and 1% kappa carrageenan) bioink was combined with nanosilicates (2%) to obtain a mechanically reinforced and highly printable Nanoengineered-ICE (NICE) bioink.(211) Interestingly, this study showed that reinforcement of GelMA (16.5 kPa) with either ICE or nSi reinforcement alone led to a roughly 2 fold increase in compressive modulus (~35kPa), while combining both together synergistically increased compressive modulus by four fold to 71 kPa.(211)

Nanocomposite reinforcement has also been combined with supramolecular polymers to obtain elastomeric bioinks. For example, a poly(N-acryloyl glycinamide) (PNAGA) - nanoclay supramolecular hydrogel was developed for 3D printing scaffolds for bone tissue regeneration. The bioink was composed of 20wt%PNAGA + 7wt% nanoclay (Laponite), with a water content of only 74%, resulting in a water stable, printable ink. The printed structure was mechanically stiff (compressive modulus 228±10 kPa) and ductile, able to elongate to 1042±97% of its relaxed length before breaking. The inclusion of nanoclay rendered the precursor printable and reinforced the hydrogels (228 vs. 160 kPa without clay at 20% PNAGA). By relying on nanoclays for printability, the issue of poor printability of supramolecular precursors was overcome.(288)

4.5.2 Sliding ring crosslinks

One of the weaknesses of single network hydrogels is their heterogeneous network architecture. The random nature of their crosslinks causes stress concentration on the shortest chains, causing failure at lower strains than expected. In response, many efforts have been made to increase

hydrogel homogeneity, notably through the use of mechanically interlocked molecules including sliding ring crosslink systems like polyrotaxanes. These rings dynamically slide across chains to redistribute forces evenly among crosslinks to avoid stress concentrations throughout the network, resulting in hydrogels with superior extensibility and rupture strength **(Figure 4-6)**. Most of these systems require non-cytocompatible steps like high temperatures or DMSO use because polyrotaxane is insoluble in water, and so this approach has not yet gained much traction for biomedical applications. However, recently a new sliding crosslinker have been developed that incorporates succinic functional groups onto the polyrotaxane, rendering it water soluble.(311) This allowed a cytocompatible 3D culture of human mesenchymal stem cells(hMSCs) in the sliding hydrogel with a compressive modulus of 10 kPa. This technology could be adapted for bioprinting as it continues to develop more simple and cytocompatible methods, especially as more research is done on the effect of sliding crosslink hydrogels on encapsulated cell behavior.(212, 311-313)

4.5.3 Jammed Hydrogel Microspheres

Another upcoming trend worth discussing is the emergence of hydrogel microsphere bioinks. These bioinks are a densely packed, or jammed, slurry of micron-scale hydrogel microspheres whose surfaces can be crosslinked together after extrusion. This approach allows porosity to be controlled independently of bioink composition, enabling highly interconnected, microporous scaffolds to be created while also providing a stiff microenvironment for cells.(314-316) Microsphere printing can also be used to build heterogeneous scaffolds using microspheres with different compositions and encapsulated cells.(315, 317) Recent publications have reported using

microspheres with different stiffnesses to affect fibroblast proliferation and spreading,(315) and creating mixtures of microspheres containing either osteo- or chondrogenically differentiated mesenchymal stem cells.(317) Microspheres used in this way may enable micron-scale heterogeneity to be incorporated into bioprinted scaffolds without requiring micron-scale resolution.

Some recent publications have demonstrated encouraging printability results using microsphere bioinks, including centimeter-scale freestanding scaffolds.(317, 318) Shear thinning, yield stress, and shear recovery properties have also been reported,(317, 319) however, the factors behind microsphere printability remain poorly understood. Variables including microsphere size, polydispersity, packing density, surface interactions, and suspension medium may affect printability, but more research is necessary to evaluate these factors.(318-320) The increased porosity of microsphere scaffolds also reduces their mechanical properties, with one study reporting a reduction in compressive modulus from 15 kPa to 5 kPa when comparing conventional hydrogel scaffolds to crosslinked microspheres.(319) However, there has been very little investigation into the mechanical properties of microsphere scaffolds. The dependence of a scaffold's bulk mechanical properties on factors like particle packing, void fraction, microparticle mechanical properties, size distribution, particle-particle contact area, and crosslinking will require systematic investigation to better understand their application to bioprinting. Bioprinting hydrogel microspheres represents an interesting new approach to incorporate micron-scale porosity and heterogeneity into bioinks, and early *in vivo* tests on injected microspheres report improved vascularization and wound healing in skin lesions compared to conventional hydrogel.(316, 321) These encouraging results are likely to facilitate more research into microsphere bioprinting.

4.5.4 Micron-Scale Thermoplastic Reinforcement

In contrast to the macro-scale thermoplastic reinforcement discussed earlier, which acts as structures containing hydrogel, smaller nano- and micro- scale fibers can be incorporated into hydrogel bioinks to alter the hydrogel's mechanical properties. For example, melt electrospinning writing (MEW) can form highly porous and fibrous scaffolds of nanofibers to mimic native tissue microstructure using melted polymer instead of conventional volatile solvent solutions.(322-326) In one recent study, MEW was used to deposit a micron-scale thermoplastic network that increased Young's modulus by 18-fold over the PEG + heparin hydrogel network alone, while taking up only 5.6% of the scaffold volume. This reinforcement was caused by the thermoplastic network restricting hydrogel swelling, thereby enabling compressive forces to be transferred to the thermoplastic network as tensile stress. This design is reminiscent of cartilage's architecture, and the dynamic mechanical properties of the scaffolds showed similar responses to loading over time to cartilage, suggesting that mimicking the structural architecture of cartilage tissue may help us replicate its physical properties.(323, 325, 327)

However, it should be noted that these scaffolds were molded and not bioprinted. Despite its attractive properties, MEW is not compatible with bioprinting in its current form because printing speed is too slow, where even a small volume can take many hours,(221) and the presence of hydrogel on the build plate could interfere with the MEW process. MEW has not been combined with bioprinting for these reasons, but its incorporation into the bioprinting toolkit could be very beneficial for obtaining high strength bioprints in the future.(323, 325, 327)

Nevertheless, biocompatible incorporation of small-scale fibers into bioinks can significantly affect mechanical properties, as demonstrated by the recent reinforcement of an alginate bioink with sub-micron PLA fibers.(223) Similar techniques may be more easily adopted to co-bioprinting than electrospinning, like Solution Blow Spinning (SBS), which does not require an electric field and deposits much more quickly. SBS has been used to deposit poly(lactic-co-glycolic acid) (PLGA) nanofibers in situ during surgery and is gaining popularity in tissue engineering for its ease of use and biocompatibility, however the literature surrounding SBS is still light.(328) It remains to be seen whether MEW, SBS, or other technologies will successfully incorporate micron-scale thermoplastics into bioprinting, but the potential advantages of finer interfacing between bioprinting and thermoplastics remains an compelling avenue for new reinforcement techniques.(322, 329)

4.6 Conclusion

Bioinks are specialized hydrogels used to dispense suspended cells into 3D support scaffolds. The specific environmental needs of living cells pull bioinks towards dilute networks, while mechanical and flow requirements improve with higher polymer concentrations. These contradicting requirements are driving research into more advanced hydrogel designs and have raised exciting questions about efficient bioink reinforcement. Conventional single network hydrogels have neither the intrinsic fracture energy (Γ_0) nor the mechanical energy dissipation (Γ_D) capabilities of other polymer networks and are further weakened by stress concentrations arising from their random network structure. Techniques that incorporate mechanical energy dissipation

mechanisms into the hydrogel structure can dramatically improve fracture energy with only modest changes in composition. Nearly all bioink reinforcement to date uses this strategy in some form. For example, polymer functionalization increases Γ_0 by strengthening crosslinks, while interpenetrating networks, nanocomposites, and supramolecular approaches increase Γ_D by enabling applied stress to be mechanically dissipated without damaging the main network. Many of these techniques also allow ruptured bonds to heal over time, whether through reconstitution of physical bonds in ICE networks, reversible electrostatic interactions among nanoparticles and polymer chains, or by reestablishing the dynamic equilibrium of supramolecular bonds. Each of these reinforcement techniques has their own impacts on bioink viscoelastic properties, which was discussed in detail. However, exact properties are controlled by specific network architecture (polymer concentrations, identities, crosslink mechanisms, chain lengths, isotropy) and environmental properties (temperature, ion concentrations, pH), as well as strain rate, direction, and processing history. Looking forward, bioink reinforcement is expanding as its interactions with cell behavior and flow properties become clear. Combinations of multiple reinforcement techniques are expanding, and early reports indicate that combined reinforcement may have synergistic effects. New approaches like microsphere bioprinting and sliding ring crosslinks are on the horizon as well. As bioink performance improves, its potential for creating custom 3D reconstructions of patient tissue will bring it from the bench to the bedside. From a regulatory perspective, bioprinted scaffolds will be complex to regulate, since they can be simultaneously biologics, drugs, and medical devices. Fortunately, regulatory agencies have been generally proactive at providing guidelines, since it is recognized that overcoming these obstacles will be necessary for bringing 3D bioprinting towards the eventual goal of clinical use to improve patient lives.

CHAPTER 5: NANOENGINEERED IONIC-COVALENT ENTANGLEMENT (NICE) BIOINKS FOR 3D BIOPRINTING[§]

5.1 Overview

We introduce an enhanced nanoengineered ionic covalent entanglement (NICE) bioink for the fabrication of mechanically stiff and elastomeric 3D biostructures. NICE bioink formulations combine nanocomposite and ionic covalent entanglement (ICE) strengthening mechanisms to print customizable cell-laden constructs for tissue engineering with high structural fidelity and mechanical stiffness. Nanocomposite and ICE strengthening mechanisms complement each other through their synergistic interactions, improving mechanical strength, elasticity, toughness, and flow properties beyond either reinforcement technique alone. Herschel-Bulkley flow behavior shields encapsulated cells from excessive shear stresses during extrusion. The encapsulated cells readily proliferate and maintain high cell viability over 120 days within the 3D-printed structure, which is vital for long-term tissue regeneration. The unique aspect of the NICE bioink is its ability to print much taller and higher aspect ratio structures than conventional bioinks without requiring secondary supports. We envision that NICE bioinks can be used to bioprint complex, large-scale, cell-laden tissue constructs with high structural fidelity and mechanical stiffness for applications in custom bioprinted scaffolds and tissue engineered implants.

[§] Reprinted with permission from D. Chimene *et al.*, Nanoengineered Ionic-Covalent Entanglement (NICE) Bioinks for 3D Bioprinting. *ACS applied materials & interfaces* (2018).

5.2 Introduction

Three-dimensional (3D) bioprinting is emerging as a promising method for rapid fabrication of biomimetic tissue constructs using cell-containing hydrogels, called bioinks, that can be crosslinked to form a hydrated matrix for encapsulated cells.(3, 209, 330, 331) However, extrusion based 3D bioprinting has hit a bottleneck in progress due to the lack of available bioinks with high printability, mechanical strength, and biocompatibility.(332, 333) The printability of a bioink refers to the ability to print human-scale tissues and organ structures while smoothly extruding the intended architecture with high fidelity. Although recently developed bioinks enable precise deposition of viable cells, their printability in the Z-axis is hampered by limited structural integrity to support additional layers.(23, 333) Efforts to improve printability have largely focused on printing multiple materials into a single structure as well as functionalizing polymers for new crosslinking mechanisms.(23, 33, 34, 258, 334-338) Other recent developments include novel strengthening mechanisms like nanocomposites, interpenetrating networks, and self-healing hydrogels.(332, 333) Despite these efforts, existing bioinks remain severely limited when printing high aspect ratio structures over 10 mm tall.(221) These restricted vertical scales prevent replication of large scale 3D tissue organization and confines bioprinting's applications to a relatively flat plane. Some recent studies have circumvented this issue through complex thermoplastic support structures and suspension preparations.(333) However, these techniques do not address the fundamental lack of bioinks with appropriate mechanical and bioresponsive properties.

To overcome the limitations of existing bioinks, we report the development of a highly printable bioink for fabricating large scale, cell-laden, bioactive scaffolds. These improvements are achieved through a novel bioink strengthening strategy that combines nanocomposite reinforcement(6, 339)

with ionic-covalent entanglement (ICE)(340-342) to create a bioactive *Nanoengineered Ionic Covalent Entanglement (NICE)* bioink with excellent printability, mechanical properties, and shape-fidelity **(Figure 5-1a)**. Nanocomposites and ICEs have been investigated separately for improving mechanical properties, but have never been applied simultaneously to a bioink for tissue engineering or bioprinting applications.

We demonstrate this technology by taking GelMA, a popular bioactive hydrogel that is poorly printable, and applying NICE reinforcement to engineer a printable and mechanical strong bioink. The low-cost, cell adhesive, and enzymatically degradable NICE bioink can print high aspect ratio structures that are mechanically stiff and elastomeric (**Figure 5-1b**), including self-supporting, anatomically-sized structures (**Figure 5-1c**). The NICE bioink was evaluated against individual component polymers and strengthening mechanisms (nanocomposites and ICEs) to establish their contributions to NICE bioink properties. Our results demonstrate that combining nanocomposite and ICE reinforcement synergistically enhances the printability and mechanical properties without compromising bioactivity, making NICE bioinks well suited for bioprinting larger, more complex tissue structures than were possible with previous bioinks.

ICE networks are composed of two entangled-but-independent polymer networks crosslinked only to themselves through the use of distinct crosslinking mechanisms.(343) This recently developed hydrogel strengthening process is fast and cytocompatible, unlike conventional dual network strategies, making it well suited for incorporation into the 3D bioprinting toolkit. The increase in strength and toughness from ICE reinforcement is attributed to stress sharing between networks to reduce stress concentrations, as well as energy dissipation through reversible disruption of ionic network crosslinks while the more flexible covalently crosslinked network

remains intact. This mechanism also allows ICE networks to exhibit elastomeric characteristics under mechanical loading without compromising mechanical strength.(340-342)

To create a suitable ICE bioink, we combined bioactive gelatin methacryloyl (GelMA) with kappa-carrageenan (κCA). GelMA is obtained by partially hydrolyzing collagen to improve solubility, and subsequently functionalizing to allow covalent crosslinking under ultra violet (UV) light. GelMA hydrogels retain many essential properties of native extracellular matrix, including cell attachment site and matrix metalloproteinase (MMP) motifs that allow cells to remodel the hydrogel network. GelMA also undergoes thermally sensitive physical gelation around 30°C, helping to stabilize bioprinted structures.(256, 259, 344) In our system, this physical gelation is exploited by printing above the gelation temperature(37C) onto a bed below the gelation temperature(25C). This allows the bioink to quickly solidify after extrusion and improve print stability**(Figure 5-S13)**. κCA is a linear polysaccharide commonly used in foods, pharmaceuticals, and cosmetics, and was chosen as the ionic crosslinking ICE polymer for its solubility, biocompatibility, and track record of successful use in previous ICE hydrogel experiments.(345-347)

The GelMA/κCA ICE network was reinforced by incorporating two-dimensional (2D) Laponite XLG nanosilicates (nSi). These nanosilicates are disc-shaped, mineral nanoparticles 30-50 nm in diameter and ~1 nm in thickness. Negatively charged faces and positively charged edges allow reversible electrostatic interactions with the charged polymer backbones. Nanosilicate interactions can improve stiffness, elasticity, adhesiveness, viscoelastic modulus, and cell adhesion in some hydrogels, and imbue hydrogel solutions with complex fluid behavior that can improve bioprintability.(25, 27, 260) Furthermore, Laponite nanosilicates have shown broad biocompatibility in *in vivo* and *in vitro*, and are used extensively in cosmetics and toothpastes as

well as drug delivery and tissue engineering.(27, 128, 348) Previous studies have demonstrated that polyampholytic gelatin chains are strongly attracted to the negatively charged faces of nanosilicates, while κCA preferentially interacts with the positively charged edges of nanosilicates.(25, 27, 260) Dynamic light scattering and Zeta potential experiments confirm that both GelMA and κCA interact strongly with nSi **(Figure 5-S1)** as shown by the increase in hydrodynamic diameter and stabilization of zeta potential. In the NICE bioink, we hypothesize that 2D nanosilicates form reversible bonds with both GelMA and κCA, acting as a secondary electrostatic crosslinking mechanism to improve the viscoelastic properties and printability of the bioink.(290)

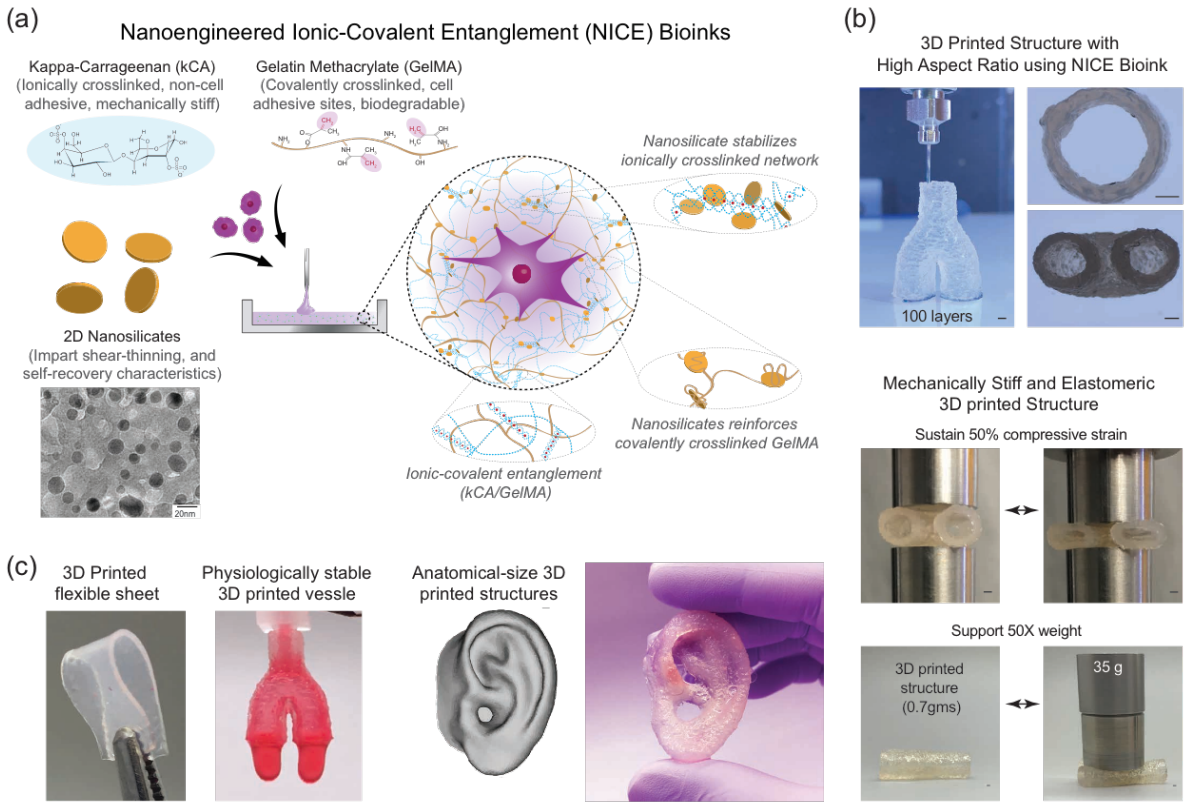

Figure 5-1. NICE bioinks combine nanocomposite reinforcement and ionic-covalent entanglement reinforcement mechanisms to create a bioink that is tough, elastic, and highly printable. (a) NICE bioinks use nanosilicates to reinforce an ionic-covalent entanglement hydrogel made from GelMA and κCA, creating a dually reinforced hydrogel network. These interactions allow the NICE bioink to behave as a solid at low shear stresses and improve shear thinning characteristics during bioprinting. After crosslinking, ICE and nanosilicate reinforcement synergistically improve mechanical strength. TEM imaging of two-dimensional nanosilicate particles showing uniform morphology. (b) NICE bioinks print freestanding hydrogel structures with a high aspect ratios and high print fidelity (scale bar = 1 mm). Crosslinked structures are stiff and elastomeric, and can support more than 50-

times their own weight. (c) 3D printed structures from NICE bioink are mechanically (film) and physiological (bifurcated vessel) stable, and have high structural fidelity (3D printed ear).

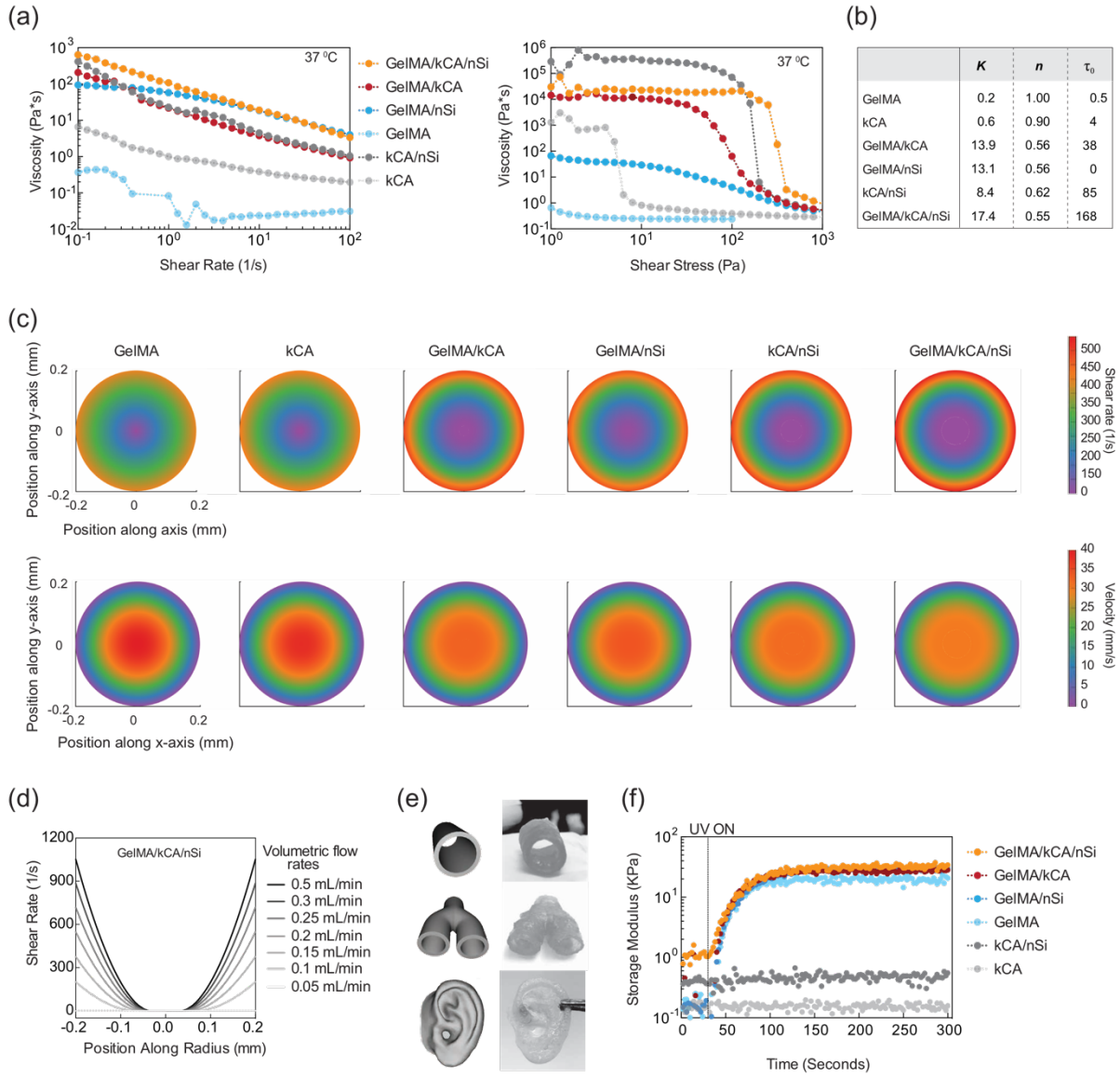

Figure 5-2. Rheological characterization of the NICE bioink. (a) Shear stress sweeps measure viscosity changes with increasing shear stress, allowing visual comparison of the yield regions of each bioink (NICE yield region shaded on graph). Shear rate sweeps illustrate the shear thinning characteristics of pre-crosslinked gels. (b) The rheological characteristics of pre-crosslinked gels derived by fitting shear stress sweep to the Herschel-

Bulkley (HB) model. HB model characteristics include *K* (consistency index), n (power law index), and τ_0 (yield stress). (c) Yield region data is fit to a Herschel-Bulkley Fluid model, allowing bioink flow through the extruder tip to be simulated under defined conditions. In these models, the shear rate and velocity profiles of the different inks is simulated under our experimental conditions (0.15 mL/min, 20mm/s at 37°C) as they pass through the extruder tip. (d) 2D profiles of the NICE bioink shear rate profile at different flow rates during extrusion printing. Flow rates from 0.05 to 0.5 mL/min are graphed, including our experimental bioink (e) NICE bioink can be used to print human-scale relevant 3D printed structures (cylindrical, Y-shaped blood vessel and ear). These three anatomical models highlight the high print fidelity between models and the printed structures. (f) UV rheology shows formation of covalently crosslinked network due to presence of GelMA when exposed to UV light (25 mW/cm^2).

5.2.1 NICE Reinforcement Improves Printability of Pre-crosslinked Bioink

Effective 3D bioprinting requires bioinks to exhibit complex fluid behaviors, but these requirements remain poorly defined despite the rapid expansion of this field. With this in mind, we examined the rheological characteristics of our bioinks (prior to crosslinking), including shear thinning behavior (shear rate sweep) and yield point (shear stress sweep, amplitude stress sweep) at physiological temperature (37 °C), compared with individual component gels (**Figure 5-2a, 5-2b, and 5-S2**). Shear rate sweep results indicate that all formulations except GelMA display clear shear-thinning behavior in that an increase in shear rate or shear stress results in a decrease in

viscosity. GelMA's gelation temperature is below physiological temperature, causing it to exhibit low viscosity fluid-like behavior (<1 Pa.s) at 37°C for all shear rates and shear stresses. The addition of nanosilicates increases the viscosities of GelMA and κCA alone and of GelMA/κCA combined.

The shear stress sweep was performed over a range of shear stress where the polymer viscosity transitions from a solid-like to liquid-like state (i.e. yield stress). This behavior can be described by the Herschel-Bulkley fluid model, $\tau = \tau_0 + K(\dot{\gamma})^n$, where τ and τ_0 represent apparent and yield stress, respectively, and $\dot{\gamma}$ is the shear rate. The consistency index (K) (Pa•s^n), is the apparent viscosity of the fluid at a shear rate of 1s^{-1}. The power law index, n, expresses how non-Newtonian a fluid is: when $n = 1$, the fluid is considered Newtonian, while $n < 1$ and $n > 1$ indicate shear thinning and thickening, respectively. The tabulated results show that all formulations exhibited shear-thinning behavior at 37 °C except GelMA ($n = 1.00$). The addition of nanosilicates reduced the power law index of GelMA (1.00 → 0.56) and κCA (0.90 → 0.62). Mixing GelMA and κCA also resulted in a low power law index that was only slightly influenced by addition of nanosilicates (0.56 → 0.55), most likely because the baseline value was already low. These reductions confirm that adding nanosilicates and κCA increases shear thinning, which improves printability by reducing flow resistance at the high shear rates generated during extrusion. Similarly, the addition of nanosilicates increased the consistency index (K) of GelMA (K:0.2→13.1) and increased both K and τ_0 of κCA (K:0.62→8.38, τ_0:4→85 Pa). Mixing GelMA with κCA also increased the consistency index and yield stress and this was further increased by addition of nanosilicates (K:13.8→17.4, τ_0:38→168 Pa). Higher yield stresses allow bioprinted structures to behave as a viscoelastic solid even before crosslinking, preventing layer spreading after extrusion and

increasing print fidelity. These results suggest that ionic-covalent entanglement and electrostatic interactions between nanosilicate and polymer chains synergistically reinforce NICE bioinks.

In addition to improving print fidelity, viscosity and high yield stress combined with shear thinning characteristics also serves to shield cells from damaging shear stresses during extrusion.(220, 225, 349) The Herschel-Bulkley fluid model parameters were used to predict shear rate and velocity distributions for fully developed flow within the extrusion tip during bioprinting (**Figure 5-2c and 5-S3**). GelMA and κCA exhibited low yield stress and shear thinning when subjected to a constant flow rate to mimic extrusion bioprinting. The addition of nanosilicates increases the size of the plug-flow region for all formulations, with NICE bioinks having the greatest area experiencing plug flow. Plug flow shields encapsulated cells from damaging shear stress and extrudes the bioink as a viscoelastic solid ($\tau < \tau_0$) thereby increasing print fidelity.(220, 225, 349) To further investigate the ability of NICE bioink for bioprinting, we determined the flow profile through a 400 μm cannula at extrusion rates between 0.05 and 0.5 mL/min, finding that plug flow occurred at all extrusion rates **(Figure 5-2d)**. Subsequently, we selected a shear rate of 0.15 mL/min for rapid bioprinting (print speed 20 mm/s). Overall, this simulation suggests that nanosilicates and κCA synergistically improve shear-thinning and yield stress in the NICE bioink, causing the NICE bioink to exhibit cell-shielding plug flow that allows the bioink to be extruded as viscoelastic solids at the optimized print parameters. The maximum predicted shear stresses (**Figure 5-S4**) were well within the safe range for bioprinted cells,(209, 350) suggesting that even higher extrusion rate bioprinting is safe with the NICE bioink.

After printing was complete, 3D-printed structures were dual-crosslinked with UV light (25 mW/cm^2 at 365 nm) and 5% KCl to obtain mechanically stable structures. The covalently crosslinked GelMA network is formed within 60-80 seconds. To quantify the gelation kinetics, a

time sweep was performed by monitoring storage modulus of bioink formulations in presence of UV light (**Figure 5-2f, 5-S5**). All bioink formulations containing photocrosslinkable GelMA (GelMA, GelMA/nSi, GelMA/κCA and GelMA/κCA/nSi) rapidly solidified under exposure to UV light. The inclusion of κCA and nanosilicates did not significantly affect the rate of UV gelation.

We next evaluated the printability of the NICE bioink by printing physiologically relevant structures **(Figure 5-2e)**. As previously mentioned, printability refers to the ability to print high aspect ratio structures at human-relevant scales, and extrude the intended structure smoothly and with high fidelity. Conventional bioinks print precisely on the x- and y-axes but collapse under the weight of subsequent layers, causing 3D structures to have poor print fidelity, particularly on the z-axis(height). Therefore, our bioinks were tested on all 3 axes to objectively quantify printability. We attempted to print the simplest possible structure that meets these requirements using each bioink: a hollow cylinder approximating the shape of a human-scale bronchus or blood vessel. The cylinder shape used for printability quantification is an 8 mm interior diameter cylinder with 1mm thick walls, and when using the NICE bioink, a stable structure was printed up to 3cm (150 layers) in height(**Figure 5-S14)**. In contrast, none of the component inks (GelMA, GelMA/nSi, κCA, κCA/nSi, GelMA/κCA) could print cylinders above 3 mm (15 layers) without collapse. Layer spreading was quantified by measuring the cylinder wall thickness of the lowest 5 and highest 5 layers, revealing that wall thickness measurements of NICE cylinders remained within ±10 % of intended diameter at all measured points. Shape fidelity was measured by comparing the printed cylinder's actual height and diameter to its intended ideal dimensions, which revealed no significant variations in either metric. More complex structures were also bioprinted to demonstrate the range of the NICE bioink's potential applications. A Y-shaped bifurcated blood

vessel was printed through a 400 μm diameter tip (each layer height: ~200 μm, extrusion width: ~500 μm) to a height of 2 cm (100 layers) with 5 mm lumen diameter and 1 mm wall thickness(**Figure 5-S11**). It is important to note that the difference between extruded width and tip diameter are caused by adjusting the rate of extrusion relative to printer movement speed, in order to match desired dimensions. The 500 μm extruded line width used here is better or comparable to existing bioprinted line widths demonstrated recent publications, which used strategies including GelMa-Alginate blends,(337) Hyaluronic acid and methacrylated hyaluronic acid,(33) gelatin with PEGX crosslinker,(23), gelatin with alginate(334), Gelatin and alginate with PEG crosslinkers(338), methacrylated hyaluronic acid,(258) and GelMA reinforced with co-printed poloxamer (221) (**Figure 5-S6**). Physiologically relevant anatomical shapes such as a human-size ear were also printed using NICE bioink. These printability results represent a significant advancement of NICE bioink over conventional bioinks in terms of both total height and aspect ratio for freestanding bioprinted structures.(23, 209, 308, 333) The development of this NICE bioink allows for a simple and direct approach to 3D printing of large biomimetic structures by improving Z-axis printability, and provides a platform technology for the creation of further bioactive bioinks. Further, combining the computational approach and experimental validation described here can be used in the future to develop a more rational approach to the design of advanced bioinks.(332, 333)

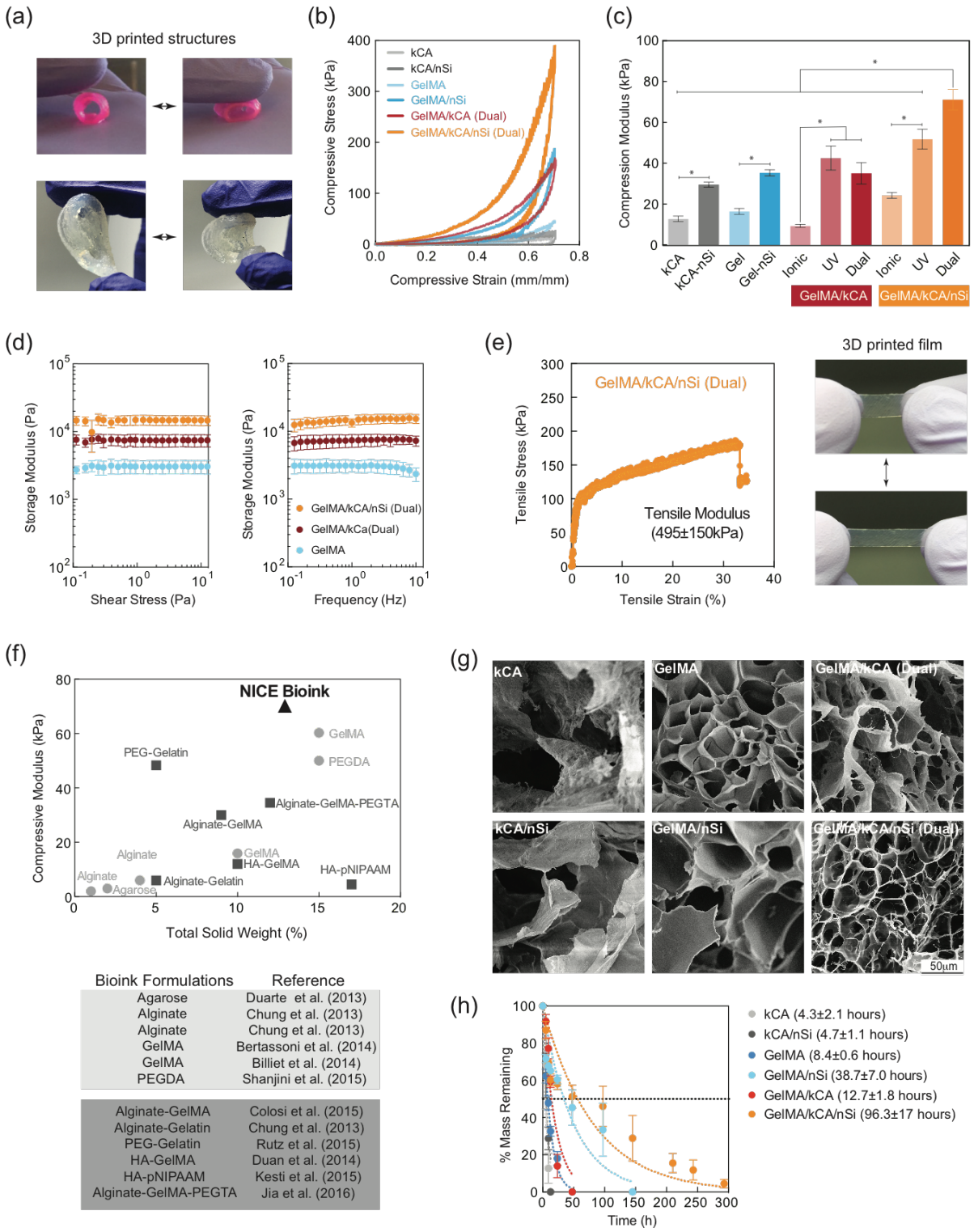

Bioink Formulations	Reference
Agarose	Duarte et al. (2013)
Alginate	Chung et al. (2013)
Alginate	Chung et al. (2013)
GelMA	Bertassoni et al. (2014)
GelMA	Billiet et al. (2014)
PEGDA	Shanjini et al. (2015)
Alginate-GelMA	Colosi et al. (2015)
Alginate-Gelatin	Chung et al. (2013)
PEG-Gelatin	Rutz et al. (2015)
HA-GelMA	Duan et al. (2014)
HA-pNIPAAM	Kesti et al. (2015)
Alginate-GelMA-PEGTA	Jia et al. (2016)

Figure 5-3 Continued. (a) The application of both sharp and blunt force demonstrate the resilience and elasticity of crosslinked NICE structures. (b) Cyclic compression to 70% strain demonstrates NICE reinforcement's synergistic effect on mechanical strength compared to either single reinforcement mechanism, ICE (GelMA/κCA) and nanocomposite-(κCA/nSi and GelMA/nSi) as well as individual polymeric hydrogels (κCA, GelMA). (c) Compression moduli data for NICE and component hydrogels. Ionic and UV columns represent ICE networks with only a single network crosslinked: UV light crosslinks only GelMA, while ionic solutions only crosslink κCA. (d) Shear stress and frequency sweeps measure hydrogel storage moduli from 0.1 to 10 Pa and 0.1 to 10 Hz. (e) Compressive modulus of various bioink plotted with respect to total polymer weight. NICE bioink outperform all other bioinks in term of mechanical stiffness. (f) Tensile stress of bioprinted NICE segments to failure. Manual extension demonstrates the elasticity of the NICE bioink. (g) SEM imaging of the porous microstructure of each crosslinked hydrogel. (h) Degradation kinetics of hydrogels under accelerated conditions. The degradation was accelerated using a heightened concentration of collagenase II, which enzymatically degrades GelMA.

5.2.2 NICE Reinforcement Improves Post-crosslinked Bioink Mechanical Properties

Mechanical properties of 3D bioprinted structures are critical for maintaining the structural integrity of scaffold and control cell behaviors including proliferation and differentiation.(209) Nevertheless, many 3D printed structures using conventional bioinks are mechanically weak and lack appropriate elastomeric characteristics due to their chemical structure as well as poor inter-layer cohesion. In contrast, the NICE dual-crosslinked bioprinted constructs were shown to be resilient under mechanical loading and to withstand severe mechanical deformation without delamination of printed layers (**Figure 5-3a**). We compared the mechanical properties of individual components and strengthening mechanism on the mechanical properties of crosslinked hydrogels (GelMA, GelMA/nSi, κCA, κCA/nSi, GelMA/κCA and GelMA/κCA/nSi). Hydrogels containing GelMA were covalently crosslinked with UV light (25 mW/cm^2 of 365nm) for 80 seconds, while hydrogels containing κCA were immersed in a 5% KCl solution to obtain ionically crosslinked networks. This amount of UV light is not . Since the GelMA/κCA/nSi (NICE bioink) and GelMA/κCA have both ionic and covalently crosslinkable networks, they were tested with both networks crosslinked (dual-crosslinking), and with only a single network crosslinked (ionic or UV only). This allowed us to isolate the effect of crosslinking from each polymer's presence alone.

We subjected different hydrogel formulations to unconstrained, uniaxial cyclic compression (70% strain) using a universal testing machine (UTM) to determine compressive modulus (from 0-20% strain region), and maximum stress (at 70% strain) during a compression ramp. The stress-strain compression data indicates that all hydrogel compositions containing GelMa can sustain 70% strain without fracture (**Figure 5-3b, 5-S7**). The results also revealed that the dual-crosslinked

NICE bioink (71.1±4.9 kPa) had a four-fold higher compressive modulus than GelMA alone (16.5±1.5 kPa) and two-fold higher modulus than either the GelMA/nSi nanocomposite (35.3±1.5 kPa) or GelMA/κCA ICE network (35.1±5.2 kPa) (**Figure 5-3c**). This pattern was consistent for maximum cycle stress at 70% strain as well (301.7±21.0 kPa) by the NICE bioink compared to component gels. Similarly, stress and frequency sweep results showed that NICE reinforcement (14.2± 1.4 kPa) resulted in a storage modulus four-fold higher than GelMA (3.1±0.3 kPa) and two-fold higher than GelMA/κCA (7.4±0.9 kPa) (**Figure 5-3d, 5-S8**). We also investigated the elastomeric characteristics of the NICE bioink *via* 5-cycle compression tests to 40% compressive strain (**Figure 5-S9**). Ionically crosslinked networks (κCA and κCA/nSi) exhibited high plastic deformation (<30% recovery), particularly during the first cycle, while covalently crosslinked networks (GelMA and GelMA/nSi) showed high recovery (>90%). Both ICE (GelMA/κCA) and NICE (GelMA/κCA/nSi) showed >75% recovery after cyclic deformation. While NICE reinforced inks show reduced recovery, their energy dissipated per cycle remains steadily higher than the singly reinforced bioinks even after 5 cycles, demonstrating that NICE reinforcement is stable over multiple cycles**(Figure 5-S9)**. Interestingly, recent evidence suggests that κCA ICE networks can completely recover from strain over time as the ionic network re-forms, although this is outside this paper's scope.(346, 347, 351) In addition to being able to sustain compression, a 3D printed NICE film could sustain stretching and had high tensile modulus (495±150 kPa) (**Figure 5-3e**). These tests confirm that combining ICE and nanocomposite reinforcement mechanisms results in a synergistic improvement in mechanical properties that translates into mechanically strong and resilient bioprinted structures.

The most common technique for improving hydrogel printability and mechanical strength is increasing crosslinking density and polymer concentration, however this approach also reduces

hydrogel porosity and water content, limiting its suitability for bioprinting encapsulated cells.(209, 333) Earlier studies have investigated polymers such as GelMA(257), alginate(32), agarose(352) and PEG(353), or polymer blends such as alginate-gelatin(32), alginate-GelMA(337), PEG-gelatin(23), hyaluronic acid (HA)-GelMA(34), HA-poly(N-isopropylacrylamide) (pNIPAAM)(33) and alginate-GelMA-PEG(338) for bioprinting. While some of these inks can provide suitable mechanical stiffness, their 3D printability remains limited, and their suitability as bioinks can be compromised due to raised polymer concentrations (**Figure 5-3f**).(209, 333) The NICE bioink formulation overcomes this limitation by combining multiple reinforcement techniques to create mechanically stiff and elastomeric 3D printed structures where, unlike conventional reinforcement by increasing polymer content, (209, 343) the mechanical improvements from the ICE and nanocomposite strengthening mechanisms are not due to a decrease in mesh size or hydration degree.

Scanning electron microscopy (SEM) imaging revealed that all formulations maintained highly interconnected porous networks with diameters ~ 20-50 μm (**Figure 5-3g**). Water content in NICE bioink (89.5±0.3%) was similar to that of GelMA/nSi nanocomposites (89.2±0.5%) and GelMA/κCA ICE network (91.6±0.8%), which are also within the typical hydration range of many body tissues (**Figure 5-S10**). Our results here demonstrated that the NICE bioink benefited from both ICE and nanoparticle reinforcement, with compression moduli doubling with each reinforcement mechanism, and without adverse effect on water content and pore size, which are both important measures of hydrogel's suitability for maintaining cell populations.(333)

NICE reinforcing mechanisms improve physiological stability of 3D printed structures while retaining proteolytic functionality. Proteolytic degradation allows encapsulated cells to locally control degradation rates, allowing remodeling and migration to proceed on cellular level.

However gradual degradation kinetics are desirable for mechanical resilience during the initial phases of tissue remodeling. The physiological stability of the NICE bioink was characterized by determining biodegradation/dissolution kinetics as described in previous work.(27) (354)A collagenase biodegradation assay was carried out in PBS with 2.5 U/mL collagenase type II to determine the susceptibility of the NICE bioink to cellular remodeling enzymes under accelerated conditions **(Figure 5-3h)**. Compared to GelMA (half-life: 8.4±0.6 hours), GelMA/nSi (38.7±7.0 hours) and GelMA/κCA (12.7±1.8 hours) exhibited extended half-lives as measured by remaining hydrogel mass, which was further increased in the NICE bioink (96.3±17 hours). These results are comparable to previous results on GelMa and GelMa nanosilicate degradation, and suggest that NICE reinforcement increases enzymatic stability even further.(27, 354)Thus, NICE bioinks demonstrate a gradual rate of enzymatically-driven degradation desirable for long-term tissue regeneration.

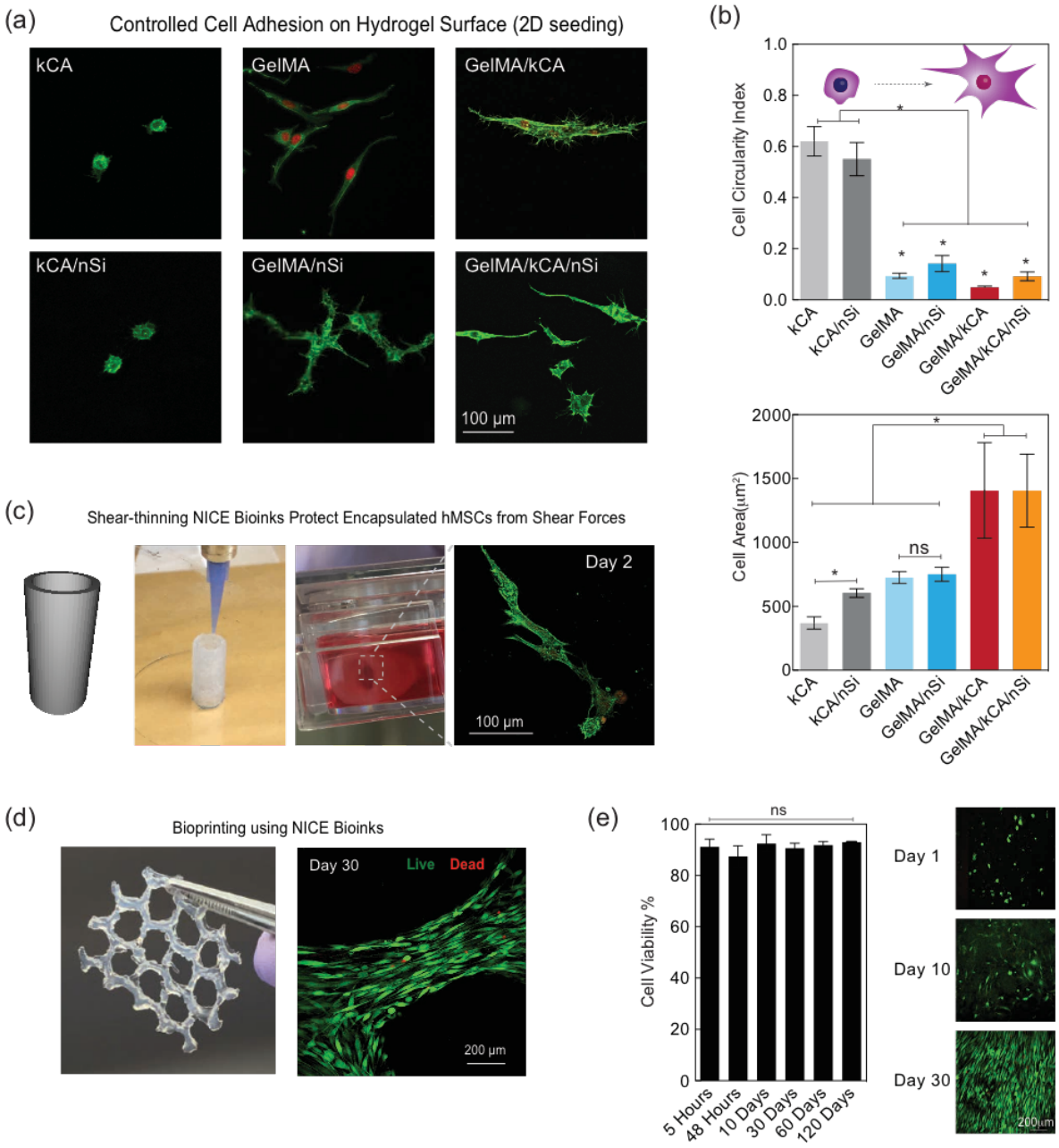

Figure 5-4. NICE Bioink Bioactivity and Biocompatibility. Cell adhesion characteristics of individual polymers (κCA, GelMA), nanocomposites (κCA/nSi and GelMA/nSi), polymer blend (GelMA/κCA) and NICE bioink (GelMA/κCA/nSi) were investigated. (a) surface seeded preosteoblasts illustrate that GelMa is the only NICE component necessary for cell

adhesion, and addition of the other components does not interfere with adhesion. (b) The addition of GelMA and nanosilicates significantly improved cell adhesion and spreading. (c) Bioprinted cylindrical structure loaded with cells show high cell spreading after 48 hours as determined by circularity index and area of adherent cells. (d) Encapsulated cells were seen aligning parallel to 3D printed scaffold structures. (e) The printed structure shows high short- and long-term cell viability (>85%), indicating that our bioprinting process is biocompatible. Short-term (48 hrs) cell viability indicates high cell survival throughout the bioprinting process, supporting predictions from earlier modeling that shear forces during extrusion would not cause significant mortality. Long term viability and adhesion allows cells to interact with and remodel scaffolds over time.

5.2.3 NICE Reinforced Scaffolds are Bioresponsive

The aim of 3D bioprinting is to regenerate functional tissues, and in this regard ECM derived bioinks like GelMA are the most promising because they support a wide array of cell-ECM interactions, enabling cell migration and remodeling and allowing bioinks to directly influence cell fate.(256, 259, 344, 355) GelMA's bioactivity has been thoroughly investigated in earlier studies, so here the NICE bioink is compared to component gels to ensure key favorable cell-material interactions are maintained.(256, 259, 355) We investigated the cell-material interactions of the bioink formulations by characterizing murine 3T3 preosteoblast adhesion to the surface of the various gel formulations. This cell line was used because previous studies have suggested that nanosilicates may promote osteogenesis, which is a future research avenue for bioprinted NICE structures.(27, 354, 356)Assessment of the extent of cell spreading was quantified by circularity index and cell size. This analysis demonstrated that cells on hydrogels containing GelMA (GelMA, GelMA/nSi, GelMA/κCA and GelMA/κCA/nSi) elongated significantly, while those on κCA or κCA/nSi did not elongate (**Figure 5-4a, b)**, indicating that the GelMa component is responsible for cell adhesion, and that NICE reinforcement by inclusion of κCA and nanosilicates does not interfere with cells' ability to adhere to the bioink. While nanosilicates had a modest effect on overall cell spreading are in κCA hydrogels, the ICE (GelMA/κCA) and NICE (GelMA/κCA/nSi) networks supported much higher cell spreading than the other formulations. GelMA contains cell adhesion sites to support strong cell-matrix adhesions, but the extent of spreading is also proportional to substrate rigidity.(357) Since the concentration of GelMA is similar in these formulations, the increase in cell area is likely due to increased mechanical stiffness in these networks.

To investigate the feasibility of this NICE ink for bioprinting applications involving cell-laden bioinks, we encapsulated cells within the NICE bioink and printed 3D constructs (cylinders with 1 cm diameter, 1 mm wall thickness, and a height of 2cm) as well as honeycomb patterns (regular hexagon 5 mm edges, 1mm thick walls). The honeycomb pattern was chosen as a low-infill density pattern to demonstrate the mechanical properties of a crosslinked NICE biostructure(**Figure 5-4c, d**). Cells spread quickly along the long axis of the bioink filaments and cell numbers visibly increased until the scaffold surface was saturated with cells. Deeper areas within the scaffold retained high cell viability and spreading, but lower cell density. This is likely due to reduced nutrient diffusion deeper into the scaffold. Cell viability was high (>90%) immediately after 3D bioprinting and remained high throughout the 120-day observation period (**Figure 5-4e**). These results support our modeling data findings that plug flow conditions during extrusion shield the cells from shear forces during extrusion, and that bioprinted NICE scaffolds are cytocompatible for long-term culture. Overall, these results demonstrated that the NICE bioink supports consistently high levels of cell viability, attachment, and proliferation**(Figures 5-4a&f, 5-S12)**, suggesting that GelMA's excellent bioactivity is maintained in NICE reinforced gels.(27, 354, 358)

5.3 Conclusion

In this study, we introduced a novel reinforcement technique, Nanoengineered Ionic Covalent Entanglement (NICE), to engineer an advanced bioactive bioink with superior printability and mechanical properties. The NICE bioink can be used to print freestanding, high aspect ratio structures over 3cm and 150 layers tall with excellent shape fidelity, and structures become tough and elastic after crosslinking. Meanwhile, bioprinted cells maintained high viability, attachment,

and spreading throughout the 120-day period. We used a Herschel-Bulkley computational model incorporating rheological data on yield point, consistency, and shear thinning characteristics to simulate bioink behavior and predict the shear stresses cells experience during bioprinting. The Herschel-Bulkley fluid behavior of the NICE bioink may explain the improved 3D printability and results in plug flow that shields bioprinted cells from shear stresses under extrusion conditions. This model can be used to identify print parameters that maximize printability. The NICE bioink demonstrated here was developed as platform technology, intended to provide researchers with a facile technique for bioprinting larger 3D tissue scaffolds without requiring costly multi-headed printing systems. Future work will investigate a broader range of material compositions to customize NICE bioinks for specific applications and tissue types. Upcoming NICE bioink developments also include localizing bioactive cues within scaffolds to spatially direct cell behavior, and arranging multiple cell types and concentrations within scaffolds to replicate multilayered tissues like cartilage and blood vessels. These approaches could enable precise spatial control over cell behavior within human-scale bioprinted structures, bringing bioprinting closer to the goal of recreating functional human tissues. The NICE bioink is unique among existing bioinks because it combines superior printability, improved mechanical properties, and excellent bioactivity into a single bioink formulation. This represents a significant advance in bioink technology, and will prove to be a useful tool for researchers seeking to replicate human tissues as large and bioactive 3D structures.

5.4 Experimental Section

5.4.1 Materials Synthesis:

The porcine gelatin (Bloom No. 300, Type A), Irgacure2959 (2-Hydroxy-4'-(2-hydroxyethoxy)-2-methylpropiophenone) and methacrylic anhydride were purchased from Sigma Aldrich (USA). Kappa-carrageenan (κCA) was obtained from TCI America (USA). Nanosilicates (Laponite XLG) were obtained from BYK Additives Inc. Gelatin methacryloyl (GelMA) (80% methacrylated) was synthesized by dissolving 10g of gelatin in 100 mL phosphate buffered saline (PBS), then heating for 1 hour at 60°C. After dissolution, 8 mL of methacrylic anhydride was added dropwise over a period of minutes. The solution was kept at 60°C for 3 hours, then 400 mL of 1X PBS was added. The solution was dialyzed at 50°C for 7 days and lyophilized. The NICE bioink (10%w/v GelMA, 1%w/v κCA, 2% w/v nanosilicates, and 0.25% w/v Irgacure2959) was obtained by 1:1 mixing of 20%w/v GelMA + 2%w/v κCA with a solution of 4% w/v nanosilicates + 0.5% w/v Irgacure 2959. The solution was vortexed and subsequently sonicated for 2 minutes to ensure homogenous dispersion of components. Solutions were stored overnight at 40°C. The bioink was covalently crosslinked via exposure to 25 mW/cm2 365nm UV light for 80 seconds. Ionic crosslinking was completed by submersion in 5% potassium chloride (KCl) for 30 minutes.

5.4.2 Physiological Stability:

Equilibrium hydration was calculated by soaking crosslinked gels in PBS overnight and obtaining their weights, then lyophilizing the gels and comparing dry weight to wet weight. Biodegradation rates were assessed in presence of 2.5 U/mL Collagenase Type II (Worthington Biochemical Corporation). 150μL hydrogels (n=3) were crosslinked and placed in pre-weighed

individual containers, then allowed to sit at room temperature overnight in 1X PBS to reach equilibrium. 15 hours later, the solution was replaced with 1X PBS with 2.5 U/mL Collagenase Type II and the hydrogels were stored in an incubator at 37°C. The mass of hydrogel remaining was measured by carefully removing all solution from the container, then weighing the hydrogel together with the container as to not damage samples. Hydration percentages were calculated using the formula Hydration (%)=[1-(dry mass/wet mass)]x100.

5.4.3 Microstructure:

The morphology of the hydrogel was visualized using scanning electron microscope (SEM) using a NeoScope JCM-5000 SEM. Hydrogel samples were frozen in liquid nitrogen, cracked with a razor blade, and lyophilized. Samples were fixed and sputter coated with gold to a thickness of 21nm.

5.5 Rheological Characterization:

Rheological testing was carried out on an Anton Paar Physica MCR-301 Rheometer, using a 10mm PP10 measuring plate and 50mm CP50-1 measuring plate. UV gelation, frequency sweeps, stress sweeps, shear stress sweeps, and shear rate sweeps were performed. For UV gelation, each hydrogel's time to gelation was tested by measuring changes in storage modulus while the gels were exposed to 15, 25, or 45 mW/cm2 of 365nm UV light **(Figure 5-S2)**. Each covalently crosslinkable bioink was tested (n=3) at 10mm diameter x .5mm thick. UV light was turned on at 30s and remained on for 300 seconds. The frequency sweep was carried out on crosslinked

hydrogels at a stress of 1 Pascal(Pa) and covered a range of frequencies from 0.1 Hz to 10 Hz. The stress sweep, also on crosslinked hydrogels, swept a range of shear stresses from 0.1 Pa to 100 Pa at a frequency of 1 Hz. Finally, stress and shear rate sweeps on non-crosslinked hydrogels were carried out sequentially to measure viscosity under a range of conditions designed to correspond to printing conditions. Shear stress was varied from 0.01 to 2000 Pa. Shear rates from 0.01 to 100 s^{-1} were tested. Gels were kept in a high humidity atmosphere to prevent dehydration from affecting results.

5.6 Bioprinting:

Printed shapes were designed in Solidworks and exported as STL files. STL files were loaded into Slic3r to customize printing options and converted into G-code printer instructions. Pro-interface was used to interface with the 3D printer. Layer height was set to 200 μm, layer width was measured as 500 μm, and print speed was kept at 20mm/s, or .15 mL/min, for all trials. When necessary, 2 μl/ml of plumbers tracing dye was added to enhance visualization. The bioink was stored at 37 °C and loaded into an extrusion tube with a 400μm nozzle tip and extrusion printed through an I3 RepRap printer. Using these settings, a hollow 2 cm tall x OD 10mm ID 8mm cylinder was printed from the bioink. A bifurcated branching blood vessel shape was printed with interior diameter of 5mm, wall thickness of 1 mm, and height of 1.5cm.

5.7 Uniaxial Compression:

Cast crosslinked hydrogel samples were cut into cylinders using a biopsy punch, making sample material cylinders 6 mm in diameter by 2.5 mm thick. Each sample was checked using digital calipers and the ADMET MTEST Quattro eXpert 7600 and variances in dimension were factored in to stress and strain calculations. Unconstrained samples were compressed and returned to starting position at 1mm/minute. Raw data for single cycle compression was processed using an Excel macro for compressive modulus (calculated from 5-15% strain region), and maximum stress at 70% strain. Raw data for multi-cycle compression (40% strain) was also processed to monitor compressive modulus, energy dissipated, and recovery using a separate macro. Compression data was taken for hydrogel samples of GelMA (10%), GelMA (10%)/nSi (2%), κCA (1%), κCA(1%)/nSi(2%), GelMA(10%)/κCa(1%), and GelMA(10%)/κCA(1%)/nSi(2%). Where applicable, gels were also tested as semi-interpenetrating networks (sIPNs) by crosslinking only one network.

5.8 Derivation of Model:

The fully-developed velocity profile for a Herschel-Bulkley fluid flowing in a tube was derived using the conservation of momentum equations in cylindrical coordinates. For laminar, isothermal flow of an incompressible fluid with no-slip boundary conditions, the equations describing flow in the r and θ directions simplified to 0, leaving only the equations describing flow in the z direction (Eq. S1).

$$\rho\left(\frac{\delta u_z}{\delta t}+u_r\frac{\delta u_z}{\delta r}+\frac{u_\theta}{r}\frac{\delta u_z}{\delta \theta}+u_z\frac{\delta u_z}{\delta z}\right)=\rho g_z-\frac{\partial P}{\partial z}+\left(\frac{1}{r}\frac{\delta(r\tau_{rz})}{\delta r}+\frac{1}{r}\frac{\delta(\tau_{\theta z})}{\delta \theta}+\frac{\delta(\tau_{zz})}{\delta z}\right) \quad \text{Eq. S1}$$

Under steady-state, with only axially directed flow, the equation further simplifies to Eq. S2.

$$\frac{\partial P}{\partial z} - \rho g_z = \frac{\Delta P}{\mathrm{L}} = \frac{1}{r}\frac{\delta(r\tau_{rz})}{\delta r} \quad \text{Eq. S2}$$

Integration with respect to r yields Eq. S4, which reaches a maximum at the wall (r = R).

$$\tau_{rz} = \frac{r}{2}\frac{\Delta P}{\mathrm{L}} \quad \text{Eq. S3}$$

$$\tau_{wall} = \frac{R}{2}\frac{\Delta P}{\mathrm{L}} \quad \text{Eq. S4}$$

Combining Eqs. S3 and S4 and relating the result to the Herschel-Bulkley model gives Eq. S5.

$$\tau_{rz} = \tau_0 + k\dot{\gamma}^n = \frac{r}{R}\tau_{wall} \quad \text{Eq. S5}$$

Solving for shear rate ($\dot{\gamma} = \frac{\partial u_z(r,\theta)}{\partial r}$) and noting the plug flow region (0 < r < R0) gives Eq. S6.

$$\frac{\partial u_z(r,\theta)}{\partial r} = \begin{cases} 0 & ,0 < r < R_0 \\ \left(\frac{\tau_{wall}}{k}\right)^{\frac{1}{n}}\left(\frac{r}{R} - \frac{\tau_0}{\tau_{wall}}\right)^{\frac{1}{n}} & ,R_0 \le r \le R \end{cases} \quad \text{Eq. S6}$$

Integration yields the velocity profile (Eq. S7) which describes the velocity profile..

$$u_z(r,\theta) = \int \frac{\partial u_z(r,\theta)}{\partial r}\partial r = \begin{cases} R\left(\frac{n}{n+1}\right)\left(\frac{\tau_{wall}}{k}\right)^{\frac{1}{n}}\left(1 - \frac{\tau_0}{\tau_{wall}}\right)^{\frac{n+1}{n}} & ,0 < r < R_0 \\ R\left(\frac{n}{n+1}\right)\left(\frac{\tau_{wall}}{k}\right)^{\frac{1}{n}}\left(\left(1 - \frac{\tau_0}{\tau_{wall}}\right)^{\frac{n+1}{n}} - \left(\frac{r}{R} - \frac{\tau_0}{\tau_{wall}}\right)^{\frac{n+1}{n}}\right) & ,R_0 \le r \le R \end{cases}$$

Eq. S7

Integration across the tube yields the volumetric flow rate (Eq. S8).

$$Q = \int_0^R u_z(r,\theta)\, dr \quad \text{Eq. S8}$$

$$= \pi R^3 \left(\frac{n}{n+1}\right)\left(\frac{\tau_{wall}}{k}\right)^{\frac{1}{n}}\left(1-\frac{\tau_0}{\tau_{wall}}\right)^{\frac{n+1}{n}}\left(1 - \frac{2n}{(2n+1)(3n+1)}\left(1-\frac{\tau_0}{\tau_{wall}}\right)\left(\frac{\tau_0}{\tau_{wall}}n + 2n + 1\right)\right)$$

$\frac{\partial u_z(r,\theta)}{\partial r} = shear\ rate$

$u_z(r,\theta) = velocity$

$Q = volumetric\ flow\ rate$

$n = flow\ behavior\ index$

$k = flow\ consistency\ index$

$\tau_0 = yield\ stress$

$R = inner\ radius\ of\ needle$

$L = length\ of\ needle$

$\Delta P = applied\ pressure$

$\tau_{wall} = stress\ at\ wall\ of\ needle$

$R_0 = radius\ of\ plug\ flow\ region$

5.9 Computational modeling:

The equations above were solved in Matlab (MathWorks, Natick, MA) to simulate extrusion through a needle. Since the flow rate of the print and the rheological constants were known, an

iterative approach was used to find τwall from Eq. S8. Once τwall was determined, the velocity and shear rate profiles (Eqs. S6 and S7) could be easily plotted for all positions within the flow.

5.10 In vitro studies:

To evaluate the hydrogel bioink's ability to culture cells, murine 3T3 preosteoblasts (MC3T3-E1 Subclone 4, ATCC CRL-2593) were seeded on 3.5 cm diameter samples. MC3T3s were cultured on hydrogels of GelMA (10%), GelMA (10%)/nSi (2%), κCA (1%), κCA(1%)/nSi(2%), GelMA(10%)/κCa(1%), and GelMA(10%)/κCA(1%)/nSi(2%). All cells were used at passage 22 and 100,000 cells were seeded onto each gel sample. Cells were cultured in normal growth media at 37°C for 3 days. After 3 days, each hydrogel was triple rinsed with PBS, soaked with paraformaldehyde for 1.5 hours, then triple rinsed again. Cells were then permeabilized by exposure to Triton X for 20 minutes and triple rinsed with PBS. 100µl of phalloidin was added to each well plate, then stored at room temperature for 1 hour. After triple rinsing with PBS, cells were incubated with RNAse for 1 hour at 37°C, triple rinsed again, and incubated with propidium iodide at 37°C for 20 minutes. Finally, cells were triple rinsed in PBS. Cells were imaged using confocal microscopy and EZC1 software. Images were taken as Z-stack.ids files, which were compiled into 3D models using EZC1 software, and compiled into focused 2D images using EZC1 or imageJ via the bioformats import and stack focuser plugins. The circularity index on imageJ was used to quantify a cell's deviation from a perfect circle, and the area size was also calculated using imageJ. Images used in analysis were taken randomly of the surfaces of the 3 replicate scaffolds.

5.11 3D Bioprinting:

Because the κCA, κCA/nSi, GelMA, GelMA/nSi, and GelMA/κCA all failed the standard cylinder test below 3mm height, bioprinting was only attempted using the NICE bioink(GelMA/κCA/nSi). 1x106 mouse preosteoblast MC3T3-E1 Subclone 4 (ATCC® CRL-2593™) cells were trypsinized for 5 minutes, 10mL of media was then added, and the solution was centrifuged for 5 minutes. The supernatant was removed, and the cell pellet was resuspended in 200 uL of media. The resuspended solution was gently mixed into 2.8 mL of the NICE bioink at 37°C by pipetting, for a final concentration of approximately 3.33x105 cells/mL. The bioink was prepared using PBS to maximize cell viability. The bioink was then transferred into the extruder and printed into several constructs using the same print setting defined in the bioprinting section: a 400um tapering luer-lock nozzle, line width of 500um, a layer height of 200um, and a print speed of 0.15 mL/min. A hollow cylinder was printed with an outer diameter of 1 cm, inner diameter of .8 cm, and height of 2 cm. 4 flat disc scaffolds 1 cm in diameter and 1 mm in height were also printed as replicates. These discs scaffolds used a 100% rectilinear infill, and were used to replicate the cell viability results. A honeycomb pattern was also used as a low-infill density pattern to demonstrate the mechanical properties of a crosslinked NICE biostructure. This pattern was a regular hexagon infill with 5 mm edges and 1mm thick walls). All printing settings were kept consistent during bioprinting as described in the bioprinting section. All scaffolds were crosslinked using UV light as described above, and soaked in a 5% KCl solution for 5 minutes, then incubated in DMEM media with 10% FBS. The ionic crosslinking time was reduced relative to the molded bioinks because the bioprinted structures were thinner than the cylindrical samples used in the earlier experiments(1mm thick vs 2.5mm thick), and concurrent research determined

that the 30 minute crosslinking time was unnecessarily long.(260) Viability was analyzed using live dead imaging was carried out by incubating cells in a PBS solution containing 1μL/ ml calcein AM and 2μL/ml ethidium homodimer for 1 hour, then soaking once in 1X PBS to limit background signal. Viability measurements were taken at 5, 24, and 48 hours, and 10, 30, 60, and 120 days. Imaging was carried out using confocal microscopy: Z-Stack images were taken of 3 randomly selected surface areas and 1 cross-section of the 3D bioprinted structures. Z-stack images were taken to a depth of 400 um using a confocal microscope and processed using EZC1 and imageJ to count total number of living and dead cells within each 3D section of the biostructure.

5.12 Statistical Analysis:

The quantitative experimental results were analyzed and graphed as mean ± standard deviation. Statistical analysis of all quantitative data was performed using one-way analysis of variance (ANOVA), and pairwise data comparison was done via Bonferroni's multiple comparison test. Statistical significance was shown as $*p < 0.05$, $**p < 0.01$, and $***p < 0.001$.

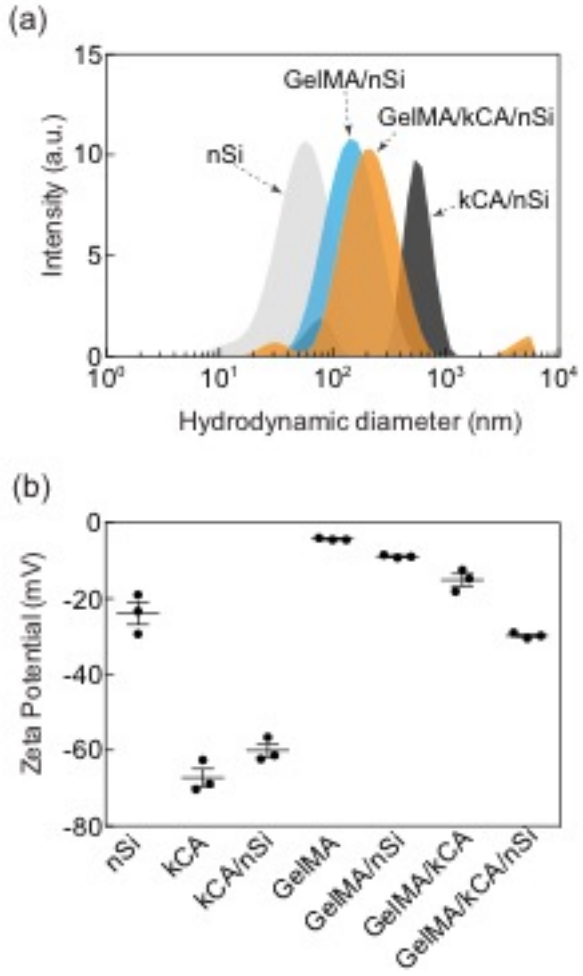

Figure 5-S1. Hydrodynamic diameter and electrophoretic mobility of nanosilicates and effect of addition of different polymer on these properties.

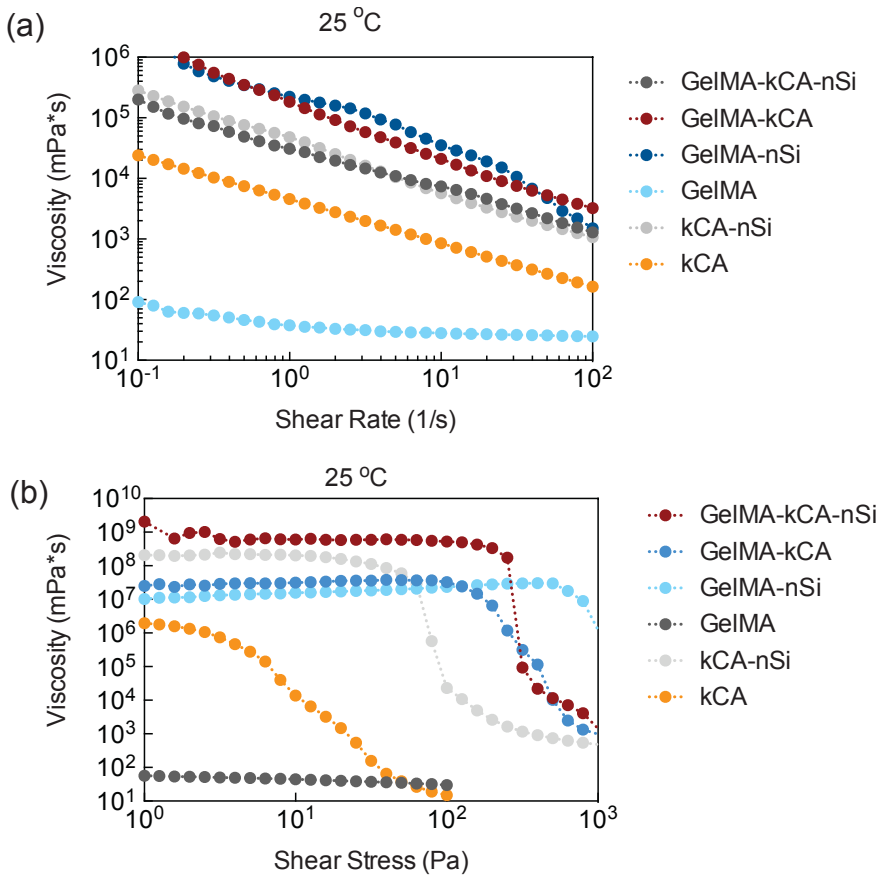

Figure 5-S2. Shear stress and shear rate sweep at room temperature(25°C).

From Figure 5-S2, the materials have a yield stress (Fig 5-S2a) and behave as power-law fluids at high shear rates (Fig 5-S2b). A Herschel-Bulkley model ($\tau = \tau_0 + k\dot{\gamma}^n$) incorporates yield stress and power-law behavior and is therefore appropriate for modeling flow of these materials. Other models, such as Cross-Carreau, can more accurately describe the behavior seen in Fig 5-S2a but require 4 to 5 fitting parameters. Although such a model will describe flow better, the benefits to using more complex models are minimal in the context of this study. In Fig 5-S2a, you can see that the viscosity of GelMA-kCA-nSi is very high below τ = 100 Pa; there will be negligible flow

below this applied pressure. Instead of using a complex model that will account for this, we can simplify the behavior to Herschel-Bulkley flow with a yield stress of approximately 100 Pa.

We used the shear stress sweep to find the three parameters (n, k, and τ_0). The shear rate sweep was not used to determine these values because the yield stress behavior was not captured in the tested range of shear rates. You cannot find n and k from Fig 5-S2b and τ_0 from Fig 5-S2a separately; doing so gives an incorrect model describing the data. The shear stress sweep was transformed into shear-rate Vs shear stress. Shear rate was obtained from apparent viscosity using $\dot{\gamma} = \frac{\tau}{\eta}$. We then fit the data to find n, k, and τ_0. There is minimal flow before the selected range of values, so this data is modeled as Herschel-Bulkley (Figure 5-S3).

(a)

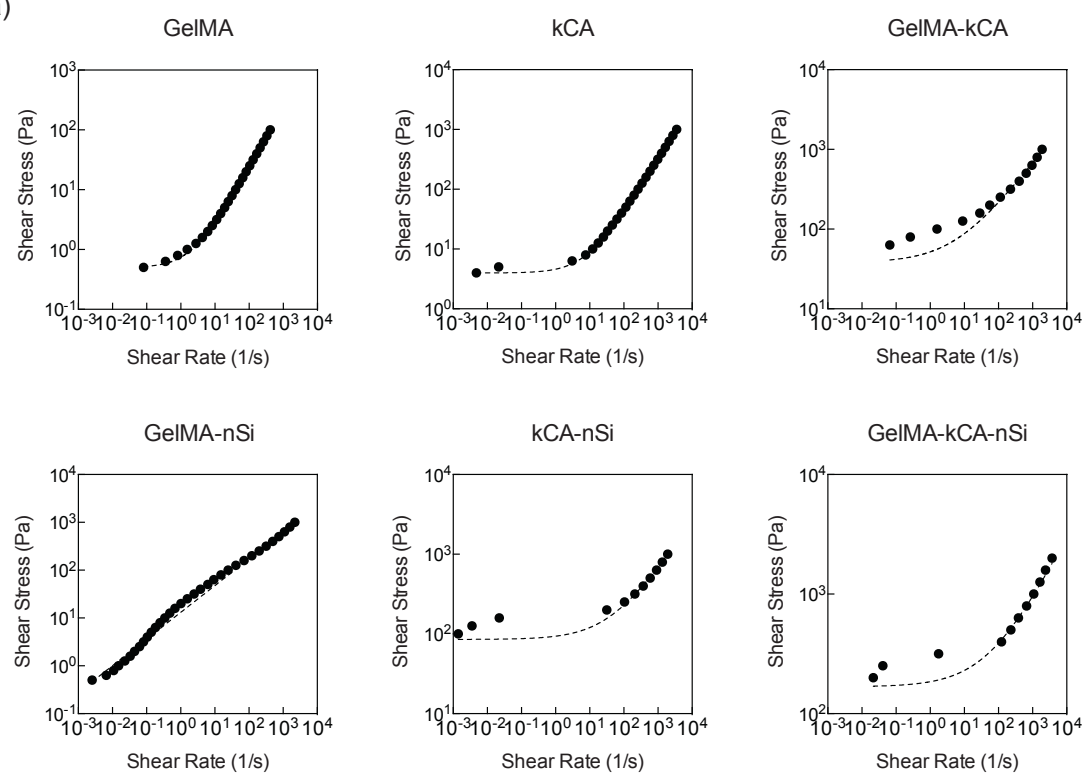

(b)

	Yield Stress (Pa)	n	K	R^2
GelMA	0.5	1.00	0.2	0.999
GelMA-nSi	0.0	0.56	13.1	0.997
kCA	4	0.90	0.6	0.999
kCA-nSi	85	0.62	8.4	0.988
GelMA-kCA	38	0.56	13.8	0.987
GelMA-kCA-nSi	168	0.55	17.4	0.976

Figure 5-S3. (a) Herschel-Bulkley model fit (dotted line) to the stress sweep data (solid dots). (b) The value of n, k and yield stress obtained from the fit are summarized in table. For each hydrogel, 3 samples were tested at 37C.

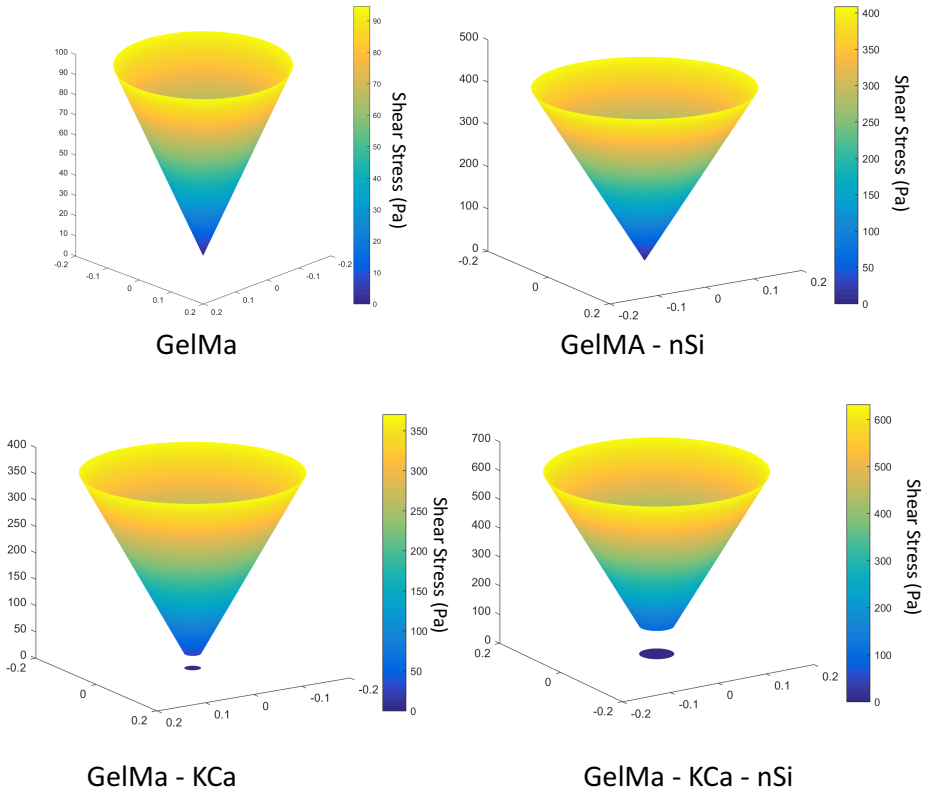

Figure 5-S4. Shear stress and position within extruder tip. Flow profile was calculated at .15 ml/min extrusion rate, matching the rate used in printing. Position on X and Y axes corresponds to distance from the center of the extruder (0,0). Only the bioink combining nano-reinforcement and ICE entanglement(GelMa - KCs - nSi) was used in for bioprinting cell-containing structures due to its superior z-axis printability. The rheological data used in these models was taken from shear stress sweeps at 37C as shown in figure 5-S3.

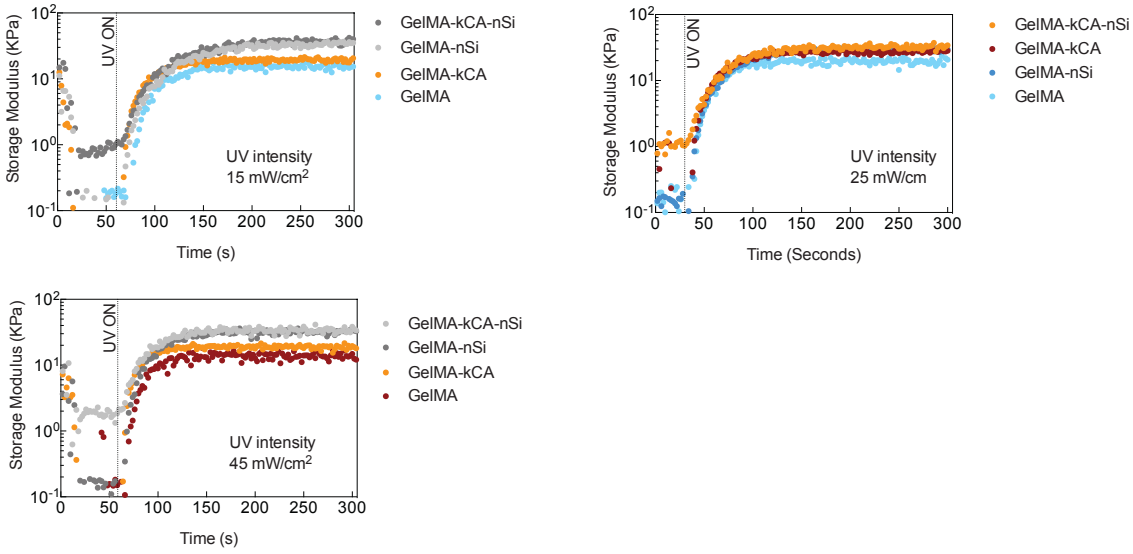

Figure 5-S5. Gelation kinetics at different UV intensities.

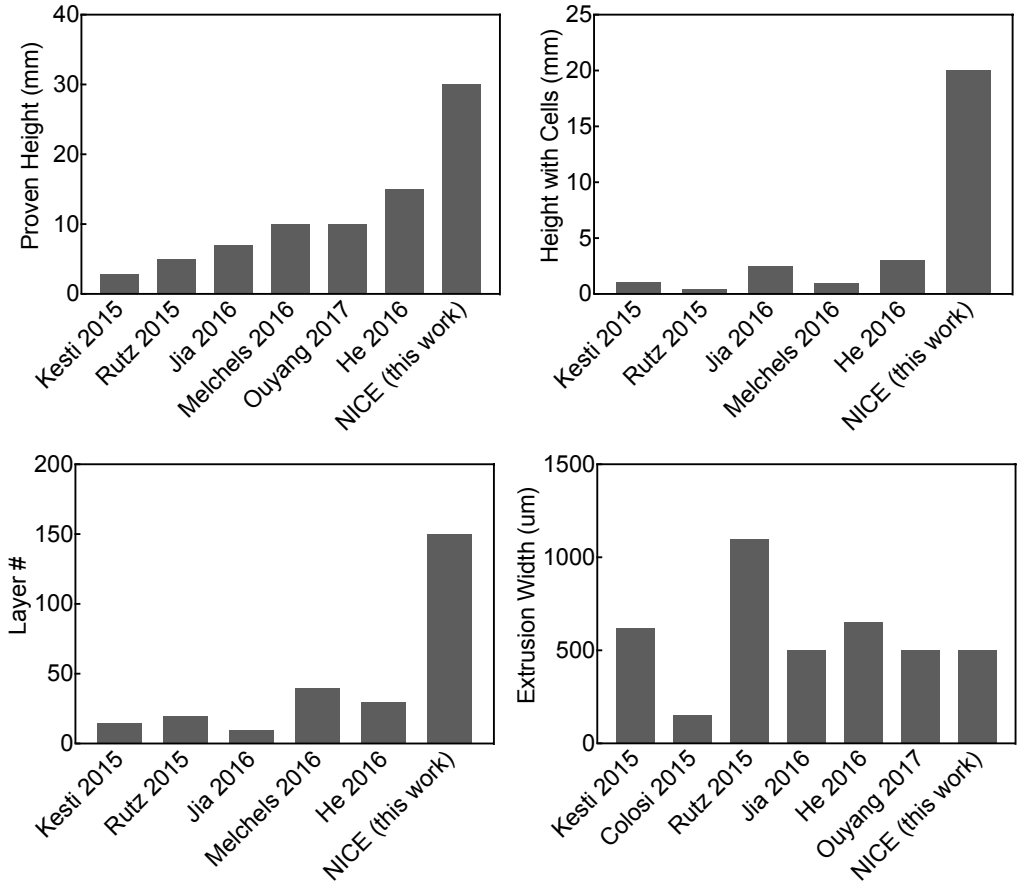

Figure 5-S6. A quantitative comparison of 3D Printability in this work to recent publications.(23, 33, 221, 258, 334, 338) Papers included freestanding bioprinted(3D printing of cell-containing hydrogel) structures. UL: Maximum printed demonstrated structure height UR: Maximum demonstrated bioprinted(cell-containing) height. LL: Number of printed layers demonstrated in paper. LR: Comparison of extrusion width data.

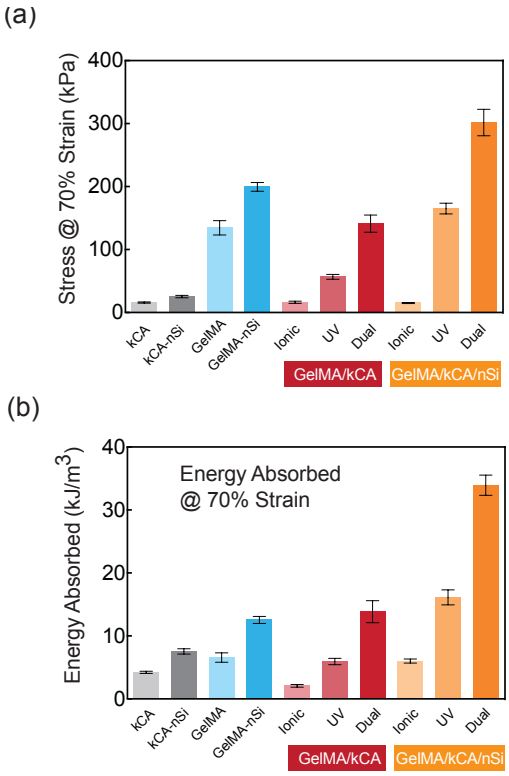

Figure 5-S7. Maximum stress and energy absorbed determined from cyclic compression data at 70% strain.

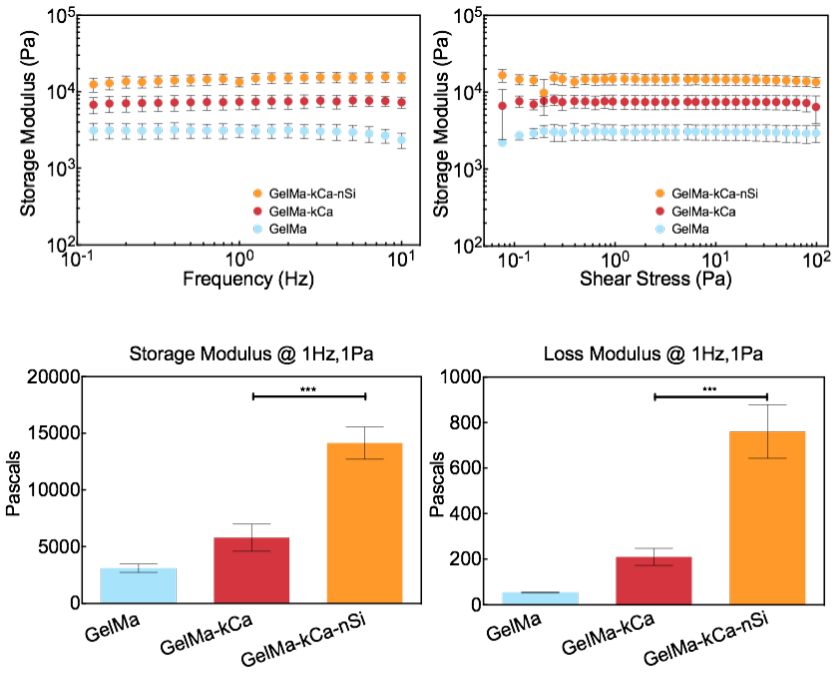

Figure 5-S8. Storage and Loss Moduli of Select Hydrogels. Frequency and Stress sweeps were performed to collect storage and loss moduli for crosslinked gels. Results indicate that gels retained their structure throughout both sweeps and that the NICE bioink (GelMA/kCa/nSi) enjoyed significant increases in both storage and loss modulus relative to the other tested gels.

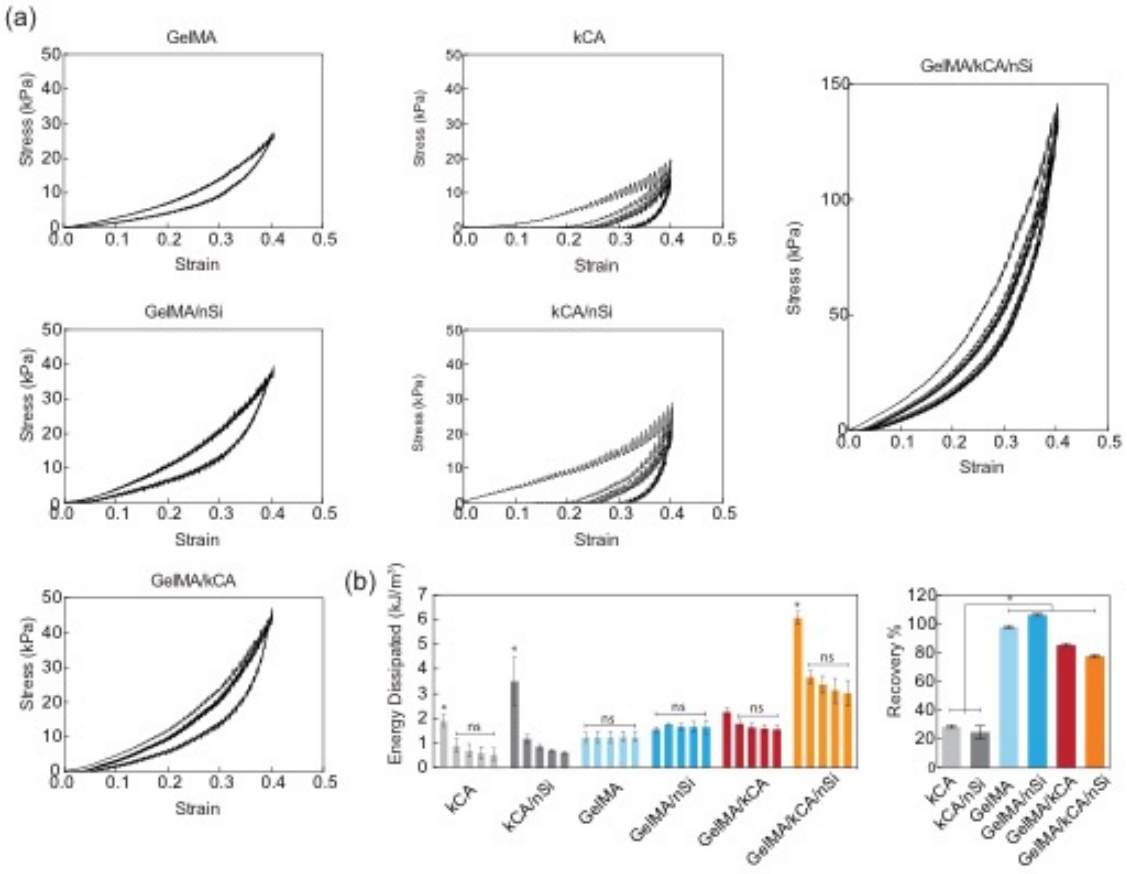

Figure 5-S9. (a) Cyclic compression (5 cycles) of different hydrogels samples at 40% strain. (b) Energy dissipated and total recovery determined from the cyclic compression data. Plastic and elastic deformation of hydrogel networks is visible here over multiple cycles. Because the GelMa network remains intact and elastic, no macroscopic plastic deformation is visible in ICE and NICE hydrogels. However, the breaking of ionic bonds can be seen in the lower recovery and energy dissipated of ICE and NICE hydrogels after cyclic compression compared to the completely elastic recovery of GelMa and GelMa-nSi nanocomposite. However, dual- reinforced NICE hydrogels maintained a higher total energy dissipation than nanoreinforced hydrogels throughout all 5 cycles.

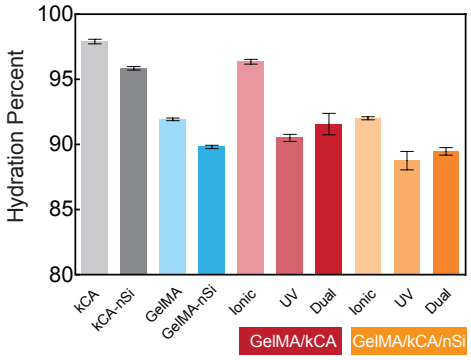

Figures 5-S10. Hydration degree of crosslinked hydrogels.

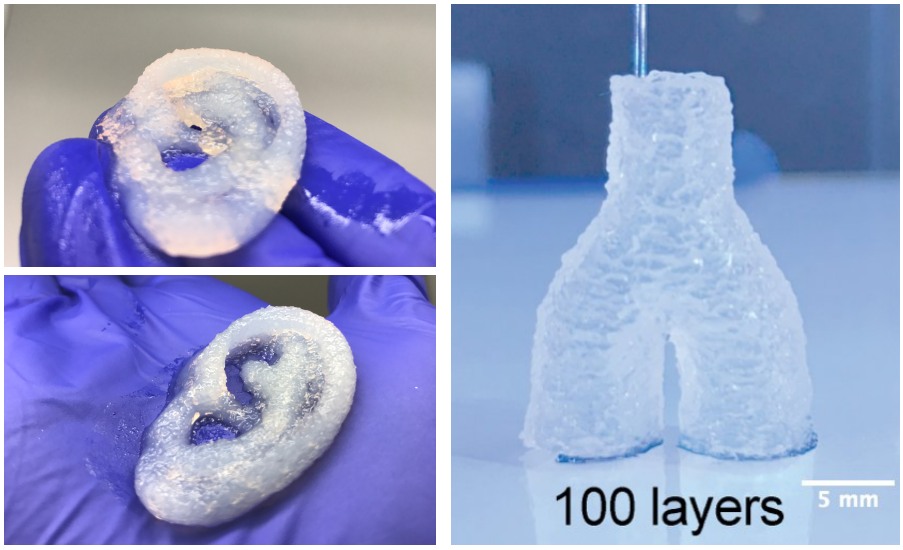

Figure 5-S11. Additional Overhang Images. Overhangs are present in the ear scaffold at both the lobe(bottom) and helix(top) of the ear. This bifurcated blood vessel demonstrates an overhang that merges two cylinders starting 8mm above the beginning of the print.

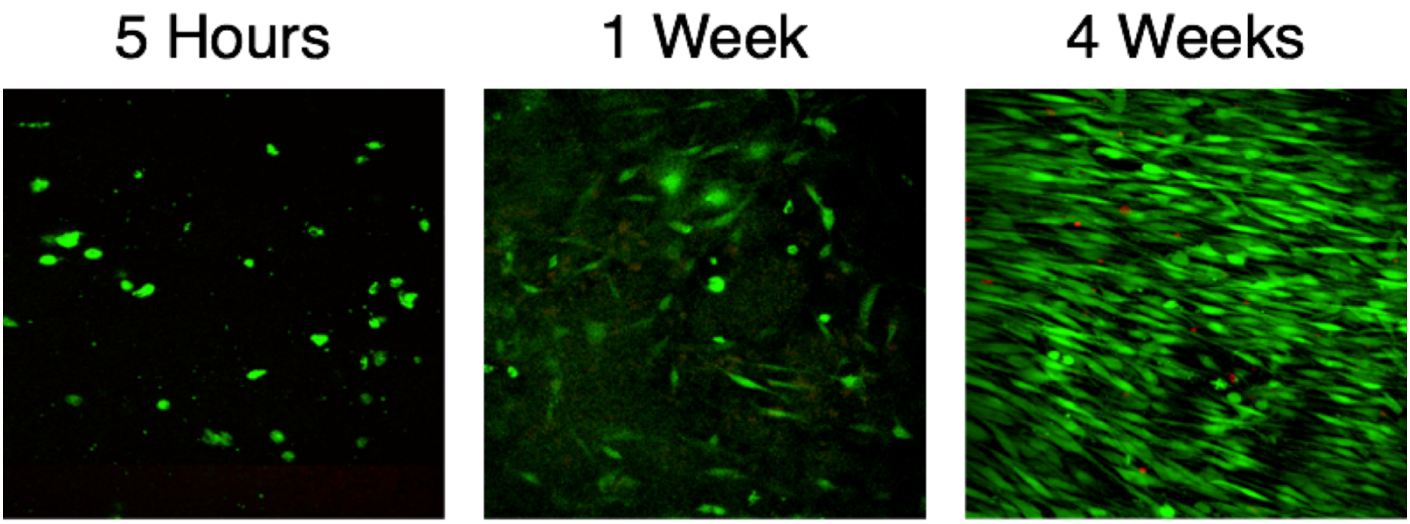

Figure 5-S12. 3D bioprinted NICE structures support Cell Proliferation. Z-Stack Images taken of a sections of a 3D bioprinted cylindrical structure with encapsulated 3T3 murine preosteoblasts dyed with calcein AM and ethidium homodimer as described in the methods section. Z-stack images were taken to a depth of 400 um using a confocal microscope and processed using EZC1 and imageJ to count total number of cells within 3D sections of the biostructure. This figure illustrates the high viability and increase in cell density that was observed.

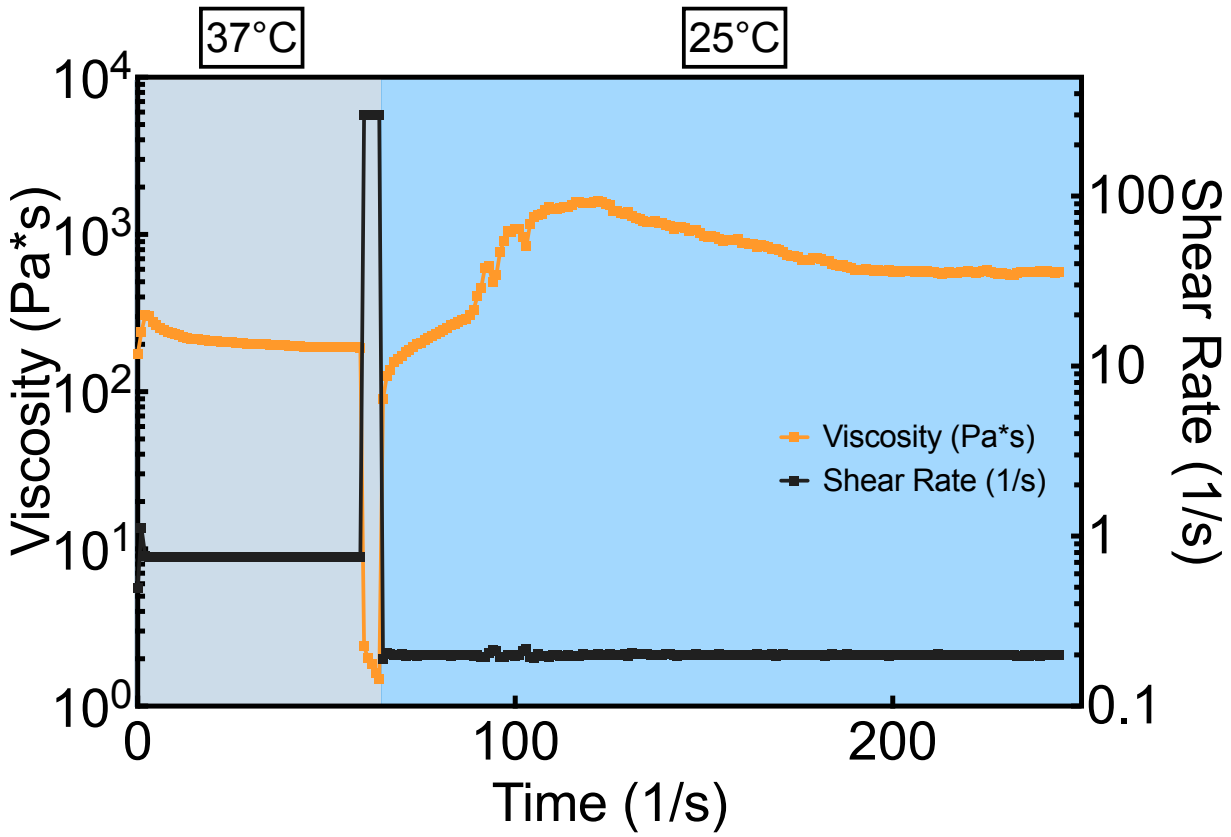

Figure 5-S13. Peak Hold Test. This test was designed to simulate the changes in viscosity during the bioprinting process that occur in response to changing shear rate and temperature. The temperatures used reflect the internal syringe barrel temperature(37 °C) and the external room temperature(25 °C), while shear rates reflect the wall shear rates in the barrel(left side), then in the extruder tip as calculated in the models described above, followed by a baseline low shear rate to represent the printed structure. These results illustrate how the NICE bioink's thermal responsiveness and shear thinning properties minimize shear stress during extrusion(left) while allowing the printed bioink's viscosity(right) to quickly recover well above its initial value. This effect contributes to the high stability of NICE bioprinted structures even prior to crosslinking.

(A)

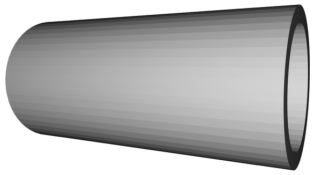

(B)

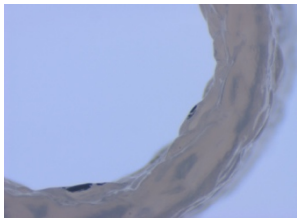

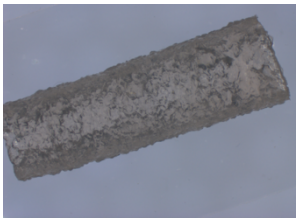

(C)

Scaffold Characteristic	Standard Value	Printability Success Criteria
Cylinder Height	3 cm	3 cm +- 5%
Wall Thickness	1 mm	1 mm +- 5%
Aspect Ratio	20	20 +- 5%
Lumen Diameter	8 mm	8 mm +- 5%
Nozzle Diameter	400 µm	n/a
Line Width	500 µm	n/a
Layer #	150 Layers	n/a
Print Speed	0.15 mL/min	n/a

Figure 5-S14. Quantification of 3D Printability Through a Standard Print. Bioprinted structures that can support large numbers of layers require a 3D test to determine suitability for printing. Here we developed a quantitative measurement of printability by creating a standard scaffold shape that can be used to quantify the quality of each print. (a) The standard prints were designed in as .stl files (b) The print quality is established using stereomicroscope images of the finished scaffold to compare to standard cylinder dimensions. Measurement were taken at both the top and bottom of the structure to ensure consistency. Only the NICE formulation could pass this test, while component gels could not be printed taller than 3mm. (c) The success criteria for printability is low deviance from the expected structure dimensions. To qualify as printable, shapes should be no more than 5% deviant in any metric.

CHAPTER 6: BIOPRINTING OSTEOGENIC SCAFFOLDS FOR BONE REPLACEMENT: A FOCUSED APPLICATION OF OPTIMIZED NICE BIOINKS

6.1 Overview

Bioprinting is an emerging type of additive manufacturing approach to fabricating patient-specific, implantable three-dimensional (3D) constructs for regenerative medicine. However, developing cell-compatible bioinks with high printability, structural stability, biodegradability, and bioactive characteristics is still a primary challenge for translating 3D bioprinting technology to pre-clinical and clinal models. To overcome this challenge, we develop a nanoengineered ionic covalent entanglement (NICE) bioink formulation optimized for bone regenerative bioprinting. The NICE bioinks allow precise control over printability, mechanical properties and degradation characteristics, enabling custom 3D fabrication of mechanically resilient, cellularized structures by combining nano-reinforcement and ionic-covalent entanglement of gelatin and kappa-carrageenan. We demonstrate cell-induced remodeling of 3D bioprinted scaffolds over 90 days demonstrating deposition of nascent extracellular matrix proteins. Interestingly, the bioprinted constructs induces endochondral differentiation of encapsulated human mesenchymal stem cells (hMSCs). Using next-generation transcriptome sequencing (RNA-seq) technology, we establish the role of nanosilicates, a bioactive component of NICE bioink, to stimulate endochondral differentiation at transcriptome level. Furthermore, we demonstrated the ability of NICE bioink to fabricate patient-specific, implantable 3D scaffolds for repair of craniomaxillofacial bone defects.

We envision transformation of this NICE bioink technology towards a realistic clinical process for 3D bioprinting patient-specific bone tissue for regenerative medicine.

6.2 Introduction

Bone grafting, the introduction of bone material to an injury in order to improve healing, is performed nearly a million times a year in the US. It is the second most common tissue transplant worldwide after blood transfusions. While autografting the patient's own bone tissue is the gold standard, it requires invasive bone harvesting surgery and is limited by the patient's supply of spare bone. These drawbacks have led to a wide variety of bone substitute attempts dating back over 50 years, including allografts, ceramics, collagen and hydroxyapatite, and more recently cell and tissue engineering. Despite significant research advancements, existing bone graft substitutes today are still missing one or more of the requirements laid out in Giannodis' Diamond Theory: osteogenic cells & vascularization, mechanical stability, growth factors, and osteconductivity/osteoinductivity.(359) In this paper, we bring newly emerging bioprinting technology to bear on this problem, and develop bioprinted structures with these requirements in mind to create a potential custom patient specific alternative to autografts.

Bioprinting is an emerging field based on layer by layer fabrication of structures containing cell-laden hydrogels, called bioinks. The promise of precisely controlling cell and biomaterial distributions to recreate the complexity of human tissue has made bioprinting a popular research area for tissue regeneration. However, the potential applications of bioprinting have been limited due to the lack of bioinks capable of meeting the demands of both 3D printing and tissue engineering.(206) For example, ideal bioinks must be capable of extruding into stable 3D

structures, while also protecting cells during and after printing, and providing an appropriate environment that can be remodeled into the target tissue. Unfortunately, conventional hydrogels are weak and poorly printable.(209) Compromising between these ideals has led to bioinks with sub-par printability and biocompatibility, with bioinks unable to print structures taller than a few millimeters.(211) This has led to intensive research on developing bioinks that are highly printable, structurally stable, and protect encapsulated cells while facilitating long term tissue formation.(360)

New techniques are being developed to more efficiently improve bioink mechanical properties and printability without compromising biocompatibility. Most of these techniques, including nanocomposites and interpenetrating networks, work by addressing two key weaknesses of conventional hydrogel networks: their heterogeneous network structures and their poor capacity for mechanical energy dissipation. By improving stress sharing across the network and allowing mechanical energy to be dissipated, hydrogel strength can be increased dramatically while maintaining a highly hydrated, biocompatible network. Further, choosing reinforcement techniques that significantly affect flow properties also allows printability to simultaneously enhanced. The efficiency of these reinforcement techniques is leading researchers to develop ways to combine different reinforcement mechanisms together to provide greater control over the bioink's mechanical and printability properties.(212, 361)

Recently, we demonstrated that by incorporating both nano-reinforcement and ionic-covalent entanglement simultaneously into a highly cell compatible gelatin-methacryloyl (GelMA) bioink, both printability and mechanical properties can be drastically improved without compromising biocompatibility. The resulting nanoengineered-ionic-covalent-entanglement (NICE) bioink is viscoelastic, and capable of bioprinting freestanding structures several centimeters tall in a variety

of shapes that were previously not possible. The bioink was shown to protect encapsulated cells throughout the printing process due to its low yield stress and shear-thinning properties. Additionally, encapsulated cells retained high viability (>89%) for more than 120 days, and bioprinted scaffolds also retained their shape and size throughout the entire four month period.(211) These properties make NICE reinforced bioinks an ideal platform for developing full-scale bioprinted structures that are both strong and enzymatically resorbable.

In this paper, we use the NICE bioink platform to create an osteoinductive bioink for bone tissue engineering for several reasons. Firstly, the high stiffness and nanosilicate content of NICE bioinks creates an osteoinductive environment in absence of growth factors.(27, 362) Secondly, the high print fidelity of NICE bioinks facilitates rapid printing of large, resilient structures needed by patients in many bone graft cases.(211) Thirdly, by creating custom resorbable scaffolds using patient's own bone cells, we may be able to facilitate faster bone healing.

In order to adapt the NICE reinforced bioinks to osteogenic tissue bioprinting, the bioink must be highly printable, mechanically strong, cause osteogenic differentiation, and be biodegradable. The difficulty of combining these requirements in a single bioink has been a major obstacle in bioprinting since its inception. Natural protein-derived polymers like GelMA are used to fabricate hydrogels that closely mimic the native microenvironment of stem cells. While hydrogels are well suited for cell growth and remodeling, they lack the printability and mechanical properties necessary for 3D bioprinting. Hydrogel polymer networks are conventionally formed as randomly crosslinked, heterogeneous networks, whose stiffness is controlled by crosslink density. While dense crosslinking improves stiffness, it causes hydrogels to quickly lose toughness and become brittle, making it ineffective for significant hydrogel reinforcement.(212) Even more importantly,

conventional hydrogel networks lack the ability to dissipate mechanical energy, since their high water content reduces molecular friction and entanglement. This energy dissipation ability is the main contributor to the toughness of many other polymer networks. Energy dissipation can be incorporated into hydrogels by introducing sacrificial bonds and reversible physical interactions, which can be ruptured to dissipate accumulated stress. This method can significantly increase fracture toughness. NICE reinforcement, described in our previous paper, combines two distinct methods of incorporating energy dissipation mechanisms into a hydrogel bioink: nano-reinforcement and ionic-covalent entanglement (ICE).(211) This dual reinforcement creates a much more robust bioink than single techniques, while keeping the bioink highly hydrated and cell friendly.(361)

Nano-reinforcement and ionic-covalent entanglement both reinforce hydrogels by enabling them to reversibly dissipate mechanical energy. For nano-reinforcement, nanosilicates (Laponite XLG) were added at 0-4 wt%. Nanosilicates (nSi) are synthetic 2D nanoclays with 1 nm in diameter and express a positive surface charge on their faces and a negative charge around their edges. These permanent surface charges allow the nanoparticles to form non-covalent electrostatic bonds with polymers. These bonds act as weak reversible crosslinks to dissipate mechanical energy without disrupting the hydrogels overall network structure, reinforcing the hydrogel.(211) These same interactions also give nanosilicates powerful effects on flow behavior that can be exploited to simultaneously improve printability. Nanosilicates-polymer solutions are highly shear thinning but have heightened viscosity at low shear.(211) This allows apparent viscosity to drop as the ink flows through the extruder tip, protecting cells, but quickly rise after extrusion, which keeps extruded bioink in place.

Ionic-covalent entanglement is a type of interpenetrating network where two separate, but interwoven polymer networks are created through distinct crosslinking methods. We added 0-3% kappa carrageenan (kCA), this ionically crosslinking polysaccharide network is kept distinct from the covalently crosslinkable GelMA network by its crosslinking mechanism. This ionically crosslinked network is brittle, while the covalently crosslinked GelMA network is much more elastic. During deformation, the ductile network disperses stress across a large damage zone region, while the more brittle network is disrupted. The combination of mechanical energy dissipation spread across a broad region greatly increases hydrogel mechanical strength.(212, 361) kCA also raises viscosity at bioprinting temperatures, preventing flow as the bioink cools.

GelMA alone is a good hydrogel for cell culture for its ECM-like environment and cell attachment sequences but is poor for bioprinting due to its thermal gelation and low viscosity. These make GelMA too fluidic to print tall structures. The combination of these mechanisms efficiently reinforces the GelMA bioink and modifies its rheology, improving its printability and structural stability. To optimize the bioink for osteogenic bioprinting, the bioink should be highly hydrated (>85% water), stiffer than 25 KPa, be capable of printing anatomical-size complex 3D structures. To examine these features a range of bioink compositions were created **(Figure 6-1A)** and examined to optimize the bioink to meet these properties.

Accordingly, development of an osteogenic NICE bioink followed several steps. First, a range of bioink formulations are developed and tested for printability performance and corresponding rheological properties, then the mechanical and degradation characteristics of the most suitable bioinks are evaluated. Finally, human mesenchymal stem cells(hMSCs) are encapsulated in the bioink and bioprinted into 3D scaffolds, which are evaluated over long term culture for histological

changes related to tissue remodeling as well as calcium deposition. Finally, practical examples of bioprinted scaffolds demonstrating potential surgical are created.

6.3 Results and Discussion

6.3.1 Designing Bioink and Optimizing its Printability and Performance

Many existing bioinks are capable of printing only low layer number structures a few millimeters tall due to their flow characteristics. However, for bioinks to be used for bone regeneration, they must be able to precisely replicate large, centimeter scale bone segments that may be irregularly shaped in all three dimensions. Therefore, optimized bioinks must be first evaluated for printability. We elected to start with a NICE formula established to be able to print tall, high aspect ratio structures to find a range of printable compositions **(Figure 6-1B)**. Each composition was printed into a standard test cylinder, where a 3 cm(150 layer) tall, hollow cylinder was printed, with a 10mm outer diameter and 1mm thick walls **(Figure 6-1C)**. Printability performance was quantified by determining (1) whether a composition could reach the full 3 cm height; (2) the absence of major defects by testing whether the cylinder could hold water; and (3) fidelity between height and diameter of the printed cylinder and its intended dimensions.

Initial testing focused on varying GelMA concentration from 5% to 15% while holding kCA (1%) and nSi (2%) concentrations constant **(Figure 6-1C, top row)**. The bioink with the lowest amount of GelMA (5% GelMA, 1% kCA, 2% nSi) sagged under its own weight and could not be printed above 1 cm in height, while higher amount of GelMA (7.5% to 12.5%) bioinks were able to print to 3 cm tall cylinder without any visible wall defects. Increasing GelMA concentrations

led to more rigid cylinders. This observation was attributed to stronger, rapid thermal gelation at higher GelMA concentrations. When GelMA concentration was raised to 15%, rapid changes in viscosity during printing caused extensive clogging, making printing difficult. These observations suggest that GelMA's thermal gelation plays a role analogous to cooling in thermoplastic printing: thermal gelation stabilizes extruded filament during printing, so insufficient gelation causes structures to "melt", while too much gelation reduces inter-layer adhesion and causes clogging.

The NICE bioink (7.5% GelMa, 1%kCA, 2% nSi) composition was the most printable, so it was used as the basis for testing nanosilicate concentration **(Figure 6-1C, middle row)**. Nanosilicates imbue bioinks with shear thinning behavior, which has been shown to improve printability by reducing apparent viscosity during extrusion. Interestingly, without nanosilicates the bioink was able to reach the full 3 cm height but was plagued with major errors and holes throughout the print caused by inconsistent extrusion. In contrast, printing with 2, 3, and 4% nSi concentrations led to smooth, consistently extruded cylinders. Because print quality was substantially equivalent at these concentrations, the 2% nSi NICE formulation was selected for future studies.

Finally, printability was tested at kCA compositions (0, 1 and 2%) **(Figure 6-1C, bottom row)**. At 0 and 0.5% kCA concentration, bioinks were not viscous enough to hold their shape and could not be printed above a few millimeters. Bioink containing 1%, 1.5%, and 2% kCA were able to print structures 3 cm high and were free of structural defects. These observations suggest without sufficient kCA, GelMA and nSi print poorly because they flow extensively before thermal gelation. The kCA contributes critical viscosity and yields stress needed to hold extruded layers in place while they cool and solidify through thermal gelation.

6.3.2 Rheological Characteristics of NICE Bioinks

Small changes in bioink composition yielded significant changes in printability, so key flow properties of each bioinks were examined rheological characteristic. Printing performance suggested a relationship between thermal gelation and print performance, so peak hold rheology tests were designed to simulate the environment of bioink during the 3D printing process. In this peak hold test, the bioink is subjected to three stages designed to replicate the conditions of the bioink during printing: a pre-extrusion phase, an extrusion phase, and a post-extrusion phase **(Figure 6-2A)**. The pre-extrusion phase is kept at 37 °C and uses a very low shear rate (1 1/s) corresponding to shear conditions in the barrel, followed by a 5-second high shear rate (300 1/s) phase simulating extrusion. The bioink was then quickly cooled to 25 °C and held at a minimum shear rate (0.2 1/s) representing the post-extrusion phase. We calculated shear rate at the extruder tip walls, which was used for the high shear rate. The entire test was carried out at 200 micron sample height, corresponding to the internal radius of the extruder tip. By matching the physical conditions found during printing as closely as possible, we can measure the rate and extent of thermal gelation through changes in apparent viscosity and observe shear thinning in action.

GelMA is the biggest contributor to thermal gelation, and peak hold experimental data is shown for the varied GelMA compositions **(Figure 6-2A)**. Peak hold tests show that apparent viscosity drops by several orders of magnitude during the high shear rate extrusion phase, then rapidly recovers within just a couple of seconds post-extrusion. Apparent viscosity then continues to increase steadily over roughly 30 seconds due to thermal gelation, as viscosity recovery exceeds 200-1000% of its pre-extrusion value. Matching up with printability observations, increasing GelMA concentration increases viscosity recovery speed and final viscosity. The NICE bioink

with 7.5% GelMA was notably less viscous at 37 °C than the 10% and 12.5% formulations before and during extrusion, which explains the observed smoother printed structures. This explains the ability to create strong, many-layered structures. Previous studies have highlighted the importance of dramatic shear thinning followed by rapid shear recovery as key to bioink printability, and the rheology data shown here for the highest performing bioinks fits well into this paradigm.(211, 220)

6.3.3 High Mechanical Stability of 3D Printed Scaffolds

A bioink's mechanical properties are key to its performance in tissue engineering. The stiffness of the extracellular environment plays a critical role in regulating cell proliferation, migration, and differentiation.(363) Human mesenchymal stem cells (hMSCs) sense and interact with their environment through an array of cytoskeletal and membrane proteins, allowing them to differentiate into appropriate body tissue based on their surroundings.(248) For example, stiffer ECM environments at least 25-40 kPa match the stiffness of osteoid tissue produced during initial bone healing, and direct hMSCs towards an osteogenic lineage.(237) Similar GelMA-nSi nanocomposites have been shown to induce osteogenic differentiation without exogenous osteoinductive factors.(27, 362) Beyond cell interactions, bioprinted structures must be strong enough to handle manipulation and implantation during surgery, and be resilient enough to maintain their integrity during neo-tissue formation.

In light of these requirements, the mechanical properties of 3D printable hydrogels were investigated. The crosslinked 3D printed hydrogels were able to sustain mechanical deformation such as shearing, bending, and stretching without apparent permanent deformation and rapidly recovered their original shape **(Figure 6-2B)**. Single cyclic compression cycle to 70% compression (unconstrained) were carried out on 3D printed structure with 100% infill. Compressive modulus

and toughness were calculated. As in the printability investigation, the hydrogels were based off of a standard formula (7.5% GelMa, 1% kCA, 2% nSi) and a single component was varied at a time. Compression modulus data **(Figure 6-2C, top)** showed that at the lowest GelMA concentration (5%), compressive modulus was 40±17 kPa, while at 7.5% GelMA the stiffness significantly increased to 103±6 kPa. Increasing GelMA concentration above 7.5% did not significantly increase modulus. The toughness of the gels also showed similar trends with significantly increased from 5 to 7.5% GelMA concentration (30±2 and 78±6 KJ/m^3, respectively). Further increases in GelMA concentration did not significantly improve toughness **(Figure 6-2C, bottom)**. In contrast, stiffness increased steadily and significantly with increasing nanosilicate concentration between 0 to 4% (44±6 kPa up to 141±8 kPa). Interestingly, while the addition of nanosilicates increased toughness(42±4 KJ/m^3 at 0% to 67±3 KJ/m^3 at 1%), further increases in nSi concentrations did not have a significant effect. Kappa carrageenan trended significantly upwards in both compressive modulus and toughness as kCA content increased(13±1 kPa and 9±1 KJ/m^3 at 0% up to 109±10 kPa and 108±7 KJ/m^3 at 2%). However, diminishing returns were clearly evident past 1% kCA.

Together, this data shows that each reinforcement mechanism leads to significant increases in stiffness and toughness. Nanosilicates steadily increase stiffness, but not toughness past 1%, while kCA increases both stiffness and toughness although returns from additional polymer seem to diminish quickly. 7.5% GelMA was also established as a minimum requirement for both compressive modulus and toughness. Since a highly hydrated and easily remodelable bioink is desired, establishing relationships between composition and mechanical properties allows us to find the lowest polymer & nanomaterial concentrations needed to create mechanically robust bioinks. In combination with the printability performance data, these mechanical results allowed

us to identify an optimal bioink for osteogenic testing and illustrates the dual roles played by the three primary bioink components in both mechanical properties and printability.

In light of these results, a final bioink concentration of 7.5% GelMA, 2% Nanosilicates, and 1% kCA was selected as the optimized bioink to be tested going forward. This composition contains the minimum polymer and nanoparticle content needed for excellent printability and exceeds the established modulus requirements for osteogenic differentiation by a comfortable margin.

Therefore, this NICE bioink represents the essential composition needed to be both highly printable and exhibit good mechanical properties.

6.3.4 Cell-assisted Matrix Remodeling of 3D Printed Structure

The ability of cells to remodel their microenvironment by degrading their surroundings to grow and deposit ECM has led to expanded interest in designing biodegradable inks. Enzymatically degradable bioinks are especially attractive for 3D bioprinting because they mimic the ability of native tissue to degrade in response to cell signaling. The covalently crosslinked GelMA network of NICE bioinks is susceptible to enzymatic (collagenase) degradation.

Degradation rate is a critical factor in successful tissue regeneration: too rapid a degradation will cause a scaffold to degrade faster than tissue can be formed to replace it, while excessively slow degradation will retard growth and healing. To get a baseline estimate of the degradation profile of NICE bioink, samples were printed and incubated under cell culture conditions in phosphate buffered saline(PBS), media, or media with concentrated collagenase (300 u/ml). Samples were mechanically tested to measure changes in mechanical properties and weighed for mass loss. Cell-containing bioinks were also printed and cultures, then imaged with a scanning electron microscope to investigate changes in microstructure.

For 3D printed structures, mechanical testing revealed that in both PBS and media, compression modulus and toughness **(Figure 6-3A)** were maintained near initial values for 14 days but suffered significant losses by day 21. For example, a 5-fold and 10-fold reduction in mechanical modulus was in media (9.5±3 kPa) and PBS (4±0.25 kPa) after 21 days, compared to initial modulus of scaffolds (47±10 kPa) on day 0. In contrast, samples subjected to collagenase were partially degraded by day 2 (15±7 kPa) and completely degraded by day 7. Mass loss data showed that 3D printed structure swelled roughly 20% mass in the first week of culture, but otherwise did not significantly lose mass through day 21. After 21 days the non-cell containing scaffolds were fragmented into pieces too small to measure. This data indicates that the scaffolds maintain their mechanical properties for at least 2 weeks, their overall mass for at least 3 weeks. In addition, the printed scaffolds are sensitive to enzymatic degradation despite the presence of a secondary ionic network. The lower starting values relative to mechanical data are to be expected, since bioprinted scaffolds swell and are not perfectly flat, which affects mechanical properties, and no delamination was observed during mechanical testing.

Importantly, cell-containing scaffolds show very different behavior. Bioprinted scaffolds retained their structural integrity and preserved over 80% of initial mass up to 60 days. SEM imaging **(Figure 6-3C)** reveals increased microstructure density starting after day 14. This suggests that substantial cell-mediated remodeling is occurring that is extensive enough to hold together the macroscopic structure of 3D printed scaffolds.

Overall, this *in vitro* biodegradability data gives us an estimated window of biodegradation that is useful for evaluating a bioink, but they are difficult to correlate to results *in vivo*. This is because degradation *in vivo* can vary widely based on immune response and extent of tissue ingrowth, and collagenase levels change by orders of magnitude based on inflammation reactions. Using a

supraphysiological collagenase concentration allows us to establish a lower limit for structural integrity. However, tissue in-growth may also be much more rapid *in vivo* due to better nutrient transfer.

6.3.5 Histological Investigation of Deposition of Nascent Extracellular Matrix

The extracellular matrix(ECM) surrounding cells plays a key role in the development of functional tissue. The properties of the ECM are critical factors in cell adhesion, motility, migration, differentiation, and proliferation. Thus, determining how bioprinted cells are interacting and remodeling their microenvironment allows us to understand how bioprinted implants are behaving in vitro and gives us insight into what we can expect under in vivo conditions.(364, 365) Here, we use histology techniques to evaluate how encapsulated hMSCs remodel NICE bioprinted scaffolds over several months, showing an endochondral ossification-like remodeling process of cartilage formation followed by mineralization that resembles natural bone formation.

The persistence of cell-containing scaffolds beyond four weeks suggests that the encapsulated are remodeling the scaffolds over time. To investigate ECM deposition by the hMSCs, cell-containing scaffolds were 3D bioprinted and cultured for 60 days and histologically examined at regular time points (0, 7, 14, 30 and 60 days). As observed under a simple light microscope, scaffolds were initially transparent on day 0, and gradually became translucent and pearlescent over by day 60 **(Figure 6-4A)**. mRNA extraction was also performed but was unsuccessful due to the charged nature of the nanosilicates interfering with mRNA extraction from the 3D encapsulated cells. However, histology still allows us insight into cell behavior through characterizing ECM deposition. Osteoblasts formed from hMSCs will produce an osteoid-like matrix, composed of

collagen I and glycosaminoglycans (GAGs) including chondroitin and keratan sulphate, and two chief glycoproteins, osteocalcin and sialoprotein.(366) This indicated that deposition such proteins should facilitate formation of bone-like ECM either directly or through an intermediate cartilage state also known as endochondral ossification.(367) The histological staining performed here are based on identifying osteoid and cartilage-like features and establishing calcium deposition **(Figure 6-4B)**. Note that bioprinted scaffolds remained intact throughout the culture period, and that fractures shown on histology images are due to sample processing.

Safranin O is a cationic stain that electrostatically binds to glycosaminoglycans (large, negatively charged polysaccharides that modify osmotic pressure and diffusion rate), which are found in both osteoid and cartilage ECM.(366) GAGs are stained red, while bone is stained purple-blue.(368) Between day 0 and 14, increasing vivid red staining indicates an increased GAG content throughout the scaffold. Past day 14, the scaffolds progressively darken to a deep bluish purple, indicating the progressive development of bone-like tissue in culture. Alcian blue, which stains proteoglycans, dyes both cartilage and osteoid a deep blue. Staining is observed to increase steadily throughout culture, including in areas of bone-like tissue as indicated by safranin O.(367)

Masson's trichrome was used as an auxiliary test to differentiate between bone and cartilage ECM, since bone is stained a dark blue while cartilage remains a pale blue. When compared to safranin O staining, light and dark blue patterns correspond to the bone and small cartilage regions seen in Safranin O staining, further indicating that these observed regions are depositing osteoid-like and cartilage regions.

In order to differentiate between osteoid and actual calcified bone, Von Kossa-Acid fuchsin and Alizarin red stains were performed. Alizarin forms an orange-red chelation complex with calcium, while Von Kossa staining precipitates silver on phosphate groups in bone, replacing calcium in

the phosphate-calcium complex. Both of these stains indicate the presence of osteogenic mineralization. As expected, neither Von Kossa nor Alizarin red show significant presence of calcium or phosphates in early time points, but after several weeks significant calcium and phosphate deposition is seen.

Together, these histological evaluations demonstrate that the 3D bioprinted scaffolds are extensively remodeled by encapsulated hMSCs, which create a cartilage and osteoid-like ECM that is mineralized over time. This shows that the optimized NICE bioink is able to induce osteogenic differentiation and tissue remodeling, even in the absence of osteoinductive factors. Further, the scaffolds maintain their overall shape and integrity during this several month incubation and remodeling, which suggests that the scaffolds biodegradation is timed well with cellular remodeling.

6.3.6 Evaluation of Matrix Mineralization

To better understand the mineralization occurring in the scaffolds, scanning electron microscopy - energy dispersive spectroscopy (SEM-EDS) and a calcium-cresolphthalein complexone assay were performed. SEM-EDS uses x-rays to eject inner-shell electrons from sample material and records the characteristic energy of photons emitted when an outer shell electron fills the vacancy. Because the energy of emitted photon is element-specific, peaks in the x-ray spectra identify the elements present and their relative proportions. Visualization of element presence detected by EDS shows is shown in Figure 6-5A. Initial EDS scans show the presence of carbon and no detectable calcium, as expected, while the 60-day culture shows calcium deposition throughout the scaffold. This elemental analysis confirms the presence of calcium deposition during culture.

Quantitative comparison of x-ray spectra between the bare NICE hydrogel and a bioprinted scaffold after 60 days of culture also showed significant differences **(Figure 6-5B)**. Cultured scaffolds showed large, new peaks for phosphorous and calcium, as would be expected for new hydroxyapatite formation. Relative peak heights indicate a 0.83 Ca:P ratio, while mature bone is closer to 1.68 Ca:P, almost exactly half of the expected calcium being present. This ratio suggests that a calcium deficient hydroxyapatite is being formed, which may be due to the artificially limited calcium available from media. However, sample roughness can significantly distort x-ray EDS data, so the highly porous lyophilized scaffolds may be interfering with the quantitative analysis. Alternatively, a silicate substituted calcium-phosphate may be forming.(369)

Finally, calcium content was quantified using a calcium cresolphthalein complexone assay. This assay forms a vivid purple complex with elemental calcium, which can be analyzed using a spectrophotometer to precisely quantify the overall concentrations of calcium in each sample. Calcium content increased steadily from undetectable at day 0 to 1.6±0.3% at 30 days, then calcium deposition increased rapidly to 5.5±1% total scaffold weight by day 60. This accelerated calcium deposition in the second is consistent with the calcification of increasingly available phosphate containing, bone-like ECM as shown by our histology data.

6.3.7 Establishing role of Nanosilicates to Induce Endochondral Differentiation

As it was difficult to obtain mRNA from 3D bioprinted NICE bioink due to highly charged nature of nanosilicates, we evaluated the effect of nanosilicates on hMSCs in 2D culture conditions. Specifically, hMSCs were exposed to nanosilicates (50 μg/mL) on day 0 and then cultured in osteoconductive media (in absence of osteoinductive agents such as dexamethasone or rhBMP2) for 21 days. mRNA was isolated and whole transcriptome sequencing (RNA-seq) was

performed to determine long term effect of nanosilicates on biological replicates of hMSCs. The high throughput sequencing of expressed transcripts (RNA-seq) provide an accurate quantification of expressed transcripts by overcoming the limitations and biases of microarrays.(370-372) Our earlier study established the role of nanosilicates in stimulating endochondral differentiation within 7 day in normal media.(373) Specifically, we established that nanosilicates significantly affect several biophysical and biochemical pathways. It is expected that if hMSCs are cultured in presence of nanosilicates for a prolonged duration, endochondral differentiation will be observed **(Figure 6-7A)**. This observation is substantiated by our histology results highlighting production of cartilage-rich ECM during early time points, and subsequent calcification of ECM to form mineralized matrix.

The biological replicates for both the conditions showed high concordance ($r=0.96$) (Figure 7B). Generalized linear models (GLMs) was used to determine the differentially gene expression (DGE) between nanosilicate treated hMSCs and untreated hMSCs. This comparison revealed significant changes in the expression level of 4,629 genes (2,271 up-regulated genes, 2,358 down-regulated genes) out of ~10,908 expressed genes (FDR-adjusted $p<0.01$) even on day 21 (Figure 7C).

Interestingly, a range of genes related to endochondral differentiation of hMSCs such as COL1A21, SMAD1/4/5/7, SOX9 are upregulated (Figure 7D). For chondrogenesis, SOX9 upregulation controls the differentiation of hMSCs into a chondrogenic lineage, and genes related to cartilage ECM production are also upregulated, including cartilage collagen protein COL11A1.(374)

Osteogenic gene expression is upregulated as well, with genes from both TGF-β and BMP signaling pathways upregulated. Expression of essential genes for osteoblast development,

including TGF-β 2 and TGF-β 2 receptor, were observed. TGF-β plays roles in osteoblast differentiation and ECM production during bone formation.(375, 376) Bone morphogenic protein pathways are also affected, including BMP1, BMP4, BMP2K. FGF, which promotes osteoblast differentiation, was upregulated as well.(375)

The SMAD protein family acts as the main transduction pathways for BMP and TGF signaling.(375) Both BMP and TGF signaling factors activate SMAD signaling pathways, with SMAD 1 and 5 being mediating BMP signaling and SMAD 2 and 3 mediating TGF. SMAD4 is a co-SMAD for both signal pathways, while SMAD 7 inhibits both TGF and BMP signaling. We observed significantly increased expression of SMADs 1, 4, 5, and 7, suggesting that BMP signaling was utilizing the SMAD pathway to mediate osteogenic behavior in bioprinted cells. Finally, osteoblast-expressed genes were also observed. Osteonectin(SPARC) expression, which is necessary for collagen mineralization in bone, was significantly increased. We also observed increased expression of cadherin-11, which is associated with osteoblast differentiation.

Overall, whole-transcriptome sequencing of hMSCs exposed to nanosilicates allowed us to identify increased gene expression indicating endochondral bone formation. Notably, both BMP and TGF signaling were present along with increased expression of their SMAD signaling pathways. Genes expressed in cartilage and bone were present at day 21, supporting our histology data showing that the NICE bioink induces endochondral differentiation in bioprinted hMSCs.

6.3.8 Fabrication of Patient-specific implantable 3D constructs

To illustrate the practical utility of NICE bioinks for bone tissue reconstruction, we demonstrate how to create full-scale bioprinted implants customized for craniofacial defects on real patient CT scans. Publicly available DICOM files were downloaded and converted into an anonymized

.NRRD file using an open source slicer program, then converted into an .STL file with the Democratiz3d tool available online. Meshmixer was used to process the models and create bone defects, and slic3rPE, and Repetier Host were used to bioprint the scaffolds. This process uses entirely open-source or free software. After bioprinting, the scaffold was crosslinked and implanted in a thermoplastic model of the mandible to demonstrate the closeness of fit **(Figure 6-4A)**. The defect in the mandible is 2x2x1 cm.

The potential for using the NICE bioink as an injectable material in smaller defects was also investigated, showing that the bioink injects easily through an 18-gauge needle into a simulated fracture, and can be rapidly crosslinked in place using 60 seconds of 365 nm light. Strength of fit was also demonstrated by injecting and crosslinking the NICE bioink between two sections of a full thickness fracture to demonstrate that the NICE bioink is able to quickly adhere surfaces together and resist shearing and delamination forces.

This process can be used for any CT scanned injury to bioprint NICE bioink implants that will fit exactly to a patient's injury.

6.4 Conclusion

The goal of this study was to take a bioink with both high print performance and enzymatic degradability, optimize its osteogenic properties, and then evaluate its osteogenic remodeling in vitro. First, we optimized an enzymatically degradable bioink to maximize printability and mechanical properties as efficiently as possible. Then, bioink remodeling was established using degradation tests and followed over 3 months with a series of histological examinations. These tests established that cells deposit a cartilage/osteoid-like matrix of GAGs, collagen, and proteoglycans over the initial few weeks of culture, followed by extended mineralization with

carbonates, phosphates, and calcium. These results are supported by further SEM-EDS data, calcium assays. This behavior is also supported by evaluation of the cellular response of hMSCs to nanosilicate exposure using whole transcriptome sequencing (RNA-seq) to identify potential signaling pathways. This data builds a strong case for bone-like tissue formation resulting from the intrinsic osteogenic effects of the optimized NICE bioink on bioprinted hMSCs. Finally, we demonstrated that this highly printable NICE bioinks can precisely reconstruct large damaged & missing bone structures reconstructed from CT scans of actual patient injuries. The end goal of this research is to enable patient-specific bioprinting of bone scaffolds to precisely match their injuries. We envision this technique will act as a customizable and easy to work with alternative to autografts that will provide surgeons with greater options for bone surgery. We are optimistic that successful adoption of this bioprinting technology will open the door for more uses of bioprinting in clinical practice.

6.5 Materials and Methods

6.5.1 Gelatin methacrylate synthesis:

Gelatin methacrylate was synthesized using porcine gelatin (Bloom No. 300, Type A) and methacrylic anhydride, both purchased from Sigma-Aldrich (USA). 80% methacrylated gelatin was created by stirring 10g gelatin into 100 mL phosphate buffered saline (PBS), and allowing to dissolve for 1 hour at 60°C. 8 ml of methacrylic anhydride was then added dropwise to the solution over a period of minutes. The solution was maintained at 60°C for 3 more hours, then 400 mL of PBS was added. The solution was then dialyzed at approximately 50°C for 7 days, then lyophilized.

6.5.2 NICE Bioink Synthesis:

K-carrageenan was obtained from TCI America, nanosilicates (Laponite XLG) were purchased from BYK Additives, and Irgacure2959 (2-Hydroxy-4′-(2-hydroxyethoxy)-2-methylpropio-phenone) was purchased from Sigma-Aldrich (USA). The NICE bioinks for optimization were created in varying compositions, but the eventual bioink chosen for investigation was composed of 7.5% w/v GelMa, 1% w/v κ-carrageenan, 2% w/v nanosilicates, and 0.25% w/v Irgacure 2959 . The final concentration was reached by 1:1 mixing of a 15% GelMa, 2% κCA, 0.5% Irgacure 2959 (w/v) solution with a 4% (w/v) Laponite XLG solution. The solution was warmed and stirred continuously overnight to maximize homogeneity. Bioinks were stored refrigerated at 4°C and warmed to 40°C before use.

6.5.3 3D Bioprinter:

The bioprinter was created by modifying a commercial ANET A8 3D printer kit to utilize screw extrusion. The thermoplastic extruder assembly was replaced with a 3D printed screw extruder assembly, which holds a stepper motor, guide rail, and a modified clay extruder. Firmware changes were made to accommodate the new extruder motor as needed. All prints used a 400 μm interior diameter tapered extruder tip.

6.5.4 3D Printing:

De-identified patient data was obtained in the form of DICOM files, which were converted into STL formats. Other printed shapes were created using Solidworks and exported as STL files. STL files were processed in Slic3r Prusa Edition to convert them into G-code printer instructions. Repetier Host was used to control the 3D printer. For printed structures, layer height was 200 μm, line width was 600 μm with a 15% overlap, print speed was 15 mm/s for all trials. The standard

3D printability test was adapted from Chimene 2018: a 10mm outer diameter hollow cylinder with 1mm thick walls was printed up to 3 cm (150 layers) in height. Printability performance was quantified by determining 1. Whether a composition could reach the full 3 cm height 2. The absence of major defects by testing whether the cylinder could hold water 3. comparing height and diameter of the printed cylinder to its intended dimensions. The prints were also qualitatively evaluated for wall smoothness by examining structures under a stereomicroscope. Bioinks were covalently crosslinked with a 365 nm UV-A light source at 25 mW/cm^2 intensity. Ionic crosslinking was through submersion in a 5% potassium chloride solution.

6.5.5 Mechanical Testing:

Hydrogel samples were printed as cylinders approximately 6mm in diameter by 2.5 mm thick. Each sample's diameter and height were verified with both digital calipers and the mechanical tester, an ADMET MTEST Quattro eXpert 7600. Any dimensional variations were factored into each sample's stress and strain calculations. Mechanical tests were run as a single cycle unconstrained compression test, where samples were compressed to 30% of their original height over 1 minute, then returned back to their original height over another minute. The force and position data recorded by the mechanical tester was analyzed using a custom excel macro to calculate compressive modulus from 0 to 20% strain, maximum stress, toughness, and energy dissipated.

6.5.6 3D Bioprinting:

Bioprinting was performed using the optimized NICE bioink: DI water containing 7.5% w/v GelMA, 1% w/v κ-carrageenan, 2% w/v nanosilicates, and 0.25% w/v Irgacure 2959. Primary

bone marrow derived hMSC stem cells were supplied from ATCC. Immediately before bioprinting, cells were trypsinized for 5 minutes, then 10 mL of media was added, and the resulting cell-media suspension was centrifuged for 5 minutes. The supernatant was removed, and the cell pellet was resuspended in 200 μL of media, which was gently mixed into the warmed and prepared bioink by pipetting. The bioprinter was moved to a biosafety cabinet and printing proceeded under sterile conditions. Print settings were kept consistent with 3D printability tests described above, using a 200 μm layer height, 600 μm line width with 15% overlap, 15 mm/s print speed, and using a 400 μm tapering luer-lock extruder tip. Other settings were also kept consistent between prints. Covalent crosslinking was carried out after printing was complete, using 25 mW/cm^2 of 365 nm UV-A light for 60 seconds. Cation content of the media was relied on for ionic crosslinking.(345, 377)

Bioprinted scaffolds were printed in several configurations, most often as 1 mm thick, 1 cm diameter discs with 100% infill to allow easy visualization. Crosshatch patterns were also created as 4cmX4cm scaffolds, and the cylindrical printability test cylinder described above was also conducted up to 3 cm in height to verify printability with high layer numbers.

6.5.7 In Vitro Studies:

Bioprinted structures were crosslinked with UV light and incubated in osteoconductive Minimum Essential Media- Alpha Modification(GE Life Sciences) with 16.5% FBS, 1% penicillin-streptomycin, 10 mmol beta-glycerophosphate, and 0.05 mmol ascorbic acid. No dexamethasone was used. Media was changed every 3-4 days.

6.5.8 Degradation Studies:

Hydrogel samples were stored in incubator conditions in PBS, media, and media with 300u/ml of collagenase. Hydrogel mass was taken by removing the hydrogel and all hydrogel pieces large enough to grasp with forceps, dabbing on a Kimwipe to wick away surface liquid, and measuring wet weight using a covered scale and weigh-boat. Mechanical testing was carried out as described above. Time points were taken at Days 0, 2, 7, 14, 21, 28, 35, and 60.

6.5.9 Scanning Electron Microscopy / Energy Dispersive Spectroscopy:

For electron microscope imaging and elemental characterization of lyophilized bioink microstructure, a FEI Quanta 600 field emission-scanning electron microscope(FEI-SEM) was used, equipped with an inbuilt Oxford EDS detector with X-ray mapping, and running INCA software. Samples were sputter coated with iridium to a thickness of 8 nanometers. Voltage was set to 15 kV, and secondary electron mode was used.

6.5.10 Shear Recovery Studies:

TA rheometer (AR 2) was used for rheology studies, with an 8mm flat geometry plate, and a gap size of 200 μm . For shear recovery testing, the shear rate was initially held at 0.75 s^{-1} for 60 seconds at 37C, then shear rate was increased to 300 s^{-1} for 5 seconds, then shear rate was dropped to 0.2 s^{-1} and temperature was dropped to 25C for 180 seconds.

6.5.11 Calcium Assay:

The calcium content assay experiment was carried out using a Calcium Assay Kit from Cayman Chemical (Item # 701220). Bioprinted scaffolds were lyophilized and weighed, then calcium was

dissolved from the scaffold using an HCL solution. Solution were then diluted with the supplied calcium assay buffer solution and calcium detector reagents were added according to the assay manual. The calcium binds to cresolphthalein complexone to form a vivid purple complex, which was quantified using a Tecan M200 Pro plate reader and normalized against dilutions of a supplied calcium solution of known concentration.

6.5.12 RNA Extraction & Assay:

2D seeded hMSC cells were cultured in normal media conditions until 65% confluency, then exposed to 50 µg/mL Laponite XLG nanosilicates for 48 hours. Cells were returned to normal media for another 5 days. Control cells remained in normal media for the entire week. Cells were then washed with PBS and pelleted, then RNA was collected using a Roche High-Purity RNA Isolation Kit according to the manufacturer's instructions. Nucleic acids were evaluated for quality using a spectrophotometer to analyze absorbance ratios.

6.5.13 RNA-seq:

hMSCs (2500 cell/cm2) were exposed to nanosilicates (50 µg/mL) and whole transcriptome sequencing (RNA-seq) was performed after 21 days. Two biological replicates of untreated and treated hMSCs were sequenced. The sequenced reads were aligned to reference genome (hg19) using RNA-seq aligner. The normalized gene expression levels were determined by calculating the reads per kilobase of transcript per million (RPKM). The replicates for both the conditions showed high concordance (r=0.96). We used generalized linear models (GLMs) to identify differentially gene expression (DGE) between nanosilicate treated hMSCs and untreated hMSCs.

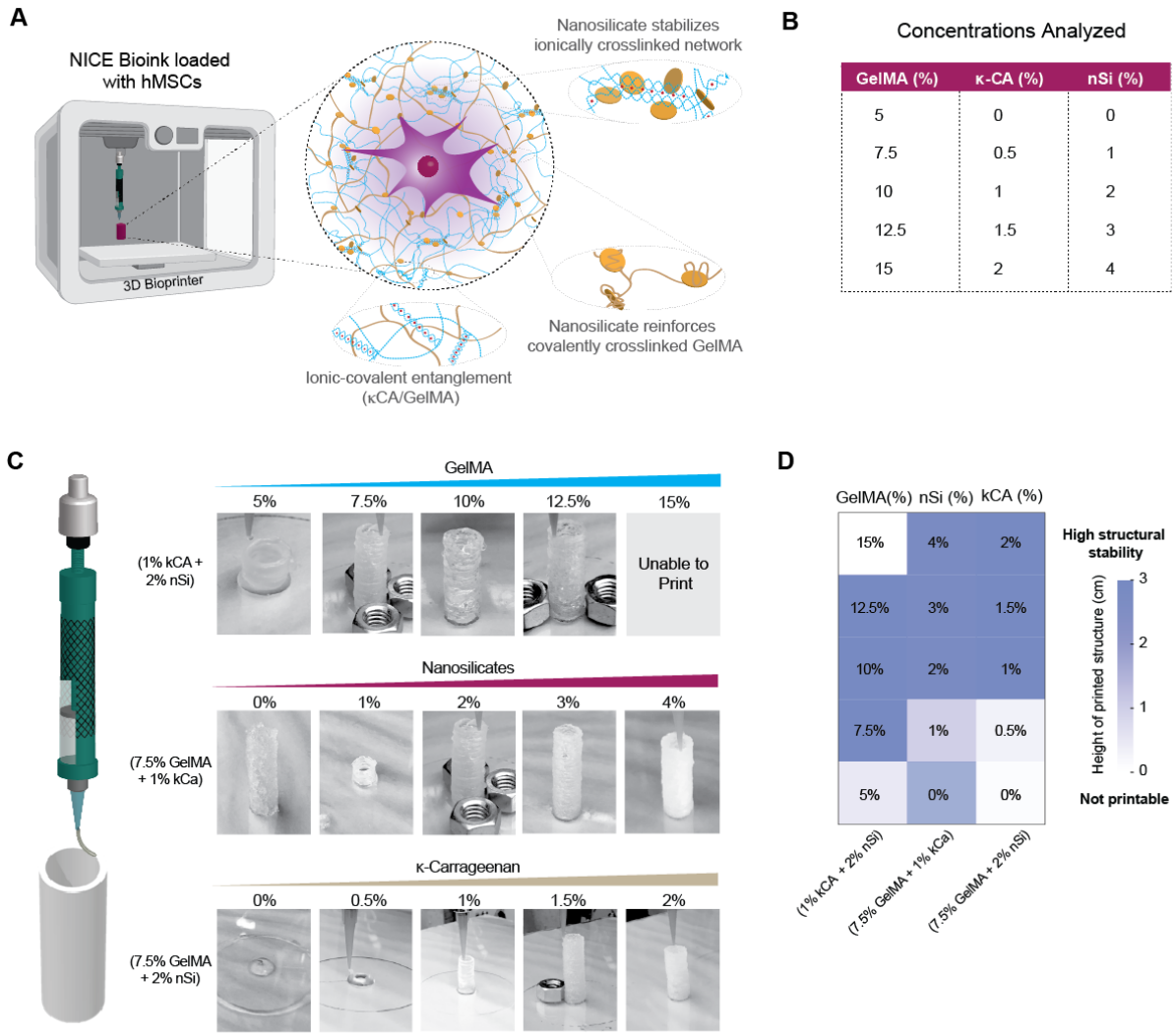

Figure 6-1. Bioink Design and Mechanical Data. The combination of gelatin methacrylate, κ- carrageenan, and laponite nanosilicates forms a nanoreinforced ionic-covalent entanglement bioink, which demonstrates superior printability and mechanical properties compared to individual components. Different compositions were tested to create a bioink that balanced the need for mechanical strength and osteogenic environment with a low polymer content, highly hydrated, remodelable environment. The 3D printability of each bioink formulation was quantified using screw-driven extrusion printing of a warmed bioink

solution to create a 3cm tall, 1cm wide hollow tube. Print success was based on height reached, conformity to expected dimensions, and lack of observable errors.

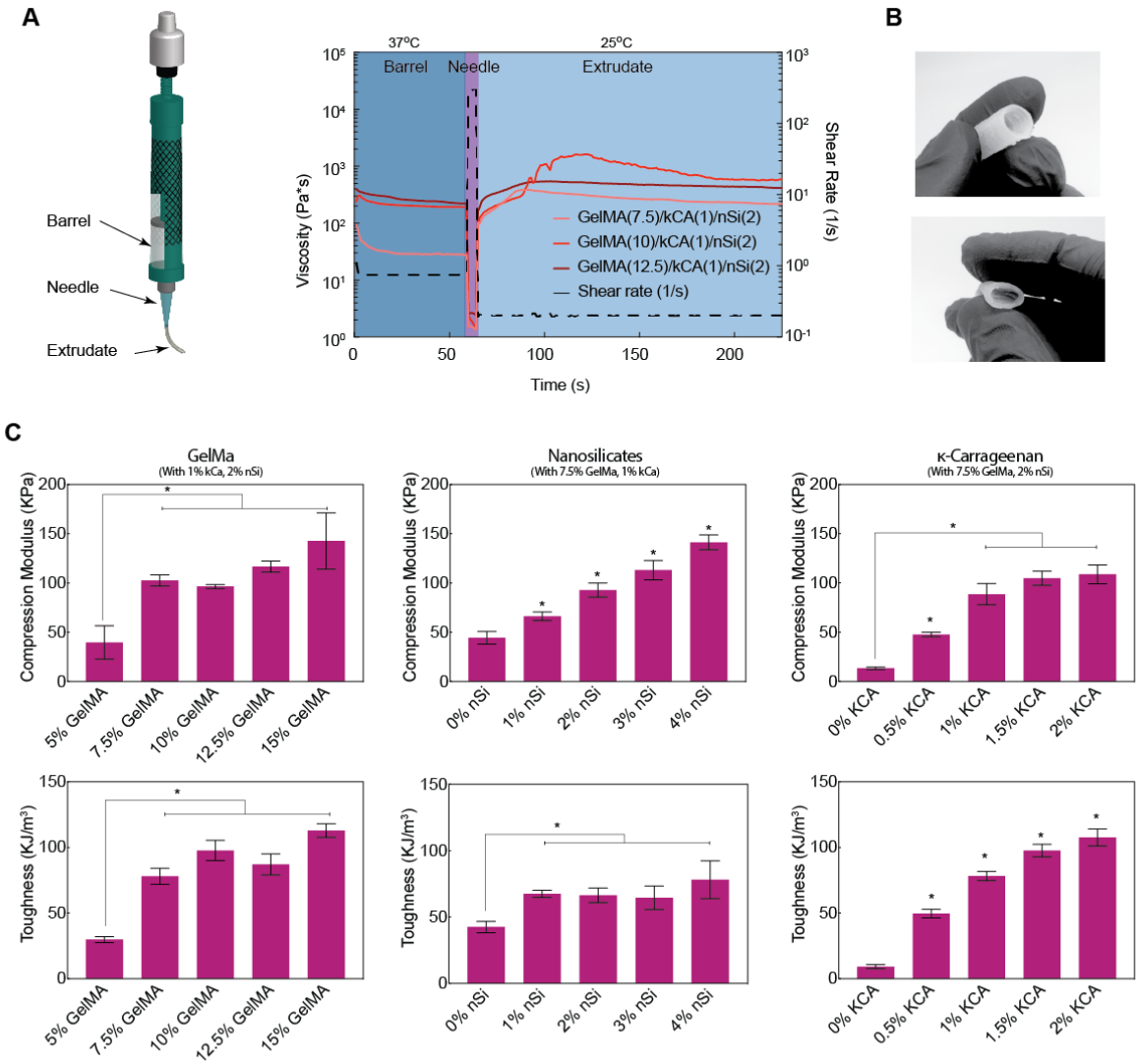

Figure 6-2. Rheology and Mechanical Experiments A. Shear recovery tests showed that print performance corresponds well with rapid viscosity recovery, which reaches over 100% recovery due to thermal gelation. B. NICE bioprinted structures are highly flexible and resilient. 3 cm tube structures can be completely collapsed and quickly regain their shape. This structure was printed with the optimized 7.5% GelMa, 1% κCa, 2% nanosilicates NICE bioink. C. Mechanical testing showed that all NICE reinforced bioinks were stiff enough to

expect osteogenic differentiation of bioprinted hMSC cells, so low polymer content compositions with good mechanical properties were chosen to create a highly hydrated, remodelable environment. Among the highest quality bioinks for printability, the lowest polymer content bioink was chosen: 7.5% GelMa, 1% κCa, 2% nanosilicates.7.5% GelMa, 1% κCa, 2% nanosilicates.

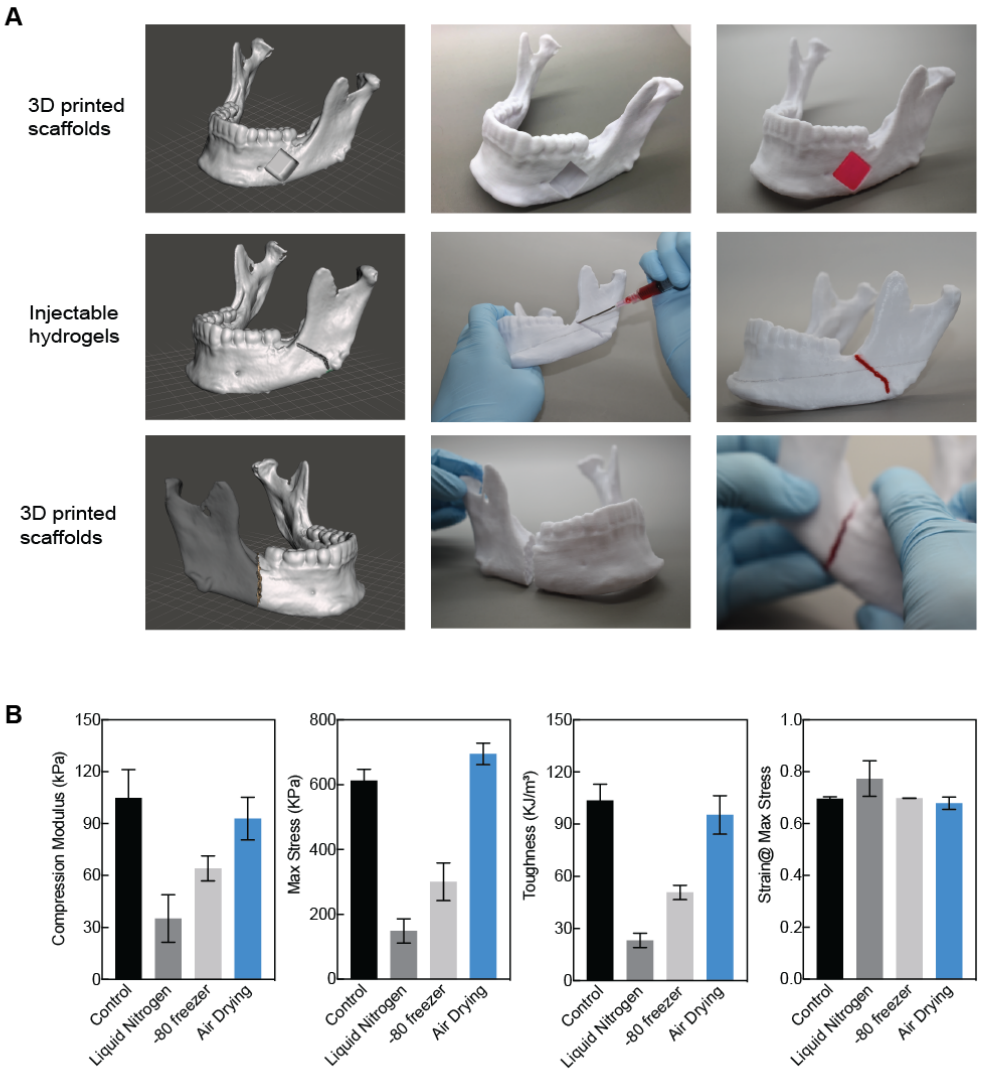

Figure 6-3. Bioprinting Practical Demonstrations and Storage Conditions A. Demonstration of the bioink's utility for recreating missing bone fragments from .stl files generated from patient data. NICE bioinks can also be injected into fractures and crosslinked securely into place. This can be used to encourage fracture healing with encapsulated hMSCs. The NICE bioinks are dyed for visibility in these images. B. Dehydrated NICE scaffolds can be rehydrated for later use without altering mechanical

properties. However, freezing in both liquid nitrogen and at -80c resulted in significantly reduced strength.

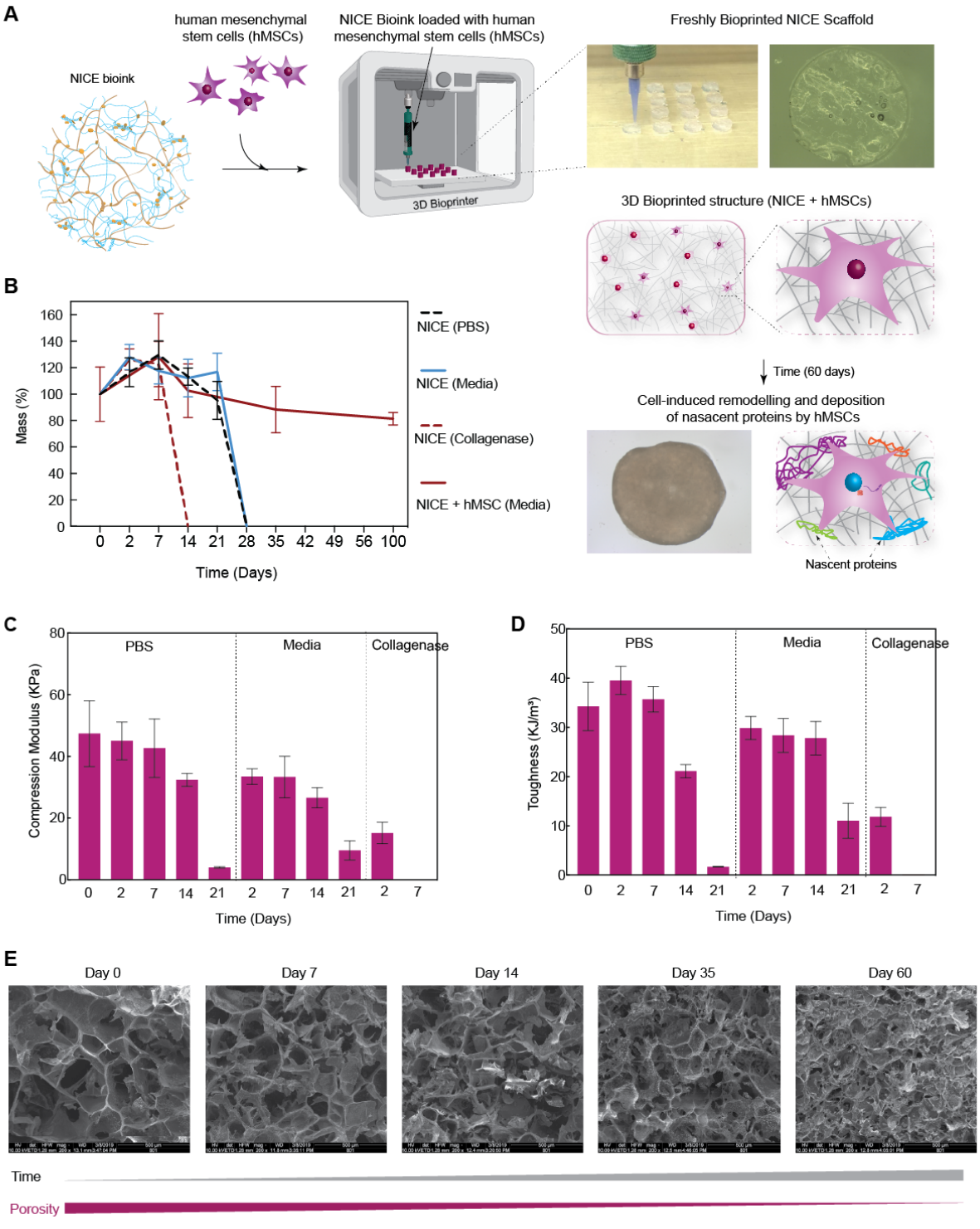
A
human mesenchymal stem cells (hMSCs)
NICE bioink
NICE Bioink loaded with human mesenchymal stem cells (hMSCs)
3D Bioprinter
Freshly Bioprinted NICE Scaffold
3D Bioprinted structure (NICE + hMSCs)
Time (60 days)
Cell-induced remodelling and deposition of nasacent proteins by hMSCs
Nascent proteins
B
Mass (%)
Time (Days)
NICE (PBS)
NICE (Media)
NICE (Collagenase)
NICE + hMSC (Media)
C
Compression Modulus (KPa)
PBS
Media
Collagenase
Time (Days)
D
Toughness (KJ/m³)
PBS
Media
Collagenase
Time (Days)
E
Day 0
Day 7
Day 14
Day 35
Day 60
Time
Porosity

Figure 6-4. Bioink Degradation: A. Bioprinting requires cells to be encapsulated in the NICE bioink, then loaded into a bioprinter and printed. Arrays of scaffold replicates are printed in batches to maximize repeatability. Remodeling in bioprinted scaffolds is easily visible at 60 days. B. When mesenchymal stem cells are encapsulated in the bioink, scaffold mass remains near initial values at least out to 100 days, while samples without cells are completely degraded by week 4. C. When no cells are present, the bioink maintains its mechanical properties for 1-2 weeks, then steadily degrades away. The presence of collagenase greatly speeds this process, indicating that degradation is controlled enzymatically. D. Scanning electron microscope images taken at different times show gradual changes in the cell-containing-bioink's microstructure.

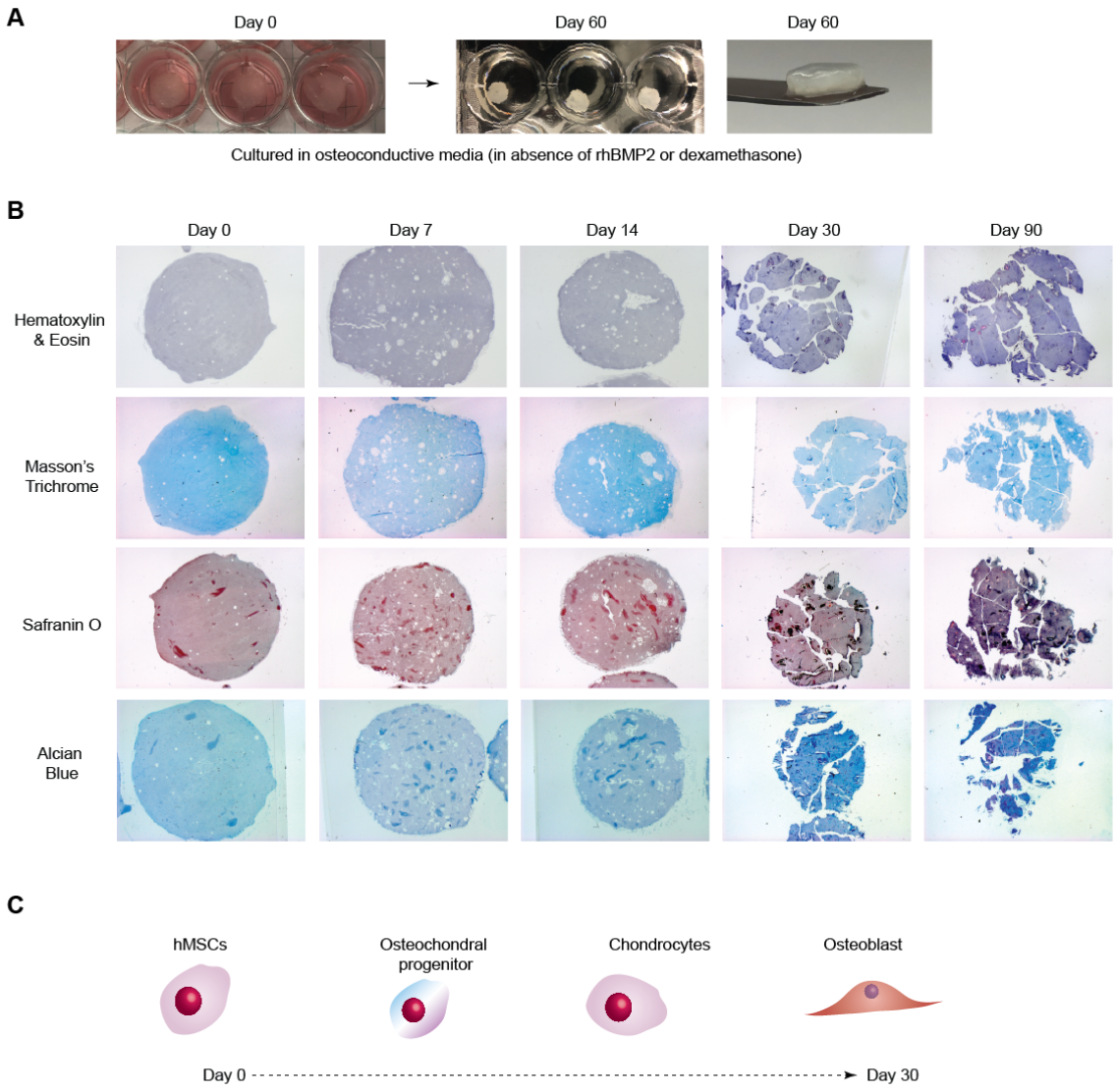

Figure 6-5. Extracellular Matrix Remodeling in Bioprinted Scaffolds A. Bioprinted structures are initially transparent or translucent depending on print settings but become clouded over time as remodeling and mineralization progress. B. Histology images show progressive changes in the ECM of bioprinted structures. Safranin O stains cartilage tissue varying shades of red, while bone tissue is bluish-purple. Alcian Blue stains connective tissue light blue and cartilage dark blue. Together, these stains demonstrate the osteochondral

production of cartilage ECM that transitions into mineralization. C. In osteochondral tissue formation, hMSCs differentiate into osteochondral progenitor cells and then into chondrocytes, producing a cartilaginous extracellular matrix. Chondrocytes can then differentiate into preosteoblasts and direct the mineralization of the surrounding matrix.

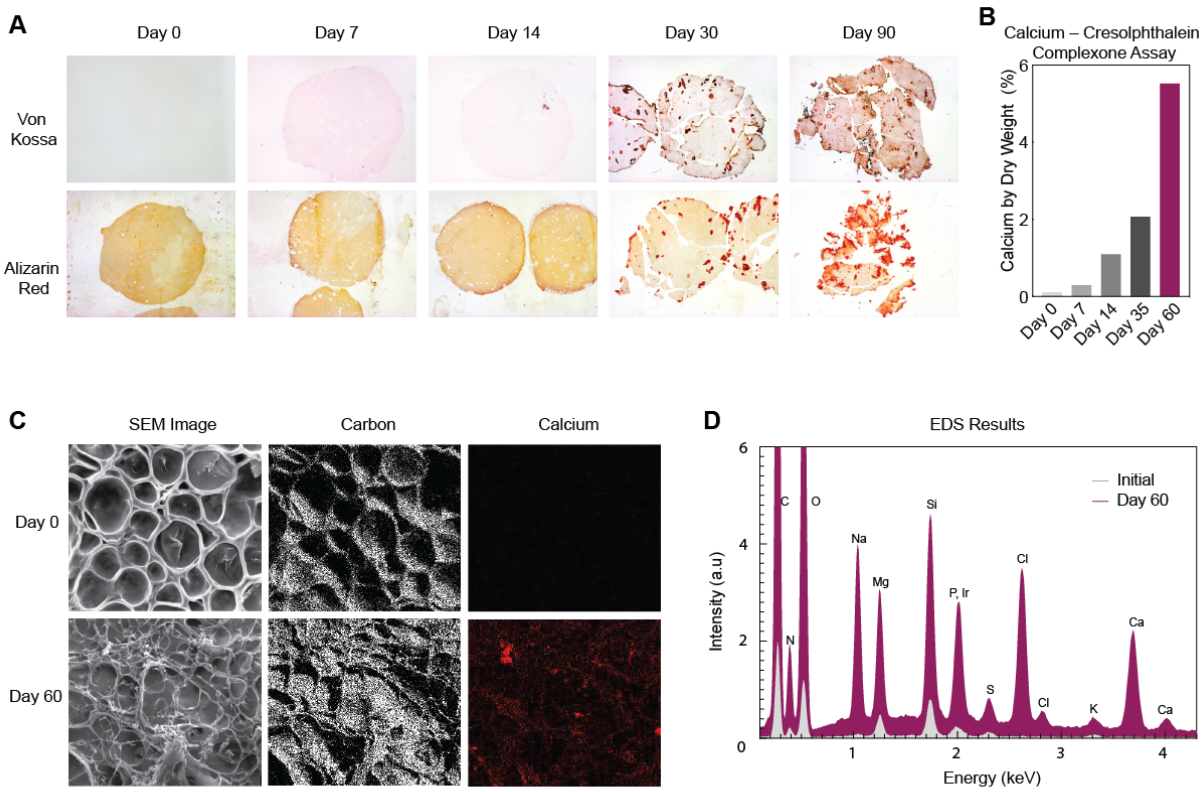

Figure 6-6. Scaffold Mineralization A. Von Kossa and Alizarin Red straining reveal mineralization with calcium, carbonates, and phosphates B. A calcium-cresolphthalein complexone assay quantified calcium content in dried gels over time. C. SEM-EDS imaging visualizes the increase in calcium expressed over time. D. EDS quantitative data shows a concurrent increase in calcium and phosphates, as would be expected with osteogenic tissue formation

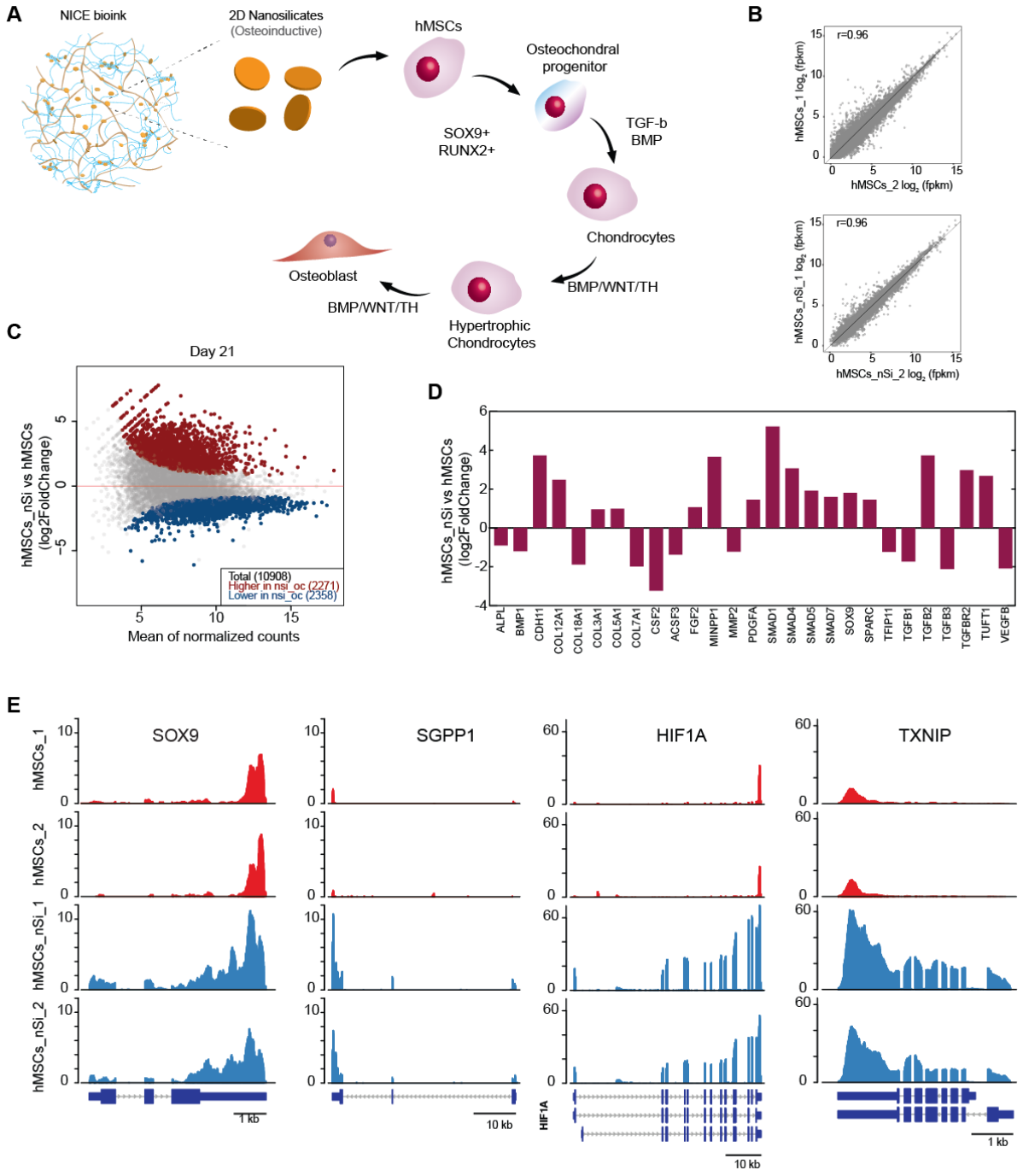

Figure 6-7. Changes in hMSC Gene Expression in Response to Nanosilicates. By directly measuring changes in gene expression caused by nanosilicates, we can investigate the osteogenic effects of nanosilicates. hMSCs differentiate down an osteochondral pathway by

SOX9 gene expression, and interplay between morphogenetic signaling molecules including TGF-β and BMP mediate between chondrogenic and osteogenic cell behavior.

SYNOPSIS

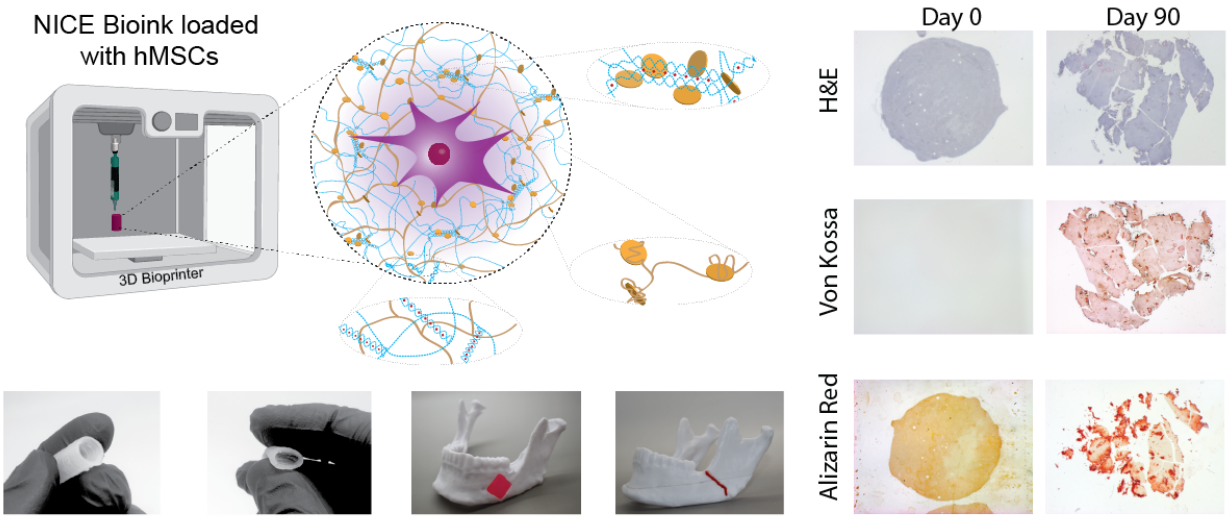

Figure 6-8. Bioprinting Optimization Overview. Nanoengineered ionic covalent entanglement (NICE) bioink for bone bioprinting is introduced by combining nano-reinforcement and ionic-covalent entanglement of polymer networks. Patient-specific, osteoinductive implantable 3D scaffolds can be bioprinted for repair of bone defects for regenerative medicine.

CHAPTER 7: CONCLUSIONS

Through this research, we've developed a novel bioink design that combines nanoengineering and ionic covalent entanglement reinforcement to create a bioink that is simultaneously mechanically stronger and superior in 3D printability that previous bioinks. The NICE bioinks provide high printability, mechanical robustness, and an enzymatically remodelable cell environment that can be used to bioprint complex, large scale, cell laden constructs. We've shown that NICE reinforced bioinks provide an osteogenic environment for human mesenchymal stem cells and are enzymatically remodelable. This research advances bioprinting by enabling scientists to construct larger and more complex cell environments that better resemble the human microenvironment. It also provides a potential alternative to bone grafting that may improve outcomes for patients by reducing the numbers of surgeries, donor site morbidity, and by allowing physicians to precisely model missing bone sections using imaging and computer programs. My future plans involve seeing in vivo testing through and making further refinements to the bioinks in order to continue to make bioprinting a clinical reality.

REFERENCES

1. F. P. Melchels *et al.*, Additive manufacturing of tissues and organs. *Progress in Polymer Science* **37**, 1079-1104 (2012).
2. A. Skardal, A. Atala, Biomaterials for Integration with 3-D Bioprinting. *Ann Biomed Eng* **43**, 730-746 (2015).
3. S. V. Murphy, A. Atala, 3D bioprinting of tissues and organs. *Nat Biotech* **32**, 773-785 (2014).
4. J. Malda *et al.*, 25th anniversary article: engineering hydrogels for biofabrication. *Advanced Materials* **25**, 5011-5028 (2013).
5. A. S. Hoffman, Hydrogels for biomedical applications. *Advanced drug delivery reviews* **64**, 18-23 (2012).
6. A. K. Gaharwar, N. A. Peppas, A. Khademhosseini, Nanocomposite hydrogels for biomedical applications. *Biotechnology and Bioengineering* **111**, 441-453 (2014).
7. B. V. Slaughter, S. S. Khurshid, O. Z. Fisher, A. Khademhosseini, N. A. Peppas, Hydrogels in regenerative medicine. *Advanced Materials* **21**, 3307-3329 (2009).
8. M. W. Tibbitt, K. S. Anseth, Hydrogels as extracellular matrix mimics for 3D cell culture. *Biotechnology and Bioengineering* **103**, 655-663 (2009).
9. O. Z. Fisher, A. Khademhosseini, R. Langer, N. A. Peppas, Bioinspired materials for controlling stem cell fate. *Accounts of Chemical Research* **43**, 419-428 (2010).
10. J. K. Carrow, A. K. Gaharwar, Bioinspired Polymeric Nanocomposites for Regenerative Medicine. *Macromolecular Chemistry and Physics* **216**, 248-264 (2015).

11. A. M. Kloxin, C. J. Kloxin, C. N. Bowman, K. S. Anseth, Mechanical Properties of Cellularly Responsive Hydrogels and Their Experimental Determination. *Advanced Materials* **22**, 3484-3494 (2010).

12. D. E. Discher, D. J. Mooney, P. W. Zandstra, Growth factors, matrices, and forces combine and control stem cells. *Science* **324**, 1673-1677 (2009).

13. S. V. Murphy, A. Skardal, A. Atala, Evaluation of hydrogels for bio-printing applications. *Journal of Biomedical Materials Research Part A* **101A**, 272-284 (2013).

14. M. Stanton, J. Samitier, S. Sánchez, Bioprinting of 3D hydrogels. *Lab on a Chip* **15**, 3111-3115 (2015).

15. V. Mironov *et al.*, Organ printing: tissue spheroids as building blocks. *Biomaterials* **30**, 2164-2174 (2009).

16. V. Mironov, N. Reis, B. Derby, Review: bioprinting: a beginning. *Tissue engineering* **12**, 631-634 (2006).

17. N. G. Durmus, S. Tasoglu, U. Demirci, Bioprinting: Functional droplet networks. *Nat Mater* **12**, 478-479 (2013).

18. L. E. Bertassoni *et al.*, Hydrogel bioprinted microchannel networks for vascularization of tissue engineering constructs. *Lab on a Chip* **14**, 2202-2211 (2014).

19. A. Atala, J. J. Yoo, *Essentials of 3D Biofabrication and Translation* (Elsevier Science Publishing Company Incorporated, 2015).

20. T. Billiet, M. Vandenhaute, J. Schelfhout, S. Van Vlierberghe, P. Dubruel, A review of trends and limitations in hydrogel-rapid prototyping for tissue engineering. *Biomaterials* **33**, 6020-6041 (2012).

21. D. M. Kirchmajer, R. Gorkin Iii, M. in het Panhuis, An overview of the suitability of hydrogel-forming polymers for extrusion-based 3D-printing. *Journal of Materials Chemistry B* **3**, 4105-4117 (2015).

22. H.-W. Kang *et al.*, A 3D bioprinting system to produce human-scale tissue constructs with structural integrity. *Nat Biotech* **advance online publication** (2016).

23. A. L. Rutz, K. E. Hyland, A. E. Jakus, W. R. Burghardt, R. N. Shah, A Multimaterial Bioink Method for 3D Printing Tunable, Cell-Compatible Hydrogels. *Advanced Materials* **27**, 1607-1614 (2015).

24. N. Annabi *et al.*, 25th Anniversary Article: Rational Design and Applications of Hydrogels in Regenerative Medicine. *Advanced materials (Deerfield Beach, Fla.)* **26**, 85-124 (2014).

25. D. Chimene, D. L. Alge, A. K. Gaharwar, Two-dimensional nanomaterials for biomedical applications: emerging trends and future prospects. *Advanced Materials* **27**, 7261-7284 (2015).

26. A. K. Gaharwar *et al.*, Bioactive Silicate Nanoplatelets for Osteogenic Differentiation of Human Mesenchymal Stem Cells. *Advanced Materials* **25**, 3329-3336 (2013).

27. J. R. Xavier *et al.*, Bioactive Nanoengineered Hydrogels for Bone Tissue Engineering: A Growth-Factor-Free Approach. *ACS Nano* **9**, 3109-3118 (2015).

28. N. Masoumi *et al.*, Design and testing of a cyclic stretch and flexure bioreactor for evaluating engineered heart valve tissues based on poly(glycerol sebacate) scaffolds. *Proceedings of the Institution of Mechanical Engineers, Part H: Journal of Engineering in Medicine* **228**, 576-586 (2014).

29. C. Hou, Y. Duan, Q. Zhang, H. Wang, Y. Li, Bio-applicable and electroactive near-infrared laser-triggered self-healing hydrogels based on graphene networks. *Journal of Materials Chemistry* **22**, 14991-14996 (2012).

30. M. A. Azagarsamy, K. S. Anseth, Bioorthogonal click chemistry: An indispensable tool to create multifaceted cell culture scaffolds. *ACS macro letters* **2**, 5-9 (2012).

31. L. Gasperini, J. F. Mano, R. L. Reis, Natural polymers for the microencapsulation of cells. *Journal of the Royal Society Interface* **11**, 20140817 (2014).

32. J. H. Chung *et al.*, Bio-ink properties and printability for extrusion printing living cells. *Biomaterials Science* **1**, 763-773 (2013).

33. M. Kesti *et al.*, A versatile bioink for three-dimensional printing of cellular scaffolds based on thermally and photo-triggered tandem gelation. *Acta Biomaterialia* **11**, 162-172 (2015).

34. B. Duan, E. Kapetanovic, L. A. Hockaday, J. T. Butcher, Three-dimensional printed trileaflet valve conduits using biological hydrogels and human valve interstitial cells. *Acta Biomaterialia* **10**, 1836-1846 (2014).

35. T. Bhattacharjee *et al.*, Writing in the granular gel medium. *Science advances* **1**, e1500655 (2015).

36. M. A. Haque, T. Kurokawa, J. P. Gong, Super tough double network hydrogels and their application as biomaterials. *Polymer* **53**, 1805-1822 (2012).

37. T. C. Suekama, J. Hu, T. Kurokawa, J. P. Gong, S. H. Gehrke, Double-Network Strategy Improves Fracture Properties of Chondroitin Sulfate Networks. *ACS Macro Letters* **2**, 137-140 (2013).

38. S. E. Bakarich, R. Gorkin, M. i. h. Panhuis, G. M. Spinks, 4D Printing with Mechanically Robust, Thermally Actuating Hydrogels. *Macromolecular Rapid Communications* **36**, 1211-1217 (2015).

39. Q. Chen, H. Chen, L. Zhu, J. Zheng, Fundamentals of double network hydrogels. *Journal of Materials Chemistry B* **3**, 3654-3676 (2015).

40. D. M. Kirchmajer, M. i. h. Panhuis, Robust biopolymer based ionic-covalent entanglement hydrogels with reversible mechanical behaviour. *Journal of Materials Chemistry B* **2**, 4694-4702 (2014).

41. Q. Chen *et al.*, Fracture of the Physically Cross-Linked First Network in Hybrid Double Network Hydrogels. *Macromolecules* **47**, 2140-2148 (2014).

42. S. Hong *et al.*, 3D Printing of Highly Stretchable and Tough Hydrogels into Complex, Cellularized Structures. *Advanced Materials* **27**, 4035-4040 (2015).

43. M. K. Jaiswal *et al.*, Mechanically Stiff Nanocomposite Hydrogels at Ultralow Nanoparticle Content. *ACS Nano* **10**, 246–256 (2016).

44. T. Thakur *et al.*, Photocrosslinkable and Elastomeric Hydrogels for Bone Regeneration. *Journal of Biomedical Materials Research Part A*, DOI:10.1002/jbm.a.35621 (2016).

45. P. Kerativitayanan, J. K. Carrow, A. K. Gaharwar, Nanomaterials for Engineering Stem Cell Responses. *Advanced healthcare materials* (2015).

46. G. Gao *et al.*, Bioactive nanoparticles stimulate bone tissue formation in bioprinted three-dimensional scaffold and human mesenchymal stem cells. *Biotechnology journal* **9**, 1304-1311 (2014).

47. L. R. Hart, J. L. Harries, B. W. Greenland, H. M. Colquhoun, W. Hayes, Healable supramolecular polymers. *Polymer Chemistry* **4**, 4860-4870 (2013).

48. L. Yang, X. Tan, Z. Wang, X. Zhang, Supramolecular Polymers: Historical Development, Preparation, Characterization, and Functions. *Chemical Reviews* 10.1021/cr500633b (2015).

49. C. B. Highley, C. B. Rodell, J. A. Burdick, Direct 3D Printing of Shear-Thinning Hydrogels into Self-Healing Hydrogels. *Advanced Materials* **27**, 5075–5079 (2015).

50. N. Castro, J. O'Brien, L. G. Zhang, Integrating Biologically Inspired Nanomaterials and Table-top Stereolithography for 3D Printed Biomimetic Osteochondral Scaffolds. *Nanoscale* 10.1039/C5NR03425F (2015).

51. J. Thiele, Y. Ma, S. Bruekers, S. Ma, W. T. Huck, 25th Anniversary article: designer hydrogels for cell cultures: a materials selection guide. *Advanced materials* **26**, 125-148 (2014).

52. Y. Xu, X. Wang, Application of 3D biomimetic models in drug delivery and regenerative medicine. *Current Pharmaceutical Design* **21**, 1618-1626 (2015).

53. F. Guilak *et al.*, Control of Stem Cell Fate by Physical Interactions with the Extracellular Matrix. *Cell Stem Cell* **5**, 17-26 (2009).

54. F. Pati *et al.*, Printing three-dimensional tissue analogues with decellularized extracellular matrix bioink. *Nat Commun* **5** (2014).

55. V. Lee *et al.*, Design and fabrication of human skin by three-dimensional bioprinting. *Tissue Engineering Part C: Methods* **20**, 473-484 (2013).

56. V. K. Lee *et al.*, Creating perfused functional vascular channels using 3D bio-printing technology. *Biomaterials* **35**, 8092-8102 (2014).

57. A. K. Geim, K. S. Novoselov, The rise of graphene. *Nature materials* **6**, 183-191 (2007).

58. K. Novoselov *et al.*, Two-dimensional gas of massless Dirac fermions in graphene. *Nature* **438**, 197-200 (2005).

59. A. K. Geim, Graphene: status and prospects. *science* **324**, 1530-1534 (2009).

60. K. S. Novoselov *et al.*, Electric Field Effect in Atomically Thin Carbon Films. *Science* **306**, 666-669 (2004).

61. R. J. Young, I. A. Kinloch, L. Gong, K. S. Novoselov, The mechanics of graphene nanocomposites: A review. *Composites Science and Technology* **72**, 1459-1476 (2012).

62. K. S. Novoselov, Nobel Lecture: Graphene: Materials in the Flatland*. *Reviews of Modern Physics* **83**, 837-849 (2011).

63. A. Gnach, T. Lipinski, A. Bednarkiewicz, J. Rybka, J. A. Capobianco, Upconverting nanoparticles: assessing the toxicity. *Chemical Society Reviews* 10.1039/C4CS00177J (2015).

64. M. Palombo *et al.*, Pharmaceutical and Toxicological Properties of Engineered Nanomaterials for Drug Delivery. *Annual review of pharmacology and toxicology* **54**, 581-598 (2014).

65. K. L. Aillon, Y. Xie, N. El-Gendy, C. J. Berkland, M. L. Forrest, Effects of nanomaterial physicochemical properties on in vivo toxicity. *Advanced Drug Delivery Reviews* **61**, 457-466 (2009).

66. D. W. Grainger, Nanotoxicity assessment: all small talk? *Advanced Drug Delivery Reviews* **61**, 419-421 (2009).

67. P. Aggarwal, J. B. Hall, C. B. McLeland, M. A. Dobrovolskaia, S. E. McNeil, Nanoparticle interaction with plasma proteins as it relates to particle biodistribution, biocompatibility and therapeutic efficacy. *Advanced Drug Delivery Reviews* **61**, 428-437 (2009).

68. C. F. Jones, D. W. Grainger, In vitro assessments of nanomaterial toxicity. *Advanced Drug Delivery Reviews* **61**, 438-456 (2009).

69. M. J. Smith, J. M. Brown, W. C. Zamboni, N. J. Walker, From Immunotoxicity to Nanotherapy: The Effects of Nanomaterials on the Immune System. *Toxicological Sciences* **138**, 249-255 (2014).

70. Y. Chen, C. Tan, H. Zhang, L. Wang, Two-dimensional graphene analogues for biomedical applications. *Chemical Society Reviews* 10.1039/C4CS00300D (2015).

71. A. A. Shvedova, V. E. Kagan, B. Fadeel, Close Encounters of the Small Kind: Adverse Effects of Man-Made Materials Interfacing with the Nano-Cosmos of Biological Systems. *Annual Review of Pharmacology and Toxicology* **50**, 63-88 (2010).

72. X. Zhuang, Y. Mai, D. Wu, F. Zhang, X. Feng, Two-Dimensional Soft Nanomaterials: A Fascinating World of Materials. *Advanced Materials* **27**, 403-427 (2015).

73. J. M. Anderson, A. Rodriguez, D. T. Chang (2008) Foreign body reaction to biomaterials. in *Seminars in immunology* (Elsevier), pp 86-100.

74. B. D. Ratner, S. J. Bryant, Biomaterials: where we have been and where we are going. *Annu. Rev. Biomed. Eng.* **6**, 41-75 (2004).

75. S. Z. Butler *et al.*, Progress, Challenges, and Opportunities in Two-Dimensional Materials Beyond Graphene. *ACS Nano* **7**, 2898-2926 (2013).

76. M. Xu, T. Liang, M. Shi, H. Chen, Graphene-Like Two-Dimensional Materials. *Chemical Reviews* **113**, 3766-3798 (2013).

77. J. I. Dawson, R. O. C. Oreffo, Clay: New Opportunities for Tissue Regeneration and Biomaterial Design. *Advanced Materials* **25**, 4069-4086 (2013).

78. Y. Kuthati, R. K. Kankala, C.-H. Lee, Layered double hydroxide nanoparticles for biomedical applications: Current status and recent prospects. *Applied Clay Science* **112–113**, 100-116 (2015).

79. V. Nicolosi, M. Chhowalla, M. G. Kanatzidis, M. S. Strano, J. N. Coleman, Liquid exfoliation of layered materials. *Science* **340** (2013).

80. S. Pei, H.-M. Cheng, The reduction of graphene oxide. *Carbon* **50**, 3210-3228 (2012).

81. V. Rives, *Layered double hydroxides: present and future* (Nova Publishers, 2001).

82. D. Evans, R. T. Slade, "Structural Aspects of Layered Double Hydroxides" in Layered Double Hydroxides, X. Duan, D. Evans, Eds. (Springer Berlin Heidelberg, 2006), vol. 119, chap. 5, pp. 1-87.

83. M. Osada, T. Sasaki, Exfoliated oxide nanosheets: new solution to nanoelectronics. *Journal of Materials Chemistry* **19**, 2503-2511 (2009).

84. G.-B. Liu, D. Xiao, Y. Yao, X. Xu, W. Yao, Electronic structures and theoretical modelling of two-dimensional group-VIB transition metal dichalcogenides. *Chemical Society Reviews* 10.1039/C4CS00301B (2015).

85. S. Goenka, V. Sant, S. Sant, Graphene-based nanomaterials for drug delivery and tissue engineering. *Journal of Controlled Release* **173**, 75-88 (2014).

86. Y. Zhu *et al.*, Graphene and graphene oxide: synthesis, properties, and applications. *Advanced materials* **22**, 3906-3924 (2010).

87. H. Shen, L. Zhang, M. Liu, Z. Zhang, Biomedical applications of graphene. *Theranostics* **2**, 283-294 (2012).

88. H. Fan *et al.*, Fabrication, mechanical properties, and biocompatibility of graphene-reinforced chitosan composites. *Biomacromolecules* **11**, 2345-2351 (2010).

89. I. K. Moon, J. Lee, R. S. Ruoff, H. Lee, Reduced graphene oxide by chemical graphitization. *Nature Communication* **1**, 73 (2010).

90. O. C. Compton, S. T. Nguyen, Graphene Oxide, Highly Reduced Graphene Oxide, and Graphene: Versatile Building Blocks for Carbon-Based Materials. *Small* **6**, 711-723 (2010).

91. A. Bianco, Graphene: Safe or Toxic? The Two Faces of the Medal. *Angewandte Chemie International Edition* **52**, 4986-4997 (2013).

92. S. Sharifi *et al.*, Toxicity of nanomaterials. *Chemical Society Reviews* **41**, 2323-2343 (2012).

93. T. R. Nayak *et al.*, Graphene for Controlled and Accelerated Osteogenic Differentiation of Human Mesenchymal Stem Cells. *ACS Nano* **5**, 4670-4678 (2011).

94. M. Tang *et al.*, Enhancement of electrical signaling in neural networks on graphene films. *Biomaterials* **34**, 6402-6411 (2013).

95. S. R. Shin *et al.*, Carbon-nanotube-embedded hydrogel sheets for engineering cardiac constructs and bioactuators. *ACS nano* **7**, 2369-2380 (2013).

96. L. Qiu *et al.*, Mechanically Robust, Electrically Conductive and Stimuli-Responsive Binary Network Hydrogels Enabled by Superelastic Graphene Aerogels. *Advanced Materials* **26**, 3333-3337 (2014).

97. W. C. Lee *et al.*, Origin of Enhanced Stem Cell Growth and Differentiation on Graphene and Graphene Oxide. *ACS Nano* **5**, 7334–7341 (2011).

98. S. W. Crowder *et al.*, Three-dimensional graphene foams promote osteogenic differentiation of human mesenchymal stem cells. *Nanoscale* **5**, 4171-4176 (2013).

99. M. S. Mannoor *et al.*, Graphene-based wireless bacteria detection on tooth enamel. *Nature communications* **3**, 763 (2012).

100. S. Reshma, P. Mohanan, Graphene: A Multifaceted Nanomaterial for Cutting Edge Biomedical Application. *Int J Med Nano Res* **1** (2014).

101. H. Bai, C. Li, X. Wang, G. Shi, A pH-sensitive graphene oxide composite hydrogel. *Chemical Communications* **46**, 2376-2378 (2010).

102. D. Li, M. B. Müller, S. Gilje, R. B. Kaner, G. G. Wallace, Processable aqueous dispersions of graphene nanosheets. *Nature Nanotechnology* **3**, 101-105 (2008).

103. S. R. Shin *et al.*, Cell-laden Microengineered and Mechanically Tunable Hybrid Hydrogels of Gelatin and Graphene Oxide. *Advanced Materials* **25**, 6385-6391 (2013).

104. C. Cha *et al.*, Controlling Mechanical Properties of Cell-Laden Hydrogels by Covalent Incorporation of Graphene Oxide. *Small* **10**, 514-523 (2014).

105. J. Liu, L. Cui, D. Losic, Graphene and graphene oxide as new nanocarriers for drug delivery applications. *Acta Biomaterialia* **9**, 9243-9257 (2013).

106. C. L. Weaver, J. M. LaRosa, X. Luo, X. T. Cui, Electrically Controlled Drug Delivery from Graphene Oxide Nanocomposite Films. *ACS Nano* **8**, 1834-1843 (2014).

107. A. Paul *et al.*, Injectable graphene oxide/hydrogel-based angiogenic gene delivery system for vasculogenesis and cardiac repair. *ACS nano* **8**, 8050-8062 (2014).

108. R. A. Green, N. H. Lovell, G. G. Wallace, L. A. Poole-Warren, Conducting polymers for neural interfaces: Challenges in developing an effective long-term implant. *Biomaterials* **29**, 3393-3399 (2008).

109. X. Luo, C. L. Weaver, S. Tan, X. T. Cui, Pure graphene oxide doped conducting polymer nanocomposite for bio-interfacing. *Journal of Materials Chemistry B* **1**, 1340-1348 (2013).

110. S. Y. Park *et al.*, Enhanced Differentiation of Human Neural Stem Cells into Neurons on Graphene. *Advanced Materials* **23**, H263-H267 (2011).

111. M. C. Serrano *et al.*, 3D free-standing porous scaffolds made of graphene oxide as substrates for neural cell growth. *Journal of Materials Chemistry B* **2**, 5698-5706 (2014).

112. O. Akhavan, E. Ghaderi, E. Abouei, S. Hatamie, E. Ghasemi, Accelerated differentiation of neural stem cells into neurons on ginseng-reduced graphene oxide sheets. *Carbon* **66**, 395-406 (2014).

113. B. Cai *et al.*, Ultrasensitive Label-Free Detection of PNA–DNA Hybridization by Reduced Graphene Oxide Field-Effect Transistor Biosensor. *ACS Nano* **8**, 2632-2638 (2014).

114. D.-J. Kim *et al.*, Reduced graphene oxide field-effect transistor for label-free femtomolar protein detection. *Biosensors and Bioelectronics* **41**, 621-626 (2013).

115. J. Chang *et al.*, Ultrasonic-assisted self-assembly of monolayer graphene oxide for rapid detection of Escherichia coli bacteria. *Nanoscale* **5**, 3620-3626 (2013).

116. H. Zhang *et al.*, Graphitic carbon nitride nanosheets doped graphene oxide for electrochemical simultaneous determination of ascorbic acid, dopamine and uric acid. *Electrochimica Acta* **142**, 125-131 (2014).

117. J. T. Robinson *et al.*, Ultrasmall Reduced Graphene Oxide with High Near-Infrared Absorbance for Photothermal Therapy. *Journal of the American Chemical Society* **133**, 6825-6831 (2011).

118. O. Akhavan, E. Ghaderi, S. Aghayee, Y. Fereydooni, A. Talebi, The use of a glucose-reduced graphene oxide suspension for photothermal cancer therapy. *Journal of Materials Chemistry* **22**, 13773-13781 (2012).

119. H. K. Lau, K. L. Kiick, Opportunities for Multicomponent Hybrid Hydrogels in Biomedical Applications. *Biomacromolecules* (2015).

120. P. Song *et al.*, Striking multiple synergies created by combining reduced graphene oxides and carbon nanotubes for polymer nanocomposites. *Nanotechnology* **24**, 125704 (2013).

121. P. Song, L. Zhao, Z. Cao, Z. Fang, Polypropylene nanocomposites based on C60-decorated carbon nanotubes: thermal properties, flammability, and mechanical properties. *Journal of Materials Chemistry* **21**, 7782-7788 (2011).

122. M. K. Shin *et al.*, Synergistic toughening of composite fibres by self-alignment of reduced graphene oxide and carbon nanotubes. *Nat Commun* **3**, 650 (2012).

123. P. a. Song, L. Liu, G. Huang, Y. Yu, Q. Guo, Largely enhanced thermal and mechanical properties of polymer nanocomposites via incorporating C 60 @graphene nanocarbon hybrid. *Nanotechnology* **24**, 505706 (2013).

124. B. Holmes, X. Fang, A. Zarate, M. Keidar, L. G. Zhang, Enhanced human bone marrow mesenchymal stem cell chondrogenic differentiation in electrospun constructs with carbon nanomaterials. *Carbon* **97**, 1-13 (2016).

125. J. Byun, Emerging Frontiers of Graphene in Biomedicine. *Journal of microbiology and biotechnology* **25**, 145-151 (2015).

126. H. Shen, L. Zhang, M. Liu, Z. Zhang, Biomedical Applications of Graphene. *Theranostics* **2**, 283-294 (2012).

127. J. R. Xavier *et al.*, Bioactive Nanoengineered Hydrogels for Bone Tissue Engineering: A Growth-Factor-Free Approach. *ACS Nano* 10.1021/nn507488s (2015).

128. A. K. Gaharwar *et al.*, Shear-Thinning Nanocomposite Hydrogels for the Treatment of Hemorrhage. *ACS Nano* **8**, 9833-9842 (2014).

129. A. K. Gaharwar *et al.*, Bioactive Silicate Nanoplatelets for Osteogenic Differentiation of Human Mesenchymal Stem Cells. *Adv. Mater.* **25**, 3329-2226 (2013).

130. S. M. Mihaila *et al.*, The osteogenic differentiation of SSEA-4 sub-population of human adipose derived stem cells using silicate nanoplatelets. *Biomaterials* **35**, 9087-9099 (2014).

131. J. R. Xavier *et al.*, Bioactive Nanoengineered Hydrogels for Bone Tissue Engineering: A Growth-Factor-Free Approach. *ACS Nano* **DOI 10.1021/nn507488s** (2015).

132. L. Dan, W. Tao, L. Xinxing, T. Zhen, Accelerated cell sheet detachment by copolymerizing hydrophilic PEG side chains into PNIPAm nanocomposite hydrogels. *Biomedical Materials* **7**, 055008 (2012).

133. A. K. Gaharwar, P. J. Schexnailder, B. P. Kline, G. Schmidt, Assessment of using Laponite® cross-linked poly(ethylene oxide) for controlled cell adhesion and mineralization. *Acta Biomaterialia* **7**, 568-577 (2011).

134. P. J. Schexnailder *et al.*, Tuning Cell Adhesion by Incorporation of Charged Silicate Nanoparticles as Cross-Linkers to Polyethylene Oxide. *Macromolecular bioscience* **10**, 1416-1423 (2010).

135. A. K. Gaharwar *et al.*, Physically Crosslinked Nanocomposites from Silicate-Crosslinked PEO: Mechanical Properties and Osteogenic Differentiation of Human Mesenchymal Stem Cells. *Macromolecular bioscience* **12**, 779-793 (2012).

136. D. Reffitt *et al.*, Orthosilicic acid stimulates collagen type 1 synthesis and osteoblastic differentiation in human osteoblast-like cells in vitro. *Bone* **32**, 127-135 (2003).

137. C. A. Gregory, H. Singh, A. S. Perry, D. J. Prockop, The Wnt signaling inhibitor dickkopf-1 is required for reentry into the cell cycle of human adult stem cells from bone marrow. *Journal of Biological Chemistry* **278**, 28067-28078 (2003).

138. V. Luginbuehl, L. Meinel, H. P. Merkle, B. Gander, Localized delivery of growth factors for bone repair. *European Journal of Pharmaceutics and Biopharmaceutics* **58**, 197-208 (2004).

139. M. Gonçalves *et al.*, Antitumor Efficacy of Doxorubicin-Loaded Laponite/Alginate Hybrid Hydrogels. *Macromolecular Bioscience* **14**, 110-120 (2014).

140. K. Li *et al.*, Enhanced In Vivo Antitumor Efficacy of Doxorubicin Encapsulated within Laponite Nanodisks. *ACS Applied Materials & Interfaces* **6**, 12328-12334 (2014).

141. Y. L. Wu *et al.*, Folic acid-modified laponite nanodisks for targeted anticancer drug delivery. *Journal of Materials Chemistry B* **2**, 7410-7418 (2014).

142. Q. Weng *et al.*, Highly Water-Soluble, Porous, and Biocompatible Boron Nitrides for Anticancer Drug Delivery. *ACS Nano* **8**, 6123-6130 (2014).

143. R. Ma, T. Sasaki, Nanosheets of Oxides and Hydroxides: Ultimate 2D Charge-Bearing Functional Crystallites. *Advanced Materials* **22**, 5082-5104 (2010).

144. S. Khan *et al.*, Nanohybrid Based on Antibiotic Encapsulated Layered Double Hydroxide as a Drug Delivery System. *Appl Biochem Biotechnol* 10.1007/s12010-014-1211-9, 1-17 (2014).

145. X. Bi, T. Fan, H. Zhang, Novel Morphology-Controlled Hierarchical Core@Shell Structural Organo-Layered Double Hydroxides Magnetic Nanovehicles for Drug Release. *ACS Applied Materials & Interfaces* **6**, 20498-20509 (2014).

146. V. Rives, M. del Arco, C. Martín, Intercalation of drugs in layered double hydroxides and their controlled release: A review. *Applied Clay Science* **88–89**, 239-269 (2014).

147. B. Saifullah *et al.*, Development of a biocompatible nanodelivery system for tuberculosis drugs based on isoniazid-Mg/Al layered double hydroxide. *International Journal of Nanomedicine* **9**, 4749-4762 (2014).

148. R. Ma, Z. Wang, L. Yan, X. Chen, G. Zhu, Novel Pt-loaded layered double hydroxide nanoparticles for efficient and cancer-cell specific delivery of a cisplatin prodrug. *Journal of Materials Chemistry B* **2**, 4868-4875 (2014).

149. L. Li, W. Gu, J. Chen, W. Chen, Z. P. Xu, Co-delivery of siRNAs and anti-cancer drugs using layered double hydroxide nanoparticles. *Biomaterials* **35**, 3331-3339 (2014).

150. W. Sun *et al.*, Electrochemical biosensor based on graphene, Mg2Al layered double hydroxide and hemoglobin composite. *Electrochimica Acta* **91**, 130-136 (2013).

151. L.-M. Liu *et al.*, Hemoglobin/DNA/layered double hydroxide composites for biosensing applications. *Analytical Methods* **5**, 3565-3571 (2013).

152. Y. Shu, P. Yin, B. Liang, H. Wang, L. Guo, Bioinspired Design and Assembly of Layered Double Hydroxide/Poly(vinyl alcohol) Film with High Mechanical Performance. *ACS Applied Materials & Interfaces* **6**, 15154-15161 (2014).

153. M. Chakraborti, J. K. Jackson, D. Plackett, D. M. Brunette, H. M. Burt, Drug intercalation in layered double hydroxide clay: Application in the development of a nanocomposite film for guided tissue regeneration. *International Journal of Pharmaceutics* **416**, 305-313 (2011).

154. V. Sorkin, H. Pan, H. Shi, S. Y. Quek, Y. W. Zhang, Nanoscale Transition Metal Dichalcogenides: Structures, Properties, and Applications. *Critical Reviews in Solid State and Materials Sciences* **39**, 319-367 (2014).

155. M. Pumera, A. H. Loo, Layered transition-metal dichalcogenides (MoS2 and WS2) for sensing and biosensing. *TrAC Trends in Analytical Chemistry* **61**, 49-53 (2014).

156. J. Z. Ou *et al.*, Ion-Driven Photoluminescence Modulation of Quasi-Two-Dimensional MoS2 Nanoflakes for Applications in Biological Systems. *Nano Letters* **14**, 857-863 (2014).

157. D. Sarkar *et al.*, MoS2 Field-Effect Transistor for Next-Generation Label-Free Biosensors. *ACS Nano* **8**, 3992-4003 (2014).

158. K. Liu, J. Feng, A. Kis, A. Radenovic, Atomically Thin Molybdenum Disulfide Nanopores with High Sensitivity for DNA Translocation. *ACS Nano* **8**, 2504-2511 (2014).

159. D. Branton *et al.*, The potential and challenges of nanopore sequencing. *Nat Biotech* **26**, 1146-1153 (2008).

160. M. Rong *et al.*, Fluorescence sensing of chromium (VI) and ascorbic acid using graphitic carbon nitride nanosheets as a fluorescent "switch". *Biosensors & bioelectronics* **68**, 210-217 (2015).

161. Y. Yong *et al.*, WS2 nanosheet as a new photosensitizer carrier for combined photodynamic and photothermal therapy of cancer cells. *Nanoscale* **6**, 10394-10403 (2014).

162. T. Lin *et al.*, Visual detection of blood glucose based on peroxidase-like activity of WS2 nanosheets. *Biosensors and Bioelectronics* **62**, 302-307 (2014).

163. S. Wang *et al.*, Biocompatible PEGylated MoS2 nanosheets: Controllable bottom-up synthesis and highly efficient photothermal regression of tumor. *Biomaterials* **39**, 206-217 (2015).

164. S. S. Chou *et al.*, Chemically Exfoliated MoS2 as Near-Infrared Photothermal Agents. *Angewandte Chemie* **125**, 4254-4258 (2013).

165. L. Cheng *et al.*, PEGylated WS2 Nanosheets as a Multifunctional Theranostic Agent for in vivo Dual-Modal CT/Photoacoustic Imaging Guided Photothermal Therapy. *Advanced Materials* **26**, 1886-1893 (2014).

166. X. Qian, S. Shen, T. Liu, L. Cheng, Z. Liu, Two-dimensional TiS2 nanosheets for in vivo photoacoustic imaging and photothermal cancer therapy. *Nanoscale* 10.1039/C5NR00893J (2015).

167. Z. Sun *et al.*, Generalized self-assembly of scalable two-dimensional transition metal oxide nanosheets. *Nat Commun* **5** (2014).

168. L. Wang, T. Sasaki, Titanium Oxide Nanosheets: Graphene Analogues with Versatile Functionalities. *Chemical Reviews* **114**, 9455-9486 (2014).

169. M. Osada, T. Sasaki, Two-Dimensional Dielectric Nanosheets: Novel Nanoelectronics From Nanocrystal Building Blocks. *Advanced Materials* **24**, 210-228 (2012).

170. Y. Chen *et al.*, Break-up of Two-Dimensional MnO2 Nanosheets Promotes Ultrasensitive pH-Triggered Theranostics of Cancer. *Advanced Materials* **26**, 7019-7026 (2014).

171. Y. Omomo, T. Sasaki, Wang, M. Watanabe, Redoxable Nanosheet Crystallites of MnO2 Derived via Delamination of a Layered Manganese Oxide. *Journal of the American Chemical Society* **125**, 3568-3575 (2003).

172. J. Ping *et al.*, Recent advances in aptasensors based on graphene and graphene-like nanomaterials. *Biosensors and Bioelectronics* **64**, 373-385 (2015).

173. Y. Yuan, S. Wu, F. Shu, Z. Liu, An MnO2 nanosheet as a label-free nanoplatform for homogeneous biosensing. *Chemical Communications* **50**, 1095-1097 (2014).

174. R. Deng, X. Xie, M. Vendrell, Y.-T. Chang, X. Liu, Intracellular glutathione detection using MnO2-nanosheet-modified upconversion nanoparticles. *Journal of the American Chemical Society* **133**, 20168-20171 (2011).

175. Z. Fei Yin, L. Wu, H. Gui Yang, Y. Hua Su, Recent progress in biomedical applications of titanium dioxide. *Physical Chemistry Chemical Physics* **15**, 4844-4858 (2013).

176. T. Rajh, N. M. Dimitrijevic, M. Bissonnette, T. Koritarov, V. Konda, Titanium Dioxide in the Service of the Biomedical Revolution. *Chemical Reviews* **114**, 10177-10216 (2014).

177. Q. Xiang, J. Yu, M. Jaroniec, Nitrogen and sulfur co-doped TiO 2 nanosheets with exposed {001} facets: synthesis, characterization and visible-light photocatalytic activity. *Physical Chemistry Chemical Physics* **13**, 4853-4861 (2011).

178. G. Elvira *et al.*, Targeting Neural Stem Cells with Titanium Dioxide Nanoparticles Coupled to Specific Monoclonal Antibodies. *Journal of Biomaterials Applications* **26**, 1069-1089 (2012).

179. M. Liu *et al.*, An anisotropic hydrogel with electrostatic repulsion between cofacially aligned nanosheets. *Nature* **517**, 68-72 (2015).

180. C. G. Liu, X. T. Wu, X. F. Li, X. G. Zhang, Synthesis of graphene-like g-C3N4/Fe3O4 nanocomposites with high photocatalytic activity and applications in drug delivery. *RSC Advances* **4**, 62492-62498 (2014).

181. X. Zhang *et al.*, Enhanced Photoresponsive Ultrathin Graphitic-Phase C3N4 Nanosheets for Bioimaging. *Journal of the American Chemical Society* **135**, 18-21 (2012).

182. X. Zhang *et al.*, Single-Layered Graphitic-C3N4 Quantum Dots for Two-Photon Fluorescence Imaging of Cellular Nucleus. *Advanced Materials* **26**, 4438-4443 (2014).

183. L.-S. Lin *et al.*, Graphitic-phase C3N4 nanosheets as efficient photosensitizers and pH-responsive drug nanocarriers for cancer imaging and therapy. *Journal of Materials Chemistry B* **2**, 1031-1037 (2014).

184. T. Lin *et al.*, Graphite-like carbon nitrides as peroxidase mimetics and their applications to glucose detection. *Biosensors and Bioelectronics* **59**, 89-93 (2014).

185. T. Y. Ma, Y. Tang, S. Dai, S. Z. Qiao, Proton-Functionalized Two-Dimensional Graphitic Carbon Nitride Nanosheet: An Excellent Metal-/Label-Free Biosensing Platform. *Small* **10**, 2382-2389 (2014).

186. Y. Lin, J. W. Connell, Advances in 2D boron nitride nanostructures: nanosheets, nanoribbons, nanomeshes, and hybrids with graphene. *Nanoscale* **4**, 6908-6939 (2012).

187. J. Wang, R. Zhao, Z. Liu, Z. Liu, Widely tunable carrier mobility of boron nitride-embedded graphene. *Small* **9**, 1373-1378 (2013).

188. Q. Peng, W. Ji, S. De, Mechanical properties of the hexagonal boron nitride monolayer: Ab initio study. *Computational Materials Science* **56**, 11-17 (2012).

189. J. Biscarat, M. Bechelany, C. Pochat-Bohatier, P. Miele, Graphene-like BN/gelatin nanobiocomposites for gas barrier applications. *Nanoscale* **7**, 613-618 (2015).

190. W. Lei, D. Liu, S. Qin, D. Portehault, Y. I. Chen, Boron (Carbon) nitride nanomaterials. *Nanotubes and Nanosheets: Functionalization and Applications of Boron Nitride and Other Nanomaterials*, 59 (2015).

191. J. Peng *et al.*, Fabrication of graphene quantum dots and hexagonal boron nitride nanocomposites for fluorescent cell imaging. *Journal of biomedical nanotechnology* **9**, 1679-1685 (2013).

192. X. Li *et al.*, Boron nitride nanotube-enhanced osteogenic differentiation of mesenchymal stem cells. *Journal of Biomedical Materials Research Part B: Applied Biomaterials* 10.1002/jbm.b.33391, n/a-n/a (2015).

193. W. Meng, Y. Huang, Y. Fu, Z. Wang, C. Zhi, Polymer composites of boron nitride nanotubes and nanosheets. *Journal of Materials Chemistry C* **2**, 10049-10061 (2014).

194. S. Balendhran, S. Walia, H. Nili, S. Sriram, M. Bhaskaran, Elemental Analogues of Graphene: Silicene, Germanene, Stanene, and Phosphorene. *Small* **11**, 640-652 (2015).

195. M. E. Dávila, L. Xian, S. Cahangirov, A. Rubio, G. L. Lay, Germanene: a novel two-dimensional germanium allotrope akin to graphene and silicene. *New Journal of Physics* **16**, 095002 (2014).

196. N. J. Roome, J. D. Carey, Beyond Graphene: Stable Elemental Monolayers of Silicene and Germanene. *ACS applied materials & interfaces* **6**, 7743-7750 (2014).

197. D. Jose, A. Datta, Structures and chemical properties of silicene: unlike graphene. *Accounts of chemical research* **47**, 593-602 (2013).

198. E. Tasciotti *et al.*, Mesoporous silicon particles as a multistage delivery system for imaging and therapeutic applications. *Nat Nano* **3**, 151-157 (2008).

199. R. E. Serda, B. Godin, E. Blanco, C. Chiappini, M. Ferrari, Multi-stage delivery nano-particle systems for therapeutic applications. *Biochimica et Biophysica Acta (BBA) - General Subjects* **1810**, 317-329 (2011).

200. P. a. Song *et al.*, Striking multiple synergies created by combining reduced graphene oxides and carbon nanotubes for polymer nanocomposites. *Nanotechnology* **24**, 125704 (2013).

201. M.-Q. Zhao, Q. Zhang, J.-Q. Huang, F. Wei, Hierarchical Nanocomposites Derived from Nanocarbons and Layered Double Hydroxides - Properties, Synthesis, and Applications. *Advanced Functional Materials* **22**, 675-694 (2012).

202. C. W. Hull (1986) Apparatus for production of three-dimensional objects by stereolithography. (Google Patents).

203. S. S. Crump (1992) Apparatus and method for creating three-dimensional objects. (Google Patents).

204. R. R. Jose, M. J. Rodriguez, T. A. Dixon, F. Omenetto, D. L. Kaplan, Evolution of Bioinks and Additive Manufacturing Technologies for 3D Bioprinting. *ACS Biomaterials Science & Engineering* 10.1021/acsbiomaterials.6b00088 (2016).

205. K. K. VanKoevering, S. J. Hollister, G. E. Green, Advances in 3-Dimensional Printing in Otolaryngology: A Review. *JAMA Otolaryngology–Head & Neck Surgery* **143**, 178-183 (2017).

206. D. Chimene, K. K. Lennox, R. R. Kaunas, A. K. Gaharwar, Advanced bioinks for 3D printing: a materials science perspective. *Ann Biomed Eng* **44**, 2090-2102 (2016).

207. C. J. Ferris, K. G. Gilmore, G. G. Wallace, Biofabrication: an overview of the approaches used for printing of living cells. *Applied microbiology and biotechnology* **97**, 4243-4258 (2013).

208. P. Zorlutuna *et al.*, Microfabricated biomaterials for engineering 3D tissues. *Advanced materials* **24**, 1782-1804 (2012).

209. J. Malda *et al.*, 25th Anniversary Article: Engineering Hydrogels for Biofabrication. *Advanced Materials* **25**, 5011-5028 (2013).

210. A. Vedadghavami *et al.*, Manufacturing of hydrogel biomaterials with controlled mechanical properties for tissue engineering applications. *Acta Biomaterialia* **62**, 42-63 (2017).

211. D. Chimene *et al.*, Nanoengineered Ionic-Covalent Entanglement (NICE) Bioinks for 3D Bioprinting. *ACS applied materials & interfaces* (2018).

212. C. Creton, 50th Anniversary Perspective: Networks and Gels: Soft but Dynamic and Tough. *Macromolecules* **50**, 8297-8316 (2017).

213. X. Zhao, Multi-scale multi-mechanism design of tough hydrogels: building dissipation into stretchy networks. *Soft Matter* **10**, 672-687 (2014).

214. R. Long, C.-Y. Hui, Fracture toughness of hydrogels: measurement and interpretation. *Soft Matter* **12**, 8069-8086 (2016).

215. B. N. J. Persson, O. Albohr, G. Heinrich, H. Ueba, Crack propagation in rubber-like materials. *Journal of Physics: Condensed Matter* **17**, R1071 (2005).

216. C. Creton, M. Ciccotti, Fracture and adhesion of soft materials: a review. *Reports on Progress in Physics* **79**, 046601 (2016).

217. A. Gent, W. Mars (2013) Strength of Elastomers, the Science and Technology of Rubber. Chapter 10. (Elsevier).

218. D. Maugis, M. Barquins, Fracture mechanics and the adherence of viscoelastic bodies. *Journal of Physics D: Applied Physics* **11**, 1989 (1978).

219. T. Zhang, S. Lin, H. Yuk, X. Zhao, Predicting fracture energies and crack-tip fields of soft tough materials. *Extreme Mechanics Letters* **4**, 1-8 (2015).

220. V. H. Mouser *et al.*, Yield stress determines bioprintability of hydrogels based on gelatin-methacryloyl and gellan gum for cartilage bioprinting. *Biofabrication* **8**, 035003 (2016).

221. F. P. Melchels *et al.*, Hydrogel-based reinforcement of 3D bioprinted constructs. *Biofabrication* **8**, 035004 (2016).

222. N. Paxton *et al.*, Proposal to assess printability of bioinks for extrusion-based bioprinting and evaluation of rheological properties governing bioprintability. *Biofabrication* **9**, 044107 (2017).

223. A. Kosik-Kozioł *et al.*, PLA short sub-micron fiber reinforcement of 3D bioprinted alginate constructs for cartilage regeneration. *Biofabrication* **9**, 044105 (2017).

224. F. P. Melchels, W. J. Dhert, D. W. Hutmacher, J. Malda, Development and characterisation of a new bioink for additive tissue manufacturing. *Journal of Materials Chemistry B* **2**, 2282-2289 (2014).

225. S. Sathaye *et al.*, Rheology of peptide-and protein-based physical hydrogels: Are everyday measurements just scratching the surface? *Wiley Interdisciplinary Reviews: Nanomedicine and Nanobiotechnology* **7**, 34-68 (2015).

226. M. Sarker, X. B. Chen, Modeling the Flow Behavior and Flow Rate of Medium Viscosity Alginate for Scaffold Fabrication With a Three-Dimensional Bioplotter. *Journal of Manufacturing Science and Engineering* **139**, 081002-081002-081014 (2017).

227. M. A. Rao, "Flow and functional models for rheological properties of fluid foods" in Rheology of fluid, semisolid, and solid foods. (Springer, 2014), pp. 27-61.

228. H. A. Barnes, Thixotropy—a review. *Journal of Non-Newtonian fluid mechanics* **70**, 1-33 (1997).

229. H. Li, S. Liu, L. Lin, Rheological study on 3D printability of alginate hydrogel and effect of graphene oxide. *International Journal of Bioprinting* **2**, 13 (2016).

230. S. Kyle, Z. M. Jessop, A. Al-Sabah, I. S. Whitaker, ‘printability'of Candidate Biomaterials for Extrusion Based 3d Printing: State-of-the-art. *Advanced healthcare materials* (2017).

231. Y. Jin, C. Liu, W. Chai, A. Compaan, Y. Huang, Self-Supporting Nanoclay as Internal Scaffold Material for Direct Printing of Soft Hydrogel Composite Structures in Air. *ACS applied materials & interfaces* **9**, 17456-17465 (2017).

232. S. A. Wilson, L. M. Cross, C. W. Peak, A. K. Gaharwar, Shear-Thinning and Thermo-Reversible Nanoengineered Inks for 3D Bioprinting. *ACS applied materials & interfaces* (2017).

233. T. Ahlfeld *et al.*, Development of a clay based bioink for 3D cell printing for skeletal application. *Biofabrication* **9**, 034103 (2017).

234. V. H. Mouser *et al.*, Development of a thermosensitive HAMA-containing bio-ink for the fabrication of composite cartilage repair constructs. *Biofabrication* **9**, 015026 (2017).

235. J. S. Park *et al.*, The effect of matrix stiffness on the differentiation of mesenchymal stem cells in response to TGF-β. *Biomaterials* **32**, 3921-3930 (2011).

236. G. Huang *et al.*, Functional and Biomimetic Materials for Engineering of the Three-Dimensional Cell Microenvironment. *Chemical Reviews* **117**, 12764-12850 (2017).

237. A. J. Engler, S. Sen, H. L. Sweeney, D. E. Discher, Matrix elasticity directs stem cell lineage specification. *Cell* **126**, 677-689 (2006).

238. N. Huebsch *et al.*, Harnessing traction-mediated manipulation of the cell/matrix interface to control stem-cell fate. *Nature materials* **9**, 518-526 (2010).

239. A. Bauer *et al.*, Hydrogel substrate stress-relaxation regulates the spreading and proliferation of mouse myoblasts. *Acta biomaterialia* **62**, 82-90 (2017).

240. O. Chaudhuri *et al.*, Hydrogels with tunable stress relaxation regulate stem cell fate and activity. *Nat Mater* **15**, 326-334 (2016).

241. R. Goetzke, A. Sechi, L. De Laporte, S. Neuss, W. Wagner, Why the impact of mechanical stimuli on stem cells remains a challenge. *Cellular and Molecular Life Sciences*, 1-16 (2018).

242. K. H. Vining, D. J. Mooney, Mechanical forces direct stem cell behaviour in development and regeneration. *Nature Reviews Molecular Cell Biology* **18**, 728 (2017).

243. J. K. Mouw, J. T. Connelly, C. G. Wilson, K. E. Michael, M. E. Levenston, Dynamic compression regulates the expression and synthesis of chondrocyte-specific matrix molecules in bone marrow stromal cells. *Stem cells* **25**, 655-663 (2007).

244. A. Tondon, R. J. P. o. Kaunas, The direction of stretch-induced cell and stress fiber orientation depends on collagen matrix stress. **9**, e89592 (2014).

245. Y. Li, K. A. Kilian, Bridging the Gap: From 2D Cell Culture to 3D Microengineered Extracellular Matrices. *Advanced Healthcare Materials* **4**, 2780-2796 (2015).

246. D. A. Foyt, M. D. Norman, T. T. Yu, E. Gentleman, Exploiting Advanced Hydrogel Technologies to Address Key Challenges in Regenerative Medicine. *Advanced healthcare materials* **7**, 1700939 (2018).

247. K. J. France, F. Xu, T. Hoare, Structured Macroporous Hydrogels: Progress, Challenges, and Opportunities. *Advanced Healthcare Materials* **7**, 1700927 (2017).

248. A. J. Steward, D. J. Kelly, Mechanical regulation of mesenchymal stem cell differentiation. *Journal of anatomy* **227**, 717-731 (2015).

249. C. W. Peak, S. Nagar, R. D. Watts, G. Schmidt, Robust and Degradable Hydrogels from Poly(ethylene glycol) and Semi-Interpenetrating Collagen. *Macromolecules* **47**, 6408-6417 (2014).

250. J. Lou, R. Stowers, S. Nam, Y. Xia, O. Chaudhuri, Stress relaxing hyaluronic acid-collagen hydrogels promote cell spreading, fiber remodeling, and focal adhesion formation in 3D cell culture. *Biomaterials* **154**, 213-222 (2018).

251. Y. S. Zhang, A. Khademhosseini, Advances in engineering hydrogels. *Science* **356**, eaaf3627 (2017).

252. R. F. Pereira, P. J. Bártolo, 3D bioprinting of photocrosslinkable hydrogel constructs. *Journal of Applied Polymer Science* **132** (2015).

253. H. Shirahama, B. H. Lee, L. P. Tan, N.-J. Cho, Precise tuning of facile one-pot gelatin methacryloyl (GeLMA) synthesis. *Scientific reports* **6**, 31036 (2016).

254. B. H. Lee, H. Shirahama, N.-J. Cho, L. P. Tan, Efficient and controllable synthesis of highly substituted gelatin methacrylamide for mechanically stiff hydrogels. *RSC Advances* **5**, 106094-106097 (2015).

255. W. Liu *et al.*, Extrusion Bioprinting of Shear-Thinning Gelatin Methacryloyl Bioinks. *Advanced Healthcare Materials* **6** (2017).

256. B. J. Klotz, D. Gawlitta, A. J. Rosenberg, J. Malda, F. P. Melchels, Gelatin-Methacryloyl Hydrogels: Towards Biofabrication-Based Tissue Repair. *Trends in biotechnology* **34**, 394-407 (2016).

257. L. E. Bertassoni *et al.*, Direct-write bioprinting of cell-laden methacrylated gelatin hydrogels. *Biofabrication* **6**, 024105 (2014).

258. L. Ouyang, C. B. Highley, W. Sun, J. A. Burdick, A Generalizable Strategy for the 3D Bioprinting of Hydrogels from Nonviscous Photo-crosslinkable Inks. *Advanced Materials* **29** (2017).

259. K. Yue *et al.*, Synthesis, properties, and biomedical applications of gelatin methacryloyl (GelMA) hydrogels. *Biomaterials* **73**, 254-271 (2015).

260. A. Thakur *et al.*, Injectable shear-thinning nanoengineered hydrogels for stem cell delivery. *Nanoscale* (2016).

261. S. M. Mihaila *et al.*, Photocrosslinkable Kappa-Carrageenan Hydrogels for Tissue Engineering Applications. *Advanced healthcare materials* **2**, 895-907 (2013).

262. M. Rizwan *et al.*, Sequentially-crosslinked bioactive hydrogels as nano-patterned substrates with customizable stiffness and degradation for corneal tissue engineering applications. *Biomaterials* **120**, 139-154 (2017).

263. S. Bertlein *et al.*, Thiol–Ene Clickable Gelatin: A Platform Bioink for Multiple 3D Biofabrication Technologies. *Advanced Materials* (2017).

264. S. Stichler, S. Bertlein, J. Tessmar, T. Jüngst, J. Groll (2017) Thiol-ene Cross-Linkable Hydrogels as Bioinks for Biofabrication. in *Macromolecular Symposia* (Wiley Online Library), pp 102-107.

265. T. E. Brown, K. S. Anseth, Spatiotemporal hydrogel biomaterials for regenerative medicine. *Chemical Society Reviews* **46**, 6532-6552 (2017).

266. S. Stichler *et al.*, Thiol-ene clickable poly (glycidol) hydrogels for biofabrication. *Ann Biomed Eng* **45**, 273-285 (2017).

267. M. W. Tibbitt, A. M. Kloxin, L. A. Sawicki, K. S. Anseth, Mechanical properties and degradation of chain and step-polymerized photodegradable hydrogels. *Macromolecules* **46**, 2785-2792 (2013).

268. K. Vats *et al.*, Nanoscale physicochemical properties of chain-and step-growth polymerized PEG hydrogels affect cell-material interactions. *Journal of Biomedical Materials Research Part A* **105**, 1112-1122 (2017).

269. S. Das *et al.*, Bioprintable, cell-laden silk fibroin–gelatin hydrogel supporting multilineage differentiation of stem cells for fabrication of three-dimensional tissue constructs. *Acta biomaterialia* **11**, 233-246 (2015).

270. Y. Shi *et al.*, Tyrosinase-doped bioink for 3D bioprinting of living skin constructs. *Biomedical Materials* **13**, 035008 (2018).

271. C. B. Highley, C. B. Rodell, J. A. Burdick, Direct 3D Printing of Shear-Thinning Hydrogels into Self-Healing Hydrogels. *Advanced Materials* 10.1002/adma.201501234, n/a-n/a (2015).

272. J. L. Mann, C. Y. Anthony, G. Agmon, E. A. Appel, Supramolecular polymeric biomaterials. *Biomaterials science* (2018).

273. E. A. Appel, J. del Barrio, X. J. Loh, O. A. Scherman, Supramolecular polymeric hydrogels. *Chemical Society Reviews* **41**, 6195-6214 (2012).

274. S. Seiffert, J. Sprakel, Physical chemistry of supramolecular polymer networks. *Chemical Society Reviews* **41**, 909-930 (2012).

275. T. Lorson *et al.*, A Thermogelling Supramolecular Hydrogel with Sponge-Like Morphology as a Cytocompatible Bioink. *Biomacromolecules* **18**, 2161-2171 (2017).

276. X. Dai *et al.*, A Mechanically Strong, Highly Stable, Thermoplastic, and self-healable supramolecular polymer hydrogel. *Advanced Materials* **27**, 3566-3571 (2015).

277. C. Loebel, C. B. Rodell, M. H. Chen, J. A. Burdick, Shear-thinning and self-healing hydrogels as injectable therapeutics and for 3D-printing. *nature protocols* **12**, 1521 (2017).

278. L. Ouyang, C. B. Highley, C. B. Rodell, W. Sun, J. A. Burdick, 3D Printing of Shear-Thinning Hyaluronic Acid Hydrogels with Secondary Cross-Linking. *ACS Biomaterials Science & Engineering* **2**, 1743-1751 (2016).

279. C. B. Rodell, N. N. Dusaj, C. B. Highley, J. A. Burdick, Injectable and Cytocompatible Tough Double-Network Hydrogels through Tandem Supramolecular and Covalent Crosslinking. *Advanced Materials* **28**, 8419-8424 (2016).

280. K. Liu *et al.*, Coordination-Triggered Hierarchical Folate/Zinc Supramolecular Hydrogels Leading to Printable Biomaterials. *ACS applied materials & interfaces* **10**, 4530-4539 (2018).

281. M. Shin, J. H. Galarraga, M. Y. Kwon, H. Lee, J. A. Burdick, Gallol-derived ECM-mimetic adhesive bioinks exhibiting temporal shear-thinning and stabilization behavior. *Acta Biomaterialia* https://doi.org/10.1016/j.actbio.2018.10.028 (2018).

282. C. Li *et al.*, Rapid Formation of a Supramolecular Polypeptide–DNA Hydrogel for In Situ Three-Dimensional Multilayer Bioprinting. *Angewandte Chemie International Edition* **54**, 3957-3961 (2015).

283. J. P. Gong, Materials both tough and soft. *Science* **344**, 161-162 (2014).

284. Q. Chen, H. Chen, L. Zhu, J. Zheng, Engineering of tough double network hydrogels. *Macromolecular Chemistry and Physics* **217**, 1022-1036 (2016).

285. D. Wu *et al.*, 3D bioprinting of gellan gum and poly (ethylene glycol) diacrylate based hydrogels to produce human-scale constructs with high-fidelity. *Materials & Design* **160**, 486-495 (2018).

286. L. L. Wang *et al.*, 3D extrusion bioprinting of single-and double-network hydrogels containing dynamic covalent crosslinks. *Journal of Biomedical Materials Research Part A* (2018).

287. F. Bonaccorso *et al.*, Graphene, related two-dimensional crystals, and hybrid systems for energy conversion and storage. *Science* **347**, 1246501 (2015).

288. X. Zhai *et al.*, 3D-printed high strength bioactive supramolecular polymer/clay nanocomposite hydrogel scaffold for bone regeneration. *ACS Biomaterials Science & Engineering* **3**, 1109-1118 (2017).

289. X. Zhai *et al.*, 3D-Bioprinted Osteoblast-Laden Nanocomposite Hydrogel Constructs with Induced Microenvironments Promote Cell Viability, Differentiation, and Osteogenesis both In Vitro and In Vivo. *Advanced Science* (2017).

290. A. Klein, P. G. Whitten, K. Resch, G. Pinter, Nanocomposite hydrogels: Fracture toughness and energy dissipation mechanisms. *Journal of Polymer Science Part B: Polymer Physics* **53**, 1763-1773 (2015).

291. H. Xin, H. R. Brown, S. Naficy, G. M. Spinks, Mechanical recoverability and damage process of ionic-covalent PAAm-alginate hybrid hydrogels. *Journal of Polymer Science Part B: Polymer Physics* **54**, 53-63 (2016).

292. M. Izadifar, D. Chapman, P. Babyn, X. Chen, M. E. Kelly, UV-Assisted 3D Bioprinting of Nanoreinforced Hybrid Cardiac Patch for Myocardial Tissue Engineering. *Tissue Engineering Part C: Methods* (2017).

293. X. Zhou *et al.*, 3D bioprinted graphene oxide-incorporated matrix for promoting chondrogenic differentiation of human bone marrow mesenchymal stem cells. *Carbon* **116**, 615-624 (2017).

294. S. R. Shin *et al.*, Reduced graphene oxide-gelMA hybrid hydrogels as scaffolds for cardiac tissue engineering. *Small* **12**, 3677-3689 (2016).

295. C.-T. Huang, L. K. Shrestha, K. Ariga, S.-h. Hsu, A graphene–polyurethane composite hydrogel as a potential bioink for 3D bioprinting and differentiation of neural stem cells. *Journal of Materials Chemistry B* (2017).

296. J. Yang, C.-R. Han, J.-F. Duan, F. Xu, R.-C. Sun, Mechanical and Viscoelastic Properties of Cellulose Nanocrystals Reinforced Poly(ethylene glycol) Nanocomposite Hydrogels. *ACS Applied Materials & Interfaces* **5**, 3199-3207 (2013).

297. G. Chinga-Carrasco, Potential and limitations of nanocelluloses as components in biocomposite inks for three-dimensional bioprinting and for biomedical devices. *Biomacromolecules* **19**, 701-711 (2018).

298. S. Shin *et al.*, Cellulose Nanofibers for the Enhancement of Printability of Low Viscosity Gelatin Derivatives. *BioResources* **12**, 2941-2954 (2017).

299. K. Markstedt *et al.*, 3D bioprinting human chondrocytes with nanocellulose–alginate bioink for cartilage tissue engineering applications. *Biomacromolecules* **16**, 1489-1496 (2015).

300. A. Habib, V. Sathish, S. Mallik, B. Khoda, 3D printability of alginate-carboxymethyl cellulose hydrogel. *Materials* **11**, 454 (2018).

301. N. Law *et al.*, Characterisation of hyaluronic acid methylcellulose hydrogels for 3D bioprinting. *Journal of the Mechanical Behavior of Biomedical Materials* **77**, 389-399 (2018).

302. C. S. Wyss, P. Karami, P.-E. Bourban, D. P. Pioletti, Cyclic loading of a cellulose/hydrogel composite increases its fracture strength. *Extreme Mechanics Letters* **24**, 66-74 (2018).

303. D. Tuğrul Tolga, I. Gülseren, G. Menemşe, A bioprintable form of chitosan hydrogel for bone tissue engineering. *Biofabrication* **9**, 035003 (2017).

304. S. T. Bendtsen, S. P. Quinnell, M. Wei, Development of a novel alginate-polyvinyl alcohol-hydroxyapatite hydrogel for 3D bioprinting bone tissue engineered scaffolds. *Journal of Biomedical Materials Research Part A* **105**, 1457-1468 (2017).

305. M. Lee *et al.*, Exploitation of Cationic Silica Nanoparticles for Bioprinting of Large-Scale Constructs with High Printing Fidelity. *ACS Applied Materials & Interfaces* 10.1021/acsami.8b13166 (2018).

306. E. A. Appel *et al.*, Self-assembled hydrogels utilizing polymer–nanoparticle interactions. *Nature communications* **6**, 6295 (2015).

307. J. Wolfram *et al.*, Safety of nanoparticles in medicine. *Current drug targets* **16**, 1671-1681 (2015).

308. H.-W. Kang *et al.*, A 3D bioprinting system to produce human-scale tissue constructs with structural integrity. *Nature biotechnology* **34**, 312-319 (2016).

309. K. Zhang *et al.*, 3D bioprinting of urethra with PCL/PLCL blend and dual autologous cells in fibrin hydrogel: An in vitro evaluation of biomimetic mechanical property and cell growth environment. *Acta Biomaterialia* **50**, 154-164 (2017).

310. C.-S. Chen *et al.*, Three-Dimensionally Printed Silk-Sericin-Based Hydrogel Scaffold: A Promising Visualized Dressing Material for Real-Time Monitoring of Wounds. *ACS Applied Materials & Interfaces* **10**, 33879-33890 (2018).

311. X. Tong, F. Yang, Sliding hydrogels with mobile molecular ligands and crosslinks as 3D stem cell niche. *Advanced Materials* **28**, 7257-7263 (2016).

312. I. Bin, Molecular weight dependency of polyrotaxane-cross-linked polymer gel extensibility. *Chemical Communications* **52**, 13757-13759 (2016).

313. L. Jiang *et al.*, Highly Stretchable and Instantly Recoverable Slide-Ring Gels Consisting of Enzymatically Synthesized Polyrotaxane with Low Host Coverage. *Chemistry of Materials* **30**, 5013-5019 (2018).

314. A. Sheikhi *et al.*, Microfluidic-enabled bottom-up hydrogels from annealable naturally-derived protein microbeads. *Biomaterials* **192**, 560-568 (2019).

315. J. M. de Rutte, J. Koh, D. Di Carlo, Hydrogels: Scalable High-Throughput Production of Modular Microgels for In Situ Assembly of Microporous Tissue Scaffolds (Adv. Funct. Mater. 25/2019). *Advanced Functional Materials* **29**, 1970174 (2019).

316. L. Riley, L. Schirmer, T. Segura, Granular hydrogels: emergent properties of jammed hydrogel microparticles and their applications in tissue repair and regeneration. *Current Opinion in Biotechnology* **60**, 1-8 (2019).

317. O. Jeon, Y. B. Lee, T. J. Hinton, A. W. Feinberg, E. Alsberg, Cryopreserved cell-laden alginate microgel bioink for 3D bioprinting of living tissues. *Materials Today Chemistry* **12**, 61-70 (2019).

318. S. Xin, D. Chimene, J. E. Garza, A. K. Gaharwar, D. L. Alge, Clickable PEG hydrogel microspheres as building blocks for 3D bioprinting. *J Biomaterials Science* **7**, 1179-1187 (2019).

319. C. B. Highley, K. H. Song, A. C. Daly, J. A. Burdick, Jammed Microgel Inks for 3D Printing Applications. *Advanced Science* 10.1002/advs.201801076 (2018).

320. J. E. Mealy *et al.*, Injectable Granular Hydrogels with Multifunctional Properties for Biomedical Applications. *Advanced Materials* **30**, 1705912 (2018).

321. D. R. Griffin, W. M. Weaver, P. O. Scumpia, D. Di Carlo, T. Segura, Accelerated wound healing by injectable microporous gel scaffolds assembled from annealed building blocks. *Nature Materials* **14**, 737-744 (2015).

322. J. L. Daristotle, A. M. Behrens, A. D. Sandler, P. Kofinas, A review of the fundamental principles and applications of solution blow spinning. *ACS applied materials & interfaces* **8**, 34951-34963 (2016).

323. J. Visser *et al.*, Reinforcement of hydrogels using three-dimensionally printed microfibres. *Nature communications* **6**, 6933 (2015).

324. O. Bas *et al.*, Enhancing structural integrity of hydrogels by using highly organised melt electrospun fibre constructs. *European Polymer Journal* **72**, 451-463 (2015).

325. O. Bas *et al.*, Biofabricated soft network composites for cartilage tissue engineering. *Biofabrication* **9**, 025014 (2017).

326. O. Bas *et al.*, Rational design and fabrication of multiphasic soft network composites for tissue engineering articular cartilage: a numerical model-based approach. *Chemical Engineering Journal* (2018).

327. P. D. Dalton, Melt electrowriting with additive manufacturing principles. *Current Opinion in Biomedical Engineering* **2**, 49-57 (2017).

328. A. M. Behrens *et al.*, In situ deposition of PLGA nanofibers via solution blow spinning. *ACS Macro Letters* **3**, 249-254 (2014).

329. C. Chen, A. D. Townsend, S. A. Sell, R. S. Martin, Microchip-based 3D-cell culture using polymer nanofibers generated by solution blow spinning. *Analytical Methods* **9**, 3274-3283 (2017).

330. B. Derby, Printing and prototyping of tissues and scaffolds. *Science* **338**, 921-926 (2012).

331. A. Khademhosseini, R. Langer, A decade of progress in tissue engineering. *Nature Protocols* **11**, 1775-1781 (2016).

332. R. D. Farahani, M. Dubé, D. Therriault, Three-Dimensional Printing of Multifunctional Nanocomposites: Manufacturing Techniques and Applications. *Advanced Materials* **28**, 5794-5821 (2016).

333. D. Chimene, L. K. Kimberly, R. R. Kaunas, A. K. Gaharwar, Advanced Bioinks for 3D Printing: A Materials Science Perspective. *Annals of Biomedical Engineering*, DOI: 10.1007/s10439-10016-11638-y (2016).

334. Y. He *et al.*, Research on the printability of hydrogels in 3D bioprinting. *Scientific Reports* **6**, 29977 (2016).

335. W. Liu *et al.*, Rapid Continuous Multimaterial Extrusion Bioprinting. *Advanced Materials* **29**, 1604630 (2017).

336. C. B. Highley, C. B. Rodell, J. A. Burdick, Direct 3D printing of shear-thinning hydrogels into self-healing hydrogels. *Advanced Materials* **27**, 5075-5079 (2015).

337. C. Colosi *et al.*, Microfluidic Bioprinting of Heterogeneous 3D Tissue Constructs Using Low-Viscosity Bioink. *Advanced Materials* **28**, 677-684 (2016).

338. W. Jia *et al.*, Direct 3D Bioprinting of Perfusable Vascular Constructs Using a Blend Bioink. *Biomaterials* (2016).

339. Q. Wang *et al.*, High-water-content mouldable hydrogels by mixing clay and a dendritic molecular binder. *Nature* **463**, 339-343 (2010).

340. J.-Y. Sun *et al.*, Highly stretchable and tough hydrogels. *Nature* **489**, 133-136 (2012).

341. S. E. Bakarich, M. i. h. Panhuis, S. Beirne, G. G. Wallace, G. M. Spinks, Extrusion printing of ionic-covalent entanglement hydrogels with high toughness. *Journal of Materials Chemistry B* **1**, 4939-4946 (2013).

342. K. R. Shull, Materials science: A hard concept in soft matter. *Nature* **489**, 36-37 (2012).

343. P. Matricardi, C. Di Meo, T. Coviello, W. E. Hennink, F. Alhaique, Interpenetrating Polymer Networks polysaccharide hydrogels for drug delivery and tissue engineering. *Advanced Drug Delivery Reviews* **65**, 1172-1187 (2013).

344. E. Jabbari, J. Leijten, Q. Xu, A. Khademhosseini, The matrix reloaded: the evolution of regenerative hydrogels. *Materials Today* **19**, 190-196 (2016).

345. M. R. Mangione *et al.*, K+ and Na+ effects on the gelation properties of κ-Carrageenan. *Biophysical Chemistry* **113**, 129-135 (2005).

346. S. Liu, L. Li, Recoverable and Self-Healing Double Network Hydrogel Based on κ-Carrageenan. *ACS Applied Materials & Interfaces* **8**, 29749-29758 (2016).

347. L. Stevens, P. Calvert, G. G. Wallace, Ionic-covalent entanglement hydrogels from gellan gum, carrageenan and an epoxy-amine. *Soft Matter* **9**, 3009-3012 (2013).

348. M. Ghadiri, W. Chrzanowski, R. Rohanizadeh, Antibiotic eluting clay mineral (Laponite®) for wound healing application: An in vitro study. *Journal of Materials Science: Materials in Medicine* **25**, 2513-2526 (2014).

349. L. M. Marquardt, S. C. Heilshorn, Design of Injectable Materials to Improve Stem Cell Transplantation. *Current Stem Cell Reports* 10.1007/s40778-016-0058-0, 1-14 (2016).

350. K. Nair *et al.*, Characterization of cell viability during bioprinting processes. *Biotechnology journal* **4**, 1168-1177 (2009).

351. X. Lu *et al.*, Super-tough and thermo-healable hydrogel - promising for shape-memory absorbent fiber. *Journal of Materials Chemistry B* **2**, 7631-7638 (2014).

352. D. F. D. Campos *et al.*, Three-dimensional printing of stem cell-laden hydrogels submerged in a hydrophobic high-density fluid. *Biofabrication* **5**, 015003 (2012).

353. Y. Shanjani, C. Pan, L. Elomaa, Y. Yang, A novel bioprinting method and system for forming hybrid tissue engineering constructs. *Biofabrication* **7**, 045008 (2015).

354. T. Thakur *et al.*, Photocrosslinkable and elastomeric hydrogels for bone regeneration. *Journal of Biomedical Materials Research Part A* **104**, 879-888 (2016).

355. J. W. Nichol *et al.*, Cell-laden microengineered gelatin methacrylate hydrogels. *Biomaterials* **31**, 5536-5544 (2010).

356. L. M. Cross, A. Thakur, N. A. Jalili, M. Detamore, A. K. Gaharwar, Nanoengineered biomaterials for repair and regeneration of orthopedic tissue interfaces. *Acta Biomaterialia* **42**, 2-17 (2016).

357. T. Yeung *et al.*, Effects of substrate stiffness on cell morphology, cytoskeletal structure, and adhesion. *Cell motility and the cytoskeleton* **60**, 24-34 (2005).

358. E. Kaemmerer *et al.*, Gelatine methacrylamide-based hydrogels: an alternative three-dimensional cancer cell culture system. *Acta biomaterialia* **10**, 2551-2562 (2014).

359. V. Campana *et al.*, Bone substitutes in orthopaedic surgery: from basic science to clinical practice. *Journal of materials science. Materials in medicine* **25**, 2445-2461 (2014).

360. D. Chimene, R. Kaunas, A. K. Gaharwar, Hydrogel Bioink Reinforcement for Additive Manufacturing: A Focused Review of Emerging Strategies. *Advanced Materials*, In press (2019).

361. D. Chimene, R. Kaunas, A. K. Gaharwar, Hydrogel Bioink Reinforcement for Additive Manufacturing: A Focused Review of Emerging Strategies. (2019).

362. A. Paul *et al.*, Nanoengineered biomimetic hydrogels for guiding human stem cell osteogenesis in three dimensional microenvironments. *Journal of Materials Chemistry B* **4**, 3544-3554 (2016).

363. T. Zhang *et al.*, Regulating osteogenesis and adipogenesis in adipose-derived stem cells by controlling underlying substrate stiffness. *Journal of cellular physiology* **233**, 3418-3428 (2017).

364. F.-M. Chen, X. Liu, Advancing biomaterials of human origin for tissue engineering. *Progress in Polymer Science* **53**, 86-168 (2016).

365. D. Loessner *et al.*, Functionalization, preparation and use of cell-laden gelatin methacryloyl–based hydrogels as modular tissue culture platforms. *Nature Protocols* **11**, 727 (2016).

366. J. S. Lowe, P. G. Anderson, "Chapter 13 - Musculoskeletal System" in Stevens & Lowe's Human Histology (Fourth Edition) (Fourth Edition), J. S. Lowe, P. G. Anderson, Eds.

(Mosby, Philadelphia, 2015), https://doi.org/10.1016/B978-0-7234-3502-0.00013-9, pp. 239-262.

367. Y. An, K. L. Martin, *Handbook of Histology Methods for Bone and Cartilage* (2003), 10.1007/978-1-59259-417-7.

368. B. Bergmann, J. Mölne, I. Gjertsson, The Bone-Inflammation-Cartilage (BIC) Stain: A Novel Staining Method Combining Safranin O and Van Gieson's Stains. *J Histochem Cytochem* **63**, 737-740 (2015).

369. R. F. De Godoy, S. Hutchens, C. Campion, G. Blunn, Silicate-substituted calcium phosphate with enhanced strut porosity stimulates osteogenic differentiation of human mesenchymal stem cells. *Journal of Materials Science: Materials in Medicine* **26**, 54 (2015).

370. J. Shendure, The beginning of the end for microarrays? *Nat Methods* **5**, 585-587 (2008).

371. N. Cloonan *et al.*, Stem cell transcriptome profiling via massive-scale mRNA sequencing. *Nat Methods* **5**, 613-619 (2008).

372. A. Mortazavi, B. A. Williams, K. McCue, L. Schaeffer, B. Wold, Mapping and quantifying mammalian transcriptomes by RNA-Seq. *Nat Methods* **5**, 621-628 (2008).

373. J. K. Carrow *et al.*, Widespread changes in transcriptome profile of human mesenchymal stem cells induced by two-dimensional nanosilicates. *Proceedings of the National Academy of Sciences* **115**, E3905-E3913 (2018).

374. A. Rutkovskiy, K.-O. Stensløkken, I. J. Vaage, Osteoblast Differentiation at a Glance. *Med Sci Monit Basic Res* **22**, 95-106 (2016).

375. M. Wu, G. Chen, Y.-P. Li, TGF-β and BMP signaling in osteoblast, skeletal development, and bone formation, homeostasis and disease. *Bone Research* **4**, 16009 (2016).

376. R. Bortell, L. M. Barone, M. S. Tassinari, J. B. Lian, G. S. Stein, Gene expression during endochondral bone development: Evidence for coordinate expression of transforming growth factor β1 and collagen type I. *Journal of Cellular Biochemistry* **44**, 81-91 (1990).

377. A. M. Hermansson, E. Eriksson, E. Jordansson, Effects of potassium, sodium and calcium on the microstructure and rheological behaviour of kappa-carrageenan gels. *Carbohydrate Polymers* **16**, 297-320 (1991).